CORA Cork Open Research Archive
Cartlann Taighde Oscailte Chorcaí

| | |
|---|---|
| Title | Thermoelectric properties of PbTe-based materials driven near the ferroelectric phase transition from first principles |
| Authors | Murphy, Aoife Rose |
| Publication date | 2017 |
| Original Citation | Murphy, A. R. 2017. Thermoelectric properties of PbTe-based materials driven near the ferroelectric phase transition from first principles. PhD Thesis, University College Cork. |
| Type of publication | Doctoral thesis |
| Rights | © 2017, Aoife Rose Murphy. - http://creativecommons.org/licenses/by-nc-nd/3.0/ |
| Download date | 2026-11-01 22:23:40 |
| Item downloaded from | https://hdl.handle.net/10468/5893 |

UCC
University College Cork, Ireland
Coláiste na hOllscoile Corcaigh

# Thermoelectric Properties of PbTe-based Materials Driven Near the Ferroelectric Phase Transition from First Principles

Aoife Rose Murphy
B.Sc.

**Thesis submitted for the degree of**
**Doctor of Philosophy**



NATIONAL UNIVERSITY OF IRELAND, CORK
College of Science, Engineering and Food Science
Department of Physics
Tyndall National Institute

October, 2017

Head of Department: Prof. John G. McInerney

Supervisors: Dr. Ivana Savić
Prof. Stephen Fahy

# Contents

List of Figures . . . iv
List of Tables . . . xiv
Acknowledgements . . . xviii
Abstract . . . xix

**1 Introduction 1**
1.1 Thermoelectric materials . . . 1
1.2 Optimising thermoelectric performance . . . 5
1.3 *Ab initio* calculation of thermoelectric transport properties . . . 8
1.3.1 Lattice thermal conductivity . . . 9
1.3.2 Electronic thermoelectric properties . . . 11
1.4 Thesis outline . . . 13

**2 Computational Methods 15**
2.1 Total energy calculations . . . 15
2.1.1 Many-body Hamiltonian . . . 15
2.1.2 Density functional theory . . . 17
2.1.2.1 Hohenberg-Kohn theorems . . . 17
2.1.2.2 Kohn-Sham equations . . . 18
2.1.3 Plane waves . . . 19
2.1.4 Pseudopotential approximation . . . 21
2.1.5 Exchange-correlation functional . . . 22
2.1.6 Structural relaxation . . . 23
2.2 Lattice thermal conductivity . . . 24
2.2.1 Crystal potential . . . 24
2.2.2 Dynamical matrix . . . 25
2.2.3 Second quantisation . . . 26
2.2.4 Boltzmann transport equation . . . 28
2.2.5 Anharmonic phonon lifetimes . . . 31
2.2.6 Phonon lifetimes due to mass disorder . . . 35
2.2.7 Implementation . . . 37
2.3 Charge carrier mobility . . . 38
2.3.1 Boltzmann transport equation . . . 38
2.3.2 Electron-phonon coupling . . . 41
2.3.3 Density functional perturbation theory . . . 44

**3 Lattice thermal conductivity of PbTe-based materials driven near the ferroelectric phase transition 47**
3.1 Introduction . . . 47
3.1.1 Motivation . . . 47
3.1.2 Calculation details . . . 48
3.1.3 Verification of approach . . . 49
3.2 PbTe materials driven near the phase transition . . . 50
3.2.1 Strained PbTe . . . 50
3.2.2 Strained $PbSe_{0.5}Te_{0.5}$ alloy . . . 51

3.2.3 $Pb_{1-x}Ge_xTe$ alloys . . . 52
3.3 Impact on phonon lifetimes . . . 53
3.3.1 Strained PbTe . . . 53
3.3.2 Strained $PbSe_{0.5}Te_{0.5}$ alloy . . . 54
3.3.3 $Pb_{0.51}Ge_{0.49}Te$ alloy . . . 55
3.3.4 Impact of soft TO mode . . . 57
3.4 Impact on thermal conductivity . . . 62
3.4.1 Strained PbTe . . . 62
3.4.2 Strained $PbSe_{0.5}Te_{0.5}$ alloy . . . 63
3.4.3 $Pb_{0.51}Ge_{0.49}Te$ alloy . . . 64
3.4.4 Impact to phonon mean free paths . . . 66
3.5 Discussion . . . 67
3.5.1 Higher order anharmonicity . . . 67
3.5.2 Phase segregation . . . 68
3.6 Summary . . . 68

**4 Lattice thermal conductivity of $Pb_{1-x}Ge_xTe$ alloys 70**
4.1 Introduction . . . 70
4.1.1 Motivation . . . 70
4.1.2 Calculation details . . . 71
4.1.3 Verification of approach . . . 72
4.2 $Pb_{1-x}Ge_xTe$ and the ferroelectric phase transition . . . 79
4.2.1 Virtual crystal model . . . 79
4.2.2 Impact on phonon frequencies . . . 81
4.3 Impact on phonon lifetimes . . . 85
4.4 Impact on thermal conductivity . . . 89
4.4.1 $Pb_{1-x}Ge_xTe$ alloys . . . 89
4.4.2 Frequency contribution to thermal conductivity . . . 92
4.4.3 Impact of structure and resonant bonding . . . 94
4.5 Discussion . . . 99
4.5.1 Temperature dependence . . . 99
4.5.2 Structure of $Pb_{1-x}Ge_xTe$ alloys . . . 100
4.6 Summary . . . 101

**5 Electron-phonon coupling and mobility of $n$-type Ge and PbTe 103**
5.1 Introduction . . . 103
5.2 Electronic band structure of Ge and PbTe . . . 104
5.3 Modelling electronic mobility . . . 110
5.4 Electron-phonon coupling . . . 111
5.4.1 Intervalley and intravalley optical scattering . . . 112
5.4.2 Intravalley acoustic scattering . . . 115
5.4.2.1 Deformation potential theory . . . 115
5.4.2.2 Deformation potentials of Ge and PbTe . . . 119
5.4.3 Fröhlich interaction . . . 121
5.5 Electron mobility . . . 123
5.6 Electronic band structure from hybrid functionals . . . 126

5.7 Deformation potentials from band shifts due to strain using hybrid functionals . . . . . 131
5.7.1 Uniaxial deformation potential . . . . . 131
5.7.2 Dilatation deformation potential . . . . . 133
5.8 Electronic properties of PbTe-based materials near the phase transition . . . . . 138
5.9 Summary . . . . . 139

**6 Conclusion** **140**
6.1 Conclusion . . . . . 140
6.2 Outlook . . . . . 143

**Bibliography** **145**

# List of Figures

1.1 (a): A model thermoelectric device used to generate electricity from a heat source. (b) A model thermoelectric device used to pump heat when an electric current is applied. . . . . 2
1.2 Thermoelectric power generation efficiency versus temperature of the hot side, taking the cold side as room temperature, for several values of $ZT_{\text{avg}}$. The yellow region highlights the efficiency of some typical thermoelectric power generators available today and their approximate range of operating temperatures. Also included are the efficiencies of several conventional mechanical heat engines as well as the Carnot limit. Adapted from Refs. [11, 12, 13]. . . . . 3

2.1 Sketch showing the Coulomb potential and real wavefunction in blue compared to the pseudopotential and pseudowavefunction in red, which match beyond the cut-off radius $r_c$. . . . . 21
2.2 Allowed three-phonon scattering processes given energy and momentum conservation constraints. . . . . 32
2.3 (a): Normal scattering, and (b): Umklapp scattering for class 1 events. . . . . 33
2.4 Allowed electron-phonon scattering processes to first order in the atomic displacement. . . . . 42

3.1 Phonon dispersions of PbTe: calculated using a 216 atom supercell at 0 K (solid black line), calculated using a 64 atom supercell at 0 K (dashed red line), and measured by Cochran *et al.* [153] at 300 K (blue circles). . . . . 49
3.2 Lattice thermal conductivity of PbTe as a function of temperature: calculated using a supercell with 216 atoms (solid black line), calculated using a supercell with 64 atoms (dashed red line), and measured by Devyatkova *et al.* [154] (blue circles) and by El-Sharkawy *et al.* [155] (green rectangles). . . . . 49
3.3 Phonon dispersions at 0 K for PbTe (solid black lines) and PbTe driven to the verge of the phase transition by tensile (001) strain of $\eta = 1.15\%$ (dashed red lines). Frequencies of the soft transverse optical modes at the zone centre, TO($\Gamma$), are represented with circles for PbTe, and rectangles/diamonds for PbTe driven to the transition. . . . . 51
3.4 Phonon dispersions at 0 K for $PbSe_{0.5}Te_{0.5}$ (solid black lines) and $PbSe_{0.5}Te_{0.5}$ driven to the verge of the phase transition by tensile (001) strain of $\eta = 1.32\%$ (dashed red lines). TO($\Gamma$) frequencies are shown in circles for $PbSe_{0.5}Te_{0.5}$, and rectangles/diamonds for $PbSe_{0.5}Te_{0.5}$ driven to the transition. Phonon dispersions for alloys were calculated using the virtual crystal approximation. . . . . 52

3.5 Phonon dispersions at 0 K for PbTe (solid black lines), $PbSe_{0.5}Te_{0.5}$ (dash-dotted blue lines), and $Pb_{0.51}Ge_{0.49}Te$ alloy at the verge of the phase transition (dashed red lines). TO(Γ) frequencies are represented with circles for PbTe, diamonds for $PbSe_{0.5}Te_{0.5}$, and rectangles for $Pb_{0.51}Ge_{0.49}Te$. Phonon dispersions for alloys were calculated using the virtual crystal approximation. . . . . 52
3.6 Anharmonic phonon lifetimes at 300 K and their averaged values (inset) as a function of frequency for PbTe (black pluses and solid line) and PbTe driven to the verge of the phase transition by tensile (001) strain of $\eta = 1.15\%$ (red crosses and dashed line). . . . . 54
3.7 Anharmonic phonon lifetimes at 300 K and their averaged values (inset) as a function of frequency for $PbSe_{0.5}Te_{0.5}$ (black pluses and solid line) and $PbSe_{0.5}Te_{0.5}$ driven to the verge of the phase transition by tensile (001) strain of $\eta = 1.32\%$ (red crosses and dashed line). . . . . 55
3.8 Frequency dependence of the mass disorder and phonon-phonon contributions to the phonon lifetimes (black pluses and red crosses, respectively) of $PbSe_{0.5}Te_{0.5}$ driven to the verge of the phase transition by tensile (001) strain of $\eta = 1.32\%$. . . . . 55
3.9 Anharmonic phonon lifetimes at 300 K and their averaged values (inset) as a function of frequency for PbTe (black pluses and solid line), $PbSe_{0.5}Te_{0.5}$ (blue crosses and dash-dotted line), and $Pb_{0.51}Ge_{0.49}Te$ alloy at the verge of the phase transition (red circles and dashed line). . . . . 56
3.10 Frequency dependence of the mass disorder and three-phonon contributions to the phonon lifetimes at 300 K (black pluses and red crosses, respectively) of $Pb_{0.51}Ge_{0.49}Te$ alloy at the verge of the phase transition. . . . . 56
3.11 The total anharmonic linewidth at 300 K as a function of frequency (black crosses) together with its contribution from the scattering processes that involve both acoustic and transverse optical (TO) modes (red crosses) and the contribution from all other scattering processes (green crosses) for (a) acoustic modes in PbTe, (b) optical modes in PbTe, (c) acoustic modes in strained PbTe, (d) optical modes in strained PbTe, (e) acoustic modes in $Pb_{0.51}Ge_{0.49}Te$, and (f) optical modes in $Pb_{0.51}Ge_{0.49}Te$. The acoustic-TO contribution to the anharmonic linewidth dominates over the other contributions in all these materials. . . . . 58

3.12 The ratio of the acoustic-transverse optical (TO) contribution to the total anharmonic linewidth of strained PbTe and $Pb_{0.51}Ge_{0.49}Te$ with respect to PbTe at 300 K versus mode frequency of strained PbTe and $Pb_{0.51}Ge_{0.49}Te$, respectively. (a) Acoustic modes in strained PbTe, (b) optical modes in strained PbTe, (c) acoustic modes in $Pb_{0.51}Ge_{0.49}Te$, and (d) optical modes in $Pb_{0.51}Ge_{0.49}Te$. The acoustic-TO contribution to the anharmonic linewidth of the materials driven near phase transitions is larger than that of PbTe. . . . . 59
3.13 The total anharmonic linewidth at 300 K as a function of frequency (black crosses) together with its contribution from the scattering processes that involve both acoustic and transverse optical modes close to the zone centre (labelled as $TO_1$ modes, see text for explanation) (red crosses) and the contribution from all other scattering processes (green crosses) for (a) acoustic modes in PbTe, (b) optical modes in PbTe, (c) acoustic modes in strained PbTe, (d) optical modes in strained PbTe, (e) acoustic modes in $Pb_{0.51}Ge_{0.49}Te$, and (f) optical modes in $Pb_{0.51}Ge_{0.49}Te$. The frequencies of $TO_1$ modes correspond to red crosses within black boxes. The acoustic-$TO_1$ contribution represents a considerable fraction of the anharmonic linewidth in all these materials. . . . . 60
3.14 The ratio of the acoustic-transverse optical modes close to the zone centre (labelled as $TO_1$ modes, see text for explanation) contribution to the total anharmonic linewidth of strained PbTe and $Pb_{0.51}Ge_{0.49}Te$ with respect to PbTe at 300 K versus mode frequency of strained PbTe and $Pb_{0.51}Ge_{0.49}Te$, respectively. (a) Acoustic modes in strained PbTe, (b) optical modes in strained PbTe, (c) acoustic modes in $Pb_{0.51}Ge_{0.49}Te$, and (d) optical modes in $Pb_{0.51}Ge_{0.49}Te$. The acoustic-$TO_1$ contribution to the anharmonic linewidth of the materials driven near phase transitions is larger than that of PbTe. . . . . 61
3.15 Lattice thermal conductivity versus temperature for PbTe (solid black line), PbTe driven near the phase transition by tensile (001) strain of $\eta = 1.15\%$ (dotted red line), $PbSe_{0.5}Te_{0.5}$ (dashed green line), $PbSe_{0.5}Te_{0.5}$ driven near the transition by tensile (001) strain of $\eta = 1.32\%$ (dash-dotted blue line), and $Pb_{0.51}Ge_{0.49}Te$ alloy near the transition (dash-double dotted purple line). Conductivity for strained materials is shown for the out-of-plane direction. . . . . 62
3.16 Out-of-plane lattice thermal conductivity of PbTe at 300 K as a function of (001) strain. Inset: Lowest transverse optical mode frequency at the zone centre, TO($\Gamma$), for PbTe at 0 K versus (001) strain. . . . . 62

3.17 Lattice thermal conductivity of $Pb_{1-x}Ge_xTe$ alloys at 450 K as a function of Ge content $x$: full calculation (black crosses), calculation without mass disorder (red circles) and linearly interpolated values between those calculated for PbTe and GeTe (dashed green line). Inset: TO($\Gamma$) frequency of $Pb_{1-x}Ge_xTe$ at 0 K versus Ge content $x$. . . . . 64
3.18 Normalised cumulative lattice thermal conductivity plotted as a function of phonon mean free path for PbTe (black), strained PbTe, $\eta = 1.15\%$ (red), $PbSe_{0.5}Te_{0.5}$ (green), and strained $PbSe_{0.5}Te_{0.5}$, $\eta = 1.32\%$ (blue). . . . . 66

4.1 Phonon dispersions of PbTe: calculated using a 128 atom supercell at 0 K (solid black line), calculated using a 216 atom supercell at 0 K (dashed red line), and measured by Cochran *et al.* [153] at 300 K (blue circles). . . . . 73
4.2 Phonon dispersions of GeTe: calculated using a 128 atom supercell at 0 K (solid black line), and the frequencies of zone centre Raman active modes measured by Fons *et al.* [171] at 300 K (blue circles) and Steigmeier *et al.* [172] at 300 K (red squares). . . . . 73
4.3 Phonon density of states for GeTe: calculated using a 128 atom supercell at 0 K (solid black line), measured by Wdowik *et al.* [173] and Pereira *et al.* [174]. The integral of the density of states over frequency is normalized to unity. . . . . 74
4.4 Mode Grüneisen parameters as a function of frequency obtained using finite difference (black pluses) and perturbative approaches (red crosses) for (a) GeTe, (b) PbTe, (c) $Pb_{0.49}Ge_{0.51}Te$, and (d) $Pb_{0.51}Ge_{0.49}Te$. . . . . 74
4.5 Linear thermal expansion coefficient of PbTe as a function of temperature: calculated using a 128 atom supercell (solid black line), measured by Dalven [177] (blue circles), and measured by Novikova and Abrikosov, Ref [153] and references therein (red squares). . 75
4.6 Lattice thermal conductivity of PbTe as a function of temperature: calculated using a supercell with 128 atoms (solid black line), calculated using a supercell with 216 atoms (dashed red line), measured by Devyatkova *et al.* [154] (blue circles), and measured by El-Sharkawy *et al.* [155] (green squares). . . . . 78
4.7 Lattice thermal conductivity of GeTe as a function of temperature: calculated using a 128 atom supercell (solid black line), measured by Nath *et al.* [184] (blue circles), and measured by Levin *et al.* [182] (red squares). . . . . 78
4.8 The rocksalt and rhombohedral structures of PbTe and GeTe, respectively. The differences between the two structures are the position of Te atom along the trigonal [111] axis and the angle between the primitive lattice vectors. The rocksalt phase is a special case of the rhombohedral phase with the relative Te position of $(0.5, 0.5, 0.5)$ within the primitive cell, and the angle of 60°. . 79

4.9 (a) Total energy of the rocksalt and rhombohedral phases of $Pb_xGe_{1-x}Te$ as a function of the alloy composition $x$. (b) Difference between the total energy of the rocksalt and rhombohedral phases as a function of $x$. The rocksalt structure is a special case of the rhombohedral structure, and they are identical for $x < 0.492$. 80
4.10 Calculated structural parameters as a function of $Pb_{1-x}Ge_xTe$ alloy composition: (a) lattice constant, (b) rhombohedral angle, and (c) sublattice position in the crystal lattice coordinates. . . 80
4.11 The frequency of the lowest transverse optical mode at the zone centre, TO(Γ), as a function of $Pb_{1-x}Ge_xTe$ alloy composition. . 81
4.12 Cartoon of the total energy versus Te atomic displacement from its equilibrium position in the rocksalt structure along the [111] direction for: (a) the rocksalt phase, and (b) the rhombohedral phase. . . . . 82
4.13 Phonon band structures at 0 K for GeTe (solid black line) and an alloy in the rhombohedral structure near the phase transition, $Pb_{0.49}Ge_{0.51}Te$ (dashed red line). The frequencies of the soft transverse optical phonon modes at the zone centre, TO(Γ), are highlighted in black circles for GeTe and red rectangles for $Pb_{0.49}Ge_{0.51}Te$. . . . . 84
4.14 Phonon band structures at 0 K for PbTe (solid black line) and an alloy in the rocksalt structure near the phase transition, $Pb_{0.51}Ge_{0.49}Te$ (dashed red line). The frequencies of the soft transverse optical phonon modes at the zone centre, TO(Γ), are highlighted in black circles for PbTe and red rectangles for $Pb_{0.51}Ge_{0.49}Te$. . . . . 84
4.15 Phonon band structures at 0 K for alloy compositions in the rocksalt and rhombohedral phases near the phase transition: $Pb_{0.51}Ge_{0.49}Te$ (solid black line) and $Pb_{0.49}Ge_{0.51}Te$ (dashed red line), respectively. . . . . 85
4.16 Anharmonic phonon lifetimes at 450 K and their averaged values (inset) as a function of frequency for GeTe (black pluses and solid line) and a rhombohedral alloy near the phase transition, $Pb_{0.49}Ge_{0.51}Te$ (red crosses and dashed line). . . . . 85
4.17 Anharmonic phonon lifetimes at 450 K and their averaged values (inset) as a function of frequency for PbTe (black pluses and solid line) and a rocksalt alloy near the phase transition, $Pb_{0.51}Ge_{0.49}Te$ (red crosses and dashed line). . . . . 86
4.18 Anharmonic phonon lifetimes at 450 K and their averaged values (inset) as a function of frequency for rocksalt $Pb_{0.51}Ge_{0.49}Te$ (black pluses and solid line) and rhombohedral $Pb_{0.49}Ge_{0.51}Te$ (red crosses and dashed line). . . . . 86

4.19 The acoustic-transverse optical (TO) contribution to the total anharmonic linewidth at 300 K versus frequency for (a) GeTe (black pluses) and a rhombohedral alloy near the phase transition, $Pb_{0.49}Ge_{0.51}Te$ (red crosses), (b) PbTe (black pluses) and a rocksalt alloy near the phase transition, $Pb_{0.51}Ge_{0.49}Te$ (red crosses), and (c) rocksalt $Pb_{0.51}Ge_{0.49}Te$ (black pluses) and rhombohedral $Pb_{0.49}Ge_{0.51}Te$ (red crosses). . . . . 87
4.20 (a) Phonon lifetimes due to mass disorder versus frequency for three select compositions: $Pb_{0.40}Ge_{0.60}Te$ (black pluses), $Pb_{0.30}Ge_{0.70}Te$ (red crosses), and $Pb_{0.10}Ge_{0.90}Te$ (blue circles). (b) Calculated phonon density of states for $Pb_{0.40}Ge_{0.60}Te$ (solid black line), $Pb_{0.30}Ge_{0.70}Te$ (dashed red line), and $Pb_{0.10}Ge_{0.90}Te$ (dotted blue line). The integral of the density of states over frequency is normalized to unity. . . . . 88
4.21 Phonon lifetimes due to anharmonic processes (black crosses) and mass disorder (red pluses) as a function of frequency for $Pb_{0.49}Ge_{0.51}Te$. . . . . 88
4.22 Phonon lifetimes due to mass disorder versus frequency for the rocksalt and rhombohedral structures very near the phase transition: $Pb_{0.51}Ge_{0.49}Te$ (black pluses) and $Pb_{0.49}Ge_{0.51}Te$ (red crosses), respectively. . . . . 89
4.23 Lattice thermal conductivity of $Pb_{1-x}Ge_xTe$ as a function of alloy composition at 450 K. The unfilled symbols show the thermal conductivity due to anharmonic (three-phonon) processes only, and the filled symbols show the thermal conductivity due to anharmonic processes and mass disorder. Black circles show the thermal conductivity in the rocksalt phase and its isotropic average in the rhombohedral phase. Red up and blue down triangles show the thermal conductivity perpendicular and parallel to the trigonal [111] axis in the rhombohedral phase, respectively. . . . . 90
4.24 Anharmonic contribution to the lattice thermal conductivity of $Pb_{1-x}Ge_xTe$ as a function of the alloy composition at 450 K, where the group IV element mass of each alloy composition is artificially set to that of $Pb_{0.5}Ge_{0.5}Te$. Black circles show the thermal conductivity in the rocksalt phase, while red up and blue down triangles show the thermal conductivity perpendicular and parallel to the trigonal [111] axis in the rhombohedral phase, respectively. Also shown in green crosses is the frequency of the lowest transverse optical mode at the zone centre for the same mass of the group IV element as described above. . . . . 91

4.25 The contribution to the anharmonic lattice thermal conductivity $\kappa_{\text{con}}(\omega)$ at 450 K as a function of phonon frequency. $\kappa_{\text{con}}(\omega)$ is shown for (a) GeTe parallel and perpendicular to the trigonal axis (dotted and solid black lines) and $Pb_{0.49}Ge_{0.51}Te$ parallel and perpendicular to the trigonal axis (dotted and solid red lines), (b) PbTe (solid black line) and $Pb_{0.51}Ge_{0.49}Te$ (solid red line), (c) $Pb_{0.51}Ge_{0.49}Te$ (solid black line) and $Pb_{0.49}Ge_{0.51}Te$ parallel and perpendicular to the trigonal axis (dotted and solid red lines). . 92
4.26 The contribution to the anharmonic lattice thermal conductivity $\kappa_{\text{con}}(\omega)$ at 450 K as a function of normalised phonon frequency for GeTe parallel and perpendicular to the trigonal axis (dotted and solid black lines), $Pb_{0.49}Ge_{0.51}Te$ parallel and perpendicular to the trigonal axis (dotted and solid red lines), $Pb_{0.51}Ge_{0.49}Te$ (solid blue line), and PbTe (solid green line). . . . . 93
4.27 Calculated phonon density of states for GeTe (solid black line), $Pb_{0.49}Ge_{0.51}Te$ (solid red line), $Pb_{0.51}Ge_{0.49}Te$ (solid blue line), and PbTe (solid green line). . . . . 94
4.28 Born effective charge as a function of $Pb_{1-x}Ge_xTe$ alloy composition in the rocksalt phase (red crosses), perpendicular to the trigonal [111] axis in the rhombohedral phase (green squares), and parallel to the trigonal axis in the rhombohedral phase (blue circles). 96
4.29 High-frequency dielectric constant as a function of $Pb_{1-x}Ge_xTe$ alloy composition in the rocksalt phase (red crosses), perpendicular to the trigonal axis in the rhombohedral phase (green squares), and parallel to the trigonal axis in the rhombohedral phase (blue circles). 97
4.30 Nearest neighbours within the rocksalt structure of PbTe along the [001] direction, and their counterparts for the rhombohedral structure of GeTe. . . . . 97
4.31 The trace of the harmonic interatomic force constant tensor versus atomic distance for several $Pb_{1-x}Ge_xTe$ alloy compositions in the rhombohedral phase. An alloy composition in the rocksalt phase near the phase transition, $Pb_{0.51}Ge_{0.49}Te$, is also included for comparison. . . . . 98
4.32 The trace of the harmonic interatomic force constant tensor versus atomic distance for several $Pb_{1-x}Ge_xTe$ alloy compositions in the rocksalt phase. . . . . 98
4.33 The quasi-binary phase diagram of $Pb_{1-x}Ge_xTe$ alloys, reproduced from experimental data from Ref. [157] and references therein. The miscibility gap is shown with black circles, the liquidus and solidus temperatures are shown in black squares for each alloy composition. 100

5.1 Electronic band structure of Ge, calculated using the LDA and HGH pseudopotentials excluding spin orbit interaction (a) showing several valence and conduction band states, and (b) zoomed in near the conduction band minimum to highlight the energy ordering of the L, Γ, and Δ valleys. The energies of the valence band maximum (blue dashed line) and conduction band minimum (red dashed line) are also highlighted. . . . . 105
5.2 Electronic band structure of PbTe, calculated using the LDA and HGH pseudopotentials (a) excluding spin orbit interaction, and (b) including spin orbit interaction. The energies of the valence band maximum (blue dashed line) and conduction band minimum (red dashed line) are also highlighted. . . . . 106
5.3 Electronic band structure of PbTe along the Γ-L-W line calculated using the LDA (a) excluding SOI and (b) including SOI. A solid red (blue) line shows a state whose character mostly corresponds to that of the conduction (valence) band as deduced from wavefunction overlaps. The overlaps of the cell periodic parts of the wavefunctions between the 1st electronic states counting upward (labelled as e) and downward (labelled as h) from the zero temperature Fermi level at L and those states at $\mathbf{k}$ are shown (c) excluding SOI and (d) including SOI. The following wavefunction overlaps are plotted: $|\langle u_{L,\mathrm{e}}|u_{\mathbf{k},\mathrm{e}}\rangle|^2$ (dot-dashed black line), $|\langle u_{L,\mathrm{e}}|u_{\mathbf{k},\mathrm{h}}\rangle|^2$ (dotted red line), $|\langle u_{L,\mathrm{h}}|u_{\mathbf{k},\mathrm{h}}\rangle|^2$ (large-dashed blue line), $|\langle u_{L,\mathrm{h}}|u_{\mathbf{k},\mathrm{e}}\rangle|^2$ (small-dashed green line). . . . . 108
5.4 (a) Bottommost conduction band state of Ge calculated using LDA-HGH (solid black line) relative to the band minimum, compared to the parabolic bands fit shown with red and blue dashed lines, for 2/5 of the line L→Γ (parallel to L) and 1/5 of the line L→W (perpendicular to L). (b) Bottommost conduction band state of PbTe calculated using LDA-HGH (solid black line) relative to the band minimum compared to the parabolic bands fit shown with red and blue dashed lines, for 1/5 of the line L→Γ and 1/5 of the line L→W. . . . . 109
5.5 Cartoon illustrating (a) scattering between L valleys (intervalley) via an X-point phonon and (b) scattering within an L valley (intravalley) in the limit of $\mathbf{q} \to 0$ in PbTe. . . . . 112
5.6 Electron scattering rates in an L valley as a function of electronic energy at 300 K in Ge. Scattering is due to electron-phonon coupling from intervalley emission (solid black line) and absorption (dashed red line), and intravalley optical emission (dotted blue line) and absorption (dot-dashed green line). . . . . 114

5.7 Calculated electron-phonon intravalley matrix elements in Ge as a function of phonon momentum $|\mathbf{q}|$, for transitions $\mathrm{L} \rightarrow \mathrm{L} + \mathbf{q}$ (red crosses) and $\mathrm{L} - \mathbf{q}/2 \rightarrow \mathrm{L} + \mathbf{q}/2$ (blue pluses). These yield (a) the uniaxial deformation potential, where $3C = \Xi_u^{\mathrm{L}}|\mathbf{q}|$ for an acoustic transverse phonon along [010], and (b) the dilatation deformation potential, where $C = \Xi_d^{\mathrm{L}}|\mathbf{q}|$ for an acoustic longitudinal phonon along $[0\bar{1}1]$. Quadratic fits to the matrix elements are shown with solid red and dashed blue lines. $a_0$ is the lattice constant of Ge. 119

5.8 Calculated electron-phonon intravalley matrix elements in PbTe as a function of phonon momentum $|\mathbf{q}|$, for transitions $\mathrm{L} \rightarrow \mathrm{L}+\mathbf{q}$ (red crosses) and $\mathrm{L} - \mathbf{q}/2 \rightarrow \mathrm{L} + \mathbf{q}/2$ (blue pluses). These yield (a) the uniaxial deformation potential, where $3C = |\Xi_u^{\mathrm{L}}||\mathbf{q}|$ for an acoustic transverse phonon along [010], and (b) the dilatation deformation potential, where $C = |\Xi_d^{\mathrm{L}}||\mathbf{q}|$ for an acoustic longitudinal phonon along $[0\bar{1}1]$. Quadratic fits to the matrix elements are shown with solid red and dashed blue lines. $a_0$ is the lattice constant of PbTe. 120

5.9 The calculated electronic mobilities of Ge limited by intervalley (green dot-dashed line), intravalley optical (dashed red line) and intravalley acoustic (dotted blue line) scattering. The total electronic mobility of Ge limited by electron-phonon coupling is shown by the solid black line. . . . . 124

5.10 Calculated electronic mobility of Ge compared to measurements of a single crystalline sample by Glicksman [230]. . . . . 124

5.11 The calculated electronic mobilities of PbTe limited by intravalley acoustic (dotted blue line) and polar optical (dashed red line) scattering. The total electronic mobility of PbTe due to electron-phonon coupling is shown by the solid black line. . . . . 125

5.12 Calculated electronic mobility of PbTe compared to experimental measurements by Allgaier and Scanlon [231]. . . . . 125

5.13 Electronic band structure of PbTe, calculated using the HSE03 hybrid functional and PAW potentials including spin orbit interaction. The energies of the valence band maximum (blue dashed line) and conduction band minimum (red dashed line) are also highlighted. . . . . 127

5.14 Electronic band structure of PbTe along the Γ-L-W line including SOI calculated using (a): the HSE03 hybrid functional, and (b): the PBE functional. A solid red (blue) line shows a state whose character mostly corresponds to that of the conduction (valence) band as deduced from wavefunction overlaps. The overlaps of the cell periodic parts of the wavefunctions between the 1st electronic states counting upward (labelled as e) and downward (labelled as h) from the zero temperature Fermi level at L and those states at **k** are shown for (c): the HSE03 hybrid functional and (d): the PBE functional. The following wavefunction overlaps are plotted: $|\langle u_{L,\mathrm{e}}|u_{\mathbf{k},\mathrm{e}}\rangle|^2$ (dot-dashed black line), $|\langle u_{L,\mathrm{e}}|u_{\mathbf{k},\mathrm{h}}\rangle|^2$ (dotted red line), $|\langle u_{L,\mathrm{h}}|u_{\mathbf{k},\mathrm{h}}\rangle|^2$ (large-dashed blue line), $|\langle u_{L,\mathrm{h}}|u_{\mathbf{k},\mathrm{e}}\rangle|^2$ (small-dashed green line). . . . . 129

5.15 Electronic bands for PbTe calculated using the HSE03 functional including SOI (solid black lines) compared with those calculated using the LDA functional (a) excluding SOI (dashed blue lines) and (b) including SOI (dashed red lines). . . . . 130

5.16 Total average potential $V(z)$ for an 8-atom Ge heterostructure consisting of unstrained and strained regions meeting at a (001) interface. The solid blue (red) lines show the total average potential of the unstrained (strained) region, with average potential energies $V'(0)$ and $V'(\epsilon)$ respectively. The total average potential for each value of $z$ in the bulk unstrained and strained material are shown with dashed black lines, aligned to the heterostructure such that $V(0) = V'(0)$ and $V(\epsilon) = V'(\epsilon)$ respectively. . . . . 134

# List of Tables

1.1 Thermoelectric properties of bulk state-of-the-art materials in the low, mid, and high temperatures ranges at their optimum carrier concentrations. Values are shown for alloys of $Bi_2Te_3$ at 300 K, PbTe at 700 K, and SiGe at 1100 K, for both *p*- and *n*-type. $\kappa_{\text{total}}$ is the total thermal conductivity. . . . . 5

4.1 Thermal expansion coefficients $\alpha$ of GeTe at 300 K for lattice constant $A$, the angle between the lattice vectors $\Phi$, and the Te atom position along the [111] direction $R$ in the non-primitive pseudo-cubic lattice. The thermal expansion coefficients from Refs. [179, 180, 181, 182, 183] were extracted by linearly fitting the measured lattice parameters between $\sim 300$ K and $\sim 400 - 550$ K. 77

5.1 Electronic band gap and conduction band effective electron masses at L of Ge calculated using the LDA functional compared to experiment. . . . . 105

5.2 Direct electronic band gap and effective electron masses of PbTe calculated using the LDA functional including and excluding spin orbit interaction compared to experimental values measured at 4 K. The sign of the band gap is determined from the ordering of electronic states at L, as explained in the text. . . . . 107

5.3 Born effective charges and high-frequency dielectric constant of PbTe calculated with the LDA excluding and including SOI compared to experimental measurements. . . . . 110

5.4 Intervalley and intravalley optical deformation potentials for Ge compared to previous calculations from the literature and experiment. . . . . 114

5.5 Calculated deformation potential coefficients for the L valleys of Ge and PbTe. . . . . 118

5.6 Deformation potentials for Ge compared to previous results from the literature and experiment. Deformation potentials are extracted from a quadratic fit to the $\text{L} \rightarrow \text{L} + \mathbf{q}$ matrix elements, and also from a quadratic fit to the $\text{L} - \mathbf{q}/2 \rightarrow \text{L} + \mathbf{q}/2$ matrix elements (in brackets). . . . . 119

5.7 Deformation potentials for PbTe compared to previous results from the literature and experiment. Deformation potentials are extracted from a quadratic fit to the $\text{L} \rightarrow \text{L} + \mathbf{q}$ matrix elements, and also from a quadratic fit (where we enforce a positive linear term and neglect the matrix elements that are very close to zero) to the $\text{L} - \mathbf{q}/2 \rightarrow \text{L} + \mathbf{q}/2$ matrix elements (in brackets). . . . . 121

5.8 The electronic band gap and effective electron masses of PbTe calculated with the PBE, HSE03, and HSE06 functionals respectively including SOI compared to HSE03 and quasi-particle self-consistent *GW* calculations from the literature and experiment, "+sc" signifies the inclusion of semicore electrons ($5d^{10}$ of Pb) in the valence region. . . . . 128
5.9 Hydrostatic pressure gap coefficients for PbTe calculated with the LDA, PBE, and HSE03 functionals with and without SOI, compared to experimental measurements at 4 K, 7 K, and 300 K. Pressure was simulated by setting the lattice constant to $0.999 \times a_0$, where $a_0$ is its theoretically predicted equilibrium value. . . . . 130
5.10 Uniaxial deformation potential of Ge calculated from the splitting of previously degenerate L-valleys under strain using the LDA and HGH pseudopotentials in ABINIT. $\Xi_u^{\mathrm{L}}$ is compared to our values calculated using DFPT, previous calculations from the literature, and experiment. . . . . 132
5.11 Uniaxial deformation potential of PbTe calculated from the splitting of previously degenerate L-valleys under strain for the LDA, PBE (inc. SOI), and HSE03 (inc. SOI) functionals. They are compared to our values calculated using DFPT, a previous calculation from the literature, and experiment. . . . . 133
5.12 Dilatation deformation potential of Ge calculated from the energy shift of the L-valley under strain using the LDA and HGH pseudopotentials in ABINIT. $\Xi_d^{\mathrm{L}}$ is compared to our values calculated using DFPT, previous calculations from the literature, and experiment. . . . . 136
5.13 Deformation potentials of PbTe calculated from the energy shift of the L-valley under strain using the LDA and HGH pseudopotentials excluding SOI in ABINIT. They are compared to our values calculated using DFPT, and previous results from the literature, and experiment. . . . . 137
5.14 Dilatation deformation potentials for PbTe calculated using the LDA functional excluding/including SOI in ABINIT and with the PBE and HSE03 functionals including SOI in VASP, shown for multiple supercell sizes. . . . . 137

I, Aoife Rose Murphy, certify that this thesis is my own work and I have not obtained a degree in this university or elsewhere on the basis of the work submitted in this thesis.

*Aoife Rose Murphy*

Dedicated to my parents, Helen and Billy Murphy

# Acknowledgements

First and foremost, I would like to thank my supervisors, Ivana Savić and Stephen Fahy, for giving me the opportunity to work on this topic to begin with and for their support over the past few years. In particular, I'd like to thank them for securing funding from Science Foundation Ireland for the entirety of my PhD. I'd like to extend thanks to the other members of the Materials Theory group past and present, Phillip Murphy, Éamonn Murray, Martin Vaughan, Anna Hauber, Mark Hartnett, Shane O'Mahony, Jiang Cao, Jose Querales, and Djordje Dangić. All of whom have contributed in one way or another throughout years of (admittedly long) group meetings, whether it was something as simple as a tip for using the Tyndall cluster or finding a missing factor in an equation. A special thanks to Nicolas Cordero for sitting on my thesis committee and providing invaluable feedback.

I would also like to thank my parents, for always encouraging me in my scientific interests growing up and for the support, along with that of my brother and sister, they've given my throughout the course of my PhD. A thank you to all the friends I've made over nearly a decade of studying physics in UCC and Tyndall, all of whom have contributed to making this a truly remarkable experience. In particular, those around Tyndall (Shane, Amy, Jiang, Jose, Djordje, Alfonso, Christian, Conor, Katya, Saroj) who've been there for coffee breaks and to discuss the latest tv shows, which was instrumental in bringing this work together. A final thank you to Karen Acheson, for being there to talk about all the joys we've had as PhD students and so much more!

# Abstract

The thermoelectric figure of merit, $ZT$, is a dimensionless parameter used to characterise the efficiency of a thermoelectric material. A material has a high $ZT$ if its electrical conductivity and Seebeck coefficient are high, and its lattice thermal conductivity is low. One of the most common techniques to improve the thermoelectric figure of merit is to suppress lattice thermal conductivity via nanostructuring. However, this approach often comes with the cost of reduced electrical conductivity and Seebeck coefficient, resulting in only modest increases to $ZT$. Using the first principles Boltzmann transport framework, we show that driving PbTe-based materials to the verge of the soft mode (ferroelectric) phase transition could be a powerful strategy to reduce their lattice thermal conductivity while potentially preserving the electrical properties beneficial for a large $ZT$. The proposed concept is based on the induction of considerably softened zone-centre transverse optical modes, increasing their anharmonic coupling with low-frequency heat-carrying acoustic phonons and reducing phonon lifetimes at all frequencies. We illustrate this concept by applying biaxial tensile (001) strain to PbTe and its alloys with PbSe; and by alloying PbTe with a rhombohedral material, GeTe, achieving reductions in the lattice thermal conductivity by a factor of $2-3$ compared to PbTe. Furthermore, by tuning the chemical composition of $Pb_{1-x}Ge_xTe$ alloys, we also investigate the roles of proximity to the phase transition, mass disorder, and phase of the alloy in reducing the lattice thermal conductivity. Finally, we take the first steps towards a fully *ab initio* calculation of the figure of merit of PbTe-based materials near the phase transition by considering electron-phonon interactions, and find fair agreement between the calculated electronic mobility of PbTe and experiment. Furthermore, due to symmetry forbidden electron-phonon coupling between the extremely soft modes and the conduction and valence band edges, we anticipate that our outlined approach may not degrade electronic properties beneficial for a large $ZT$. This proposed concept is general and applicable to other thermoelectric materials near a soft mode phase transition. Thus, we offer a promising new strategy to lower lattice thermal conductivity and potentially increase thermoelectric efficiency.

# Chapter 1

# Introduction

## 1.1 Thermoelectric materials

Thermoelectrics are an important class of materials that allow for the interconversion of thermal and electrical energy. The generation of a voltage difference due to a temperature gradient across a material is known as the Seebeck effect [1]. It was discovered in 1821 by Thomas Johann Seebeck, who observed that the junction of two dissimilar metals at different temperatures would deflect a compass needle [2]. Conversely, the Peltier effect is the appearance of a temperature gradient from the application of an electric current in a material [1]. It was discovered by Jean-Charles Peltier in 1834, who observed heating/cooling at the junction of two dissimilar metals when an electric current was applied [2]. The first commercial application of the thermoelectric effect was an oil burning lamp coupled with zinc-antimony/constantan thermoelectric elements used to power a radio in 1948 in the USSR [3], which followed from the work of Abram Fedorovich Ioffe.

When a thermal gradient is maintained across a material, free charge carriers will have higher kinetic energies at the hot end and tend to diffuse towards the cold end [4]. A thermoelectric power generator thus consists of alternating $p$- and $n$-type thermoelectric legs, connected in series electrically, and connected in parallel with respect to a heat current [5], see Fig. 1.1 (a) for a model device. Closing the circuit generates an electric current. Conversely, by applying an electric current one may drive carriers away from a surface, reducing its temperature. This is demonstrated in Fig. 1.1 (b) which shows a model device used to pump heat. Thus, thermoelectrics could be extremely useful for harnessing waste heat to generate electricity, and may provide an important role in the push for green energy [1, 5, 6]. The efficient control of thermoelectric energy conversion processes is particularly desirable as nearly 60% of all energy consumed worldwide is wasted

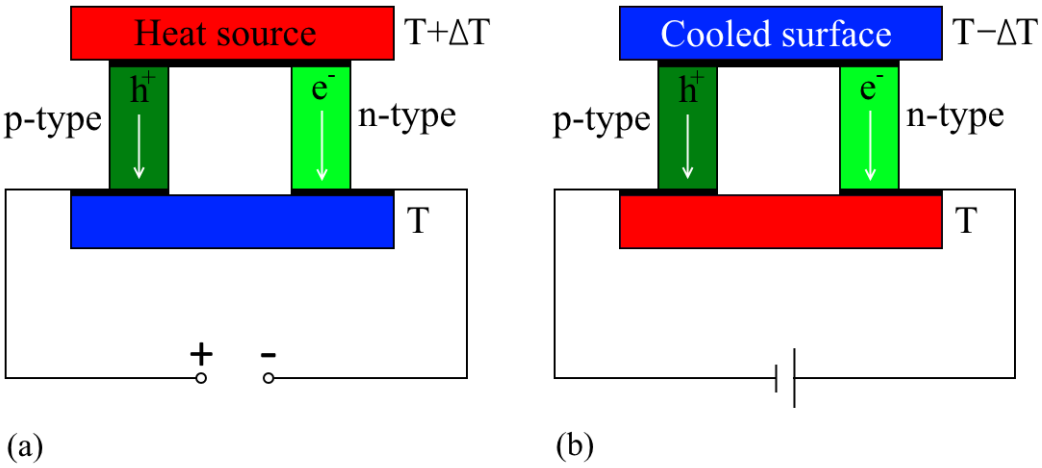



Figure 1.1: (a): A model thermoelectric device used to generate electricity from a heat source. (b) A model thermoelectric device used to pump heat when an electric current is applied.

in the form of heat [7].

In order to efficiently convert heat to electricity, or vice-versa, we need a measure of the effectiveness of a thermoelectric material. A good thermoelectric must be able to maintain a heat difference and easily allow for an electric current through the device, necessitating a low thermal conductivity and high electrical conductivity respectively [8]. For power generation, we need a large voltage to be generated from a heat gradient, requiring a large Seebeck coefficient [8]. Indeed, the efficiency of a thermoelectric material depends on the dimensionless figure of merit, $ZT$ [9, 10]:

$$ZT = \frac{\sigma S^2}{\kappa_{\text{elec}} + \kappa_{\text{latt}}} T, \tag{1.1}$$

where $\sigma$ is the electrical conductivity, $S$ is the Seebeck coefficient, $T$ is the temperature, and $\kappa_{\text{elec}}$ and $\kappa_{\text{latt}}$ are the thermal conductivities due to charge carriers and lattice vibrations respectively. $\sigma S^2$ is typically referred to as the power factor.

The maximum efficiency of a thermoelectric device may be written as a function of the Carnot efficiency, $\eta_{\text{Carnot}} = (T_{\text{h}} - T_{\text{c}})/T_{\text{h}}$, and the figure of merit [1, 10]:

$$\eta_{\text{max}} = \eta_{\text{Carnot}} \frac{\sqrt{1 + ZT_{\text{avg}}} - 1}{\sqrt{1 + ZT_{\text{avg}}} + \frac{T_{\text{c}}}{T_{\text{h}}}}, \tag{1.2}$$

where $T_{\text{h}}$ and $T_{\text{c}}$ are the absolute temperatures of the hot and cold sides of the device respectively, and $ZT_{\text{avg}}$ is the average figure of merit of the thermoelectric legs within a device over the operating temperature range. In Fig. 1.2

we reproduce the efficiency $\eta_{\max}$ of thermoelectric devices as a function of $T_{\rm h}$, taking $T_{\rm c}$ = 300K, for several $ZT_{\rm avg}$ values ranging from currently available to optimistic targets. The yellow region highlights the power generation efficiency and operating temperatures of typical thermoelectric devices available today. Also included are the efficiencies of several heat sources (geothermal, industrial waste, solar, nuclear, and coal) in combination with several thermal-to-electric conversion technologies (organic Rankine, Kalina cycle, Stirling, Brayton, and steam Rankine) reproduced from data in Refs. [11, 12, 13].

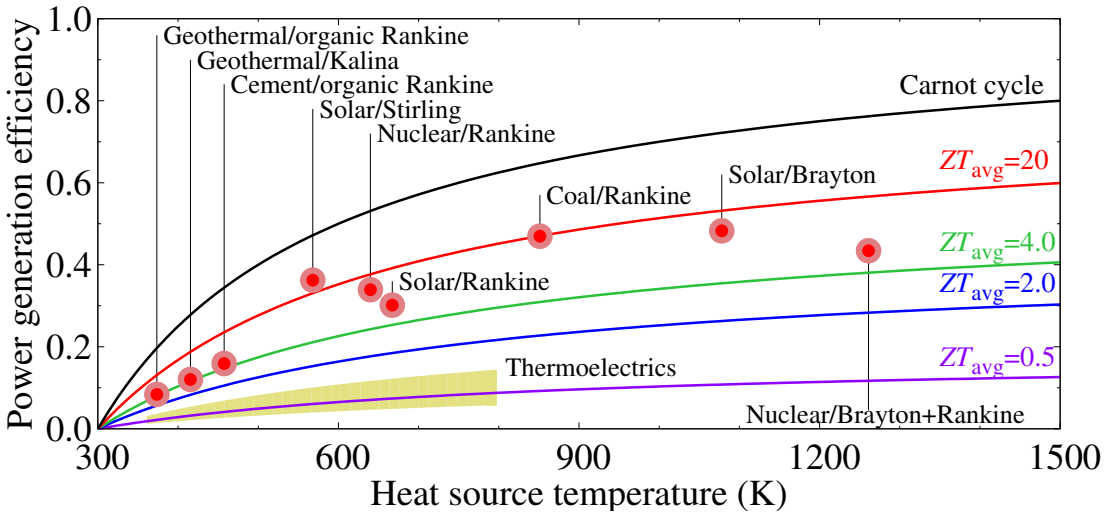



Figure 1.2: Thermoelectric power generation efficiency versus temperature of the hot side, taking the cold side as room temperature, for several values of $ZT_{\rm avg}$. The yellow region highlights the efficiency of some typical thermoelectric power generators available today and their approximate range of operating temperatures. Also included are the efficiencies of several conventional mechanical heat engines as well as the Carnot limit. Adapted from Refs. [11, 12, 13].

Modern thermoelectric devices may operate up to $ZT \lesssim 1.0$ at high temperatures. However, for a typical thermoelectric device with $ZT_{\rm avg}\sim$0.5 and operating temperatures of $T_{\rm c}$ = 300 K and $T_{\rm h}$ = 600 K an efficiency of only $\eta_{\max} \sim 6\%$ is achievable for power generation, severely limiting their range of application [1, 11]. In spite of these limitations thermoelectric devices have found several niche applications, for example, regulating the temperature of semiconductor lasers and radioisotope thermoelectric power generators for space applications [6, 13]. Nevertheless, such low efficiencies have lead to a big drive within the thermoelectrics community to achieve a target $ZT$ of greater than 2. Furthermore, by increasing $ZT$ to >3 and assuming a large temperature difference ($T_{\rm c}$ = 300 K and $T_{\rm h}$ = 1000 K) one may achieve an efficiency of up to $\eta_{\max} \sim 30\%$ for power generation [1], possibly enabling the application of thermoelectrics in

green energy and waste heat harvesting [12].

However, maximising $ZT$ and expanding the range of applications is not a trivial task given that thermoelectric properties are heavily intertwined, with an increase in one not necessarily yielding an enhancement to $ZT$. Indeed, even optimising the power factor, $\sigma S^2$, is itself a difficult task. For a degenerate semiconductor with parabolic bands, assuming that the introduction of a dopant does not significantly alter the electronic band structure, the Seebeck coefficient is given by [14]:

$$S = \frac{8\pi^2 k_{\mathrm{B}}^2}{3eh^2} m^*_{\mathrm{DOS}} T \left(\frac{\pi}{3n}\right)^{2/3}, \tag{1.3}$$

where $k_{\mathrm{B}}$ is the Boltzmann constant, $e$ the electron charge, $h$ the Planck constant, $m^*_{\mathrm{DOS}}$ the density of states effective mass of the carriers, and $n$ the charge carrier concentration. The electrical conductivity is given by [14]:

$$\sigma = ne\mu, \tag{1.4}$$

where we assume the mobility $\mu$ is independent of $n$. Thus, while increasing the carrier concentration will increase $\sigma$, $S$ will decrease as dictated by Eq. (1.3). Careful attention must then be paid when optimising properties of the materials such as the carrier concentration, to avoid either $S$ or $\sigma$ falling too low. The Seebeck coefficient tends to be lower for metals where electrical conductivity is large, while $S$ is large in poor conductors. This results in optimal power factors typically being observed in heavily doped semiconductors [11], with carrier concentrations circa $10^{19} - 10^{21}$ cm$^{-3}$ [5].

Furthermore, the electrical conductivity and electronic thermal conductivity are linked via the Wiedemann–Franz law [15]:

$$\frac{\kappa_{\mathrm{elec}}}{\sigma} = LT, \tag{1.5}$$

where $L$ is the Lorenz number, and is approximately $\frac{\pi^2}{3}\left(\frac{k_{\mathrm{B}}}{e}\right)^2$ for all metals [16]. Thus an increase to $\sigma$ must be carefully weighed against the degradation to $ZT$ from the corresponding increase to thermal conductivity. Since $\kappa_{\mathrm{latt}}$ is dependent on phononic, rather than electronic properties of the material, it is usually treated as being largely decoupled from the other thermoelectric properties of a material. However, conventional strategies to reduce $\kappa_{\mathrm{latt}}$, such as nanostructuring to impede phonon transport, can themselves degrade electronic properties beneficial for a large $ZT$.

Before proceeding with strategies to improve thermoelectric efficiency, we

Table 1.1: Thermoelectric properties of bulk state-of-the-art materials in the low, mid, and high temperatures ranges at their optimum carrier concentrations. Values are shown for alloys of $Bi_2Te_3$ at 300 K, PbTe at 700 K, and SiGe at 1100 K, for both $p$- and $n$-type. $\kappa_{\text{total}}$ is the total thermal conductivity.

| Material | Dopant | $n$ | $\kappa_{\text{total}}$ | $\sigma$ | $\lvert S\rvert$ | $ZT$ | Ref. |
|---|---|---|---|---|---|---|---|
| | | $\text{cm}^{-3}$ | W/mK | kS/m | $\mu$V/K | | |
| $n$-PbTe | I | $1.7\times10^{19}$ | 1.20 | 56.0 | 206 | 1.40 | [17] |
| $p$-PbTe | Na | $9.0\times10^{19}$ | 1.26 | 38.9 | 261 | 1.47 | [18] |
| $n$-$Bi_2(Te,Se)_3$ | – | $4.3\times10^{19}$ | 1.65 | 90.4 | 230 | 0.85 | [19] |
| $p$-$(Bi,Sb)_2Te_3$ | – | $\sim10^{19}$ | 1.39 | 98.9 | 214 | 0.97 | [20] |
| $n$-SiGe | P | $1\text{-}3\times10^{20}$ | 4.01 | 50.8 | 250 | 0.87 | [21] |
| $p$-SiGe | B | $2\text{-}4\times10^{20}$ | 4.14 | 33.8 | 237 | 0.51 | [21] |

reproduce the properties of prototypical bulk state-of-the-art thermoelectric materials at their optimum carrier concentrations in Table 1.1. In the low temperature range up to 500 K, $Bi_2Te_3$ alloyed with either $Sb_2Te_3$ or $Bi_2Se_3$ are the highest performing thermoelectrics. They achieve a peak $ZT\sim0.9$ at $\sim$300 K [19, 20], and are primarily used for thermoelectric cooling applications [22]. In the mid temperature range of $500-900$ K, PbTe is the prototypical thermoelectric material, hitting a peak $ZT\sim1.4$ at $\sim$700 K [17, 18]. For high temperature applications at $900-1300$ K SiGe is typically used, reaching $ZT\sim0.9$ for $n$-type and $ZT\sim0.5$ for $p$-type at $\sim1100-1200$ K [21].

## 1.2 Optimising thermoelectric performance

Obtaining a large figure of merit is clearly a considerably difficult task, with numerous techniques and approaches employed to achieve $ZT>2$. We first review the more widely known classes of materials with inherently good thermoelectric performance. One such class are complex compounds with intrinsically low lattice thermal conductivity, such as skutterudites, clathrates, and zintl compounds [1, 5, 14, 23]. Their impressive thermoelectric performance is due to features such as voids in the crystal structure, atomic mismatch within the unit cell, and the presence of "rattler" atoms which strongly impede phonon transport. However, we are not limited to these materials only. For example, half-Heusler compounds lack a complex crystalline structure, resulting in relatively high lattice thermal conductivity, but possess high power factors due to large carrier effective masses

[1, 24]. It is the chalcogenide family of compounds that are perhaps the most famous for offering good thermoelectric performance, due to characteristically low lattice thermal conductivities [1, 14]. Copper chalcogenides and complex bismuth chalcogenides are two notable subgroups, but PbTe, SnSe, and $Bi_2Te_3$ are perhaps the most prototypical within this family.

In particular, PbTe is a narrow band gap semiconductor that crystallises in the rocksalt structure. It is the prototypical thermoelectric in the mid temperature range, achieving $ZT{\sim}1.4$ at ∼750 K when optimally doped with sodium (hole density of $\sim 9{\times}10^{19}$ cm$^{-3}$) or iodine (electron density of $\sim 2{\times}10^{19}$ cm$^{-3}$) [17, 18, 25]. PbTe possesses an intrinsically low lattice thermal conductivity of ∼2 W/mK at room temperature, which plays a significant role in its impressive thermoelectric performance. The underlying mechanism for low lattice thermal conductivity is the strong anharmonic coupling of the heat carrying acoustic modes with the soft transverse optical (TO) phonon modes, resulting in very short phonon lifetimes [26, 27, 28]. It is because of these properties that considerable effort has been expended in studying PbTe-based materials in an effort to enhance its thermoelectric performance.

There exist several successful strategies within the literature to enhance a material's thermoelectric performance even further. To obtain these gains to $ZT$, it is common to treat the electronic and phononic properties as being largely decoupled and respectively optimise them, though obviously a complete decoupling of these is not possible. For the electronic properties, strategies to enhance $ZT$ include optimising the carrier concentration via doping, enhancing charge carrier effective masses, band convergence to increase the degeneracy of band extrema, and improving the carrier mobility [8, 11, 13, 29]. Optimizing the electronic local density of states via the introduction of resonant impurities in semiconductors has also been shown to be a powerful strategy to boost $ZT$ [30, 31].

While these strategies are general and applicable to a wide range of thermoelectrics, we examine their application to PbTe. La and $PbI_2$ doping may be used to optimise charge carrier density in $n$-type PbTe [32, 33], while Na doping optimises hole density in $p$-type PbTe [18, 34, 35]. The introduction of In dopants into PbTe maintains its high $S$ by eliminating minority ($p$-type) carriers and eliminating the thermal conductivity due to bipolar diffusion of electron hole pairs [32]. On the other hand, Tl doped PbTe exploits the introduction of resonant impurity levels near the Fermi level which significantly increases thermoelectric performance [31]. Furthermore, Pei *et al.* heavily doped $p$-type $PbSe_xTe_{1-x}$ alloys

to achieve $ZT\sim1.8$ at 850 K, via the convergence of the L and $\Sigma$ valence band maxima at a desired temperature by tuning the alloy composition [35]. Such a "valence band convergence" mechanism also appears to be responsible for the high $ZT$ of $Pb_{0.13}Ge_{0.87}Te$ nanostructured materials [36]. In fact, recent work by Hong *et al.* [37] has predicted a maximum theoretically possible attainable $ZT$ of 3.1 for PbTe via the optimisation of the carrier density and convergence of valence band maxima.

Efforts to impede phonon transport and thus reduce the lattice thermal conductivity also offer substantial opportunities to greatly enhance thermoelectric performance. Alloying to scatter phonons via atomic mismatch, nanostructuring, nanocomposites, and scattering of phonons by crystal grain boundaries have all demonstrated large reductions to $\kappa_{\text{latt}}$ [1, 8, 11, 13, 14, 29]. However, several of these methods leave all important low-frequency heat carrying phonons unimpeded. Thus, engineering efficient phonon scattering across the entire spectrum was recently tackled by fabricating complex IV-VI materials with multi-scale hierarchical design [34, 38, 39, 40, 41]. This is achieved through the combined action of mesoscale grain boundaries that scatter low-frequency heat carrying phonons, and nanoscale precipitates and atomic disorder that affect mid- and high-frequencies. The use of superlattices, nanowires and low dimensional thermoelectrics have also been shown to be very promising approaches to boost $ZT$ [11, 42]. In particular, calculations by Hicks and Dresselhaus show that low-dimensionality may be exploited to increase the power factor while simultaneously suppressing the lattice thermal conductivity [9, 43]. Thus, there exists a strong desire within the community to combine aspects of nanostructuring to improve thermoelectric performance via a simultaneous improvement of the power factor and thermal transport [42]. However, in practice such techniques do not often realise a simultaneous improvement of thermal conductivity and the power factor, while also being impractical when it comes to large-scale production of thermoelectric devices [8].

For PbTe, the use of multi-scale hierarchical nanostructuring decreased the lattice thermal conductivity by a factor of 2-3 and simultaneously enhanced the power factor, which raised its $ZT$ above the target value of 2 [34, 39, 41]. In particular, Biswas *et al.* [34] measured $ZT\sim2.2$ at 900 K in nanostructured PbTe due to the combined approach of doping with Na, the inclusion SrTe nanoparticles, and the creation of mesoscale grain boundaries with spark plasma sintering. This thermoelectric performance was aided by an enhanced power factor at high temperatures, resulting from an increase to the hole carrier density through the

dissolution of otherwise grain-boundary-confined Na into the bulk matrix [34]. Optimisation of an all-scales design could result in further $\kappa_{\text{latt}}$ reductions, since nanostructured PbTe without mesoscale grain boundaries can exhibit four to five times lower $\kappa_{\text{latt}}$ than that of PbTe [44, 45, 46]. Such approaches may also be combined with band engineering, such as the "valence band convergence" demonstrated in $PbSe_{1-x}Te_x$ [35] and nanostructured $Pb_{0.13}Ge_{0.87}Te$ [36], potentially enhancing $ZT$ even further. However, it is often the case that electrical conductivity and Seebeck coefficient may be negatively affected in that process due to enhanced electron scattering at the interfaces [34, 39, 45, 46]. It is thus desirable to establish alternative concepts to realize efficient phonon scattering in PbTe and related materials throughout the spectrum without degrading their electronic thermoelectric properties.

One potential strategy to reduce the lattice thermal conductivity while preserving or even enhancing the power factor is to exploit the fascinating properties of thermoelectric materials near phase transitions. Recent work has shown that the intrinsically low $\kappa_{\text{latt}}$ of PbTe is due to its proximity to the ferroelectric phase transition [27, 28]. Furthermore, the record breaking $ZT{\sim}2.6$ at 900 K in SnSe has also been linked to its proximity to a soft mode phase transition [47, 48, 49]. The underlying mechanism is the strong anharmonic coupling of the heat carrying acoustic modes with the soft optical phonon mode. Thus, exploiting the properties of materials near soft mode phase transitions is an emerging concept that may offer an alternative strategy in the quest to increase $ZT$. One advantage of this approach over other methods discussed previously is the possibility of preserving the high electrical conductivity and Seebeck coefficient [50] necessary for a large $ZT$, owing to weak coupling between the soft phonon modes and electrons.

## 1.3 *Ab initio* calculation of thermoelectric transport properties

Within the thermoelectrics research community, the use of computational methods offers a unique perspective in the effort to improve thermoelectric performance. Atomic simulations from first principles avoid empirical parametrisation for thermal and charge carrier transport, allowing for the discovery of new materials with intrinsically low thermal conductivity or high power factors not yet realised experimentally. Furthermore, the origins of high $ZT$ may be studied in detail, potentially yielding new approaches to improve a material's thermoelectric performance.

### 1.3.1 Lattice thermal conductivity

Several different atomistic methods have sought to describe the phenomenon of thermal transport in bulk materials in recent years. Such methods include the Boltzmann transport equation (BTE) [51] and molecular dynamics (MD) [52]. Each approach comes with its own advantages and disadvantages, along with various flavour of implementation, such as equilibrium molecular dynamics (EMD) [52], non-equilibrium molecular dynamics (NEMD) [52, 53], the Boltzmann transport equation in the relaxation time approximation (BTE-RTA) [51], and an iterative approach to solving the BTE self-consistently (BTE-SC) [54, 55, 56, 57, 58, 59, 60, 61].

Molecular dynamics has been a very successful approach to simulate a wide range of physical phenomena and is particularly advantageous in that it yields the time evolution of the system and does not require assumptions specific to the process being investigated. However, MD suffers from several issues, most notably slow convergence with respect to the size of the system and simulation time. In order to achieve a converged value for lattice thermal conductivity, work by He *et al.* showed that system sizes of at least $\sim 10^5$ atoms for crystalline Si, and $\sim 10^4$ for crystalline Ge were required [62]. In particular, there is debate as to whether even $\sim 10^6$ atoms is sufficient to achieve a converged value of $\kappa_{\text{latt}}$ in alloys such as $Si_{0.5}Ge_{0.5}$ [62]. It is because of these large system sizes that empirical interatomic potentials are most often used in MD approaches, limiting the application of so called *ab initio* molecular dynamics (AIMD) which incorporates interatomic forces derived from density functional theory (DFT).

Moving to an approach such as the BTE, we solve several of these issues associated with MD, and most importantly migrate to a framework where we may more easily utilise *ab initio* techniques. The use of first principles calculations from either DFT or density functional perturbation theory (DFPT) allows us to design and propose new materials with good thermoelectric performance in situations where empirical parametrisation is unavailable. Furthermore, we may treat phonon populations with the quantum, Bose-Einstein distribution function, compared with their classical treatment under MD. However, the BTE approach does not come without its downsides. Most significantly, each order of phonon-phonon interaction must be individually taken into account, typically resulting in the truncation of anharmonic processes at third order and the neglection of higher order anharmonic processes. This is in contrast to MD, where all orders of phonon-phonon interactions are implicitly taken into account during the simulation. Furthermore, interatomic force constants (IFCs) necessary for

solving the BTE are calculated at 0 K within DFT/DFPT, losing information about their temperature dependence. Solving for the lattice thermal conductivity of a nanostructured material with the BTE would also be impractical given the size of such systems.

Despite these limitations, the BTE approach has been shown to give lattice thermal conductivity values in good agreement with experiment [28, 60, 61, 63, 64, 65]. And it is this agreement, coupled with predictive capabilities from the use of *ab initio* techniques, that allows us to calculate the lattice thermal conductivity of new materials. However, when considering materials near the phase transition like those based on PbTe in this thesis, we must consider the limitations of the BTE approach as outlined previously, in particular, the effect of $4^{\text{th}}$ and higher order phonon-phonon interactions. The neglect of these effects results in the BTE failing to capture the deviation of the lattice thermal conductivity from the expected temperature dependence of $\sim T^{-1}$ in simple semiconductors [66]. However, we will still capture important qualitative information on the physics of thermoelectrics driven near the phase transition, including the all important interaction between the soft mode and heat carrying acoustic phonons. Thus, to a first approximation, we may make predictions about the qualitative changes and trends in the $\kappa_{\text{latt}}$ of PbTe-based materials driven near the ferroelectric phase transition.

Within the BTE, there are two distinct approaches employed to calculate lattice thermal conductivity, the relaxation time approximation and a self-consistent iterative procedure. The BTE-RTA is equivalent to the first iteration of the self-consistent cycle to the BTE-SC [67], and it can adequately capture $\kappa_{\text{latt}}$ values in the thermoelectric materials studied in this work. Within the RTA, normal scattering is purely resistive [68]. This typically results in the BTE-RTA underestimating $\kappa_{\text{latt}}$ compared to the BTE-SC which correctly accounts for normal processes which play a critical role in redistributing phonons for thermal relaxation. This is most evident in materials with large thermal conductivities which typically have weak umklapp scattering in comparison to normal processes. The RTA fails to adequately capture $\kappa_{\text{latt}}$ for materials such as diamond [61], graphite [69, 70], and graphene [70], necessitating the use of the BTE-SC. In systems with lower lattice thermal conductivity umklapp scattering dominates over normal scattering, and the BTE-RTA falls within 5% of the BTE-SC solution for silicon, germanium and group III-V semiconductors [65]. It is within this regime that thermoelectric materials typically fall, and are therefore characterised quite well by the BTE-RTA [67, 68]. Thus, our approach will be sufficient

to adequately capture the physics of phonon-phonon interactions and lattice thermal conductivity, without the need for the extra computational load of a self-consistent cycle. Further, we note that as temperature increases, umklapp scattering becomes more significant [71].

Recent work has sought to move beyond some of the limitations in current implementations of the BTE. These approaches include techniques to capture temperature dependent interatomic force constants and the effects of $4^{\text{th}}$ and higher order phonon-phonon interactions. One such method uses a combination of the temperature dependent effective potential technique and *ab initio* molecular dynamics to capture higher order anharmonicity and temperature dependent interatomic force constants for lattice dynamics calculations [72, 73, 74]. This was successfully used by Romero *et al.* [66] to reproduce the increase of the TO mode with temperature in PbTe. Furthermore, van Roekeghem *et al.* [75] use an approach inspired by the self-consistent *ab initio* lattice dynamics method [76] to obtain temperature dependence IFCs and partially capture the effects of quartic anharmonicity, to correctly reproduce the negative thermal expansion of $ScF_3$ with temperature.

### 1.3.2 Electronic thermoelectric properties

While considerable progress has been made in the *ab initio* study of lattice thermal conductivity, transport of charge carriers from first principles remains a considerably more daunting task. This poses a stumbling block in the development of an easy to use framework for the calculation of *ab initio* thermoelectric figures of merit for a wide range of materials. The most acute issue in this regard is the computational cost and difficulty in calculating the scattering rates of charge carriers. Within semiconductors, the most dominant scattering mechanisms are electron-phonon interaction, neutral and charged impurity scattering, alloy scattering, and interface roughness [77, 78]. Typically, calculating electron scattering rates for these processes has relied on approaches such as empirical deformation potentials for electron-phonon interaction [79, 80, 81]. One of the simplest approaches is to treat the electronic lifetime as a free parameter or choose a constant value, the so-called constant relaxation time approximation [78]. While this approach usually describes the Seebeck coefficient surprisingly well in a large number of cases, it notably fails to reproduce the correct sign of the Seebeck coefficient for Li [82]. Furthermore, it fails to describe the electrical conductivity while also failing to account for their respective temperature and carrier concentration dependences.

Only recently has there been a considerable push by the community to describe

electron scattering rates from first principles [83, 84, 85, 86, 87, 88, 89]. The major issue lies with the requirement of very fine sampling of electronic states in the proximity of the Fermi surface [90], making the calculation of electron-phonon scattering rates computationally expensive. Wannier interpolation has been successfully used to sample the Brillouin zone sufficiently densely to achieve convergence while considerably reducing the computational cost [85, 86, 91]. However, such approaches are limited to non-polar semiconductors, neglecting materials such as group III-V and II-VI compounds where Fröhlich interaction dominates [77]. Despite this limitation, the decay of excited electrons in the prototypical polar semiconductor GaAs from first principles has been obtained to good agreement with experiment [84].

Only very recent work by Sjakste *et al.* [88] has extended a Wannier interpolation scheme to take into account Fröhlich interaction using an analytical formula based off the Vogl model [92]. This approach was recently combined with an iterative solution to the linearised electron-phonon Boltzmann transport equation by Liu *et al.* [93] that captured the electronic mobility of GaAs to excellent agreement with experiment. By similarly splitting electron-phonon coupling into short range and long range parts, Zhou and Bernardi [94] also developed an *ab initio* approach to calculate the electronic mobility of polar semiconductors. The computational cost in this case is approximately the same as that of a non-polar material. However, there remains considerable debate as to whether the RTA is valid for polar semiconductors with low longitudinal optical frequencies, or if an iterative solution to the electron-phonon Boltzmann transport equation is necessary [93, 94].

The approach of Murphy-Armando and Fahy [83] offers an alternative method to calculate electron-phonon scattering rates in a computationally expeditious manner. By considering only low-lying valleys in the conduction band relevant for electron transport the need for very fine sampling of the entire Brillouin zone is sidestepped. Combined with deformation potential theory [79, 95] the electronic mobility of $n$-type $Si_xGe_{1-x}$ alloys is calculated to excellent agreement with experiment [83]. This approach also allows the strength of different electron-phonon coupling mechanisms to be easily compared, and is trivial to extend for higher carrier concentration and higher temperature regimes. This method coupled with the Fröhlich model of polar-optical scattering offers an excellent starting point to calculate the electronic mobility of PbTe, constituting the first step towards *ab initio* figures of merit of PbTe-based materials near the ferroelectric phase transition.

## 1.4 Thesis outline

The goal of this thesis is to show computationally that it is possible to exploit the unique properties that arise from proximity to the soft mode (ferroelectric) phase transition in PbTe to substantially decrease lattice thermal conductivity. We showed that by driving PbTe-based materials to the verge of the phase transition, anharmonic coupling between heat carrying acoustic modes and extremely softened TO modes is substantially increased, leading to considerably shorter phonon lifetimes across the frequency spectrum. This enables the scattering of phonons in the whole spectrum without relying on the concept of nanostructuring. We demonstrate three distinct strategies to achieve this, applying biaxial tensile (001) strain to PbTe and PbTe's alloy with PbSe, and furthermore by alloying PbTe with a rhombohedral group IV-VI material, GeTe. Ultimately, by combining the effects of increased proximity to the phase transition and mass disorder, we achieve reductions in lattice thermal conductivity by a factor of $2-3$ compared to PbTe. Furthermore, we extend the study of $Pb_{1-x}Ge_xTe$ alloys to investigate the interplay of proximity to the phase transition, mass disorder, and phase of the alloy in minimizing the lattice thermal conductivity. The role of high symmetry structures versus their lower symmetry distorted counterparts is also investigated in this regard. We find that the anharmonic contribution to lattice thermal conductivity is minimized at the phase transition, and that neither the rocksalt nor rhombohedral phases is inherently better for suppressing $\kappa_{\text{latt}}$. The minimal lattice thermal conductivity of $Pb_{1-x}Ge_xTe$ alloys is reduced by a factor of 3.5 compared to PbTe, and 7.5 compared to GeTe.

We take the first step towards a full *ab initio* calculation of the thermoelectric figure of merit by calculating the charge carrier mobility of $n$-type Ge and PbTe. We find excellent agreement with experiment for Ge, and reasonable agreement for PbTe when coupled with the Fröhlich model for polar-optical interaction. From a symmetry analysis and our DFPT calculations, we also find that electron-phonon coupling between the TO mode at $\Gamma$ and the conduction (valence) band minimum (maximum) is forbidden by symmetry in PbTe. Thus, electronic properties beneficial for a large $ZT$ may not be degraded by increased proximity to the phase transition. Coupled with these substantial reductions to $\kappa_{\text{latt}}$, tuning PbTe to the verge of the ferroelectric phase transition may be a promising strategy to greatly enhance thermoelectric performance.

The rest of this thesis is organised as follows.

In chapter 2, we discuss the theoretical background to the Boltzmann transport equation in the relaxation time approximation as used to calculate the lattice

thermal conductivity and electronic thermoelectric properties. This includes a discussion of density functional theory, which pertains to computing interatomic force constants to solve for the lattice thermal conductivity, and the description of electron-phonon interactions within the DFT formalism. We also include a brief discussion on modelling alloys in the context of thermal transport.

In chapter 3, we present a first principles study of the lattice thermal conductivity of PbTe-based materials driven to the verge of the ferroelectric phase transition using biaxial tensile (001) strain and/or alloying. We will discuss the impact to acoustic-TO phonon anharmonic coupling due to the increased proximity to the phase transition, and the decrease of phonon lifetimes and lattice thermal conductivity as a result of the increased acoustic-TO interaction.

In chapter 4, we investigate and quantify the impact of proximity to the ferroelectric phase transition and mass disorder on the lattice thermal conductivity of $Pb_{1-x}Ge_xTe$ alloys by varying their chemical composition. We will argue that both of these mechanisms, along with the average atomic mass, play a more crucial role in suppressing lattice thermal conductivity in comparison to effects arising from differences in the crystal structure between the two phases of the alloy.

In chapter 5, we calculate the charge carrier mobility of $n$-type PbTe and Ge considering the effects of electron-phonon interaction as the first step to obtaining a full *ab initio* calculation of the thermoelectric figure of merit. We use first principles approaches, deformation potential theory, and the Fröhlich model to achieve this.

In chapter 6, we summarise the main results of this work and give concluding remarks, followed by a brief outlook on future work.

The original work presented in this thesis has been published in the following papers:

- Ronan M. Murphy, Éamonn D. Murray, Stephen Fahy, and Ivana Savić, "Broadband phonon scattering in PbTe-based materials driven near ferroelectric phase transition by strain or alloying," *Phys. Rev. B*, **93**, 104304, 2016.

- Ronan M. Murphy, Éamonn D. Murray, Stephen Fahy, and Ivana Savić, "Ferroelectric phase transition and the lattice thermal conductivity of $Pb_{1-x}Ge_xTe$ alloys," *Phys. Rev. B*, **95**, 144302, 2017.

# Chapter 2

# Computational Methods

In this chapter we present the theoretical background to the first principles computational methods used in this thesis. We describe the basis of density functional theory, the main workhorse of this work, and briefly discuss some of the approximations used in its derivation. This is followed by a discussion of the Boltzmann transport equation in the relaxation time approximation (BTE-RTA) as applied to phonons, which allows us to compute the lattice thermal conductivity. We derive phonon scattering rates due to the anharmonicity of the crystal and mass disorder. We also briefly discuss the implementation of this approach and computational details. We finish with the BTE-RTA as applied to charge carriers, which yields the electronic thermoelectric properties; the electrical conductivity, Seebeck coefficient, and the electrical contribution to thermal conductivity, and the charge carrier mobility. This includes the derivation of electron scattering rates due to electron-phonon coupling in the DFT formalism, and how they may be calculated from density functional perturbation theory.

## 2.1 Total energy calculations

### 2.1.1 Many-body Hamiltonian

We begin by considering the Hamiltonian for a system of electrons and nuclei, given by:

$$\hat{H} = -\frac{\hbar^2}{2m_e}\sum_i \nabla_i^2 + \sum_{i\neq j}\frac{e^2}{|\mathbf{r}_i - \mathbf{r}_j|} + \sum_{i,K}\frac{Q_K e^2}{|\mathbf{r}_i - \mathbf{R}_K|} - \sum_K \frac{\hbar^2}{2m_K}\nabla_K^2 + \sum_{K\neq J}\frac{Q_K Q_J e^2}{|\mathbf{R}_K - \mathbf{R}_J|}, \tag{2.1}$$

where $\hbar$ is the Dirac constant, $m_e$, $\mathbf{r}_i$, and $e$ are the mass, coordinates, and charge of a given electron $i$, and $m_K$, $\mathbf{R}_K$, and $Q_K$ are the mass, coordinates, and charge

of a given nucleus $K$. The first term is the kinetic energy operator, the second is the electron-electron interaction, and the third is the potential acting on the electrons due to the nuclei with charge $Q_K$ at positions $\mathbf{R}_K$, which we label $\hat{T}$, $\hat{U}$, and $\hat{V}_{ext}$ respectively. The last two terms represent the kinetic energy of the nuclei and the nuclear-nuclear interaction respectfully.

We exploit the Born-Oppenheimer approximation [96], which separates the motions of the electrons and nuclei, allowing for a significant simplification of the above Hamiltonian. It follows that the wavefunction of a solid may be written as the product of the wavefunctions of the electrons and nuclei:

$$\psi_{\text{solid}} = \psi_{\text{electrons}}(\mathbf{r}_i, \mathbf{R}_K)\psi_{\text{nuclei}}(\mathbf{R}_K). \tag{2.2}$$

We treat the nuclear coordinates as fixed relative to the much more rapidly moving electrons, and then solve the time-independent Schrödinger equation for the system of electrons. Thus, we neglect the kinetic energy of the nuclei and the nuclear-nuclear interaction for the electronic problem, reducing the above Hamiltonian to:

$$\hat{H} = -\frac{\hbar^2}{2m_e}\sum_i \nabla_i^2 + \sum_{i\neq j}\frac{e^2}{|\mathbf{r}_i - \mathbf{r}_j|} + \sum_{i,K}\frac{Q_K e^2}{|\mathbf{r}_i - \mathbf{R}_K|}. \tag{2.3}$$

We define the interaction between an electron at $\mathbf{r}_i$ and an electron at $\mathbf{r}_j$ as:

$$U(\mathbf{r}_i, \mathbf{r}_j) = \frac{e^2}{|\mathbf{r}_i - \mathbf{r}_j|}, \tag{2.4}$$

with the potential felt by an electron at $\mathbf{r}$ due to the nuclei defined as:

$$V_{ext}(\mathbf{r}) = \sum_K \frac{Q_K e^2}{|\mathbf{r} - \mathbf{R}_K|}. \tag{2.5}$$

Thus, we re-write the Hamiltonian as:

$$\hat{H} = -\frac{\hbar^2}{2m_e}\sum_i \nabla_i^2 + \sum_{i\neq j} U(\mathbf{r}_i, \mathbf{r}_j) + \sum_i V_{ext}(\mathbf{r}_i) = \hat{T} + \hat{U} + \hat{V}_{ext}. \tag{2.6}$$

This gives the following many-body Schrödinger equation for a system of $N_e$ electrons each moving through an external potential $V_{ext}(\mathbf{r})$:

$$\left[\sum_i^{N_e}\left(-\frac{\hbar^2\nabla_i^2}{2m} + V_{ext}(\mathbf{r}_i)\right) + \sum_{i\neq j} U(\mathbf{r}_i, \mathbf{r}_j)\right]\Psi(\mathbf{r}_1, \mathbf{r}_2..., \mathbf{r}_{N_e}) = E\Psi(\mathbf{r}_1, \mathbf{r}_2..., \mathbf{r}_{N_e}). \tag{2.7}$$

## 2.1.2 Density functional theory

### 2.1.2.1 Hohenberg-Kohn theorems

Density Functional Theory (DFT) allows us to map the many-body problem of $N_e$ interacting electrons into one of a single electron moving in an effective potential. The foundations of DFT are the Hohenberg-Kohn theorems [97]:

Theorem 1: The external potential on electrons due to nuclei, $V_{ext}(\mathbf{r})$, is, to within a constant, a unique functional of the electron density $n(\mathbf{r})$. As a result, the ground state density uniquely determines the external potential and all other ground state properties of the system.

Theorem 2: There exists a universal functional for the energy $E[n]$ defined in terms of the density $n(\mathbf{r})$, where the exact ground state is the global minimum value of this functional.

Thus, we re-write the problem in terms of the electron density, $n(\mathbf{r})$, given by [98]:

$$n(\mathbf{r}) = N_e \int d^3\mathbf{r}_2 ... d^3\mathbf{r}_{N_e} \Psi^*(\mathbf{r}, \mathbf{r}_2 ..., \mathbf{r}_{N_e}) \Psi(\mathbf{r}, \mathbf{r}_2 ..., \mathbf{r}_{N_e}). \tag{2.8}$$

Hohenberg and Kohn showed that there is a one-to-one relationship between the external potential $V_{ext}(\mathbf{r})$, and the non-degenerate ground state wavefunction $\Psi$, and that there is a one-to-one relationship between $\Psi$ and the ground state density $n(\mathbf{r})$ of an $N_e$-electron system.

Since all ground state properties are uniquely determined by the electron density, the total energy may be expressed as a functional of $n(\mathbf{r})$:

$$\begin{aligned} E_{HK}[n(\mathbf{r})] &= T[n(\mathbf{r})] + U[n(\mathbf{r})] + V_{ext}[n(\mathbf{r})] \\ &= T[n] + U[n] + V_{ext}[n] \\ &= T[n] + U[n] + \int n(\mathbf{r}) V_{ext}(\mathbf{r}) d\mathbf{r} \\ &= F_{HK}[n] + \int n(\mathbf{r}) V_{ext}(\mathbf{r}) d\mathbf{r}, \end{aligned} \tag{2.9}$$

where $F_{HK}[n]$ is universal, may be applied to any $V_{ext}[n]$ [98], and includes the non-classical electron-electron self-interaction correction, exchange and Coulomb correlation. The energy functional $E_{HK}[n]$ also satisfies the Rayleigh-Ritz variational principle [99], yielding the ground state energy [98, 100]:

$$E_{GS} = \min_{n(\mathbf{r})} E_{HK}[n, V_{ext}], \tag{2.10}$$

for the ground state electron density under the constraint that the integral of $n(\mathbf{r})$ equals the total number of electrons.

While all ground state properties of the system may be determined from the ground state $n(\mathbf{r})$, in practice we are still left with the task of solving the many-body Schrödinger equation.

#### 2.1.2.2 Kohn-Sham equations

In 1965, Kohn and Sham transformed the problem of solving the many-body Schrödinger equation into one of solving an auxiliary system of non-interacting particles in a self-consistent mean field [101]. In order to do this they introduced a decomposition of the functional in Eq. (2.9):

$$F_{HK}[n] = T_s[n] + \frac{1}{2}\int d\mathbf{r}\ n(\mathbf{r})\Phi(\mathbf{r}) + E_{xc}[n], \tag{2.11}$$

where $T_s[n]$ is the kinetic energy in the ground state of a system of $N_e$ non-interacting electrons with density $n(\mathbf{r})$, and $\Phi(\mathbf{r}) = e^2 \int \frac{n(\mathbf{r}')}{|\mathbf{r}-\mathbf{r}'|} d\mathbf{r}'$ is the classical Coulomb potential for the electrons, both of which are known explicitly. $E_{xc}[n]$ is the exchange-correlation energy, and contains all the unknowns for the system:

$$E_{xc}[n] = (\langle \hat{T}[n] \rangle - T_s[n]) + \left( \langle \hat{U}[n] \rangle - \frac{1}{2}\int d\mathbf{r}\ n(\mathbf{r})\Phi(\mathbf{r}) \right), \tag{2.12}$$

where $\hat{T}[n]$ and $\hat{U}[n]$ are defined in Eq. (2.6). The correlation energy is the difference between the exact and Hartree-Fock energies, and the exchange energy is due to the Pauli exclusion principle [100, 102, 103]. Overall, $E_{xc}[n]$ is the energy difference between the kinetic and internal energies of the interacting many-body problem and the independent particle system with the same charge density $n(\mathbf{r})$. Solving this explicitly is of tremendous importance for DFT.

Applying the variational principle to Eqs. (2.9) and (2.11) yields [98]:

$$\frac{\delta E[n]}{\delta n(\mathbf{r})} = \frac{\delta T_s}{\delta n(\mathbf{r})} + V_{ext}(\mathbf{r}) + \Phi(\mathbf{r}) + V_{xc}[n], \tag{2.13}$$

with the requirement to retain a constant number of electrons, and where $V_{xc}[n] = \delta E_{xc}[n]/\delta n(\mathbf{r})$. If we compare the above equation to a corresponding auxiliary system of non-interacting electrons with the same density in a fixed potential $V(\mathbf{r})$:

$$\frac{\delta E[n]}{\delta n(\mathbf{r})} = \frac{\delta T_s}{\delta n(\mathbf{r})} + V(\mathbf{r}). \tag{2.14}$$

We see that both Eqs. (2.13) and (2.14) are identical provided:

$$V(\mathbf{r}) = V_{ext}(\mathbf{r}) + \Phi(\mathbf{r}) + V_{xc}[n], \tag{2.15}$$

which we label $V^{\mathrm{KS}}(\mathbf{r})$.

The solution for Eq. (2.14) may be obtained by solving the Schrödinger equation for non-interacting particles:

$$\hat{H}^{\mathrm{KS}}\psi_i(\mathbf{r}) = \left[-\frac{\hbar^2}{2m_e}\nabla^2 + V^{\mathrm{KS}}(\mathbf{r})\right]\psi_i(\mathbf{r}) = \epsilon_i\psi_i(\mathbf{r}), \tag{2.16}$$

which yields:

$$n(\mathbf{r}) = 2\sum_{i=1}^{N_e/2} f_i|\psi_i(\mathbf{r})|^2, \tag{2.17}$$

where the index $i$ denotes the eigenstate with eigenvalue $\epsilon_i$. $\psi_i$ are the Kohn-Sham (KS) orbitals and $f_i$ are the occupation numbers. Eqs. (2.15-2.17) are known as the Kohn-Sham equations, and may be solved iteratively until self-consistency is reached between the electron density $n(\mathbf{r})$ and potential $V^{\mathrm{KS}}(\mathbf{r})$. The ground state energy of the system may be written in terms of the Kohn-Sham eigenvalues $\epsilon_i$ [99]:

$$E[n] = 2\sum_{i=1}^{N_e/2}\epsilon_i - \frac{1}{2}\int d\mathbf{r}\; n(\mathbf{r})\Phi(\mathbf{r}) + E_{xc}[n] - \int n(\mathbf{r})V_{xc}[n]d\mathbf{r}. \tag{2.18}$$

This transforms the problem into one of solving the single particle Schrödinger equation, which is numerically trivial. However, the exchange-correlation energy, $E_{xc}[n]$, remains unknown, though various approximations to its form exist - see section 2.1.5, below.

### 2.1.3 Plane waves

The many-body problem of a system of electrons has now been reduced to an effective single particle problem. However, there is still the problem of solving for an infinite number of electrons moving in a static potential due to an infinite number of ions. Crystalline materials with a periodic lattice have a periodic potential which obeys $V(\mathbf{r}) = V(\mathbf{r} + \mathbf{R})$, where $\mathbf{R}$ is any vector of the Bravais lattice. Thus, we use Bloch's theorem [16, 104], which states that the electronic wavefunction at a wavevector $\mathbf{k}$ in a periodic solid may be written as the product of a plane wave and lattice-periodic part [16, 104]:

$$\psi_{i,\mathbf{k}}(\mathbf{r}) = \frac{1}{\sqrt{N_l}}e^{i\mathbf{k}\cdot\mathbf{r}}u_{i,\mathbf{k}}(\mathbf{r}), \tag{2.19}$$

where $N_l$ is the number of primitive cells, and the lattice periodic part satisfies

$u_{i,\mathbf{k}}(\mathbf{r}+\mathbf{R}) = u_{i,\mathbf{k}}(\mathbf{r})$. This may then be re-written as:

$$\psi_{i,\mathbf{k}}(\mathbf{r}+\mathbf{R}) = e^{i\mathbf{k}\cdot\mathbf{R}}\psi_{i,\mathbf{k}}(\mathbf{r}), \tag{2.20}$$

which allows us to reproduce the electronic wavefunction with a plane wave expansion in terms of the reciprocal lattice vector $\mathbf{G}$:

$$u_{i,\mathbf{k}}(\mathbf{r}) = \frac{1}{\sqrt{\Omega}}\sum_{\mathbf{G}} c_{i,\mathbf{k}+\mathbf{G}} e^{i\mathbf{G}\cdot\mathbf{r}}, \tag{2.21}$$

where $\Omega$ is the primitive cell volume, and $c_{i,\mathbf{k}+\mathbf{G}}$ are the Fourier coefficients. This allows us to write the wavefunction in terms of a discrete set of plane waves:

$$\psi_{i,\mathbf{k}}(\mathbf{r}) = \frac{1}{\sqrt{N_l\Omega}}\sum_{\mathbf{G}} c_{i,\mathbf{k}+\mathbf{G}} e^{i(\mathbf{k}+\mathbf{G})\cdot\mathbf{r}}. \tag{2.22}$$

Thus, we may rewrite Eq. (2.16) to obtain a matrix equation for the plane wave coefficients, $c_{i,\mathbf{k}+\mathbf{G}}$ [104]:

$$\sum_{\mathbf{G}'}\left(\frac{\hbar^2}{2m_e}|\mathbf{k}+\mathbf{G}|^2\delta_{\mathbf{G}\mathbf{G}'} + V^{\mathrm{KS}}(\mathbf{G}-\mathbf{G}')\right)c_{i,\mathbf{k}+\mathbf{G}'} = \epsilon_i c_{i,\mathbf{k}+\mathbf{G}}. \tag{2.23}$$

where $\delta_{ij}$ is the Kronecker delta, which equals 0 for $i \neq j$ and 1 for $i = j$. The problem of calculating an infinite number of electronic wavefunctions has now been cast in terms of a finite number of wavefunctions on an infinite number of $\mathbf{k}$ points with a discrete plane wave basis set.

Electronic wavefunctions will be almost identical at $\mathbf{k}$ points very near each other. Thus, we may approximate the infinite $\mathbf{k}$ grid with a finite one, where each point represents the electronic wavefunction over a small region of $\mathbf{k}$ space. One popular scheme for generating this finite grid of points to accurately capture the electronic properties and total energy of a system is the Monkhorst and Pack scheme [105]. In principle, an infinite plane wave basis set is required to expand the electronic wavefunctions. In practice, we may choose an energy cut-off, taking only those wavevectors $\mathbf{G}$ that satisfy $\frac{\hbar^2}{2m_e}|\mathbf{k}+\mathbf{G}|^2 < E_{\mathrm{cut}}$, limiting the expansion of the plane waves to a finite set. We note that plane waves with kinetic energy smaller than $\frac{\hbar^2}{2m_e}|\mathbf{k}+\mathbf{G}|^2$ are typically more important than those with higher kinetic energy [104].

Calculations are typically performed within the first Brillouin zone, which is a uniquely defined primitive cell in reciprocal space, and completely characterises a periodic solid as per Bloch's theorem. However, numerically, one must converge with respect to the $\mathbf{k}$ grid density and value of $E_{\mathrm{cut}}$ to ensure an accurate value

for the total energy of the system.

### 2.1.4 Pseudopotential approximation

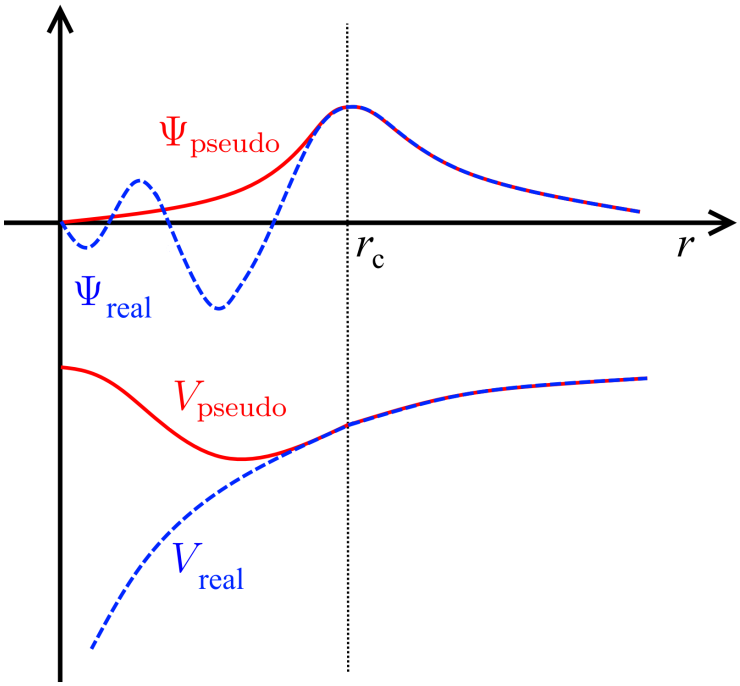



Figure 2.1: Sketch showing the Coulomb potential and real wavefunction in blue compared to the pseudopotential and pseudowavefunction in red, which match beyond the cut-off radius $r_c$.

The Kohn-Sham orbitals, $\psi_i$, have now been cast in terms of a plane wave basis set, as discussed. However, describing core electrons can still be quite a computationally demanding task. This arises from the fact that core and valence states oscillate rapidly near the nuclei to maintain mutual orthogonality, necessitating the use of a considerably large basis set. As a result of this rapid oscillation, valence electrons also have large kinetic energies, which roughly cancel with the strong Coulomb potential in the core region. This results in the valence electrons being considerably less bound to the nucleus compared to core electrons.

As the chemical bonding and interatomic forces of a material depend on the valence states far more than they do on the core states, we may in practice use the pseudopotential approximation. We replace the core electrons and strong Coulomb potential with an effective pseudopotential within a cut-off radius $r_c$, see Fig. 2.1 [106, 107, 108]. The wavefunctions of these core electrons are also replaced with pseudowavefunctions which vary smoothly in the core region.

Pseudopotentials and pseudowavefunctions are constructed in a manner such that outside a specified cut-off radius, $r_c$, they yield the same result for the potential and wavefunctions as that of the all electron case. Replacing the nucleus and core electrons with a pseudopotential thus considerably reduces the number of orbitals (the core orbitals having been removed) and size of the plane wave basis set when solving for the total energy of the system. This reduces the problem to that of a much weaker potential acting on valence electrons only.

A pseudopotential is generally constructed with local and non-local parts:

$$V_{\text{ps}} = V_{\text{local}}(r) + \sum_{lm} V_l(r) \left|Y_{lm}\right\rangle \left\langle Y_{lm}\right| , \tag{2.24}$$

where $Y_{lm}$ are the spherical harmonics, $l, m$ are the angular momentum quantum numbers, and $r$ is the distance from the nucleus. The local part operates on all one-particle wavefunctions in the same manner. The non-local part produces a potential dependent on the quantum numbers $l, m$ of the valence electron, such that pseudowavefunctions reproduce the same scattering properties as the nucleus and core electrons.

Norm conserving pseudopotentials are perhaps the most popular choice of pseudopotential, and come with the stipulation that the norm of each pseudowavefunction is the same as that of the all electron case, both inside and outside $r_c$ [109]. Relativistic effects may also be included in the pseudopotential construction so that a non-relativistic calculation may reproduce these effects in heavier atoms where these properties are more relevant [110]. Unless otherwise stated, all DFT calculations in this thesis use the norm-conserving pseudopotentials of Hartwigsen, Goedecker and Hutter (HGH) [110].

### 2.1.5 Exchange-correlation functional

The exchange-correlation energy, $E_{xc}$, is not explicitly known, adding to the difficulty of calculating the ground state energy with the DFT formalism. This has resulted in numerous approaches being employed to gain an approximate expression for $E_{xc}$. However, the simplest method to approximate $E_{xc}$, originally proposed by Kohn and Sham [101], is still in wide use to this day. If $n(\mathbf{r})$ is sufficiently slowly varying, $E_{xc}$ may be approximated with the Local Density Approximation (LDA) [101]:

$$E_{xc}^{\text{LDA}}[n] = \int n(\mathbf{r}) \epsilon^{\text{LDA}}(n(\mathbf{r})) d^3\mathbf{r} \tag{2.25}$$

where $\epsilon^{\mathrm{LDA}}(n)$ is the exchange-correlation energy per particle of a homogeneous electron gas with density $n$. The exchange-correlation potential is given by:

$$V_{xc}^{\mathrm{LDA}}[n] = \frac{\delta E_{xc}^{\mathrm{LDA}}[n]}{\delta n(\mathbf{r})} = \epsilon_{xc}[n] + n(\mathbf{r})\frac{\partial \epsilon^{\mathrm{LDA}}(n)}{\partial n}. \tag{2.26}$$

The LDA is known to give surprisingly good performance, far beyond the cases it was originally intended for. This good performance originates from its systematic error cancellation, whereby it typically overestimates the exchange energy but underestimates the correlation energy [111, 112]. It holds for situations where the density is almost constant [97], and at high densities where the kinetic energy dominates the exchange and correlation terms [101]. However, the LDA will fail in situations where the density varies rapidly. Unless otherwise stated, all DFT calculations in this work have been performed with the Teter-Pade parametrisation of the LDA [113].

Another popular choice for the $E_{xc}$ is the generalised gradient approximation (GGA) [114], which builds upon the LDA by adding a gradient term which describes the spatial derivative of the charge density. There are many flavours of implementation, with one of the more popular choices being that of Perdew, Burke, and Ernzerhof (GGA-PBE) [115]. This idea of building upon previous approximations for $E_{xc}$ is termed "Jacob's ladder", where each higher "rung" describes an extra level of sophistication [98]. Further, more elaborate choices for the exchange-correlation energy include meta-GGAs and hybrid functionals, each advancing up higher "rungs" in turn [116].

### 2.1.6 Structural relaxation

According to the Hellmann-Feynman theorem [117], the forces on atom $K$ are given by:

$$\mathbf{F}_K = -\frac{\partial E_F}{\partial \mathbf{R}_K} = -\left\langle \psi \right| \frac{\partial \hat{H}_F}{\partial \mathbf{R}_K} \left| \psi \right\rangle . \tag{2.27}$$

where the Hamiltonian $\hat{H}_F$ is that for a system of electrons defined previously with the addition of nuclear-nuclear interaction. Minimising with respect to these forces allows us to find the equilibrium configuration of a system. Within this work, structural optimisation carried out in the ABINIT code has been performed with the Broyden-Fletcher-Goldfarb-Shanno minimisation [118].

## 2.2 Lattice thermal conductivity

### 2.2.1 Crystal potential

In this section we derive the lattice dynamics for a general three-dimensional crystal in terms of interatomic force constants, as detailed in Ref. [51]. We start from the potential energy $V$ of such a crystal where the $l$th unit cell lattice vector is labelled $\mathbf{R}_l$ and the $b$th atom has mass $m_b$. Due to lattice periodicity we can map the entire crystal from the original basis unit cell with these lattice vectors. Expanding the potential energy in a Taylor series in powers of the atomic displacement $\mathbf{u}^{lb}$ from its equilibrium position and truncating to third order, we get:

$$\begin{aligned} V =& V_0 + \sum_{lb}\sum_{\alpha} \left.\frac{\partial V}{\partial u_\alpha^{lb}}\right|_0 u_\alpha^{lb} + \frac{1}{2}\sum_{lb,l'b'}\sum_{\alpha\beta} \left.\frac{\partial^2 V}{\partial u_\alpha^{lb}\partial u_\beta^{l'b'}}\right|_0 u_\alpha^{lb}u_\beta^{l'b'} \\ &+ \frac{1}{3!}\sum_{lb,l'b',l''b''}\sum_{\alpha\beta\gamma} \left.\frac{\partial^3 V}{\partial u_\alpha^{lb}\partial u_\beta^{l'b'}\partial u_\gamma^{l''b''}}\right|_0 u_\alpha^{lb}u_\beta^{l'b'}u_\gamma^{l''b''}, \end{aligned} \tag{2.28}$$

where $\alpha, \beta, \gamma$ are Cartesian directions, and $V_0$ is a constant that we set to zero for convenience. The second term, the first derivative of the potential energy with respect to atomic displacement, is zero due to the fact that energy is a minimum at equilibrium. We now define $\mathbf{\Phi}$ to be the interatomic force constant tensor. For the second order derivatives of the energy with respect to atomic displacement, we get the second order force constants:

$$\Phi_{\alpha\beta}^{lb,l'b'} = \left.\frac{\partial^2 V}{\partial u_\alpha^{lb}\partial u_\beta^{l'b'}}\right|_0, \tag{2.29}$$

and similarly we get the third order forces constants from the third order derivatives of the energy with respect to atomic displacement:

$$\Phi_{\alpha\beta\gamma}^{lb,l'b',l''b''} = \left.\frac{\partial^3 V}{\partial u_\alpha^{lb}\partial u_\beta^{l'b'}\partial u_\gamma^{l''b''}}\right|_0. \tag{2.30}$$

Writing the potential energy in terms of the interatomic force constant tensors, we arrive at:

$$V = \frac{1}{2}\sum_{lb,l'b'}\sum_{\alpha\beta}\Phi_{\alpha\beta}^{lb,l'b'}u_\alpha^{lb}u_\beta^{l'b'} + \frac{1}{3!}\sum_{lb,l'b',l''b''}\sum_{\alpha\beta\gamma}\Phi_{\alpha\beta\gamma}^{lb,l'b',l''b''}u_\alpha^{lb}u_\beta^{l'b'}u_\gamma^{l''b''} \tag{2.31}$$

where the first term is the harmonic potential, $V_{harm}$, and the second term is the third-order anharmonic potential, $V_{anh}$.

### 2.2.2 Dynamical matrix

The harmonic approximation treats a crystal as a system of harmonic oscillators that act independently of each other. The displacements of the harmonic potential, $V_{harm}$ in Eq. (2.31), may be written in terms of a set of decoupled normal vibrational modes. Classically there are $3N$ such modes for a system of $N$ atoms with 3 degrees of freedom. Writing the equation of motion for this system:

$$m_b \frac{\partial^2 u_\alpha^{lb}}{\partial t^2} = -\frac{\partial V_{harm}}{\partial u_\alpha^{lb}} = -\sum_{l'b'} \sum_{\beta} \Phi_{\alpha\beta}^{lb,l'b'} u_\beta^{l'b'}. \tag{2.32}$$

By exploiting the translational invariance of the force constant tensor $\mathbf{\Phi}$, we may re-write the force constants in term of the relative position between unit cells, $\Phi_{\alpha\beta}^{lb,l'b'} = \Phi_{\alpha\beta}^{0b,l'b'}$, which allows the equation of motion to be rewritten:

$$m_b \frac{\partial^2 u_\alpha^{lb}}{\partial t^2} = -\sum_{l'b'} \sum_{\beta} \Phi_{\alpha\beta}^{0b,l'b'} u_\beta^{l'b'}. \tag{2.33}$$

Plane wave solutions may be found to the above equation assuming temporal, $e^{i(-\omega t)}$, and spatial, $e^{i(\mathbf{q}.\mathbf{R}_l)}$ dependences:

$$u_\alpha^{lb} = \frac{1}{\sqrt{m_b}} \sum_{\mathbf{q}s} e_{\alpha b}^s(\mathbf{q}) e^{i(\mathbf{q}.\mathbf{R}_l - \omega_{\mathbf{q}s} t)}, \tag{2.34}$$

where $\omega_{\mathbf{q}s}$ is the frequency of a vibrational mode with wavevector $\mathbf{q}$ and polarisation $s$ in the first Brillouin zone. $e_{\alpha b}^s(\mathbf{q})$ is a polarisation vector that characterises the motion of atom $b$. Substituting the above solution into Eq. (2.33) yields:

$$\omega_{\mathbf{q}s}^2 e_{\alpha b}^s(\mathbf{q}) = \sum_{b'\beta} D_{\alpha\beta}^{bb'}(\mathbf{q}) e_{\beta b'}^s(\mathbf{q}), \tag{2.35}$$

where $D_{\alpha\beta}^{bb'}(\mathbf{q})$ is the dynamical matrix, given by:

$$D_{\alpha\beta}^{bb'}(\mathbf{q}) = \frac{1}{\sqrt{m_b m_{b'}}} \sum_{l'} \Phi_{\alpha\beta}^{0b,l'b'} e^{i(\mathbf{q}.\mathbf{R}_l)}. \tag{2.36}$$

Re-writing Eq. (2.35) as a determinant equation gives a non-trivial solution:

$$|D_{\alpha\beta}^{bb'}(\mathbf{q}) - \omega_{\mathbf{q}s}^2 \delta_{\alpha\beta}\delta_{bb'}| = 0. \tag{2.37}$$

Diagonalising the dynamical matrix thus yields the normal mode frequencies, $\omega_{\mathbf{q}s}$, and normal mode eigenvectors, $\mathbf{e}_b^s(\mathbf{q})$ for a given $\mathbf{q}$. These normal modes of the harmonic crystal are called phonons, and have a momentum $\mathbf{q}$, with

branch index $s$. There are $3N$ such eigenvalues $\omega^2_{\mathbf{q}s}$, with the branch index correspondingly taking values $s = 1, 2, ..., 3N$. Further, the eigenvectors $\mathbf{e}^s_b(\mathbf{q})$ obey the orthonormality and completeness relations:

$$\sum_{b,\alpha} e^{*s}_{\alpha b}(\mathbf{q}) e^{s'}_{\alpha b}(\mathbf{q}) = \delta_{ss'}, \tag{2.38}$$

$$\sum_{s} e^{*s}_{\beta b'}(\mathbf{q}) e^{s'}_{\alpha b}(\mathbf{q}) = \delta_{\alpha\beta}\delta_{bb'}. \tag{2.39}$$

Thus, the dispersion relation (frequency dependence of the momentum) may be obtained throughout the first Brillouin zone. However, expanding the potential energy $V$ of the crystal up to second order only describes non-interacting phonons. The inclusion of higher order, anharmonic, terms captures the effects of phonons interacting with each other, as will be discussed in the following sections.

### 2.2.3 Second quantisation

To simplify the description of phonon dynamics, we cast the crystal Hamiltonian in terms of the phonon creation ($\hat{a}^\dagger_{\mathbf{q}s}$) and annihilation ($\hat{a}_{\mathbf{q}s}$) operators, so called second quantisation. To begin, we state the Hamiltonian in terms of the coordinate $\mathbf{u}^{lb}$ and momentum $\mathbf{p}^{lb}$ variables:

$$\begin{aligned}\hat{H} =& \sum_{lb} \frac{\mathbf{p}^{lb}.\mathbf{p}^{lb}}{2m_b} + \frac{1}{2}\sum_{lb,l'b'}\sum_{\alpha\beta} \Phi^{lb,l'b'}_{\alpha\beta} u^{lb}_\alpha u^{l'b'}_\beta \\ &+ \frac{1}{3!}\sum_{lb,l'b',l''b''}\sum_{\alpha\beta\gamma} \Phi^{lb,l'b',l''b''}_{\alpha\beta\gamma} u^{lb}_\alpha u^{l'b'}_\beta u^{l''b''}_\gamma\end{aligned} \tag{2.40}$$

where the second and third terms are the harmonic and anharmonic terms of the crystal potential respectively.

Initially, we perform a Fourier analysis and obtain $\mathbf{u}^{lb}$ and $\mathbf{p}^{lb}$ in terms of the wavevector $\mathbf{q}$ and normal coordinate operators $\mathbf{X}_{\mathbf{q}b}$ and $\mathbf{P}_{\mathbf{q}b}$ respectively:

$$\mathbf{u}^{lb} = \frac{1}{\sqrt{N_l}}\sum_{\mathbf{q}} \mathbf{X}_{\mathbf{q}b} e^{i\mathbf{q}\cdot\mathbf{R}_l}, \qquad \mathbf{p}^{lb} = \frac{1}{\sqrt{N_l}}\sum_{\mathbf{q}} \mathbf{P}_{\mathbf{q}b} e^{i\mathbf{q}\cdot\mathbf{R}_l}. \tag{2.41}$$

The next transformation introduces the polarisation vector $\mathbf{e}^s_b(\mathbf{q})$ and casts these normal coordinate operators in terms of the phonon branch index, $s$:

$$\mathbf{X}_{\mathbf{q}s} = \sum_b \sqrt{m_b}\mathbf{e}^{*s}_b(\mathbf{q}) \cdot \mathbf{X}_{\mathbf{q}b}, \qquad \mathbf{P}_{\mathbf{q}s} = \sum_b \frac{1}{\sqrt{m_b}}\mathbf{e}^s_b(\mathbf{q}) \cdot \mathbf{P}_{\mathbf{q}b}. \tag{2.42}$$

Finally, we introduce the phonon creation and annihilation operators:

$$\hat{a}^{\dagger}_{\mathbf{q}s} = \frac{1}{\sqrt{2\hbar\omega_{\mathbf{q}s}}} P^{\dagger}_{\mathbf{q}s} + i\sqrt{\frac{\omega_{\mathbf{q}s}}{2\pi}} X_{\mathbf{q}s}, \tag{2.43}$$

$$\hat{a}_{\mathbf{q}s} = \frac{1}{\sqrt{2\hbar\omega_{\mathbf{q}s}}} P_{\mathbf{q}s} - i\sqrt{\frac{\omega_{\mathbf{q}s}}{2\hbar}} X^{\dagger}_{\mathbf{q}s}, \tag{2.44}$$

which act on the phonon eigenstates, $n_{\mathbf{q}s} = n(\omega_{\mathbf{q}s})$, as follows:

$$\hat{a}^{\dagger}_{\mathbf{q}s} \left| n_{\mathbf{q}s} \right\rangle = \sqrt{n_{\mathbf{q}s} + 1} \left| n_{\mathbf{q}s} + 1 \right\rangle, \tag{2.45}$$

$$\hat{a}_{\mathbf{q}s} \left| n_{\mathbf{q}s} \right\rangle = \sqrt{n_{\mathbf{q}s}} \left| n_{\mathbf{q}s} - 1 \right\rangle, \tag{2.46}$$

respectively raising or lowering the occupation of a phonon mode $\mathbf{q}s$.

We may now write the displacement and momentum as [16, 119]:

$$\mathbf{u}^{lb} = \sum_{\mathbf{q}s} \left( \frac{\hbar}{2m_b \omega_{\mathbf{q}s} N_l} \right)^{\frac{1}{2}} \mathbf{e}^{s}_{b}(\mathbf{q}) \left( \hat{a}_{\mathbf{q}s} + \hat{a}^{\dagger}_{-\mathbf{q}s} \right) e^{i\mathbf{q}\cdot\mathbf{R}_l}, \tag{2.47}$$

$$\mathbf{p}^{lb} = -i \sum_{\mathbf{q}s} \left( \frac{\hbar m_b \omega_{\mathbf{q}s}}{2N_l} \right)^{\frac{1}{2}} \mathbf{e}^{s}_{b}(\mathbf{q}) \left( \hat{a}_{\mathbf{q}s} - \hat{a}^{\dagger}_{-\mathbf{q}s} \right) e^{i\mathbf{q}\cdot\mathbf{R}_l}. \tag{2.48}$$

Taking the harmonic part of the Hamiltonian in Eq. (2.40), we utilise the transformations above to express it in terms of creation and annihilation operators:

$$\hat{H}_{harm} = \sum_{\mathbf{q}s} \hbar\omega_{\mathbf{q}s} \left( \hat{a}^{\dagger}_{\mathbf{q}s} \hat{a}_{\mathbf{q}s} + \frac{1}{2} \right), \tag{2.49}$$

which is a sum over harmonic oscillators, with the total energy given as:

$$E = \sum_{\mathbf{q}s} \left( n_{\mathbf{q}s} + \frac{1}{2} \right) \hbar\omega_{\mathbf{q}s}. \tag{2.50}$$

Furthermore, taking the anharmonic potential and applying the transformations above, we obtain:

$$\begin{aligned} V_{anh} = & \frac{1}{3!} \sum_{\mathbf{q}s,\mathbf{q}'s',\mathbf{q}''s''} \delta_{\mathbf{G},\mathbf{q}+\mathbf{q}'+\mathbf{q}''} \mathbf{\Psi}_{\mathbf{q}s,\mathbf{q}'s',\mathbf{q}''s''} \\ & \times \left( \hat{a}^{\dagger}_{\mathbf{q}s} - \hat{a}_{-\mathbf{q}s} \right) \left( \hat{a}^{\dagger}_{\mathbf{q}'s'} - \hat{a}_{-\mathbf{q}'s'} \right) \left( \hat{a}^{\dagger}_{\mathbf{q}''s''} - \hat{a}_{-\mathbf{q}''s''} \right), \end{aligned} \tag{2.51}$$

where:

$$\mathbf{\Psi}_{\mathbf{q}s,\mathbf{q}'s',\mathbf{q}''s''} = i\left(\frac{\hbar^3}{8N_l}\right)^{\frac{1}{2}} \sum_{bb'b''}\sum_{\alpha\beta\gamma} \Phi^{\mathbf{q}b,\mathbf{q}'b',\mathbf{q}'b''}_{\alpha\beta\gamma} \frac{e^{s}_{\alpha b}(\mathbf{q})}{\sqrt{m_b\omega_{\mathbf{q}s}}} \frac{e^{s'}_{\beta b}(\mathbf{q}')}{\sqrt{m_{b'}\omega_{\mathbf{q}'s'}}} \frac{e^{s''}_{\gamma b}(\mathbf{q}'')}{\sqrt{m_{b''}\omega_{\mathbf{q}''s''}}}, \tag{2.52}$$

which represents a summation over three-phonon collision operators, and governs which three-phonon processes occur as a result of the anharmonicity of the crystal potential.

### 2.2.4 Boltzmann transport equation

The general form of the Boltzmann transport equation is written as:

$$\frac{\partial f}{\partial t} = \left.\frac{\partial f}{\partial t}\right|_{\text{force}} + \left.\frac{\partial f}{\partial t}\right|_{\text{diff}} + \left.\frac{\partial f}{\partial t}\right|_{\text{scatt}}, \tag{2.53}$$

where $f$ is associated with the number of particles in the system. The terms on the right hand side of the equation represent the change in $f$ due to external forces acting on the particles, diffusion and scattering, respectively.

The lattice thermal conductivity of a material may be calculated using the Boltzmann transport equation as applied to phonons, where $f$ is the phonon distribution function $n_{\mathbf{q}s}$. In the absence of a heat current phonons are in their equilibrium state, and obey Bose-Einstein statistics with the distribution function given as:

$$\bar{n}_{\mathbf{q}s} = \frac{1}{e^{\hbar\omega_{\mathbf{q}s}/k_{\text{B}}T} - 1}. \tag{2.54}$$

In the presence of a finite temperature gradient, $\nabla_{\mathbf{r}}T$, the equilibrium distribution function is perturbed by an amount proportional to $\nabla_{\mathbf{r}}T$. Two terms are responsible for the rate of change of the distribution function, the diffusion and scattering terms respectively, which must equal zero in the steady state of heat flow through the material:

$$\left.\frac{\partial n_{\mathbf{q}s}}{\partial t}\right|_{\text{diff}} + \left.\frac{\partial n_{\mathbf{q}s}}{\partial t}\right|_{\text{scatt}} = 0. \tag{2.55}$$

The diffusion term may be written as $\left.\frac{\partial n_{\mathbf{q}s}}{\partial t}\right|_{\text{diff}} = -v_{\mathbf{q}s}.\nabla_{\mathbf{r}}T\frac{\partial n_{\mathbf{q}s}}{\partial T}$ where $v_{\mathbf{q}s}$ is the phonon group velocity, yielding the phonon Boltzmann transport equation in its general form [51, 55, 56]:

$$-v_{\mathbf{q}s}.\nabla_{\mathbf{r}}T\frac{\partial n_{\mathbf{q}s}}{\partial T} + \left.\frac{\partial n_{\mathbf{q}s}}{\partial t}\right|_{\text{scatt}} = 0, \tag{2.56}$$

where the left term describes a system of non-interacting phonons diffusing and the right term describes all scattering processes of phonons into and out of state $\mathbf{q}s$. Such processes may be elastic in nature, such as those due to mass disorder, or inelastic processes due to the crystal anharmonicity, as will be discussed in more detail in the following sections.

Solving Eq. (2.56) is a difficult task. To simplify this we utilise the relaxation time approximation (RTA), as follows. The equilibrium distribution function, $\bar{n}_{\mathbf{q}s}$, does not change with time. Assuming a small deviation of the phonon distribution from equilibrium in the presence of a small temperature gradient, we arrive at:

$$n_{\mathbf{q}s} = \bar{n}_{\mathbf{q}s} + n'_{\mathbf{q}s}, \tag{2.57}$$

which is the Taylor expansion about the equilibrium $\bar{n}_{\mathbf{q}s}$ up to the linear term $n'_{\mathbf{q}s}$, the perturbed phonon population. We now define $\tau_{\mathbf{q}s}$ as the time taken for the perturbed states to relax back to equilibrium. This is referred to as the single mode relaxation time (SMRT) and is a single effective phonon lifetime that expresses all scattering processes for a given mode under the assumption that all other modes are in equilibrium. Thus, we re-write the second term in Eq. (2.56) as:

$$\left.\frac{\partial n_{\mathbf{q}s}}{\partial t}\right|_{\text{scatt}} = -\frac{n_{\mathbf{q}s} - \bar{n}_{\mathbf{q}s}}{\tau_{\mathbf{q}s}}. \tag{2.58}$$

Secondly, we assume that in steady state the deviation from equilibrium due to a finite temperature gradient is small such that $n_{\mathbf{q}s} \approx \bar{n}_{\mathbf{q}s}$ in the diffusive term in Eq. (2.56). This allows us to write the linearised Boltzmann transport equation in the relaxation time approximation (BTE-RTA):

$$-v_{\mathbf{q}s}.\nabla_{\mathbf{r}} T \frac{\partial \bar{n}_{\mathbf{q}s}}{\partial T} = \frac{n_{\mathbf{q}s} - \bar{n}_{\mathbf{q}s}}{\tau_{\mathbf{q}s}}, \tag{2.59}$$

which holds for elastic scattering processes, and is also used to approximate the treatment of inelastic scattering processes.

Under Fourier's law, the rate of heat flow per unit area may be written as:

$$\mathbf{Q} = -\kappa \nabla_{\mathbf{r}} T, \tag{2.60}$$

where $\kappa$ is the thermal conductivity. More specifically, the heat flow in direction $\alpha$ due to a temperature gradient in direction $\beta$ may be written as a sum over phonon modes of the energy carried by a phonon, its group velocity, and perturbed phonon

population:

$$\mathbf{Q}_\alpha = -\frac{1}{N_l\Omega}\sum_{\mathbf{q}s}\hbar\omega_{\mathbf{q}s}v_{\mathbf{q}s,\alpha}n_{\mathbf{q}s} = -\kappa_{\alpha\beta}|\nabla T|_\beta. \tag{2.61}$$

Taking the phonon Boltzmann equation, Eq. (2.56), and assuming a temperature gradient along $\beta$, we obtain:

$$-v_{\mathbf{q}s,\beta}.|\nabla T|_\beta\frac{\partial n_{\mathbf{q}s}}{\partial T} = \frac{n_{\mathbf{q}s}-\bar{n}_{\mathbf{q}s}}{\tau_{\mathbf{q}s}}. \tag{2.62}$$

Re-writing this, we arrive at an expression for the perturbed phonon population:

$$n_{\mathbf{q}s}-\bar{n}_{\mathbf{q}s} = -v_{\mathbf{q}s,\beta}|\nabla T|_\beta\frac{\partial n_{\mathbf{q}s}}{\partial T}\tau_{\mathbf{q}s}, \tag{2.63}$$

Substituting this expression into Eq. (2.61), we obtain the lattice thermal conductivity:

$$\kappa_{\alpha\beta} = \frac{1}{N_l\Omega}\sum_{\mathbf{q}s}\hbar\omega_{\mathbf{q}s}\frac{\partial\bar{n}_{\mathbf{q}s}}{\partial T}v_{\mathbf{q}s,\alpha}v_{\mathbf{q}s,\beta}\tau_{\mathbf{q}s}, \tag{2.64}$$

which we may re-write as a tensor:

$$\boldsymbol{\kappa}_{\text{latt}} = \frac{1}{N_l\Omega}\sum_{\mathbf{q}s}c_{\mathbf{q}s}v^2_{\mathbf{q}s}\tau_{\mathbf{q}s}, \tag{2.65}$$

where $c_{\mathbf{q}s}$ is the quantum heat capacity for a given mode $\mathbf{q}s$ [62, 119]:

$$c_{\mathbf{q}s} = \hbar\omega_{\mathbf{q}s}\frac{\partial\bar{n}_{\mathbf{q}s}}{\partial T} = k_B\left(\frac{\hbar\omega_{\mathbf{q}s}}{k_BT}\right)^2\frac{e^{\hbar\omega_{\mathbf{q}s}/k_BT}}{(e^{\hbar\omega_{\mathbf{q}s}/k_BT}-1)^2}. \tag{2.66}$$

The phonon group velocities $v_{\mathbf{q}s}$ are calculated from first order perturbation theory [62, 119]:

$$v_{\mathbf{q}s,\alpha} = \frac{\partial\omega_{\mathbf{q}s}}{\partial\mathbf{q}_{\boldsymbol{\alpha}}} = \frac{1}{2\omega_{\mathbf{q}s}}\sum_{bb'}\sum_{\beta\gamma}e^{*s}_{\beta b}(\mathbf{q})\frac{\partial D^{bb'}_{\beta\gamma}(\mathbf{q})}{\partial\mathbf{q}}e^{s}_{\gamma b}(\mathbf{q}). \tag{2.67}$$

The total lifetime of a given phonon mode may be expressed as a sum of contributions from elastic and inelastic processes, added together using Matthiessen's rule [16]:

$$\frac{1}{\tau^{total}_{\mathbf{q}s}} = \frac{1}{\tau^{elastic}_{\mathbf{q}s}} + \frac{1}{\tau^{inelastic}_{\mathbf{q}s}}, \tag{2.68}$$

where elastic processes are those that arise from such effects as boundary scattering, points defects, and mass disorder due to isotopes or alloying. Inelastic processes are phonon-phonon interactions that arise from the anharmonicity of the crystal potential. In the following sections, we will derive expressions for $\tau_{\mathbf{q}s}$

due to anharmonic (three-phonon) interactions and mass disorder respectively. We note that typically only anharmonic processes up to third order are treated, with higher order terms generally being weaker in comparison [120].

### 2.2.5 Anharmonic phonon lifetimes

The single mode relaxation time may be more formally expressed from the phonon collision operator acting on the deviation of a given phonon mode $\mathbf{q}s$ from equilibrium, assuming that all phonon states $\mathbf{q}'s' \neq \mathbf{q}s$ are in equilibrium. We begin by treating $\psi_{\mathbf{q}s}$ as a measure of the deviation of mode $\mathbf{q}s$ from equilibrium. In order to linearise net scattering rates, we expand the perturbed phonon population $n_{\mathbf{q}s}$ about equilibrium in terms of this first order perturbation:

$$\begin{aligned} n_{\mathbf{q}s} = \frac{1}{e^{\hbar\omega_{\mathbf{q}s}/k_{\mathrm{B}}T - \psi_{\mathbf{q}s}} - 1} \approx & \bar{n}_{\mathbf{q}s} - \frac{k_{\mathrm{B}}T}{\hbar}\frac{\partial \bar{n}_{\mathbf{q}s}}{\partial \omega_{\mathbf{q}s}}\psi_{\mathbf{q}s} \\ = & \bar{n}_{\mathbf{q}s} + \bar{n}_{\mathbf{q}s}(\bar{n}_{\mathbf{q}s}+1)\psi_{\mathbf{q}s}, \end{aligned} \tag{2.69}$$

analogous to Eq. (2.57).

We now take the phonon collision operator $P$ whose elements $P_{\mathbf{q}s}^{\mathbf{q}'s'}$ provide a measure of the transition probability of a mode $\mathbf{q}s$, which we approximate within the single mode relaxation time as:

$$(P\psi)_{\mathbf{q}s} \approx P_{\mathbf{q}s,\mathbf{q}s}\psi_{\mathbf{q}s} = \Gamma_{\mathbf{q}s}\psi_{\mathbf{q}s} = -\left.\frac{\partial n_{\mathbf{q}s}}{\partial t}\right|_{scatt} \tag{2.70}$$

where $\Gamma_{\mathbf{q}s}$ is the diagonal part of the phonon collision operator $P_{\mathbf{q}s,\mathbf{q}s}$, and includes the diagonal part of the anharmonic operator and all operators representing elastic processes. Thus, from Eqs. (2.69) and (2.70)

$$\Gamma_{\mathbf{q}s}\psi_{\mathbf{q}s} = \frac{n_{\mathbf{q}s} - \bar{n}_{\mathbf{q}s}}{\tau_{\mathbf{q}s}} = \frac{\bar{n}_{\mathbf{q}s}(\bar{n}_{\mathbf{q}s}+1)\psi_{\mathbf{q}s}}{\tau_{\mathbf{q}s}}, \tag{2.71}$$

giving us the single mode relaxation time:

$$\frac{1}{\tau_{\mathbf{q}s}} = \frac{\Gamma_{\mathbf{q}s}}{\bar{n}_{\mathbf{q}s}(\bar{n}_{\mathbf{q}s}+1)}. \tag{2.72}$$

In this section, we derive the expression for $\tau_{\mathbf{q}s}$ due to three-phonon processes, which arise from the third order anharmonicity of the crystal potential in Eq. (2.31). To begin, we look at this anharmonic potential in terms of phonon

collision operators as given in Eq. (2.51):

$$V_{anh} = \frac{1}{3!} \sum_{\mathbf{q}s,\mathbf{q}'s',\mathbf{q}''s''} \delta_{\mathbf{G},\mathbf{q}+\mathbf{q}'+\mathbf{q}''} \mathbf{\Psi}_{\mathbf{q}s,\mathbf{q}'s',\mathbf{q}''s''} \times \left( \hat{a}_{-\mathbf{q}s} \hat{a}_{-\mathbf{q}'s'} \hat{a}^{\dagger}_{\mathbf{q}''s''} - \hat{a}^{\dagger}_{\mathbf{q}s} \hat{a}_{-\mathbf{q}'s'} \hat{a}^{\dagger}_{\mathbf{q}''s''} - \hat{a}_{-\mathbf{q}s} \hat{a}^{\dagger}_{\mathbf{q}'s'} \hat{a}^{\dagger}_{\mathbf{q}''s''} \right), \tag{2.73}$$

where we are left with only three terms that do not violate energy and momentum conservation laws after the expansion of the phonon creation and annihilation operators.

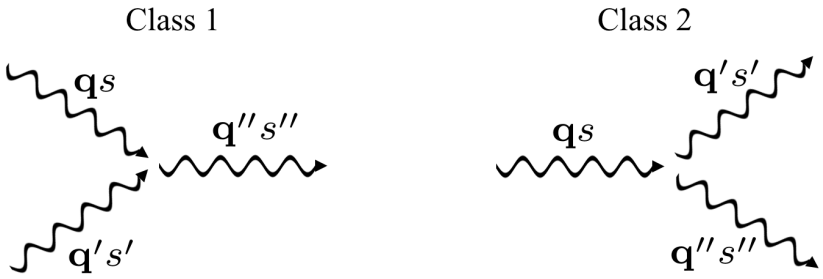



Figure 2.2: Allowed three-phonon scattering processes given energy and momentum conservation constraints.

These terms represent two distinct scattering processes, class 1 and class 2 events respectively, see Fig. 2.2. Class 1 events are coalescing processes, which refer to the annihilation of two phonons and the creation of a third. Class 2 events are decay processes, which refer to the annihilation of one phonon and the creation of two phonons. Thus, for an initial state $|i\rangle = |n_{\mathbf{q}s}, n_{\mathbf{q}'s'}, n_{\mathbf{q}''s''}\rangle$, the final state $|f\rangle$ is given by:

$$\begin{aligned} \text{Class 1}: \ |f\rangle &= |n_{\mathbf{q}s} - 1, n_{\mathbf{q}'s'} - 1, n_{\mathbf{q}''s''} + 1\rangle \,, \\ \text{Class 2}: \ |f\rangle &= |n_{\mathbf{q}s} - 1, n_{\mathbf{q}'s'} + 1, n_{\mathbf{q}''s''} + 1\rangle \,, \end{aligned} \tag{2.74}$$

Where each process obeys the following energy and momentum conservation relations:

$$\begin{aligned} \text{Class 1}: \hbar\omega_{\mathbf{q}s} + \hbar\omega_{\mathbf{q}'s'} &= \hbar\omega_{\mathbf{q}''s''}, \\ \mathbf{q} + \mathbf{q}' &= \mathbf{q}'' + \mathbf{G}, \end{aligned} \tag{2.75}$$

$$\begin{aligned} \text{Class 2}: \hbar\omega_{\mathbf{q}s} &= \hbar\omega_{\mathbf{q}'s'} + \hbar\omega_{\mathbf{q}''s''}, \\ \mathbf{q} &= \mathbf{q}' + \mathbf{q}'' + \mathbf{G}, \end{aligned} \tag{2.76}$$

where $\mathbf{G} = 0$ for normal processes, and $\mathbf{G} \neq 0$ for (Peierl's resistive) umklapp scattering, see Fig. 2.3. Normal processes occur within the first Brillouin zone and conserve phonon momentum. In the limit of constant group velocity, i.e.

for long-wavelength acoustic modes, such processes do not contribute to thermal resistance within a material. Conversely umklapp scattering, as termed by Peierls [121], does not conserve phonon momentum, losing crystal momentum $\mathbf{G}$ to the lattice. This reverses the phonon direction and heat flow, contributing to thermal resistance within a material.

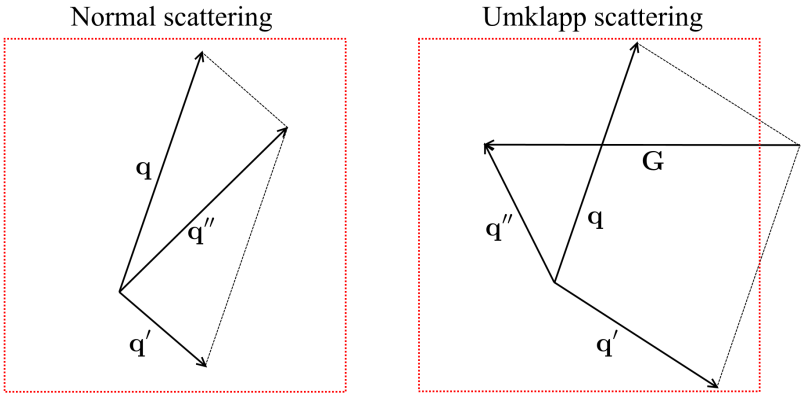



Figure 2.3: (a): Normal scattering, and (b): Umklapp scattering for class 1 events.

To calculate $\tau_{\mathbf{q}s}$ we use Fermi's Golden Rule, which gives the transition probability from states $|i\rangle \rightarrow |f\rangle$. From first order quantum perturbation theory, this scattering rate is given as [122, 123]:

$$P_i^f(3ph) = \frac{2\pi}{\hbar} |\langle f| V_{anh} |i\rangle|^2 \delta(E_f - E_i), \tag{2.77}$$

where the delta function ensures conservation of energy is maintained.

For class 1 events, where two phonons coalesce to form one new phonon, the transition probability is:

$$\begin{aligned} P_{\mathbf{q}s,\mathbf{q}'s'}^{\mathbf{q}''s''} =& \frac{2\pi}{\hbar^2} |\mathbf{\Psi}_{-\mathbf{q}s,-\mathbf{q}'s',\mathbf{q}''s''}|^2 n_{\mathbf{q}s} n_{\mathbf{q}'s'} (n_{\mathbf{q}''s''} + 1) \\ & \times \delta(-\omega_{\mathbf{q}s} - \omega_{\mathbf{q}'s'} + \omega_{\mathbf{q}''s''}) \delta_{\mathbf{G},\mathbf{q}+\mathbf{q}'+\mathbf{q}''}, \end{aligned} \tag{2.78}$$

where the factor of $\frac{1}{3!}$ in the expression for $V_{anh}$ is cancelled by the 3! equivalent terms when summing over phonon wavevectors $\mathbf{q}, \mathbf{q}', \mathbf{q}''$. Similarly, the transition probability for class 2 events, decay processes, may be written:

$$\begin{aligned} P_{\mathbf{q}s}^{\mathbf{q}'s',\mathbf{q}''s''} =& \frac{2\pi}{\hbar^2} |\mathbf{\Psi}_{-\mathbf{q}s,\mathbf{q}'s',\mathbf{q}''s''}|^2 n_{\mathbf{q}s} (n_{\mathbf{q}'s'} + 1)(n_{\mathbf{q}''s''} + 1) \\ & \times \delta(-\omega_{\mathbf{q}s} + \omega_{\mathbf{q}'s'} + \omega_{\mathbf{q}''s''}) \delta_{\mathbf{G},\mathbf{q}+\mathbf{q}'+\mathbf{q}''}. \end{aligned} \tag{2.79}$$

Summing over the probabilities of class 1 and class 2 events and including

the possibility of backscattering, we arrive at the total change in the phonon distribution due to three-phonon processes:

$$-\left.\frac{\partial n_{\mathbf{q}s}}{\partial t}\right|_{3ph} = \sum_{\mathbf{q}'s',\mathbf{q}''s''} \left[ \left( P^{\mathbf{q}''s''}_{\mathbf{q}s,\mathbf{q}'s'} - P^{\mathbf{q}s,\mathbf{q}'s'}_{\mathbf{q}''s''} \right) + \frac{1}{2}\left( P^{\mathbf{q}'s',\mathbf{q}''s''}_{\mathbf{q}s} - P^{\mathbf{q}s}_{\mathbf{q}'s',\mathbf{q}''s''} \right) \right], \quad (2.80)$$

where the factor of $\frac{1}{2}$ is to prevent double-counting of indistinguishable class 2 events where $\mathbf{q}'s'$ and $\mathbf{q}''s''$ swap order without affecting the phonon distribution.

In order to linearise the net scattering rates for class 1 and class 2 events, we take the expansion of the perturbed phonon population $n_{\mathbf{q}s}$ about equilibrium in terms of a first order perturbation $\psi_{\mathbf{q}s}$ from Eq. (2.69). Thus, we may write the scattering rate for class 1 events as:

$$P^{\mathbf{q}''s''}_{\mathbf{q}s,\mathbf{q}'s'} - P^{\mathbf{q}s,\mathbf{q}'s'}_{\mathbf{q}''s''} = \widetilde{P}^{\mathbf{q}''s''}_{\mathbf{q}s,\mathbf{q}'s'}(\psi_{\mathbf{q}s} + \psi_{\mathbf{q}'s'} - \psi_{\mathbf{q}''s''}) \quad (2.81)$$

where:

$$\begin{aligned} \widetilde{P}^{\mathbf{q}''s''}_{\mathbf{q}s,\mathbf{q}'s'} =& \frac{2\pi}{\hbar^2}|\mathbf{\Psi}_{-\mathbf{q}s,-\mathbf{q}'s',\mathbf{q}''s''}|^2 \bar{n}_{\mathbf{q}s}\bar{n}_{\mathbf{q}'s'}(\bar{n}_{\mathbf{q}''s''}+1) \\ & \times \delta(-\omega_{\mathbf{q}s} - \omega_{\mathbf{q}'s'} + \omega_{\mathbf{q}''s''})\delta_{\mathbf{G},\mathbf{q}+\mathbf{q}'+\mathbf{q}''}. \end{aligned} \quad (2.82)$$

Similarly, the scattering rate for class 2 events may be written as:

$$P^{\mathbf{q}'s',\mathbf{q}''s''}_{\mathbf{q}s} - P^{\mathbf{q}s}_{\mathbf{q}'s',\mathbf{q}''s''} = \widetilde{P}^{\mathbf{q}'s',\mathbf{q}''s''}_{\mathbf{q}s}(\psi_{\mathbf{q}s} - \psi_{\mathbf{q}'s'} - \psi_{\mathbf{q}''s''}), \quad (2.83)$$

where:

$$\begin{aligned} \widetilde{P}^{\mathbf{q}'s',\mathbf{q}''s''}_{\mathbf{q}s} =& \frac{2\pi}{\hbar^2}|\mathbf{\Psi}_{-\mathbf{q}s,\mathbf{q}'s',\mathbf{q}''s''}|^2 \bar{n}_{\mathbf{q}s}(\bar{n}_{\mathbf{q}'s'}+1)(\bar{n}_{\mathbf{q}''s''}+1) \\ & \times \delta(-\omega_{\mathbf{q}s} + \omega_{\mathbf{q}'s'} + \omega_{\mathbf{q}''s''})\delta_{\mathbf{G},\mathbf{q}+\mathbf{q}'+\mathbf{q}''}. \end{aligned} \quad (2.84)$$

Thus, we may write the total change in phonon population due to anharmonic, three-phonon processes as:

$$\begin{aligned} -\left.\frac{\partial n_{\mathbf{q}s}}{\partial t}\right|_{3ph} = \sum_{\mathbf{q}'s',\mathbf{q}''s''} \Bigg[ & \widetilde{P}^{\mathbf{q}''s''}_{\mathbf{q}s,\mathbf{q}'s'}(\psi_{\mathbf{q}s} + \psi_{\mathbf{q}'s'} - \psi_{\mathbf{q}''s''}) \\ & + \frac{1}{2}\widetilde{P}^{\mathbf{q}'s',\mathbf{q}''s''}_{\mathbf{q}s}(\psi_{\mathbf{q}s} - \psi_{\mathbf{q}'s'} - \psi_{\mathbf{q}''s''}) \Bigg]. \end{aligned} \quad (2.85)$$

For the single mode relaxation time approximation we assume that all phonon modes are in equilibrium, except for the phonon mode whose lifetime is being calculated. We also assume that the contribution from all scattering events may be expressed as a single effective lifetime. In effect, we set $\psi^{s'}_{\mathbf{q}'} = \psi^{s''}_{\mathbf{q}''} = 0$ in

Eq. (2.85) to get:

$$-\left.\frac{\partial n_{\mathbf{q}s}}{\partial t}\right|_{3ph} = \sum_{\mathbf{q}'s',\mathbf{q}''s''} \left[ \widetilde{P}^{\mathbf{q}''s''}_{\mathbf{q}s,\mathbf{q}'s'} \psi_{\mathbf{q}s} + \frac{1}{2} \widetilde{P}^{\mathbf{q}'s',\mathbf{q}''s''}_{\mathbf{q}s} \psi_{\mathbf{q}s} \right] = \Gamma_{\mathbf{q}s} \psi_{\mathbf{q}s}. \tag{2.86}$$

From this and Eq. (2.72) it follows that the effective lifetime for a phonon involved in anharmonic (three-phonon) processes is:

$$\tau^{-1}_{\mathbf{q}s} = \frac{1}{\bar{n}_{\mathbf{q}s}(\bar{n}_{\mathbf{q}s}+1)} \sum_{\mathbf{q}'s',\mathbf{q}''s''} \left[ \widetilde{P}^{\mathbf{q}''s''}_{\mathbf{q}s,\mathbf{q}'s'} + \frac{1}{2} \widetilde{P}^{\mathbf{q}'s',\mathbf{q}''s''}_{\mathbf{q}s} \right] \tag{2.87}$$

With Eqs. (2.78) and (2.79) we arrive at:

$$\begin{aligned} \tau^{-1}_{\mathbf{q}s} =& \frac{2\pi}{\hbar^2} \sum_{\mathbf{q}'s',\mathbf{q}''s''} |\mathbf{\Psi}_{\mathbf{q}s,\mathbf{q}'s',\mathbf{q}''s''}|^2 \delta_{\mathbf{G},\mathbf{q}+\mathbf{q}'+\mathbf{q}''} \\ & \times \left[ \frac{\bar{n}_{\mathbf{q}'s'}(\bar{n}_{\mathbf{q}''s''}+1)}{(\bar{n}_{\mathbf{q}s}+1)} \delta(-\omega_{\mathbf{q}s} - \omega_{\mathbf{q}'s'} + \omega_{\mathbf{q}''s''}) \right. \\ & \left. + \frac{1}{2} \frac{\bar{n}_{\mathbf{q}'s'}\bar{n}_{\mathbf{q}''s''}}{\bar{n}_{\mathbf{q}s}} \delta(-\omega_{\mathbf{q}s} + \omega_{\mathbf{q}'s'} + \omega_{\mathbf{q}''s''}) \right] \end{aligned} \tag{2.88}$$

The above expression for $\tau^{-1}_{\mathbf{q}s}$ may be simplified further with the use of two identities, derived in the absence of a temperature gradient under the condition that the net scattering rate of back and forward processes is zero at equilibrium:

$$\bar{n}_{\mathbf{q}'s'} - \bar{n}_{\mathbf{q}''s''} = \frac{\bar{n}_{\mathbf{q}'s'}(\bar{n}_{\mathbf{q}''s''}+1)}{(\bar{n}_{\mathbf{q}s}+1)}, \tag{2.89}$$

$$1 + \bar{n}_{\mathbf{q}'s'} + \bar{n}_{\mathbf{q}''s''} = \frac{\bar{n}_{\mathbf{q}'s'}\bar{n}_{\mathbf{q}''s''}}{\bar{n}_{\mathbf{q}s}}. \tag{2.90}$$

Thus, we obtain the expression for the single mode relaxation time due to anharmonic (three-phonon) processes:

$$\begin{aligned} \tau^{-1}_{\mathbf{q}s} =& \frac{2\pi}{\hbar^2} \sum_{\mathbf{q}'s',\mathbf{q}''s''} |\mathbf{\Psi}_{\mathbf{q}s,\mathbf{q}'s',\mathbf{q}''s''}|^2 \delta_{\mathbf{G},\mathbf{q}+\mathbf{q}'+\mathbf{q}''} \\ & \times \left[ (\bar{n}_{\mathbf{q}'s'} - \bar{n}_{\mathbf{q}''s''}) \delta(-\omega_{\mathbf{q}s} - \omega_{\mathbf{q}'s'} + \omega_{\mathbf{q}''s''}) \right. \\ & \left. + \frac{1}{2}(1 + \bar{n}_{\mathbf{q}'s'} + \bar{n}_{\mathbf{q}''s''}) \delta(-\omega_{\mathbf{q}s} + \omega_{\mathbf{q}'s'} + \omega_{\mathbf{q}''s''}) \right] \end{aligned} \tag{2.91}$$

### 2.2.6 Phonon lifetimes due to mass disorder

In order to model alloys, we employ the virtual crystal approximation (VCA) first introduced by Abeles [124]. This takes the disordered crystal and treats it as an

ordered one with average lattice parameters, atomic mass, and interatomic force constants as per the composition of the alloy. The pseudopotential of this average atom may be constructed as follows, for a hypothetical alloy $A_xB_{1-x}$ [125]:

$$\begin{aligned} V_{\mathrm{ps}}^{\mathrm{VCA}} = & xV_{\mathrm{local}}^{A}(r) + (1-x)V_{\mathrm{local}}^{B}(r) \\ & + \sum_{lm} \left|Y_{lm}^{A}\right\rangle xV_{l}^{A}(r) \left\langle Y_{lm}^{A}\right| + \sum_{lm} \left|Y_{lm}^{B}\right\rangle (1-x)V_{l}^{B}(r) \left\langle Y_{lm}^{B}\right|. \end{aligned} \tag{2.92}$$

Despite being a crude approximation, the VCA works well for chemically similar atoms, such as those from the same group of the periodic table.

We treat the effect of mass disorder on phonon lifetimes in an alloy via a perturbing Hamiltonian to the ordered average crystal [126]:

$$\hat{H} = \hat{H}_0 + \hat{H}_I, \tag{2.93}$$

where $\hat{H}_0$ is the Hamiltonian expanded up to the harmonic term of the average crystal with average mass at atomic site $b$ defined as:

$$\bar{m}_b = \frac{1}{N_l}\sum_{l} m_{lb} = \sum_{i} f_{ib}m_{ib}, \tag{2.94}$$

where $f_{ib}$ and $m_{ib}$ are the fraction and the atomic mass of the $i$th atomic species occupying atomic site $b$ in the virtual crystal lattice. $\hat{H}_I$ is the perturbing Hamiltonian:

$$\hat{H}_I = \frac{1}{2}\sum_{lb}(m_{lb} - \bar{m}_b)(\dot{u}^{lb})^2. \tag{2.95}$$

Taking the atomic displacement defined in Eq. (2.47) as a function of $\bar{m}_b$, and substituting into Eq. (2.95) we obtain the following perturbing Hamiltonian:

$$\begin{aligned} \hat{H}_I = -\frac{\hbar}{4N_l}\sum_{lb}\sum_{\mathbf{q}s,\mathbf{q}'s'} (\omega_{\mathbf{q}s}\omega_{\mathbf{q}'s'})^{\frac{1}{2}} \left(\frac{m_{lb}-\bar{m}_b}{\bar{m}_b}\right) \mathbf{e}_b^{s}(\mathbf{q})\cdot\mathbf{e}_b^{s'}(\mathbf{q}') \\ \times \left(\hat{a}_{\mathbf{q}s}\hat{a}^{\dagger}_{-\mathbf{q}'s'} + \hat{a}^{\dagger}_{-\mathbf{q}s}\hat{a}_{\mathbf{q}'s'}\right) e^{i(\mathbf{q}+\mathbf{q}')\cdot\mathbf{R}_l}, \end{aligned} \tag{2.96}$$

where the terms $\hat{a}^{\dagger}_{\mathbf{q}s}\hat{a}^{\dagger}_{-\mathbf{q}'s'}$ and $\hat{a}_{\mathbf{q}s}\hat{a}_{-\mathbf{q}'s'}$ in the expansion of the phonon operators have been omitted due to violation of conservation of energy. Thus, from second order perturbation theory, we arrive at an effective phonon lifetime due to mass disorder for a diatomic crystal [126, 127]:

$$\frac{1}{\tau_{\mathbf{q}s}^{md}} = \frac{\pi}{2N_l}\omega_{\mathbf{q}s}^2 \sum_{\mathbf{q}'s'} \delta(\omega_{\mathbf{q}s} - \omega_{\mathbf{q}'s'}) \sum_{b} g_b |\mathbf{e}_b^{*s'}(\mathbf{q}')\cdot\mathbf{e}_b^{s}(\mathbf{q})|^2, \tag{2.97}$$

where $g_b$ is the measure of mass disorder and is given by:

$$g_b = \sum_i f_{ib} \left(1 - \frac{m_{ib}}{\bar{m}_b}\right)^2. \tag{2.98}$$

This expression may then by combined with $\tau^{anh}_{\mathbf{qs}}$ using Matthiessen's rule, allowing the lattice thermal conductivity to be solved as per Eq. (2.65). However, we note that disorder in the force constants due to alloying is not treated in our implementation of the BTE-RTA due to the challenging nature of the problem [62, 128].

### 2.2.7 Implementation

To calculate the lattice thermal conductivity within the BTE-RTA, we must compute the harmonic and third order anharmonic interatomic force constants. In our implementation, IFCs are calculated from Hellmann-Feynman forces using a real-space finite difference supercell approach [63, 129, 130]. These forces are calculated from the derivative of the potential energy with respect to atomic displacement:

$$\mathbf{F}^{lb}_{\alpha} = -\frac{\partial V}{\partial \mathbf{u}^{lb}_{\alpha}}, \tag{2.99}$$

Allowing us to write the harmonic force constants as:

$$\Phi^{lb,l'b'}_{\alpha\beta} \simeq -\frac{\mathbf{F}^{l'b'}_{\beta}[\mathbf{u}^{lb}]}{u^{lb}_{\alpha}}, \tag{2.100}$$

and similarly the third order anharmonic force constants:

$$\Phi^{lb,l'b',l''b''}_{\alpha\beta\gamma} \simeq -\frac{\mathbf{F}^{l''b''}_{\gamma}[\mathbf{u}^{lb};\mathbf{u}^{l'b'}]}{u^{lb}_{\alpha}u^{l'b'}_{\beta}}, \tag{2.101}$$

where $\mathbf{F}^{l'b'}_{\beta}[\mathbf{u}^{lb}]$ is defined as the atomic force measured at position $\boldsymbol{\tau}^{l'b'}$ under an atomic displacement $\mathbf{u}^{lb}$ in a supercell. $\mathbf{F}^{l''b''}_{\gamma}[\mathbf{u}^{lb};\mathbf{u}^{l'b'}]$ is defined as the atomic force measured at position $\boldsymbol{\tau}^{l''b''}$ under a pair of atomic displacements $\mathbf{u}^{lb}$ and $\mathbf{u}^{l'b'}$ in a supercell. These forces are computed under the assumption of a small atomic displacement, in our case 0.02 Å.

We use the Phonopy and Phono3py codes [119, 129, 130, 131] to generate a minimal set of atomic displacements from which a full set of harmonic and third order anharmonic IFCs may be reconstructed using lattice symmetries. These supercell configurations are passed to the Abinit code [132], where DFT calculations are performed at 0 K to obtain the Hellman-Feynman forces. These

forces, Eq. (2.100) and (2.101), form systems of linear equations which may be solved using the Moore-Penrose pseudoinverse technique within the PHONO3PY code [119, 130]. This yields the harmonic and third order anharmonic IFCs respectively. These IFCs are then passed to an in-house code which calculates the phonon frequencies, group velocities, lifetimes and ultimately the lattice thermal conductivity. This code is also responsible for the calculation of other physical quantities shown in this work, such as mode Grüneisen parameters, thermal expansion coefficients, and phonon densities of states.

Further calculation details are as follows. All DFT calculations are performed using the local density approximation (LDA) and Hartwigsen-Goedecker-Hutter norm-conserving pseudopotentials [110]. Phonon dispersions are generated with the PHONOPY code [129, 133] from the calculated harmonic IFCs. Born effective charges and dielectric permittivity tensors are calculated using DFPT, as implemented in ABINIT [132, 134, 135]. We accounted for the long range ion-ion interaction using an interpolation in the calculation of phonon frequencies at general $\mathbf{q}$ points with the non-analytical term correction [136].

## 2.3 Charge carrier mobility

### 2.3.1 Boltzmann transport equation

We have already discussed in depth the calculation of the lattice thermal conductivity, now our attention shifts to the other thermoelectric properties in the figure of merit, namely the electrical conductivity, Seebeck coefficient, and electronic thermal conductivity. To model these, we once again return to the Boltzmann transport equation in the relaxation time approximation. In doing so, we also derive an expression for the charge carrier mobility, $\mu$, which contains all the pertinent charge carrier transport information necessary to solve for $\sigma$, $S$, and $\kappa_{\text{elec}}$. Thus, it suffices to calculate $\mu$ as the initial step to obtaining an *ab initio* thermoelectric figure of merit when coupled with calculations of $\kappa_{\text{latt}}$.

Starting from the Boltzmann transport equation, the change in energy carrier population, $f_{n\mathbf{k}} = f(\epsilon_{n\mathbf{k}})$, is given for a state $\mathbf{k}$ and band $n$ as [78]:

$$\frac{\partial f_{n\mathbf{k}}}{\partial t} = -\mathbf{v}_{n\mathbf{k}} \cdot \nabla_{\mathbf{r}} T \frac{\partial f_{n\mathbf{k}}}{\partial T} - \frac{e}{\hbar}\left(\mathbf{E} + \frac{1}{c}\mathbf{v}_{n\mathbf{k}} \times \mathbf{H}\right) \cdot \frac{\partial f_{n\mathbf{k}}}{\partial \mathbf{k}} + \left.\frac{\partial f_{n\mathbf{k}}}{\partial t}\right|_{\text{scatt}}, \quad (2.102)$$

where $\mathbf{v}_{n\mathbf{k}} = 1/\hbar \nabla_{\mathbf{k}} \epsilon_{n\mathbf{k}}$ is the electronic group velocity. The first term on the right hand side is due to diffusion of energy carriers, the second due to the influence

of electric **E** or magnetic **H** fields, with the third due to scattering. We derive electronic thermoelectric transport properties following a similar procedure to that as laid out in the previous section for deriving phonon transport.

In their equilibrium configuration, $f^0_{n\mathbf{k}}$, electrons will obey Fermi-Dirac statistics:

$$f^0(\epsilon_{n\mathbf{k}}) = \frac{1}{e^{(\epsilon_{n\mathbf{k}} - E_\mathrm{F})/k_\mathrm{B}T} + 1}, \tag{2.103}$$

where $E_\mathrm{F}$ is the Fermi level. We assume a small perturbation of electronic states from equilibrium and thus may use the relaxation time approximation to obtain an expression for the scattering rate of electrons analogous to that of phonons (Eq. (2.58)):

$$\left.\frac{\partial f_{n\mathbf{k}}}{\partial t}\right|_\mathrm{scatt} = -\frac{f_{n\mathbf{k}} - f^0_{n\mathbf{k}}}{\tau_{n\mathbf{k}}}, \tag{2.104}$$

where $\tau_{n\mathbf{k}}$ is the relaxation time for electronic states. In semiconductors, electron-phonon coupling and neutral and ionized impurities are the dominant scattering mechanisms [77]. We neglect the effect of impurity scattering in mobility calculations, which is only significant at high carrier concentrations or very low temperatures. Thus, we calculate $\tau_{n\mathbf{k}}$ from the effects of electron-phonon interaction, as will be discussed in more detail in chapter 5.

Taking external perturbations to be small, we may assume $f_{n\mathbf{k}} \approx f^0_{n\mathbf{k}}$ in the first and second terms of Eq. (2.102), and coupled with Eq. (2.104):

$$-\mathbf{v}_{n\mathbf{k}} \cdot \nabla_\mathbf{r} T \frac{\partial f^0_{n\mathbf{k}}}{\partial T} - \frac{e}{\hbar}\left(\mathbf{E} + \frac{1}{c}\mathbf{v}_{n\mathbf{k}} \times \mathbf{H}\right) \cdot \frac{\partial f^0_{n\mathbf{k}}}{\partial \mathbf{k}} - \frac{f_{n\mathbf{k}} - f^0_{n\mathbf{k}}}{\tau_{n\mathbf{k}}} = 0, \tag{2.105}$$

where the overall change in charge carrier population is 0 in the steady state. This is the linearised Boltzmann transport equation for charge carriers in the relaxation time approximation, equivalent to that for phonons, see Eq. (2.59). We now assume the absence of all external fields other than a weak electric field and small thermal gradient, and re-write the above equation as [89]:

$$f_{n\mathbf{k}} = f^0_{n\mathbf{k}} - e\left(\frac{\partial f^0_{n\mathbf{k}}}{\partial \epsilon_{n\mathbf{k}}}\right)\tau_{n\mathbf{k}}\mathbf{v}_{n\mathbf{k}} \cdot \mathbf{E} - \left(\frac{\partial f^0_{n\mathbf{k}}}{\partial \epsilon_{n\mathbf{k}}}\right)\tau_{n\mathbf{k}}\mathbf{v}_{n\mathbf{k}}(\epsilon_{n\mathbf{k}} - \mu)\frac{\nabla_\mathbf{r} T}{T}. \tag{2.106}$$

Within the linear response, the electrical current density is related to external fields via the thermoelectric transport coefficients, $\sigma$, $S$, $\Pi$, and $\kappa_\mathrm{elec}$, as [78, 89, 137]:

$$\mathbf{j}_e = \sigma\mathbf{E} - \sigma S \nabla_\mathbf{r} T, \tag{2.107}$$

with the thermal current density defined as [78, 89, 137]:

$$\mathbf{j}_q = \sigma \Pi \mathbf{E} - \left(\kappa_{\text{elec}} + T\sigma S^2\right)\nabla_{\mathbf{r}} T, \tag{2.108}$$

where $\Pi = TS$ is the Peltier coefficient. Strictly speaking, the thermoelectric transport coefficients are tensorial quantities, however for cubic materials they reduce to scalars. Within this formalism, $\mathbf{E}$ is the effective electric field arising from an electric and chemical potential gradient, $\mathbf{E} = \nabla_{\mathbf{r}}(\phi - \mu/e)$ [89].

Starting from Eqs. (2.106) and (2.107) and taking the thermal gradient to be zero in the charge current density, we write the electrical conductivity as [78, 89]:

$$\sigma = \frac{1}{N_{\mathbf{k}}\Omega} e^2 \sum_{n\mathbf{k}} \mathbf{v}_{n\mathbf{k}}^2 \tau_{n\mathbf{k}} \left(-\frac{\partial f_{n\mathbf{k}}^0}{\partial \epsilon_{n\mathbf{k}}}\right), \tag{2.109}$$

where $N_{\mathbf{k}}$ is the number of $\mathbf{k}$-points. The Seebeck coefficient is defined as the voltage gradient produced by a given temperature gradient when the electrical current is zero, and thus [78, 89]:

$$S = \frac{1}{N_{\mathbf{k}}\Omega} \frac{e k_{\text{B}}}{\sigma} \sum_{n\mathbf{k}} \mathbf{v}_{n\mathbf{k}}^2 \tau_{n\mathbf{k}} \left(\frac{\epsilon_{n\mathbf{k}} - \mu}{k_{\text{B}} T}\right) \left(-\frac{\partial f_{n\mathbf{k}}^0}{\partial \epsilon_{n\mathbf{k}}}\right). \tag{2.110}$$

The electrical contribution to thermal conductivity is defined as the heat current produced per unit of temperature gradient when the electrical current is zero, and is written from Eqs. (2.106) and (2.108) as [78, 89]:

$$\kappa_{\text{elec}} = \frac{1}{N_{\mathbf{k}}\Omega} k_{\text{B}}^2 T \sum_{n\mathbf{k}} \mathbf{v}_{n\mathbf{k}}^2 \tau_{n\mathbf{k}} \left(\frac{\epsilon_{n\mathbf{k}} - \mu}{k_{\text{B}} T}\right)^2 \left(-\frac{\partial f_{n\mathbf{k}}^0}{\partial \epsilon_{n\mathbf{k}}}\right) - T\sigma S^2. \tag{2.111}$$

The charge carrier mobility within the BTE-RTA is given as [87]:

$$\mu = \frac{\sigma}{ne} = \frac{1}{N_{\mathbf{k}}\Omega} \frac{e}{n} \sum_{n\mathbf{k}} \mathbf{v}_{n\mathbf{k}}^2 \tau_{n\mathbf{k}} \left(-\frac{\partial f_{n\mathbf{k}}^0}{\partial \epsilon_{n\mathbf{k}}}\right), \tag{2.112}$$

where $n$ is the carrier concentration:

$$n = \sum_{n\mathbf{k}} f_{n\mathbf{k}}^0. \tag{2.113}$$

From this the Fermi level is determined for a given charge carrier concentration.

In the calculation of the electronic thermoelectric properties and the charge carrier mobility, the most cumbersome quantity to compute is the lifetime $\tau_{n\mathbf{k}}$. In the following section, we briefly discuss the theoretical ground work behind the

computation of this quantity from electron-phonon interactions within the DFT Kohn-Sham formalism.

### 2.3.2 Electron-phonon coupling

Up to this point we have not considered the dynamics of a coupled electron-phonon system. To obtain their interaction within the DFT formalism, we expand the Kohn-Sham potential in terms of an atomic displacement $\mathbf{u}^{lb}$ from their equilibrium positions $\mathbf{u}_0^{lb}$, truncating the expansion to first order [138]:

$$V^{\mathrm{KS}} = V^{\mathrm{KS}}(\mathbf{u}_0^{lb}) + \sum_{lb}\sum_{\alpha} \frac{\partial V^{\mathrm{KS}}}{\partial u_\alpha^{lb}} u_\alpha^{lb}. \tag{2.114}$$

The first term is the Kohn-Sham potential due to atoms in their equilibrium positions, and the second term is the perturbed potential, labelled $V_{\mathrm{pert}}^{\mathrm{KS}}$, which we re-write as:

$$V_{\mathrm{pert}}^{\mathrm{KS}} = \sum_{\mathbf{q}s}\sum_{b}\sum_{\alpha} N_l^{-\frac{1}{2}} \left(\frac{m_c}{m_b}\right)^{\frac{1}{2}} l_{\mathbf{q}s}\Big(\hat{a}_{\mathbf{q}s} e_{\alpha b}^{s}(\mathbf{q}) + \hat{a}_{-\mathbf{q}s}^{\dagger} e_{\alpha b}^{*s}(\mathbf{q})\Big) e^{i\mathbf{q}\cdot\mathbf{r}} \partial_{\alpha b,\mathbf{q}} v^{\mathrm{KS}}, \tag{2.115}$$

where $m_c$ is an arbitrary reference mass, $l_{\mathbf{q}s} = (\hbar/2m_c\omega_{\mathbf{q}s})^{1/2}$ is the "zero-point" displacement amplitude, and $\partial_{\alpha b,\mathbf{q}} v^{\mathrm{KS}}$ is a lattice periodic function defined as [138]:

$$\partial_{\alpha b,\mathbf{q}} v^{\mathrm{KS}} = \sum_{l} e^{-i\mathbf{q}\cdot(\mathbf{r}-\mathbf{R}_l)} \frac{\partial V^{\mathrm{KS}}}{\partial u_\alpha^{lb}}\bigg|_{\mathbf{r}-\mathbf{R}_l}. \tag{2.116}$$

In the second quantisation formalism, the single particle electronic Hamiltonian can be written with the unperturbed Kohn-Sham Hamiltonian [138]:

$$\hat{H}_e = \sum_{n\mathbf{k},m\mathbf{k}'} \langle\psi_{m\mathbf{k}'}|\, \hat{H}^{\mathrm{KS}}\, |\psi_{n\mathbf{k}}\rangle\, \hat{c}_{m\mathbf{k}'}^{\dagger}\hat{c}_{n\mathbf{k}} = \sum_{n\mathbf{k}} \epsilon_{n\mathbf{k}} \hat{c}_{n\mathbf{k}}^{\dagger}\hat{c}_{n\mathbf{k}}. \tag{2.117}$$

where $\hat{c}_{n\mathbf{k}}^{\dagger}$ and $\hat{c}_{n\mathbf{k}}$ are the electron creation and annihilation operators respectively. This is analogous to the second quantisation of the Hamiltonian for phonons within the harmonic approximation, see Eq. (2.49). Similarly, the Hamiltonian due to electron-phonon interaction reads [138]:

$$\begin{aligned}\hat{H}_{ep} =& \sum_{n\mathbf{k},m\mathbf{k}'} \langle\psi_{m\mathbf{k}'}|\, V_{\mathrm{pert}}^{\mathrm{KS}}\, |\psi_{n\mathbf{k}}\rangle\, \hat{c}_{m\mathbf{k}'}^{\dagger}\hat{c}_{n\mathbf{k}} \\ =& N_l^{-\frac{1}{2}} \sum_{n\mathbf{k},m\mathbf{k}'}\sum_{\mathbf{q}s} l_{\mathbf{q}s}\mathbf{H}_{mn}(\mathbf{k};\mathbf{q}s)\Big(\hat{c}_{m\mathbf{k}'}^{\dagger}\hat{c}_{n\mathbf{k}}\hat{a}_{\mathbf{q}s} + \hat{c}_{m\mathbf{k}'}^{\dagger}\hat{c}_{n\mathbf{k}}\hat{a}_{-\mathbf{q}s}^{\dagger}\Big)\delta_{\mathbf{k}+\mathbf{q}-\mathbf{k}',\mathbf{G}}\end{aligned} \tag{2.118}$$

where the delta function $\delta_{\mathbf{k}+\mathbf{q}-\mathbf{k}',\mathbf{G}}$ arises from summation over the factor

$e^{i(\mathbf{k}+\mathbf{q}-\mathbf{k}')\cdot\mathbf{r}}$ [77, 139], and ensures conservation of crystal momentum. $\mathbf{H}_{mn}(\mathbf{k};\mathbf{q}s)$ is the electron-phonon matrix element for an electron scattering event from a state $\mathbf{k}$ and band $n$ to a state $\mathbf{k}'$ and band $m$ via a phonon $\mathbf{q}s$:

$$\mathbf{H}_{mn}(\mathbf{k};\mathbf{q}s) = \sum_b \sum_\alpha \left(\frac{m_c}{m_b}\right)^{\frac{1}{2}} e^s_{\alpha b}(\mathbf{q}) \left\langle u_{m\mathbf{k}+\mathbf{q}}\right| \partial_{\alpha b,\mathbf{q}} v^{\mathrm{KS}} \left|u_{n\mathbf{k}}\right\rangle_{\mathrm{uc}}, \tag{2.119}$$

where the subscript "uc" indicates that the integral is carried out within one unit cell. $u_{n\mathbf{k}}$ is normalized to unity in the unit cell and is the lattice periodic part of $\psi_{n\mathbf{k}}$ expressed in Bloch form as $N_l^{-1/2} u_{n\mathbf{k}} e^{i\mathbf{k}\cdot\mathbf{r}}$. We calculate the matrix element $\left\langle u_{m\mathbf{k}+\mathbf{q}}\right| \partial_{\alpha b,\mathbf{q}} v^{\mathrm{KS}} \left|u_{n\mathbf{k}}\right\rangle_{\mathrm{uc}}$ directly from the density functional perturbation theory method [99, 138] as implemented in ABINIT [132, 134, 135], discussed in the next section. We choose the mass $m_c$ to be equal to the mass of the unit cell for consistency with deformation potential definitions [140]. We note that our definition of the electron-phonon matrix element is not the typical one given within the literature, where it is usually defined as $g_{mn}(\mathbf{k};\mathbf{q}s) = l_{\mathbf{q}s}\mathbf{H}_{mn}(\mathbf{k};\mathbf{q}s)$ [87, 89].

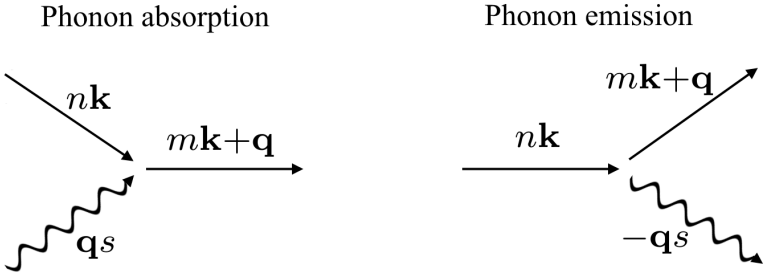



Figure 2.4: Allowed electron-phonon scattering processes to first order in the atomic displacement.

From the electron-phonon interaction Hamiltonian we see that there are two allowed scattering processes to first order in the atomic displacement. These represent electron scattering via phonon absorption and electron scattering via phonon emission respectively, see Fig. 2.4. For an initial state $|i\rangle = |n\mathbf{k}\rangle \otimes |n_{\mathbf{q}s}\rangle$, the final state $|f\rangle$ is given by:

$$\begin{aligned} \text{Phonon absorption}: \ |f\rangle &= |m\mathbf{k}'\rangle \otimes |n_{\mathbf{q}s} - 1\rangle, \\ \text{Phonon emission}: \ |f\rangle &= |m\mathbf{k}'\rangle \otimes |n_{-\mathbf{q}s} + 1\rangle, \end{aligned} \tag{2.120}$$

where each process obeys the following energy and momentum conservation relations:

$$\begin{aligned} \text{Phonon absorption}: \epsilon_{n\mathbf{k}} + \hbar\omega_{\mathbf{q}s} &= \epsilon_{m\mathbf{k}'}, \\ \mathbf{k} + \mathbf{q} &= \mathbf{k}' + \mathbf{G}, \end{aligned} \tag{2.121}$$

$$\begin{aligned} \text{Phonon emission} : \epsilon_{n\mathbf{k}} &= \epsilon_{m\mathbf{k}'} + \hbar\omega_{-\mathbf{q}s}, \\ \mathbf{k} &= \mathbf{k}' - \mathbf{q} + \mathbf{G}, \end{aligned} \tag{2.122}$$

where $\mathbf{G} = 0$ for normal processes, and $\mathbf{G} \neq 0$ for umklapp scattering.

Under the assumption that phonons are in thermal equilibrium, we use Fermi's golden rule to obtain the scattering probability from state $|n\mathbf{k}\rangle \otimes |\bar{n}_{\mathbf{q}s}\rangle$ to a state $|m\mathbf{k}'\rangle \otimes |\bar{n}_{\mp\mathbf{q}s} \pm 1\rangle$ [89]:

$$\begin{aligned} P_{n\mathbf{k}}^{m\mathbf{k}'} = \frac{2\pi}{\hbar}\frac{1}{N_l}\sum_{\mathbf{q}s} l_{\mathbf{q}s}^2 |\mathbf{H}_{mn}(\mathbf{k};\mathbf{q}s)|^2 \Big[ &\bar{n}_{\mathbf{q}s}\delta\left(\epsilon_{n\mathbf{k}} - \epsilon_{m\mathbf{k}'} + \hbar\omega_{\mathbf{q}s}\right)\delta_{\mathbf{k}+\mathbf{q}-\mathbf{k}',\mathbf{G}} \\ &+ (\bar{n}_{\mathbf{q}s}+1)\delta\left(\epsilon_{n\mathbf{k}} - \epsilon_{m\mathbf{k}'} - \hbar\omega_{\mathbf{q}s}\right)\delta_{\mathbf{k}-\mathbf{q}-\mathbf{k}',\mathbf{G}}\Big]. \end{aligned} \tag{2.123}$$

where the first term describes phonon absorption, and the second phonon emission. With the above expression we may now write the scattering integral of Eq. (2.104) in a manner analogous to that of phonons (Eq. (2.80)) in terms of the transition probability $P_{n\mathbf{k}}^{m\mathbf{k}'}$, assuming instantaneous, single collisions which are independent of the driving force [89, 139]:

$$-\frac{\partial f_{n\mathbf{k}}}{\partial t}\bigg|_{\text{scatt}} = \sum_{m\mathbf{k}'}\Big[f_{n\mathbf{k}}(1-f_{m\mathbf{k}'})P_{n\mathbf{k}}^{m\mathbf{k}'} - f_{m\mathbf{k}'}(1-f_{n\mathbf{k}})P_{m\mathbf{k}'}^{n\mathbf{k}}\Big]. \tag{2.124}$$

The second term is due to back-scattering, and the $(1-f_{m\mathbf{k}'})$ and $(1-f_{n\mathbf{k}})$ terms are blocking factors which prevent scattering to an already occupied electronic state. For equilibrium electronic distributions we arrive at the "detailed balance equation" [139, 141]:

$$\Big[f_{n\mathbf{k}}^0(1-f_{m\mathbf{k}'}^0)P_{n\mathbf{k}}^{m\mathbf{k}'} - f_{m\mathbf{k}'}^0(1-f_{n\mathbf{k}}^0)P_{m\mathbf{k}'}^{n\mathbf{k}}\Big] = 0, \tag{2.125}$$

which ensures $-\frac{\partial f_{n\mathbf{k}}}{\partial t}|_{\text{scatt}} = 0$ at equilibrium.

Taking Eqs. (2.123-2.125) and inserting into the linearised Boltzmann transport equation, we arrive at the momentum relaxation time within the RTA [139]:

$$\begin{aligned} \frac{1}{\tau_{n\mathbf{k}}} = \frac{2\pi}{\hbar}\frac{1}{N_l}\sum_{m\mathbf{k}'}\sum_{\mathbf{q}s}\frac{(1-f_{m\mathbf{k}'}^0)}{(1-f_{n\mathbf{k}}^0)}(1-\cos(\theta_{\mathbf{k}\mathbf{k}'}))l_{\mathbf{q}s}^2|\mathbf{H}_{mn}(\mathbf{k};\mathbf{q}s)|^2 \\ \times\Big[\bar{n}_{\mathbf{q}s}\delta\left(\epsilon_{n\mathbf{k}} - \epsilon_{m\mathbf{k}'} + \hbar\omega_{\mathbf{q}s}\right)\delta_{\mathbf{k}+\mathbf{q}-\mathbf{k}',\mathbf{G}} \\ + (\bar{n}_{\mathbf{q}s}+1)\delta\left(\epsilon_{n\mathbf{k}} - \epsilon_{m\mathbf{k}'} - \hbar\omega_{\mathbf{q}s}\right)\delta_{\mathbf{k}-\mathbf{q}-\mathbf{k}',\mathbf{G}}\Big], \end{aligned} \tag{2.126}$$

where $\theta_{\mathbf{k}\mathbf{k}'}$ is the scattering angle, given as [139]:

$$\cos(\theta_{\mathbf{k}\mathbf{k}'}) = \frac{\mathbf{v}_{m\mathbf{k}'}\cdot\mathbf{v}_{n\mathbf{k}}}{|\mathbf{v}_{m\mathbf{k}'}||\mathbf{v}_{n\mathbf{k}}|}. \tag{2.127}$$

The above expression for the momentum relaxation time is used for intravalley acoustic phonon scattering, as discussed by Herring [142], which is treated as a quasi-elastic process [143]. We can approximate the above expression and obtain the more familiar form for the lifetime of an electronic quasiparticle [87, 89, 139, 143]:

$$\frac{1}{\tau^{l}_{n\mathbf{k}}} = \frac{2\pi}{\hbar}\frac{1}{N_l}\sum_{m\mathbf{k}'}\sum_{\mathbf{q}s} l^2_{\mathbf{q}s}|\mathbf{H}_{mn}(\mathbf{k};\mathbf{q}s)|^2\Big[(\bar{n}_{\mathbf{q}s}+f^0_{m\mathbf{k}'})\delta\left(\epsilon_{n\mathbf{k}}-\epsilon_{m\mathbf{k}'}+\hbar\omega_{\mathbf{q}s}\right)\delta_{\mathbf{k}+\mathbf{q}-\mathbf{k}',\mathbf{G}} + (\bar{n}_{\mathbf{q}s}+1-f^0_{m\mathbf{k}'})\delta\left(\epsilon_{n\mathbf{k}}-\epsilon_{m\mathbf{k}'}-\hbar\omega_{\mathbf{q}s}\right)\delta_{\mathbf{k}-\mathbf{q}-\mathbf{k}',\mathbf{G}}\Big], \tag{2.128}$$

which corresponds approximately to setting $(1-\cos(\theta_{\mathbf{k}\mathbf{k}'}))\rightarrow 1$ in Eq. (2.126) for low doping concentrations. The above expression is valid for processes with a weak dependence on $\mathbf{k}$ and $\mathbf{k}'$, and thus applies to intervalley and intravalley optical scattering as argued by Herring [142]. Performing the summation over $\mathbf{k}'$, we arrive at:

$$\frac{1}{\tau^{l}_{n\mathbf{k}}} = \frac{2\pi}{\hbar}\frac{1}{N_l}\sum_{m\mathbf{q}s} l^2_{\mathbf{q}s}|\mathbf{H}_{mn}(\mathbf{k};\mathbf{q}s)|^2\Big[(\bar{n}_{\mathbf{q}s}+f^0_{m\mathbf{k}+\mathbf{q}})\delta\left(\epsilon_{n\mathbf{k}}-\epsilon_{m\mathbf{k}+\mathbf{q}}+\hbar\omega_{\mathbf{q}s}\right) + (\bar{n}_{\mathbf{q}s}+1-f^0_{m\mathbf{k}-\mathbf{q}})\delta\left(\epsilon_{n\mathbf{k}}-\epsilon_{m\mathbf{k}-\mathbf{q}}-\hbar\omega_{\mathbf{q}s}\right)\Big]. \tag{2.129}$$

Thus, we may calculate *ab initio* electron-phonon scattering rates on a grid within the Brillouin zone using the electron-phonon matrix elements. However, such an approach typically requires very dense sampling of the Brillouin zone [85], and only very recently has such an approach been extended to polar semiconductors [88]. Thus, we follow the approach of Murphy-Armando and Fahy [83] using our knowledge of the electronic band structure to calculate *ab initio* electron-phonon momentum relaxation times and scattering rates considering only the most relevant parts of the Brillouin zone. The details of this approach will be given in chapter 5.

### 2.3.3 Density functional perturbation theory

We employ density functional perturbation theory [99, 144, 145] as implemented in the ABINIT code [132, 134, 135] as the main workhorse to calculate electron-phonon scattering rates, further details of which will be given in chapter 5. DFPT combines density functional theory with perturbation theory, extending the Kohn-Sham formalism to allow for *ab initio* calculation of the derivatives of the total energy with respect to changes in physical parameters. Below, we reproduce the

basic formalism of DFPT, as outlined in Ref. [99], and state how the electron-phonon matrix element $\mathbf{H}_{mn}(\mathbf{k};\mathbf{q}s)$ is calculated within this framework.

Within this work, we are most interested in calculating the derivative of energy with respect to atomic perturbations. However, to generalise the argument, the external potential acting on the electrons is treated as a differentiable function of a set of parameters $\lambda = \lambda_i$, where $\lambda_i = \mathbf{R}_K$ in the case of lattice dynamics. From the Hellmann-Feynman theorem [117], we may write the first and second derivatives of the ground-state energy as [99]:

$$\frac{\partial E}{\partial \lambda_i} = \int n_\lambda(\mathbf{r}) \frac{\partial V_\lambda(\mathbf{r})}{\partial \lambda_i} d\mathbf{r}, \tag{2.130}$$

$$\frac{\partial^2 E}{\partial \lambda_i \partial \lambda_j} = \int n_\lambda(\mathbf{r}) \frac{\partial^2 V_\lambda(\mathbf{r})}{\partial \lambda_i \partial \lambda_j} d\mathbf{r} + \int \frac{\partial n_\lambda(\mathbf{r})}{\partial \lambda_i} \frac{\partial V_\lambda(\mathbf{r})}{\partial \lambda_j} d\mathbf{r}. \tag{2.131}$$

Solving this requires the computation of the ground state electron density $n_\lambda(\mathbf{r})$ from DFT along with its linear response to a nuclear distortion $\partial n_\lambda(\mathbf{r})/\partial \lambda_i$. To calculate the latter, we start by linearising the Kohn Sham orbitals of Eq. (2.17), and assuming double occupied orbitals in this case:

$$\delta^\lambda n(\mathbf{r}) = 4\mathrm{Re} \sum_{n=1}^{N_e/2} \psi_n^*(\mathbf{r}) \delta^\lambda \psi_n(\mathbf{r}) = 4 \sum_{n=1}^{N_e/2} \sum_{m \neq n} \psi_n^*(\mathbf{r}) \psi_m(\mathbf{r}) \frac{\langle \psi_m | \, \delta^\lambda V^{KS} \, | \psi_n \rangle}{\epsilon_n - \epsilon_m}, \tag{2.132}$$

where the finite-difference operator is defined as:

$$\delta^\lambda F = \sum_i \frac{\partial F_\lambda}{\partial \lambda_i} \delta \lambda_i. \tag{2.133}$$

The variation of the Kohn-Sham orbitals, $\delta^\lambda \psi_n$, is obtained with standard first-order perturbation theory [99]:

$$(\hat{H}^{\mathrm{KS}} - \epsilon_n) \left| \delta^\lambda \psi_n \right\rangle = -(\delta^\lambda V^{\mathrm{KS}} - \delta^\lambda \epsilon_n) \, | \psi_n \rangle \, , \tag{2.134}$$

where $\delta^\lambda \epsilon_n = \langle \psi_n | \, \delta^\lambda V_{KS} \, | \psi_n \rangle$ is the first-order variation of the Kohn-Sham eigenvalue, and:

$$\delta^\lambda V^{\mathrm{KS}}(\mathbf{r}) = \delta^\lambda V_{ext}(\mathbf{r}) + e^2 \int \frac{\delta^\lambda n(\mathbf{r}')}{|\mathbf{r} - \mathbf{r}'|} d\mathbf{r}' + \left. \frac{dV_{xc}[n]}{dn} \right|_{n=n(\mathbf{r})} \delta^\lambda n(\mathbf{r}), \tag{2.135}$$

is the first-order correction to the self-consistent potential. Eqs. (2.132-2.135) form a set of self-consistent equations for the perturbed system completely analogous to the Kohn-Sham equations, Eqs. (2.15-2.17), for solving for the ground-

state of a system. We note that the self-consistency requirement follows from the dependence of the right hand side of Eq. (2.134) on the solution of the linear system [99].

Re-writing Eq. (2.134) in terms of lattice-periodic functions, we arrive at [138]:

$$(\hat{H}^{\mathrm{KS}}_{\mathbf{k}+\mathbf{q}} - \epsilon_{n\mathbf{k}}) \left|\delta^{\lambda} u_{n\mathbf{k},\mathbf{q}}\right\rangle = -\partial_{\alpha b,\mathbf{q}} v^{\mathrm{KS}} \left|u_{n\mathbf{k}}\right\rangle + \left\langle u_{n\mathbf{k}}\right| \partial_{\alpha b,0} v^{\mathrm{KS}} \left|u_{n\mathbf{k}}\right\rangle_{\mathrm{uc}} u_{n\mathbf{k}}, \quad (2.136)$$

where $\hat{H}^{\mathrm{KS}}_{\mathbf{k}+\mathbf{q}} = e^{-i(\mathbf{k}+\mathbf{q})\cdot\mathbf{r}} \hat{H}^{\mathrm{KS}} e^{i(\mathbf{k}+\mathbf{q})\cdot\mathbf{r}}$. Thus we obtain directly the electron-phonon matrix elements $\mathbf{H}_{mn}(\mathbf{k};\mathbf{q}s)$ as defined in Eq. (2.119).

# Chapter 3

# Lattice thermal conductivity of PbTe-based materials driven near the ferroelectric phase transition

## 3.1 Introduction

### 3.1.1 Motivation

In this chapter, we show from *ab initio* calculations a new approach to reduce the lattice thermal conductivity by exploiting the proximity of certain excellent thermoelectric materials to a soft mode phase transition. PbTe is energetically close to the ferroelectric phase transition to the rhombohedral structure, which corresponds to the frozen-in atomic motion of the transverse optical (TO) mode along [111] direction [146]. Consequently, TO phonons have relatively low frequencies at the zone centre ($\approx$ 1 THz), and interact strongly with heat carrying acoustic modes [26, 27, 28]. These effects lead to unusually small lifetimes of TO and acoustic modes, and result in PbTe's intrinsically low lattice thermal conductivity [28]. Although the sensitivity to the volume changes of the calculated transverse optical modes and the $\kappa_{\mathrm{latt}}$ of PbTe has been reported [26, 66, 147, 148], the thermal transport properties of PbTe materials near the ferroelectric phase transition, and specific proposals how to achieve them, have never been investigated.

Here we show from first principles that a significant lattice thermal conductivity reduction and efficient scattering throughout the phonon spectrum can be achieved by driving PbTe and its alloys to the verge of the ferroelectric phase transition. These effects can be induced by applying biaxial tensile (001) strain

to PbTe or its alloys with another rocksalt IV-VI material, such as PbSe. We also present an alternative route to drive PbTe materials near the ferroelectric transition without using strain: alloying of PbTe with a rhombohedral IV-VI material, such as GeTe. Enhanced phonon scattering across the spectrum in all these materials arises due to the TO softening associated with the increased proximity to the phase transition, which causes much stronger anharmonic acoustic-TO interaction than in PbTe and $PbSe_{1-x}Te_x$ alloys. In addition to this key effect, alloy disorder further scatters high-frequency phonons in $Pb_{1-x}Ge_xTe$ and strained $PbSe_{1-x}Te_x$ alloys near the phase transition, similarly as in $PbSe_{1-x}Te_x$ alloys [149].

Overall, we find that the lattice thermal conductivities of PbTe, $PbSe_{1-x}Te_x$, and $Pb_{1-x}Ge_xTe$ alloys tuned to the verge of the phase transition as described will be significantly decreased compared to PbTe (by a factor of $2-3$). These results show that exploiting the proximity of PbTe to the ferroelectric phase transition is a powerful strategy to achieve lattice thermal conductivity reductions comparable to those achieved in all-scale structured materials with record $ZT$ values [34, 39].

### 3.1.2 Calculation details

Harmonic and third order anharmonic IFCs at 0 K were calculated from Hellmann-Feynman forces computed on 216 atom supercells, using an energy cut-off of 15 Ha and 4 shifted $2 \times 2 \times 2$ reciprocal space grids for electronic states. To account for the long-range interatomic interaction in PbTe based materials [150], we imposed a cut-off on the interaction at 8 nearest neighbour shells (NNs) for anharmonic IFCs of PbTe, $PbSe_{0.5}Te_{0.5}$ and $Pb_{0.51}Ge_{0.49}Te$. We tested decreasing the range of anharmonic IFCs to 5 NNs, and found that this affected the lattice thermal conductivity by less than 5%. Subsequently, to decrease the computational load, we cut-off the interaction at 5 NNs for $Pb_{1-x}Ge_xTe$ alloys with $0 < x < 0.49$ and 10 NNs for strained PbTe and $PbSe_{0.5}Te_{0.5}$, which is equivalent to the 5 NNs cut-off in their equilibrium counterparts. The truncation of anharmonic IFCs breaks translational invariance of the crystal, which is enforced by identifying independent IFCs, and correcting them using a Lagrange multipliers technique [67, 151] which maintains all symmetry properties of the crystal. We performed lattice thermal conductivity calculations on $40 \times 40 \times 40$ $\mathbf{q}$ point grids. Disorder in the force constants due to alloying is not treated in our implementation of the BTE-RTA due to the challenging nature of the problem [62, 128]. Therefore, the ratios of $\kappa_{\text{latt}}$ between PbTe and PbTe-based materials near the phase transition obtained here should be interpreted as the lower limit

to their actual values [152].

### 3.1.3 Verification of approach

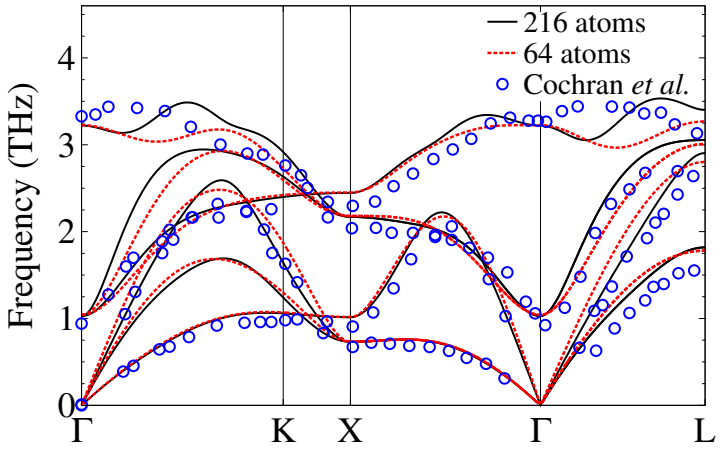



Figure 3.1: Phonon dispersions of PbTe: calculated using a 216 atom supercell at 0 K (solid black line), calculated using a 64 atom supercell at 0 K (dashed red line), and measured by Cochran *et al.* [153] at 300 K (blue circles).

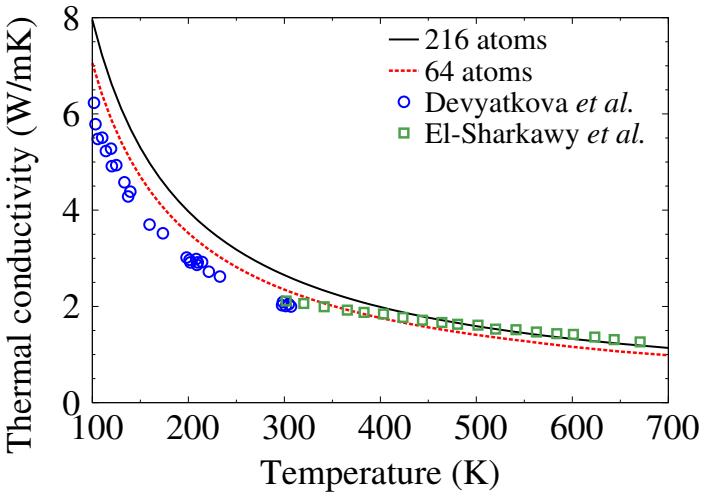



Figure 3.2: Lattice thermal conductivity of PbTe as a function of temperature: calculated using a supercell with 216 atoms (solid black line), calculated using a supercell with 64 atoms (dashed red line), and measured by Devyatkova *et al.* [154] (blue circles) and by El-Sharkawy *et al.* [155] (green rectangles).

To verify the validity of our approach, we calculated the phonon band structure and the lattice thermal conductivity of PbTe, and compared them with experiments. Harmonic and anharmonic IFCs of PbTe were calculated on

supercells with 64 and 216 atoms, and we found that it is necessary to use 216 atom supercells to obtain better convergence of the quantities of interest. Our computed phonon dispersion of PbTe is in good agreement with inelastic neutron scattering (INS) measurements of Cochran *et al.* [153], as illustrated in Fig. 3.1. In contrast, PbTe INS measurements of Delaire *et al.* [27] exhibit features that were ascribed to phonon-phonon interaction terms beyond the third order considered here. This indicates that our approach is more accurate for lower temperatures (100-300 K), where higher order anharmonic terms are less prominent.

Our calculated $\kappa_{\text{latt}}$ of PbTe is $\sim 30\%$ larger than the experimental values obtained on undoped ($\sim 10^{17}$ cm$^{-3}$) single- and poly-crystalline PbTe samples using the absolute steady-state technique in the temperature range 100-300 K [154], see Fig. 3.2. Since the $\kappa_{\text{latt}}$ of PbTe is very sensitive to the lattice constant changes within the accuracy of the DFT-LDA pseudopotential approach ($\sim 1\%$), we deem this agreement very good. On the other hand, our calculated $\kappa_{\text{latt}}$ of PbTe is in better agreement with the $\kappa_{\text{latt}}$ measured on undoped poly-crystalline PbTe samples using the plane temperature waves technique for temperatures 300-600 K [155], see Fig. 3.2. This improved agreement may be somewhat fortuitous, since the departure of the measured $\kappa_{\text{latt}}$ values from the $\sim T^{-1}$ dependence for temperatures larger than 300 K may be due to stronger higher order anharmonic terms, as argued in Ref. [66].

## 3.2 PbTe materials driven near the phase transition

### 3.2.1 Strained PbTe

To determine the amount of biaxial (001) strain which will push PbTe to the verge of the phase transition, we calculated the TO phonon frequencies at the zone centre as a function of (001) strain. Strain was simulated by constraining the lattice constant $a_{\parallel}$ in the [100] and [010] direction, and relaxing the lattice constant $a_{\perp}$ in the [001] direction. The amount of strain is defined as $\eta = (a_{\parallel} - a_0)/a_0$, where $a_0$ is the equilibrium lattice constant of PbTe obtained from structural relaxation in DFT. Since (001) strain reduces the symmetry of the rocksalt structure to tetragonal, the degeneracy of the two TO modes is lifted. Strictly speaking, these modes do not have pure TO character, but for simplicity, we will use this term.

We found that $\eta = 1.15\%$ will soften one of the TO modes from the equilibrium

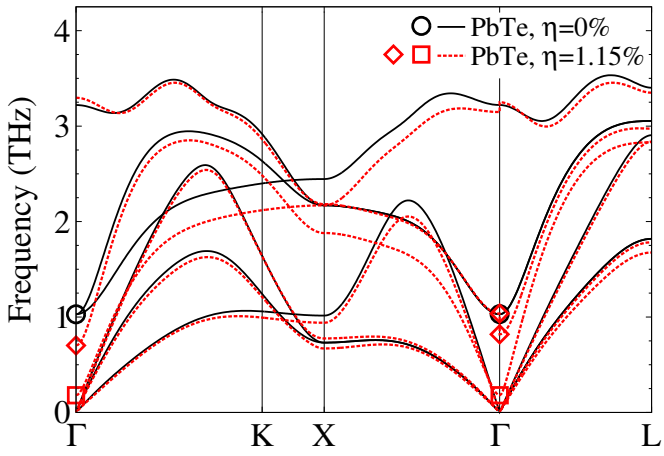



Figure 3.3: Phonon dispersions at 0 K for PbTe (solid black lines) and PbTe driven to the verge of the phase transition by tensile (001) strain of $\eta = 1.15\%$ (dashed red lines). Frequencies of the soft transverse optical modes at the zone centre, TO(Γ), are represented with circles for PbTe, and rectangles/diamonds for PbTe driven to the transition.

value of $\sim 1$ THz down to $\sim 0.1$ THz, and consequently bring PbTe close to the phase transition. This is illustrated in Fig. 3.3 that compares the phonon band structures of PbTe (solid black lines) and strained PbTe at the verge of the phase transition (dashed red lines) along high symmetry lines for the cubic symmetry. The other TO mode will also become softer due to applied strain, but to a lesser extent. The frequencies of the optical modes in strained PbTe close to the zone centre show directional dependence, which is a consequence of the non-analytic nature of the ion-ion interaction [156].

### 3.2.2 Strained $PbSe_{0.5}Te_{0.5}$ alloy

$PbSe_{1-x}Te_x$ alloys can be tuned near the phase transition in a similar manner as PbTe, by changing the amount of applied tensile (001) strain. Since these alloys are formed by mixing of two rocksalt materials, their TO(Γ) frequencies are bounded by those of PbTe and PbSe ($\sim 1$ THz and $\sim 1.2$ THz, respectively). Subsequently, they cannot be driven to the phase transition by changing the alloy composition, and they need to be strained to achieve this effect. Here we focused on the $x = 0.5$ composition since it has the lowest lattice thermal conductivity of the composition range [149], but we note that the same strategy may be applied to any other composition. Our calculations show that an extremely soft TO mode can be induced in $PbSe_{0.5}Te_{0.5}$ using tensile (001) strain of $\eta = 1.32\%$, see Fig. 3.4.

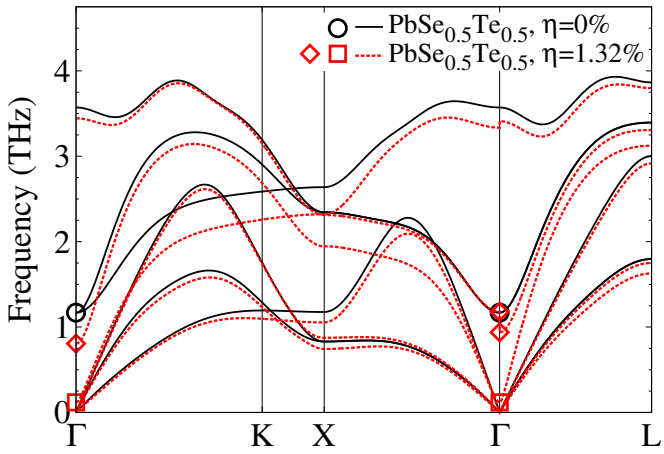



Figure 3.4: Phonon dispersions at 0 K for $PbSe_{0.5}Te_{0.5}$ (solid black lines) and $PbSe_{0.5}Te_{0.5}$ driven to the verge of the phase transition by tensile (001) strain of $\eta = 1.32\%$ (dashed red lines). TO(Γ) frequencies are shown in circles for $PbSe_{0.5}Te_{0.5}$, and rectangles/diamonds for $PbSe_{0.5}Te_{0.5}$ driven to the transition. Phonon dispersions for alloys were calculated using the virtual crystal approximation.

### 3.2.3 $Pb_{1-x}Ge_xTe$ alloys

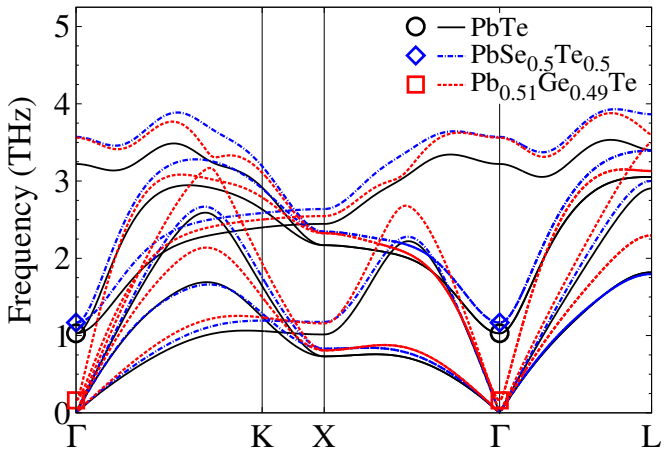



Figure 3.5: Phonon dispersions at 0 K for PbTe (solid black lines), $PbSe_{0.5}Te_{0.5}$ (dash-dotted blue lines), and $Pb_{0.51}Ge_{0.49}Te$ alloy at the verge of the phase transition (dashed red lines). TO(Γ) frequencies are represented with circles for PbTe, diamonds for $PbSe_{0.5}Te_{0.5}$, and rectangles for $Pb_{0.51}Ge_{0.49}Te$. Phonon dispersions for alloys were calculated using the virtual crystal approximation.

The proximity to the ferroelectric phase transition of PbTe materials can be dramatically increased not only by applying strain to PbTe and its alloys with other rocksalt IV-VI materials, but also by alloying PbTe with other rhombo-

hedral IV-VI materials, e.g. GeTe. $Pb_{1-x}Ge_xTe$ alloys are markedly different from $PbSe_{1-x}Te_x$ alloys because they undergo the ferroelectric phase transition from the rhombohedral to the rocksalt structure with temperature [157]. Consequently, their proximity to the phase transition and softening of TO modes can be dramatically increased by varying the alloy composition and temperature, unlike in the case of $PbSe_{1-x}Te_x$. The temperature at which the transition between the two phases occurs in $Pb_{1-x}Ge_xTe$ alloys decreases as the Ge content decreases, from $\sim 670$ K at $x = 1$ down to 0 K at $x \approx 0.01$ [157].

The temperature that brings $Pb_{1-x}Ge_xTe$ alloy near the phase transition for any composition $x > 0.01$ could be determined by computing the temperature dependence of the TO frequencies at the zone centre. Conversely, one could determine the amount of Ge that drives $Pb_{1-x}Ge_xTe$ close to the transition for any temperature $T < 670$ K by calculating the same frequencies as a function of the alloy composition. Our approach, however, does not capture the temperature effects on phonon frequencies due to the zero temperature representation of structural properties and IFCs. Nevertheless, it should describe well the qualitative changes to the lattice thermal conductivity of $Pb_{1-x}Ge_xTe$ alloys at the brink of the phase transition with respect to that of PbTe as argued in the following. Our calculations show that varying the alloy composition within our model does induce the ferroelectric phase transition. We find that the degenerate TO modes of $Pb_{1-x}Ge_xTe$ alloys become much softer than those of equilibrium PbTe and $PbSe_{1-x}Te_x$ (see Figs. 3.3 and 3.4, respectively) for the composition of $x = 0.49$. This effect is illustrated in Fig. 3.5: the TO($\Gamma$) frequency of $Pb_{0.51}Ge_{0.49}Te$ is $\sim 0.1$ THz, which is one order of magnitude lower than those of equilibrium PbTe and $PbSe_{1-x}Te_x$ alloys. Since the transition temperature of $Pb_{0.51}Ge_{0.49}Te$ is $\sim 450$ K [157], such a phonon band structure and the associated transition should describe reasonably well the lattice thermal conductivity of $Pb_{0.51}Ge_{0.49}Te$ near this temperature. The phase transition in our model of $Pb_{1-x}Ge_xTe$ alloys occurs for the composition of $x = 0.492$, which is characterised by imaginary frequencies of TO modes.

## 3.3 Impact on phonon lifetimes

### 3.3.1 Strained PbTe

The strain-engineered phonon band structure of PbTe that maximizes the TO($\Gamma$) softening decreases the phonon lifetimes, $\tau$, roughly by a factor of $\sim 2$ with respect to PbTe throughout the frequency spectrum. This is shown in Fig. 3.6 and its

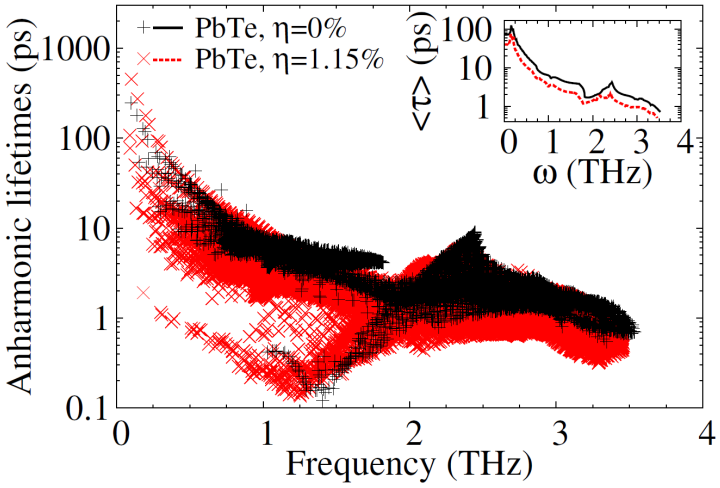



Figure 3.6: Anharmonic phonon lifetimes at 300 K and their averaged values (inset) as a function of frequency for PbTe (black pluses and solid line) and PbTe driven to the verge of the phase transition by tensile (001) strain of $\eta = 1.15\%$ (red crosses and dashed line).

inset, which represent the anharmonic (three-phonon) lifetimes, $\tau_{\text{anh}}$, at 300 K and their averaged values over frequency, respectively. The averaged phonon lifetimes have been defined as:

$$\langle \tau \rangle = \sum_{\mathbf{q}s} \tau_{\mathbf{q}s} \delta(\omega - \omega_{\mathbf{q}s}) / \sum_{\mathbf{q}s} \delta(\omega - \omega_{\mathbf{q}s}). \tag{3.1}$$

Remarkably, the lifetimes of strained PbTe are smaller than those of PbTe even for low frequency phonons that are difficult to scatter with commonly used strategies to reduce $\kappa_{\text{latt}}$, such as nanostructuring. Recently, it has been argued that low frequency phonons were efficiently scattered in multiple-scales structures by mesoscale grain boundaries [34, 38, 39, 40]. Our strategy achieves the same effect without any need for complex hierarchical design.

### 3.3.2 Strained $PbSe_{0.5}Te_{0.5}$ alloy

The anharmonic lifetimes of $PbSe_{0.5}Te_{0.5}$ alloy driven near the phase transition via strain are also significantly reduced with respect to those of $PbSe_{0.5}Te_{0.5}$, see Fig. 3.7. Strained $PbSe_{0.5}Te_{0.5}$ alloys also provide an additional advantage for enhanced phonon scattering compared to strained PbTe. Mass disorder scatters high-frequency phonons more efficiently than the three-phonon interactions, similarly as in $PbSe_{0.5}Te_{0.5}$ [149], further reducing the effective lifetimes at high frequencies, see Fig. 3.8.

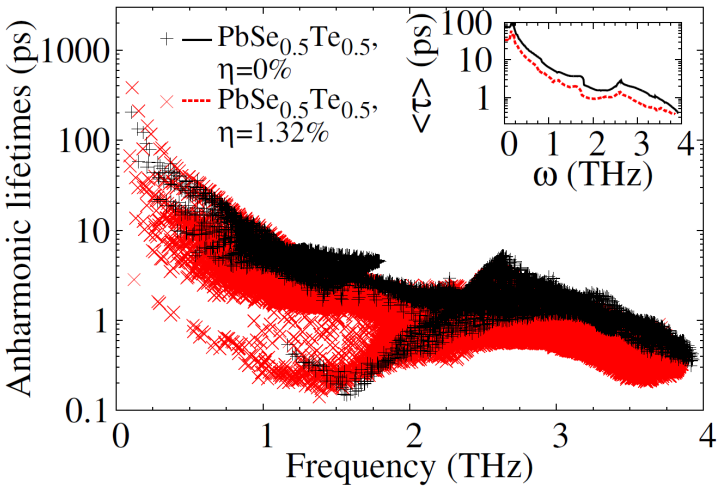



Figure 3.7: Anharmonic phonon lifetimes at 300 K and their averaged values (inset) as a function of frequency for $PbSe_{0.5}Te_{0.5}$ (black pluses and solid line) and $PbSe_{0.5}Te_{0.5}$ driven to the verge of the phase transition by tensile (001) strain of $\eta = 1.32\%$ (red crosses and dashed line).

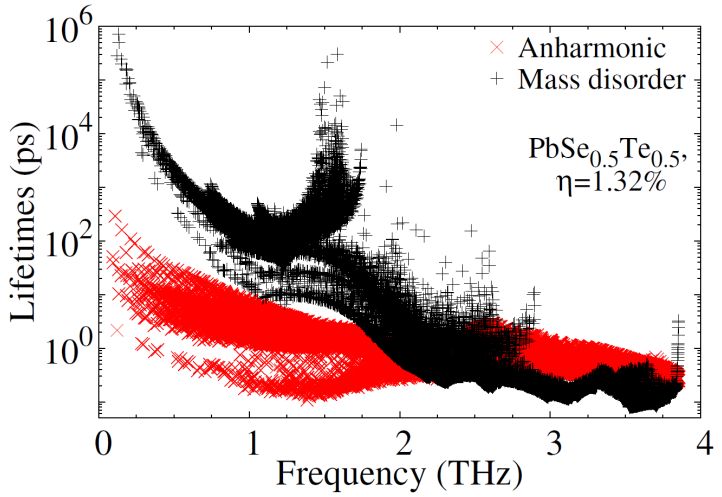



Figure 3.8: Frequency dependence of the mass disorder and phonon-phonon contributions to the phonon lifetimes (black pluses and red crosses, respectively) of $PbSe_{0.5}Te_{0.5}$ driven to the verge of the phase transition by tensile (001) strain of $\eta = 1.32\%$.

### 3.3.3 $Pb_{0.51}Ge_{0.49}Te$ alloy

The anharmonic lifetimes of $Pb_{0.51}Ge_{0.49}Te$ alloy near the phase transition are also considerably lower than those of PbTe and $PbSe_{0.5}Te_{0.5}$. The TO($\Gamma$) frequencies of PbTe and $PbSe_{0.5}Te_{0.5}$ are comparable (see Fig. 3.5), which leads to their similar three-phonon contributions to $\tau$. This effect is illustrated in Fig. 3.9 that compares the anharmonic lifetimes of PbTe (black pluses) and $PbSe_{0.5}Te_{0.5}$ (blue

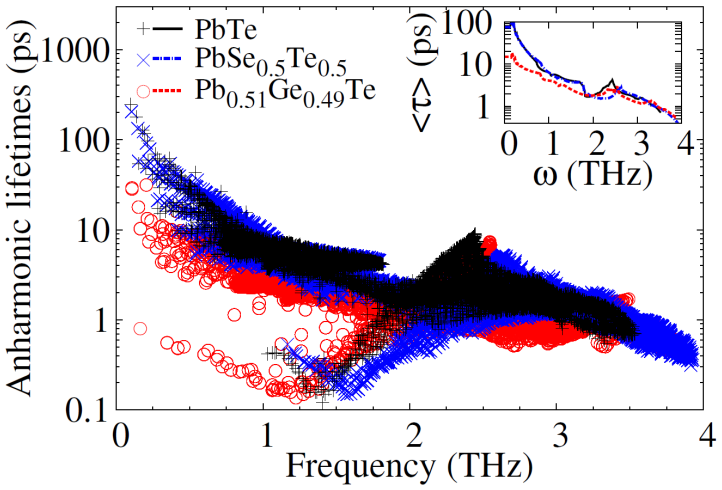



Figure 3.9: Anharmonic phonon lifetimes at 300 K and their averaged values (inset) as a function of frequency for PbTe (black pluses and solid line), $PbSe_{0.5}Te_{0.5}$ (blue crosses and dash-dotted line), and $Pb_{0.51}Ge_{0.49}Te$ alloy at the verge of the phase transition (red circles and dashed line).

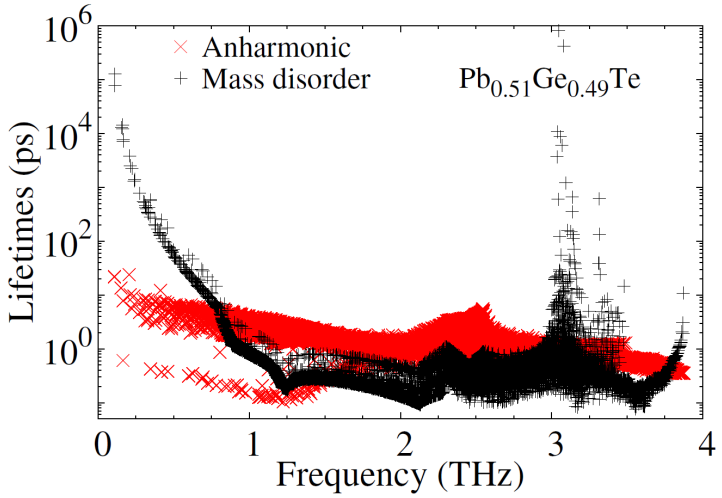



Figure 3.10: Frequency dependence of the mass disorder and three-phonon contributions to the phonon lifetimes at 300 K (black pluses and red crosses, respectively) of $Pb_{0.51}Ge_{0.49}Te$ alloy at the verge of the phase transition.

crosses). In sharp contrast, $Pb_{0.51}Ge_{0.49}Te$ alloy is energetically much closer to the phase transition, which results in its much lower TO frequencies near the zone centre (Fig. 3.5) and reduced $\tau_{anh}$ across the spectrum and particularly at low frequencies (red circles in Fig. 3.9). This finding further suggests that extremely soft TO modes near Γ have a highly beneficial role in effective scattering of a wide range of phonon frequencies. As in strained $PbSe_{0.5}Te_{0.5}$, mass disorder in $Pb_{0.51}Ge_{0.49}Te$ alloy is more efficient in scattering high-frequency phonons than

the phonon-phonon interaction, which results in an additional phonon lifetime decrease at high frequencies, see Fig. 3.10.

### 3.3.4 Impact of soft TO mode

The large decrease in the phonon lifetimes of PbTe driven near the ferroelectric phase transition via strain or alloying is a direct consequence of the softening of the TO modes and their increased anharmonic coupling with acoustic modes. To demonstrate this effect, we calculated explicitly the acoustic-TO contribution to the total anharmonic linewidth (inverse of the lifetime) in PbTe, strained PbTe and $Pb_{0.51}Ge_{0.49}Te$ at 300 K, shown in Fig. 3.11. We computed the acoustic-TO contribution to the total linewidth for all frequencies by accounting for the triplets of interacting states that contain at least one acoustic and one TO mode. For each wavevector, we labelled the two lowest phonon modes as transverse acoustic (TA) modes, and the highest mode as longitudinal optical (LO) mode. Since the ordering of TO and longitudinal acoustic (LA) modes changes throughout the Brillouin zone in all the materials considered (see Fig. 3.3, Fig. 3.4, and Fig. 3.5), we distinguished between them using the following procedure. We determined which one of those three states is mostly longitudinal by projecting their eigenvectors onto the corresponding wave vector, and classified it as LA mode, while the other two states were labelled as TO modes.

We found that the acoustic-TO contribution to the anharmonic linewidth dominates over the other contributions across the spectrum in equilibrium and strained PbTe, and in PbTe alloyed with GeTe. It accounts for $\sim 70\%$ of the anharmonic linewidth of acoustic and LO modes (except for the $\sim 2-3$ THz range), and for nearly 100% of the anharmonic linewidth of TO modes (see Fig. 3.11). Furthermore, by driving PbTe near the phase transition via strain or alloying, the acoustic-TO contribution to the anharmonic linewidth typically increases by a factor of $2-3$ throughout the spectrum, and up by a factor of $10-100$ for some frequencies. This is illustrated in Fig. 3.12 by comparing these contributions for strained PbTe and $Pb_{0.51}Ge_{0.49}Te$ to that of PbTe. We conclude that extremely soft TO modes generated by driving PbTe near the phase transition considerably increase the anharmonic acoustic-TO interaction, which in turn substantially reduces the phonon lifetimes.

Both the increased phase space and coupling strength are responsible for the increase of the acoustic-TO contribution to the linewidth by driving PbTe to the verge of the phase transition. The phase space for the three-phonon scattering is related to the energy and momentum conservation of these processes [158].

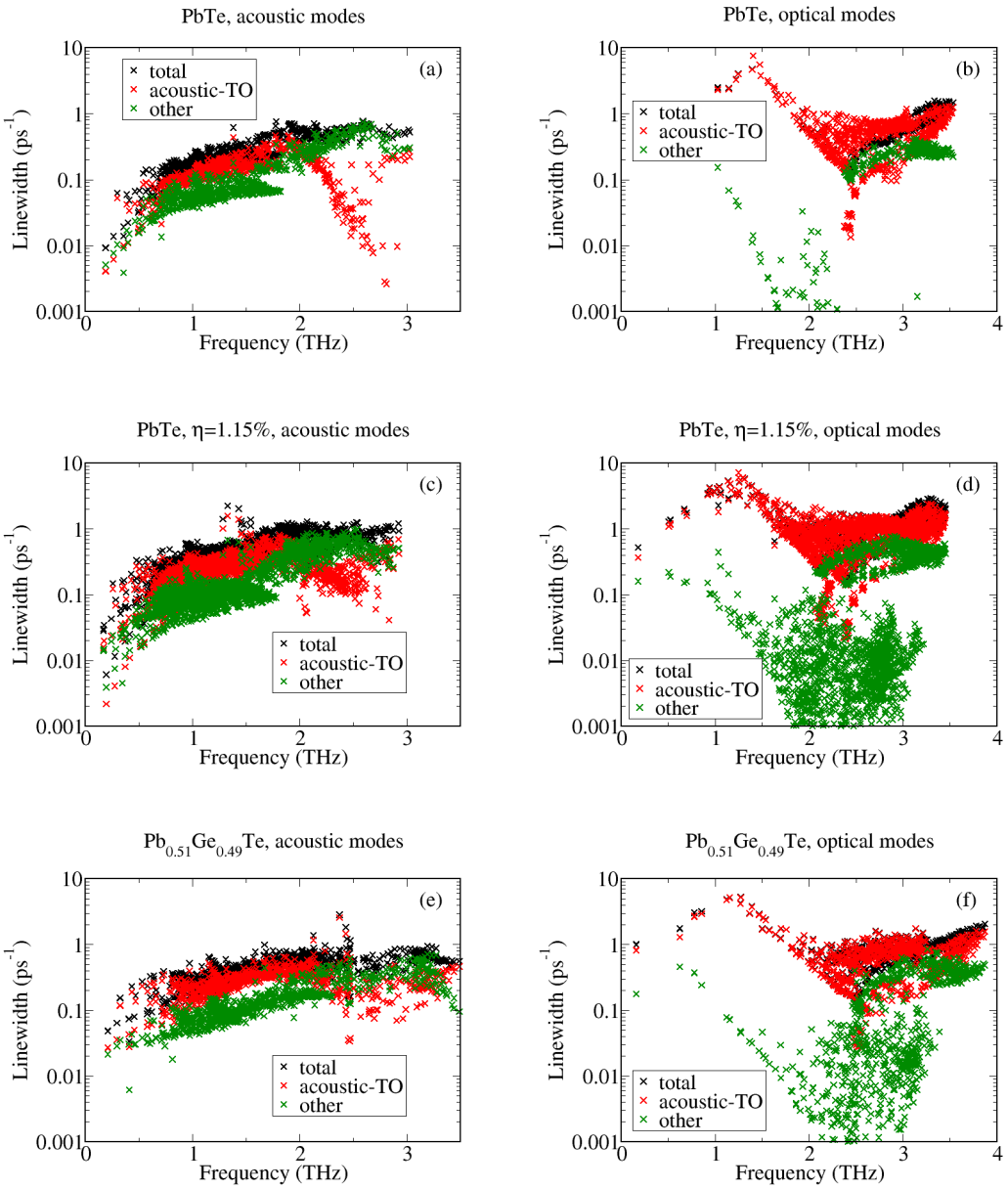



Figure 3.11: The total anharmonic linewidth at 300 K as a function of frequency (black crosses) together with its contribution from the scattering processes that involve both acoustic and transverse optical (TO) modes (red crosses) and the contribution from all other scattering processes (green crosses) for (a) acoustic modes in PbTe, (b) optical modes in PbTe, (c) acoustic modes in strained PbTe, (d) optical modes in strained PbTe, (e) acoustic modes in $Pb_{0.51}Ge_{0.49}Te$, and (f) optical modes in $Pb_{0.51}Ge_{0.49}Te$. The acoustic-TO contribution to the anharmonic linewidth dominates over the other contributions in all these materials.

The coupling strength can be quantified using the expression for the three-phonon linewidth without the energy conservation terms [63]. Our analysis of the phase space and the coupling strength associated with the acoustic-TO

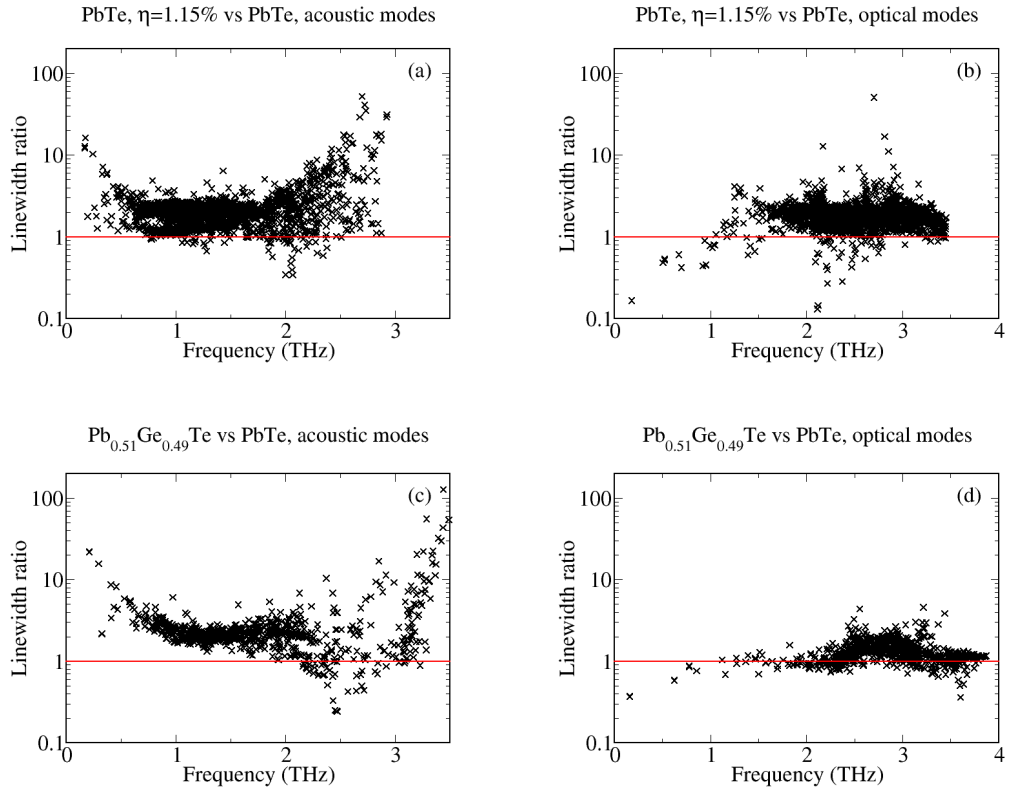



Figure 3.12: The ratio of the acoustic-transverse optical (TO) contribution to the total anharmonic linewidth of strained PbTe and $Pb_{0.51}Ge_{0.49}Te$ with respect to PbTe at 300 K versus mode frequency of strained PbTe and $Pb_{0.51}Ge_{0.49}Te$, respectively. (a) Acoustic modes in strained PbTe, (b) optical modes in strained PbTe, (c) acoustic modes in $Pb_{0.51}Ge_{0.49}Te$, and (d) optical modes in $Pb_{0.51}Ge_{0.49}Te$. The acoustic-TO contribution to the anharmonic linewidth of the materials driven near phase transitions is larger than that of PbTe.

interaction similar to that for the linewidths shows that they both increase by straining and/or alloying PbTe, and thus lead to the increase of the acoustic-TO contribution to the linewidth.

We also found that a relatively small number of soft TO modes near the zone centre that interact strongly with acoustic modes play a disproportionally large role in determining the linewidth of PbTe driven near the phase transition. To illustrate this effect, we calculated the contribution to the anharmonic linewidth due to the coupling of acoustic modes with the TO modes within the sphere centred at Γ with the radius of 1/3 of the Γ-X distance ($\sim$ 1/27 volume of the Brillouin zone), here labelled as $TO_1$ modes. Our results for PbTe, strained PbTe and $Pb_{0.51}Ge_{0.49}Te$ at 300 K are illustrated in Fig. 3.13. Even though $TO_1$ modes contribute to only $\sim$ 1.3% of the total number of modes, the acoustic-$TO_1$

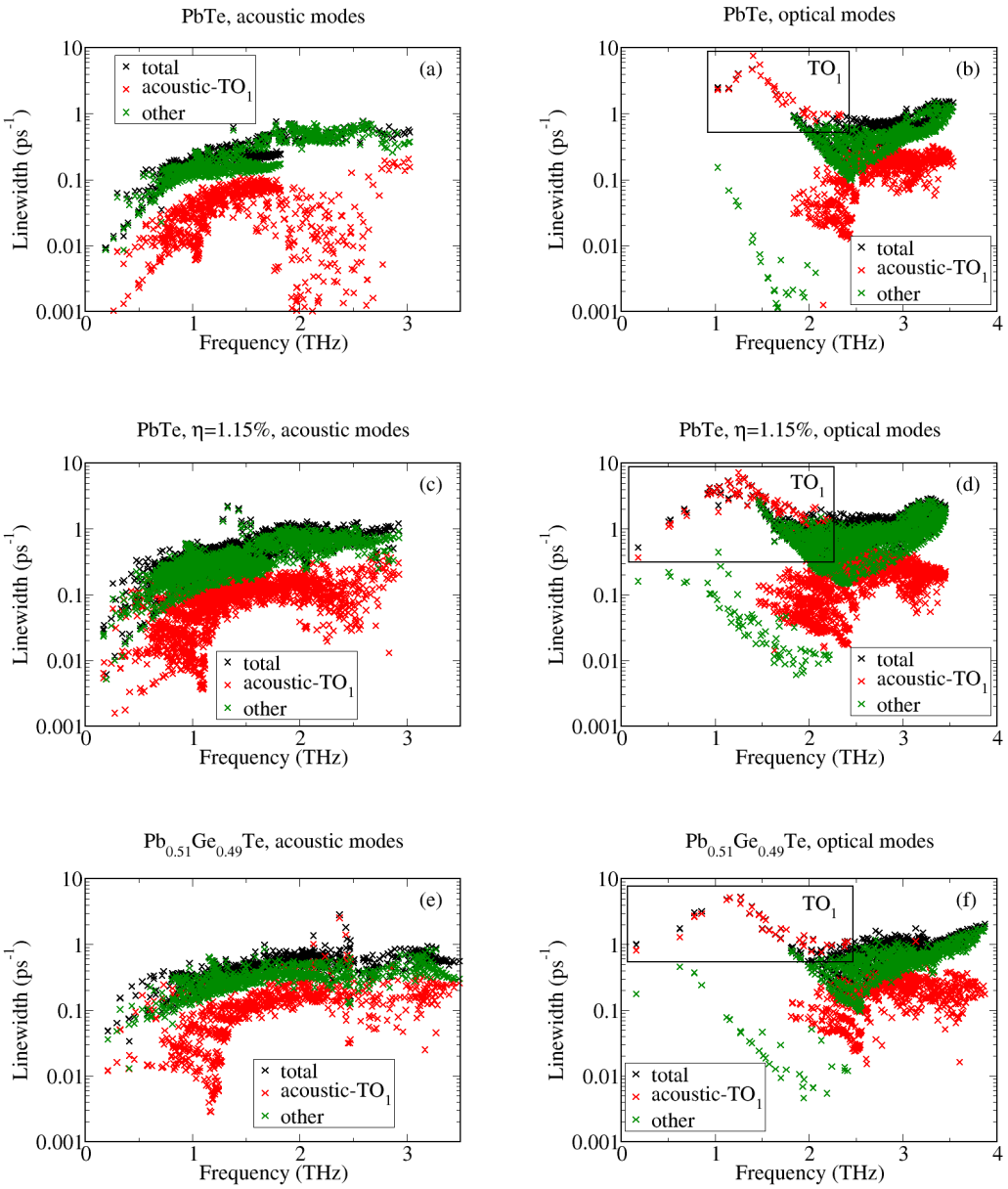



Figure 3.13: The total anharmonic linewidth at 300 K as a function of frequency (black crosses) together with its contribution from the scattering processes that involve both acoustic and transverse optical modes close to the zone centre (labelled as $TO_1$ modes, see text for explanation) (red crosses) and the contribution from all other scattering processes (green crosses) for (a) acoustic modes in PbTe, (b) optical modes in PbTe, (c) acoustic modes in strained PbTe, (d) optical modes in strained PbTe, (e) acoustic modes in $Pb_{0.51}Ge_{0.49}Te$, and (f) optical modes in $Pb_{0.51}Ge_{0.49}Te$. The frequencies of $TO_1$ modes correspond to red crosses within black boxes. The acoustic-$TO_1$ contribution represents a considerable fraction of the anharmonic linewidth in all these materials.

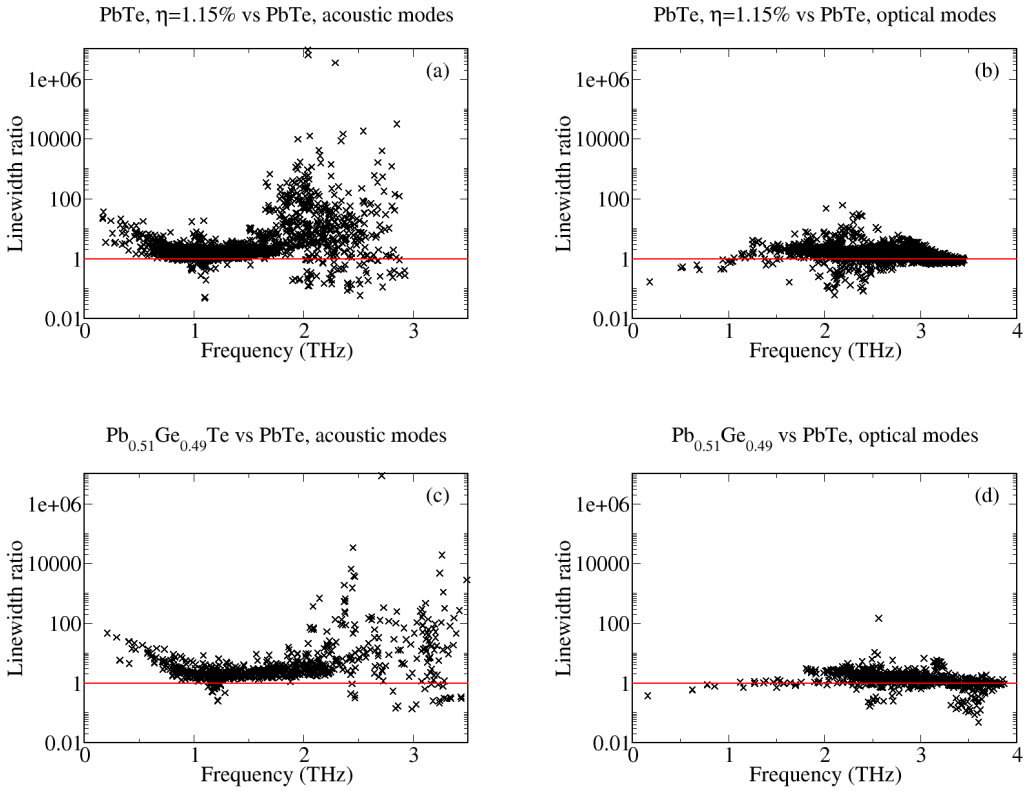



Figure 3.14: The ratio of the acoustic-transverse optical modes close to the zone centre (labelled as $TO_1$ modes, see text for explanation) contribution to the total anharmonic linewidth of strained PbTe and $Pb_{0.51}Ge_{0.49}Te$ with respect to PbTe at 300 K versus mode frequency of strained PbTe and $Pb_{0.51}Ge_{0.49}Te$, respectively. (a) Acoustic modes in strained PbTe, (b) optical modes in strained PbTe, (c) acoustic modes in $Pb_{0.51}Ge_{0.49}Te$, and (d) optical modes in $Pb_{0.51}Ge_{0.49}Te$. The acoustic-$TO_1$ contribution to the anharmonic linewidth of the materials driven near phase transitions is larger than that of PbTe.

contribution accounts for $\sim 20-30\%$ of the anharmonic linewidth throughout the spectrum, and for $\sim$ 100% of the anharmonic linewidth of $TO_1$ modes. Additionally, by driving PbTe close to the phase transition via strain or alloying with GeTe, the acoustic-$TO_1$ contribution to the anharmonic linewidth typically increases by a factor of $2-3$ across the spectrum, and up by a factor of $10^2-10^7$ for some frequencies, as shown in Fig. 3.14. These findings reveal an important contribution of extremely soft TO modes close to $\Gamma$ in increasing the anharmonic acoustic-TO interaction and reducing the phonon lifetimes in PbTe materials near the phase transition.

## 3.4 Impact on thermal conductivity

### 3.4.1 Strained PbTe

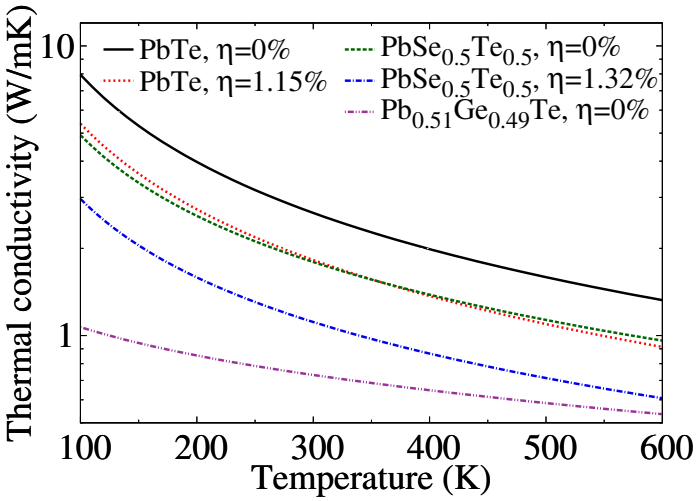



Figure 3.15: Lattice thermal conductivity versus temperature for PbTe (solid black line), PbTe driven near the phase transition by tensile (001) strain of $\eta = 1.15\%$ (dotted red line), $PbSe_{0.5}Te_{0.5}$ (dashed green line), $PbSe_{0.5}Te_{0.5}$ driven near the transition by tensile (001) strain of $\eta = 1.32\%$ (dash-dotted blue line), and $Pb_{0.51}Ge_{0.49}Te$ alloy near the transition (dash-double dotted purple line). Conductivity for strained materials is shown for the out-of-plane direction.

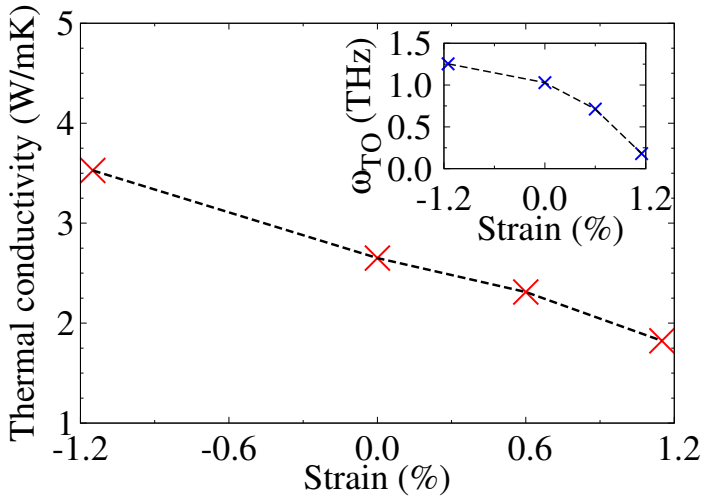



Figure 3.16: Out-of-plane lattice thermal conductivity of PbTe at 300 K as a function of (001) strain. Inset: Lowest transverse optical mode frequency at the zone centre, TO(Γ), for PbTe at 0 K versus (001) strain.

A factor of $\sim 2$ reduction of the phonon lifetimes at all frequencies in PbTe

strained near the phase transition leads to the reduction in the out-of-plane lattice thermal conductivity by a factor of 1.5 with respect to equilibrium. This is represented in Fig. 3.15 for the temperature range $100-600$ K, where solid black and dotted red lines correspond to the $\kappa_{\text{latt}}$ of equilibrium and strain-driven PbTe, respectively. The difference in the $\tau_{\text{anh}}$ and $\kappa_{\text{latt}}$ reductions is due to the larger group velocities of TO mode phonons in strained PbTe. Interestingly, in the in-plane direction, this difference becomes very small and the $\kappa_{\text{latt}}$ decreases by a factor of 1.9. We also computed the out-of-plane $\kappa_{\text{latt}}$ dependence on the amount of (001) strain at 300 K, see Fig. 3.16. The $\kappa_{\text{latt}}$ decrease directly correlates with the TO($\Gamma$) softening shown in the inset, in agreement with our conclusion that softer TO modes lead to more effective phonon scattering.

The efficiency of the proposed concept in reducing the thermal conductivity of PbTe is comparable to that of alloying with PbSe. Our computed $\kappa_{\text{latt}}$ of $PbSe_{0.5}Te_{0.5}$ (dashed green line in Fig. 3.15) is also a factor of 1.5 lower than that of PbTe, in agreement with a previous calculation [149]. Accounting for disorder in the force constants would increase the value of this factor [62, 128, 152] closer to experiments ($\sim 2$ at 300 K [154, 159]). We emphasize that two very different mechanisms cause the low lattice thermal conductivity in these two types of materials. Strained PbTe benefits from the enhanced anharmonic acoustic-TO interaction across the spectrum, while alloy disorder in $PbSe_{0.5}Te_{0.5}$ blocks the flow of high-frequency phonons only.

The low lattice thermal conductivity of strained PbTe originates from the softer TO modes near the zone centre and their increased anharmonic interaction with acoustic modes with respect to equilibrium. To illustrate this effect more quantitatively, we artificially replaced the acoustic-$TO_1$ contribution to the linewidth of strained PbTe with that of PbTe in its $\kappa_{\text{latt}}$ calculation at 300 K. The $\kappa_{\text{latt}}$ values obtained using this procedure are $\sim 7\%$ larger than those of strained PbTe. This result shows that $TO_1$ modes, which contribute only $\sim 1.3\%$ to the total number of modes but interact strongly with acoustic phonons, produce a much stronger effect on the $\kappa_{\text{latt}}$ than one would expect from their relative number.

### 3.4.2 Strained $PbSe_{0.5}Te_{0.5}$ alloy

The strategy of exploiting extremely soft TO modes to reduce the lattice thermal conductivity of PbTe will become as effective as all-scale structuring [34, 39, 41] if it is combined with alloying. This approach simultaneously incorporates the mechanisms of enhanced anharmonic acoustic-TO interaction and alloy disorder

to reduce lattice thermal conductivity more effectively. We find that driving $PbSe_{0.5}Te_{0.5}$ to the brink of the phase transition via tensile (001) strain will reduce its out-of-plane $\kappa_{\text{latt}}$ by a factor of at least 2.4 with respect to PbTe (dash-dotted blue line in Fig. 3.15). If we neglect mass disorder in our calculations, the $\kappa_{\text{latt}}$ of strained $PbSe_{0.5}Te_{0.5}$ is 1.5 times lower than that of PbTe (similarly to strained PbTe) due to the increased acoustic-TO interaction. However, mass disorder is more efficient in scattering high-frequency phonons of strained $PbSe_{0.5}Te_{0.5}$, and causes an additional $\kappa_{\text{latt}}$ decrease by a factor of 1.6 compared to its values without mass disorder. The actual reduction to lattice thermal conductivity of strained $PbSe_{0.5}Te_{0.5}$ with respect to PbTe will be even larger than the factor of 2.4 computed here, due to disorder in the force constants [152].

### 3.4.3 $Pb_{0.51}Ge_{0.49}Te$ alloy

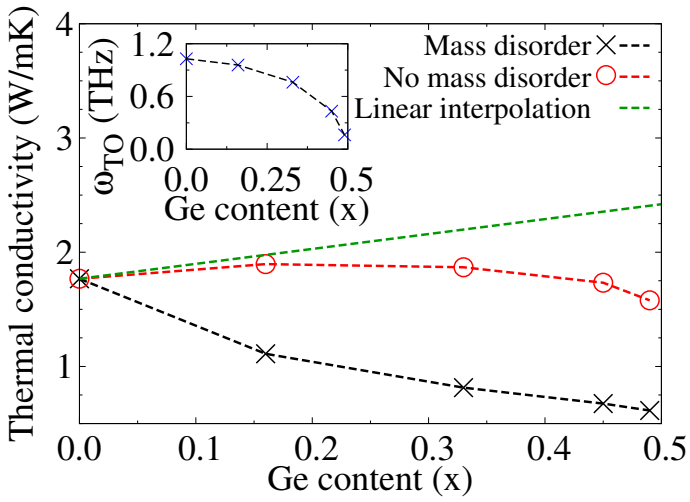



Figure 3.17: Lattice thermal conductivity of $Pb_{1-x}Ge_xTe$ alloys at 450 K as a function of Ge content $x$: full calculation (black crosses), calculation without mass disorder (red circles) and linearly interpolated values between those calculated for PbTe and GeTe (dashed green line). Inset: TO($\Gamma$) frequency of $Pb_{1-x}Ge_xTe$ at 0 K versus Ge content $x$.

The concept of combining ultra soft TO modes and alloying to substantially reduce the lattice thermal conductivity of PbTe can also be realized without strain e.g. by tuning the composition of $Pb_{1-x}Ge_xTe$ alloys to bring them near the phase transition at desired temperatures. These conditions can be achieved only in alloys of PbTe with another rhombohedral material, such as GeTe. As already discussed, $Pb_{0.51}Ge_{0.49}Te$ alloy remains close to the transition at all temperatures in our calculations, thus describing the $\kappa_{\text{latt}}$ appropriately only near the transition

temperature of $\sim$ 450 K [157]. Our results show that the $\kappa_{\text{latt}}$ of $Pb_{0.51}Ge_{0.49}Te$ alloy (dash-double dotted purple line in Fig. 3.15) will be at least 2.9 times lower than the $\kappa_{\text{latt}}$ of PbTe at 450 K, even lower than that of strained $PbSe_{0.5}Te_{0.5}$.

The very low lattice thermal conductivity of $Pb_{0.51}Ge_{0.49}Te$ alloy stems from both the increased anharmonic acoustic-TO interaction and strong alloy scattering. Fig. 3.17 and its inset show the $\kappa_{\text{latt}}$ values and the TO($\Gamma$) frequencies of $Pb_{1-x}Ge_xTe$ alloys at 450 K as a function of the alloy composition $x$ for $0 \leq x \leq 0.49$ (black crosses), where the rocksalt phase is energetically favourable. This figure also shows the corresponding $\kappa_{\text{latt}}$ computed by neglecting mass disorder (red circles). We note that if soft TO modes were not induced in $Pb_{1-x}Ge_xTe$ alloys, their $\kappa_{\text{latt}}$ without mass disorder would roughly be equal to the linearly interpolated values between the lattice thermal conductivities of their parent materials, for example, in the case of $PbSe_{1-x}Te_x$. The interpolated values between our calculated $\kappa_{\text{latt}}$ for PbTe and GeTe at 450 K are shown in the dashed green line in Fig. 3.17. Our calculated value for the isotropically averaged lattice thermal conductivity of GeTe at 450 K is 3.27 W/mK. The increased TO softening in $Pb_{1-x}Ge_xTe$ with $x$ leads to the larger reduction of the $\kappa_{\text{latt}}$ values that neglect mass disorder with respect to the interpolated values, by up to a factor of 1.6 for $x = 0.49$. Additionally, the relatively large mass difference between Pb and Ge atoms results in a large $\kappa_{\text{latt}}$ decrease with respect to the case when mass disorder is neglected, by up to a factor of 2.6 for $Pb_{0.51}Ge_{0.49}Te$. We conclude that the extra softening of TO modes in $Pb_{1-x}Ge_xTe$ alloys with respect to PbTe together with strong mass disorder makes them more suitable materials for achieving low lattice thermal conductivity compared to $PbSe_{1-x}Te_x$ alloys.

The group velocities of acoustic modes in $Pb_{1-x}Ge_xTe$ alloys increase considerably as the Ge content increases, unlike the group velocities of PbTe and $PbSe_{0.5}Te_{0.5}$ under increasing biaxial tensile (001) strain (see Figs. 3.3, 3.4, and 3.5). This is the reason why the $\kappa_{\text{latt}}$ of $Pb_{1-x}Ge_xTe$ without mass disorder does not decrease monotonously with $x$, as opposed to the $\kappa_{\text{latt}}$ of increasingly strained PbTe, see Figs. 3.16 and 3.17. Furthermore, the lattice thermal conductivity values without mass disorder for $Pb_{1-x}Ge_xTe$ are larger than those of strained PbTe and $PbSe_{0.5}Te_{0.5}$ because of the larger group velocities.

Similarly to strained PbTe, a small number of soft TO modes close to the zone centre, which interact more strongly with acoustic modes as $Pb_{1-x}Ge_xTe$ alloys are driven to the phase transition by increasing $x$, have a relatively large effect on their thermal conductivity. We quantify this by substituting the acoustic-

$TO_1$ contribution to the anharmonic linewidth of $Pb_{0.51}Ge_{0.49}Te$ with that of equilibrium PbTe in its $\kappa_{\text{latt}}$ calculation that neglects mass disorder. This results in an $\sim$ 18% larger value at 300 K than that of $Pb_{0.51}Ge_{0.49}Te$, which is even larger than the corresponding increase in strained PbTe.

### 3.4.4 Impact to phonon mean free paths

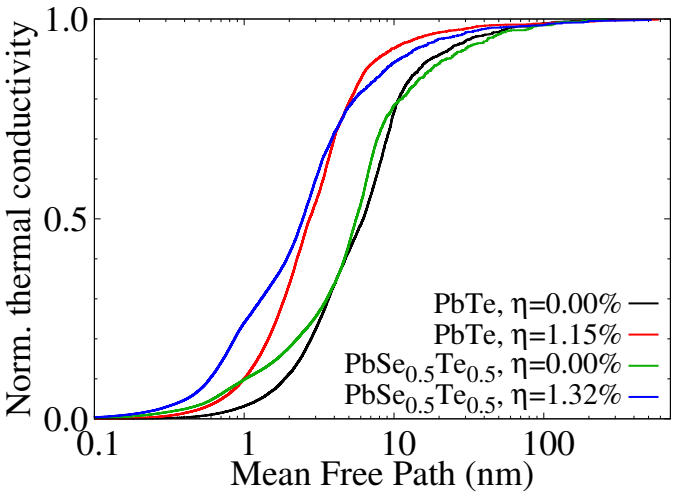



Figure 3.18: Normalised cumulative lattice thermal conductivity plotted as a function of phonon mean free path for PbTe (black), strained PbTe, $\eta = 1.15\%$ (red), $PbSe_{0.5}Te_{0.5}$ (green), and strained $PbSe_{0.5}Te_{0.5}$, $\eta = 1.32\%$ (blue).

The mean free path (MFP) of a phonon describes the average travelling distance between two phonon scattering events, and is defined as [149]:

$$\Lambda_{\mathbf{q}s} = v_{\mathbf{q}s}\tau_{\mathbf{q}s}. \tag{3.2}$$

To quantify the contribution to the lattice thermal conductivity from phonons with various MFPs, we calculate the cumulative $\kappa_{\text{latt}}$ by summing over phonon modes with a MFP shorter than a value $\Lambda$ [149]:

$$\kappa_{\text{latt}}(\Lambda) = \frac{1}{N_{\mathbf{q}}\Omega}\sum_{\mathbf{q}s}^{\Lambda_{\mathbf{q}s}<\Lambda} c_{\mathbf{q}s}v_{\mathbf{q}s}\Lambda_{\mathbf{q}s}, \tag{3.3}$$

where $N_{\mathbf{q}}$ is the number of $\mathbf{q}$-points. Applying biaxial (001) strain to PbTe and $PbSe_{0.5}Te_{0.5}$ considerably shortens the MFPs of phonons contributing to lattice thermal conductivity compared to PbTe and $PbSe_{0.5}Te_{0.5}$ respectively, see Fig. 3.18. This arises from the increased acoustic-TO interaction near the phase transition which scatters phonons with longer MFPs (lower frequencies),

and causes a redistribution of the accumulation curve to shorter MFPs (higher frequencies).

Looking at the phonon mean free paths in terms of reducing lattice thermal conductivity even further via nanostructuring to increase phonon scattering, one would need to go to very small length scales to achieve a sizeable reduction. Approximately 20% of the lattice thermal conductivity of PbTe and $PbSe_{0.5}Te_{0.5}$ arises from phonons with MFPs larger than 10 nm, see Fig. 3.18. Thus, nanostructures of characteristic length 10 nm would only reduce the lattice thermal conductivity of these unstrained materials at most by ∼20%. In strained PbTe and strained $PbSe_{0.5}Te_{0.5}$ the achievable reduction falls to $< 10\%$ for nanostructures of this length. Aiming for a reduction of about 25% would require scattering phonons whose MFP is greater than 3 nm for the strained materials, a difficult scale to nanostructure on. Since biaxial tensile (001) strain is so effective at reducing the mean free paths of phonons contributing to the lattice thermal conductivity, it makes it considerably more difficult to increase phonon scattering via nanostructuring.

## 3.5 Discussion

The proposed concept of increasing the proximity of PbTe to the ferroelectric phase transition to reduce the lattice thermal conductivity is general and would also be applicable to other materials close to soft zone centre optical mode transitions. It can be achieved by using strain, alloying, and possibly also by nanostructuring. Our proposal may be realized experimentally, for example, by metastable growth of $Pb_{1-x}Ge_xTe$ solid solutions [157], or by depositing a thin film of PbTe or $PbSe_{1-x}Te_x$ alloys on a flexible polymer substrate [160, 161], and applying biaxial tensile (001) strain directly to the polymer. We note that the mechanical stability of the tensile strained materials very near the transition may be compromised. Nevertheless, the proposed concept will hold even if the materials are not driven very close to the transition, although their $\kappa_{\text{latt}}$ reductions will be smaller, as illustrated in Figs. 3.16 and 3.17.

### 3.5.1 Higher order anharmonicity

Even if higher than third order anharmonicity terms were non-negligible for PbTe materials driven to the transition, the proposed concept would remain valid. However, the lattice thermal conductivity reductions would be lower than our results, particularly at higher temperatures. The main implication of higher

anharmonic terms on the thermal properties of PbTe is shifting the TO modes upwards, resulting in the well known TO frequency increase with temperature [27, 66, 162, 163]. This will weaken the anharmonic acoustic-TO interaction, which may result in somewhat higher $\kappa_{\text{latt}}$ values than those predicted here. This effect may become more evident for $T > 300$ K in the case of PbTe [66], and it may manifest at even lower $T$ for the materials near the phase transition. Consequently, the actual $\kappa_{\text{latt}}$ reduction may decrease with $T$ with respect to our calculations.

Experimentally, $Pb_{0.51}Ge_{0.49}Te$ undergoes the phase transition from the rhombohedral to the rocksalt structure at $\sim$ 450 K [157], while it is rocksalt for all temperatures in our calculations. Higher order anharmonicity terms would further stabilize the rocksalt phase in our virtual crystal simulations [66], due to the hardening of the TO modes. This indicates that using an alloy model beyond this approximation may be necessary to accurately describe the temperature behaviour of the $\kappa_{\text{latt}}$ of $Pb_{0.51}Ge_{0.49}Te$. This, however, will not change the main implication of our work that tuning the composition of $Pb_{1-x}Ge_xTe$ alloys to drive the material near the phase transition at a certain temperature will substantially decrease its $\kappa_{\text{latt}}$ at that temperature. The measured lattice thermal conductivity values of some of the $Pb_{1-x}Ge_xTe$ materials reported in Ref. [164] indeed exhibit pronounced dips near the transition temperature, and thus support our argument.

### 3.5.2 Phase segregation

Low lattice thermal conductivity and high figure of merit have been recently reported in $Pb_{1-x}Ge_xTe$ materials with phase separated regions and nanoscale features [36, 165, 166]. Since no dips in the $\kappa_{\text{latt}}$ values close to the transition temperature have been observed in these materials, their $\kappa_{\text{latt}}$ reduction is likely dominated by phonon scattering at the interfaces. Our study shows that substantial $\kappa_{\text{latt}}$ reductions can also be obtained in random $Pb_{1-x}Ge_xTe$ alloys without any phase separation, which may also be beneficial for electronic transport properties. More systematic studies across all compositions could resolve whether random alloys would be more efficient thermoelectric materials than nanostructured/phase separated materials for certain composition ranges.

## 3.6 Summary

With first principles calculations, we predict that driving PbTe-based materials to the verge of the ferroelectric phase transition will be a powerful strategy

to impede phonon transport in the entire frequency spectrum and considerably reduce lattice thermal conductivity. We demonstrate this strategy using two distinct approaches, applying biaxial tensile (001) strain to PbTe and $PbSe_{0.5}Te_{0.5}$, and furthermore by alloying PbTe with a rhombohedral material, GeTe. The proposed concept is based on the induced softening of the transverse optical modes at the zone centre, whose increased anharmonic interaction with heat carrying acoustic modes enhances phonon scattering. Furthermore, by combining increased proximity to the phase transition and mass disorder through alloying, we achieve reductions to the lattice thermal conductivity by a factor of $2-3$ compared to PbTe. Thus, the efficiency of this approach in reducing lattice thermal conductivity rivals that of all-scale hierarchical architecturing [34]. The presented strategy is general, and it would also be applicable to other materials close to soft zone centre optical mode transitions.

# Chapter 4

# Lattice thermal conductivity of $Pb_{1-x}Ge_xTe$ alloys

## 4.1 Introduction

### 4.1.1 Motivation

In this chapter, we investigate the impact of proximity to the ferroelectric phase transition on the lattice thermal conductivity of $Pb_{1-x}Ge_xTe$ alloys. This is inspired by the lack of a quantitative description within the literature on the effect that the proximity to a soft mode phase transition has on a material's intrinsic lattice thermal conductivity. $Pb_{1-x}Ge_xTe$ alloys undergo a soft optical mode transition between the rocksalt and rhombohedral phases as a function of the composition and temperature [157], and are known for their high thermoelectric performance [36, 164, 165, 166, 167, 168]. By tuning their composition, we investigate the interplay of proximity to the phase transition, mass disorder and crystal structure in minimising the lattice thermal conductivity of these alloys. In particular, the investigation of the role of the crystal structure is partly inspired by recent work highlighting the effect of high symmetry and so-called resonant bonding in producing an intrinsically low lattice thermal conductivity in materials such as PbTe [150, 169, 170].

Our first principles virtual-crystal calculations show that the phase transition minimizes the anharmonic component of lattice thermal conductivity due to extremely soft optical modes which maximize the anharmonic acoustic-optical coupling, especially for low-frequency phonons. Mass disorder additionally reduces $\kappa_{\text{latt}}$ via scattering of mid- and high-frequencies, which flattens the drop in the anharmonic $\kappa_{\text{latt}}$ over a wide range of compositions and moves the $\kappa_{\text{latt}}$

minimum away from the phase transition, into the rhombohedral phase of the alloy. Furthermore, we find a continuous change of the total and anharmonic lattice thermal conductivity between the rocksalt and rhombohedral phases characteristic of the second-order phase transition. We argue that the structure and its degree of resonant bonding are less crucial for lowering the $\kappa_{\text{latt}}$ in these alloys than the proximity to the phase transition, average atomic mass and mass disorder. Our findings highlight the potential of combining soft optical modes and alloying to design materials with low lattice thermal conductivity and potentially high $ZT$.

### 4.1.2 Calculation details

Harmonic and third order anharmonic IFCs at 0 K were calculated from Hellmann-Feynman forces computed on $4 \times 4 \times 4$ (128 atom) supercells, with an energy cut-off of 15 Ha. We calculated all IFCs within this supercell without imposing any additional cut-off on their range. Electronic states are described using $2 \times 2 \times 2$ 4 shifted reciprocal space grids for alloy compositions $x \leq 0.51$, while $2 \times 2 \times 2$ reciprocal space grids are used for all other compositions. We performed lattice thermal conductivity calculations on $20 \times 20 \times 20$ $\mathbf{q}$ point grids in the Brillouin zone, having verified that that the use of $40 \times 40 \times 40$ grids changes the $\kappa_{\text{latt}}$ values no more than $\sim$2.3% with respect to $20 \times 20 \times 20$ grids for selected $Pb_{1-x}Ge_xTe$ compositions ($x = 0.00, 0.49, 0.51, 1.00$).

We used $4 \times 4 \times 4$ (128 atom) supercells as they best reproduced the expected physical behaviour of the second-order phase transition in $Pb_{1-x}Ge_xTe$ alloys. We found that the continuity of harmonic interatomic force constants at the phase transition leads to physically sensible phonon dispersions in the rhombohedral phase. In $2 \times 2 \times 2$ cubic (64 atom) supercells discontinuities were found in the long-range IFCs (4th and 8th nearest neighbour) for the rocksalt and rhombohedral structures very near the phase transition, $x = 0.49$ and $x = 0.51$ respectively. This resulted in imaginary frequencies for the lowest transverse acoustic mode near $\Gamma$ in the rhombohedral structures near the phase transition. These instabilities were found to persist for larger supercells such as $3 \times 3 \times 3$ cubic (216 atoms), $5 \times 5 \times 5$ (256 atoms) and $4 \times 4 \times 4$ cubic (512 atoms). On the other hand, using density functional perturbation theory, we found that the frequencies of transverse acoustic modes for rhombohedral structures near the phase transition exhibit oscillations about the physically correct linear dependence on the wave vector near $\Gamma$ along the $\Gamma-$ X direction. While these oscillations decreased in magnitude with denser wave vector grids, they nevertheless remained for rhombohedral Brillouin

zone grid sizes up to $12 \times 12 \times 12$. While this suggests that larger supercells would be required to overcome these issues, such calculations would presently be computationally very demanding. Thus, we chose $4 \times 4 \times 4$ (128 atom) supercells as they possess continuity in the IFCs at the second-order phase transition, and exhibit the physically correct linear dependence of the acoustic mode frequencies on the wave vectors near Γ. However, further investigation is necessary to better understand the effect of these long range interactions in $Pb_{1-x}Ge_xTe$ alloys.

Our method that only accounts for third order anharmonic terms does not account for the temperature dependence of structural parameters and IFCs. As a result, we do not capture the phase transition in $Pb_{1-x}Ge_xTe$ alloys from the rhombohedral to rocksalt phases with increasing temperature at a given composition [157]. The temperature at which the phase transition occurs increases as a function of Ge content, from 0 K at $x \approx 0.01$ to ∼670 K for $x = 1$ [157]. Nonetheless, we find that the phonon dispersions, thermal expansion coefficients, and $\kappa_{\text{latt}}$ of PbTe and GeTe agree fairly well with experimental data, as will be demonstrated next. Furthermore, our model captures the soft optical mode phase transition as a function of the alloy composition, as we will show in the following section. This suggests that our approach will correctly predict qualitative changes in the $\kappa_{\text{latt}}$ of $Pb_{1-x}Ge_xTe$ alloys by varying $x$.

### 4.1.3 Verification of approach

To verify the validity of our approach, we compare our calculated phonon band structure, thermal expansion coefficients and lattice thermal conductivity on $4 \times 4 \times 4$ (128 atom) supercells for PbTe and GeTe with experimental data. We also included the validation of our computed third-order IFCs through Grüneisen parameter calculations.

The phonon dispersion of PbTe for 128 atom supercells is in good agreement with the inelastic neutron scattering measurements of Cochran *et al.* [153] (see Fig. 4.1), except for transverse modes along Γ-X and Γ-K directions. Our computed dispersion for 216 atom cubic supercells does not exhibit such deviations from the experiment. However, as discussed earlier, we can describe correctly the second order phase transition behaviour across the whole range of alloy compositions only using 128 atom supercells. Our calculated phonon dispersion of GeTe for 128 atom supercells is shown in Fig. 4.2. To the best of our knowledge, there are no reports of the measured phonon dispersions of GeTe in the literature. Our computed frequencies of zone centre Raman active modes compare well with the measurements of Refs. [171, 172] at 300 K. We also calculated the phonon density

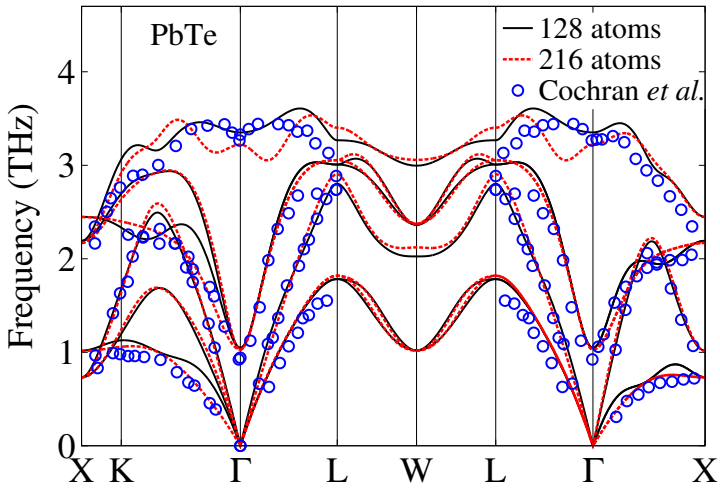



Figure 4.1: Phonon dispersions of PbTe: calculated using a 128 atom supercell at 0 K (solid black line), calculated using a 216 atom supercell at 0 K (dashed red line), and measured by Cochran *et al.* [153] at 300 K (blue circles).

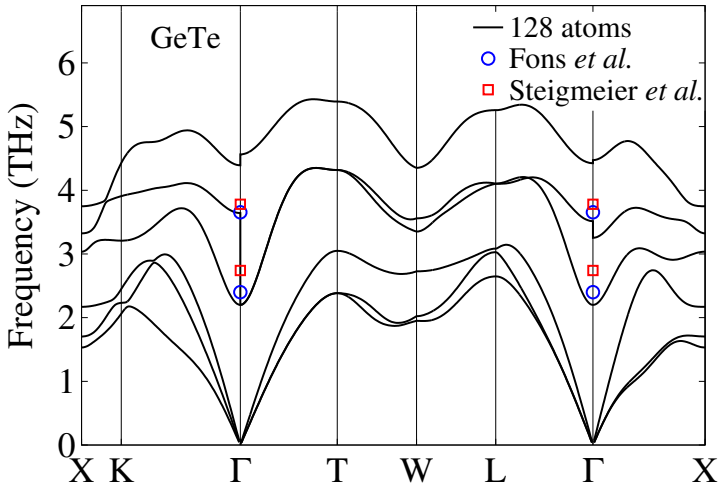



Figure 4.2: Phonon dispersions of GeTe: calculated using a 128 atom supercell at 0 K (solid black line), and the frequencies of zone centre Raman active modes measured by Fons *et al.* [171] at 300 K (blue circles) and Steigmeier *et al.* [172] at 300 K (red squares).

of states of GeTe (Fig. 4.3), which is in good agreement with the experimental results of Refs. [173, 174]. Our phonon dispersion of GeTe also agrees well with a previous density functional perturbation theory calculation [175].

We verified the accuracy of our computed third-order anharmonic interatomic force constants by calculating the mode Grüneisen parameters of $Pb_{1-x}Ge_xTe$ alloys using two different approaches. Mode Grüneisen parameters are defined

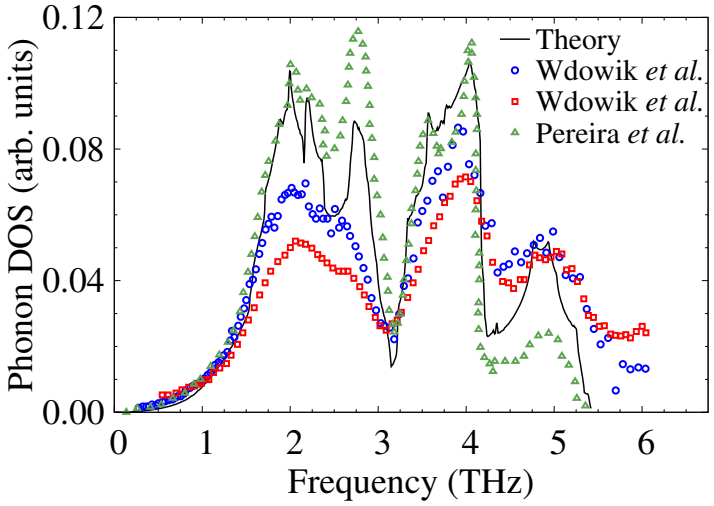



Figure 4.3: Phonon density of states for GeTe: calculated using a 128 atom supercell at 0 K (solid black line), measured by Wdowik *et al.* [173] and Pereira *et al.* [174]. The integral of the density of states over frequency is normalized to unity.

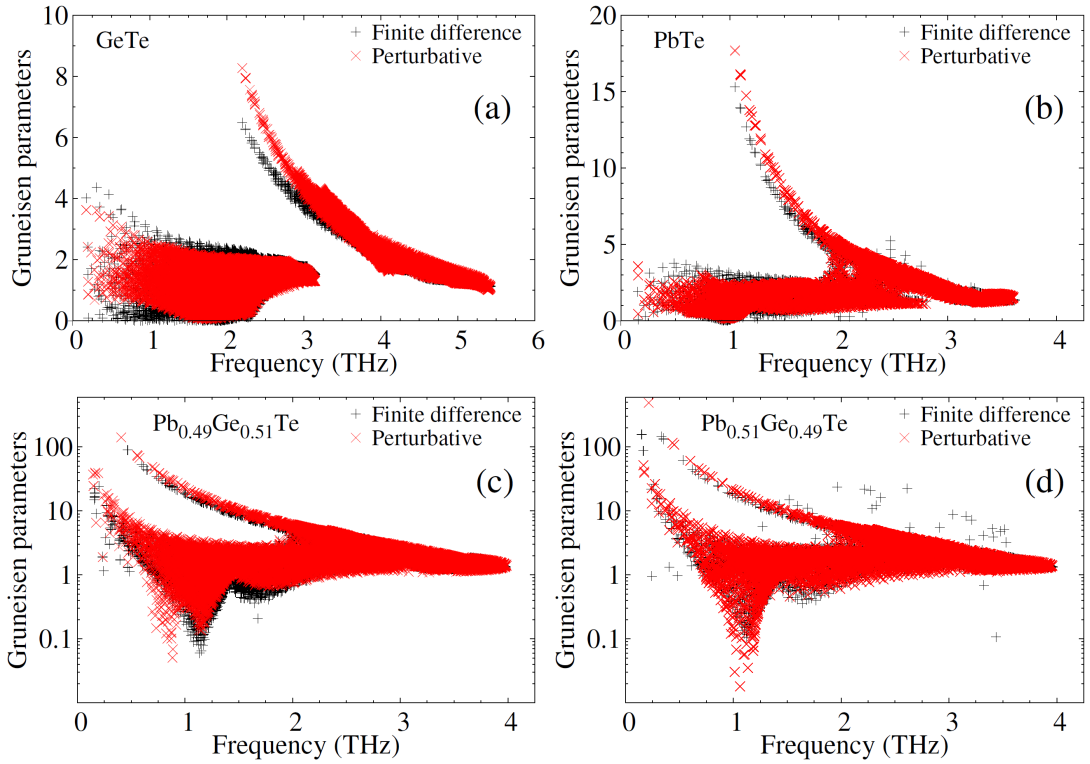



Figure 4.4: Mode Grüneisen parameters as a function of frequency obtained using finite difference (black pluses) and perturbative approaches (red crosses) for (a) GeTe, (b) PbTe, (c) $Pb_{0.49}Ge_{0.51}Te$, and (d) $Pb_{0.51}Ge_{0.49}Te$.

as:

$$\gamma_{\mathbf{q}s} = -\frac{\mathrm{d}(\log \omega_{\mathbf{q}s})}{\mathrm{d}(\log \Omega)} = \frac{\Omega}{\omega_{\mathbf{q}s}} \frac{\partial \omega_{\mathbf{q}s}}{\partial \Omega}. \tag{4.1}$$

To calculate $\gamma_{\mathbf{q}s}$, we used a finite difference approach that requires computing phonon frequencies at different crystal volumes using Eq. (4.1). We also used a first-order perturbative approach to express Grüneisen parameters in terms of third-order anharmonic IFCs [59, 176]:

$$\gamma_{\mathbf{q}s} = -\frac{1}{6\omega_{\mathbf{q}s}^2} \sum_{lb,l'b',l''b''} \sum_{\alpha\beta\gamma} \Phi_{\alpha\beta\gamma}^{lb,l'b',l''b''} \frac{e_{\alpha b}^{*s}(\mathbf{q}) e_{\beta b'}^{s}(\mathbf{q})}{\sqrt{m_b m_{b'}}} e^{i\mathbf{q}\cdot\mathbf{R}_{l'}} \boldsymbol{\tau}_{\gamma}^{l''b''}. \tag{4.2}$$

Eq. (4.2) is derived under the assumptions that the crystal is cubic, and the atomic positions within the crystal remain fixed upon volume changes. This condition is not fully satisfied for rhombohedral lattices. Consequently, to compare the mode Grüneisen parameters obtained with Eq. (4.2) with those of the finite difference approach for nearly cubic $Pb_{1-x}Ge_xTe$ alloys, we varied only their lattice constants in the finite difference calculations. Fig. 4.4 shows the Grüneisen parameters in the whole Brillouin zone obtained using the two described approaches for GeTe, PbTe, and the alloy compositions near the phase transition, $Pb_{0.49}Ge_{0.51}Te$ and $Pb_{0.51}Ge_{0.49}Te$. The results obtained from the two approaches agree very well with each other for all these materials, which confirms the accuracy of our computed third-order IFCs.

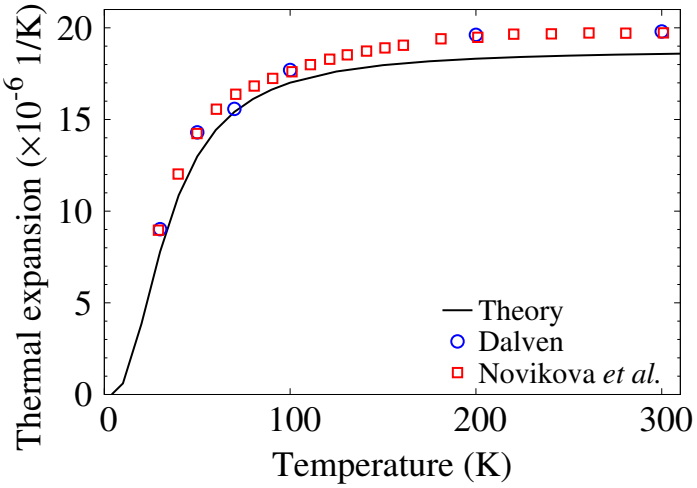



Figure 4.5: Linear thermal expansion coefficient of PbTe as a function of temperature: calculated using a 128 atom supercell (solid black line), measured by Dalven [177] (blue circles), and measured by Novikova and Abrikosov, Ref [153] and references therein (red squares).

We also computed the linear thermal expansion coefficient of PbTe as [51]:

$$\alpha = \frac{1}{3N_{\mathbf{q}}\Omega B}\sum_{\mathbf{q}s} c_{\mathbf{q}s}\gamma_{\mathbf{q}s}, \tag{4.3}$$

where $B$ is the bulk modulus. Our calculated bulk modulus of PbTe is 47.94 GPa, from the Burch-Murnaghan equation of state. Fig. 4.5 shows the linear thermal expansion coefficient of PbTe versus temperature obtained with the Grüneisen parameters computed using the perturbative approach, and illustrates good agreement with the measurements on single crystalline PbTe samples [153, 177].

We also derived the generalized expressions for the thermal expansion coefficients of the rhombohedral lattice in a similar manner as done in Ref. [178], and calculated these coefficients for GeTe. The relative positions of Ge and Te atoms within the rhombohedral primitive cell are $(0,0,0)$ and $(0.5+r, 0.5+r, 0.5+r)$ with $r = 0.0237$ in our calculations, and the angle between the lattice vectors is $\phi = 60^\circ - \theta$ with $\theta = 1.2093^\circ$. The change of the zero temperature total energy with respect to the small deviations of the lattice constant $a$, the angle $\phi$ and the Te displacement along the [111] direction $r$ is given as:

$$\begin{aligned}\Delta E =& \frac{1}{2}C_{aa}(\Delta a)^2 + \frac{1}{2}C_{\phi\phi}(\Delta\phi)^2 + \frac{1}{2}C_{rr}(\Delta r)^2 \\ &+ C_{a\phi}(\Delta a)(\Delta\phi) + C_{ar}(\Delta a)(\Delta r) + C_{\phi r}(\Delta\phi)(\Delta r).\end{aligned} \tag{4.4}$$

We calculate the symmetric matrix $[C]$ using density functional theory, and find its inverse matrix $[S] = [C]^{-1}$. The thermal expansion coefficients for $a$, $\phi$ and $r$ can be expressed as:

$$\alpha_a = \frac{1}{N_{\mathbf{q}}a}\sum_{\mathbf{q}s} c_{\mathbf{q}s}\left(\frac{S_{aa}}{a}\gamma^a_{\mathbf{q}s} + \frac{S_{a\phi}}{\phi}\gamma^\phi_{\mathbf{q}s} + \frac{S_{ar}}{r}\gamma^r_{\mathbf{q}s}\right), \tag{4.5}$$

$$\alpha_\phi = \frac{1}{N_{\mathbf{q}}\phi}\sum_{\mathbf{q}s} c_{\mathbf{q}s}\left(\frac{S_{a\phi}}{a}\gamma^a_{\mathbf{q}s} + \frac{S_{\phi\phi}}{\phi}\gamma^\phi_{\mathbf{q}s} + \frac{S_{\phi r}}{r}\gamma^r_{\mathbf{q}s}\right), \tag{4.6}$$

$$\alpha_r = \frac{1}{N_{\mathbf{q}}r}\sum_{\mathbf{q}s} c_{\mathbf{q}s}\left(\frac{S_{ar}}{a}\gamma^a_{\mathbf{q}s} + \frac{S_{\phi r}}{\phi}\gamma^\phi_{\mathbf{q}s} + \frac{S_{rr}}{r}\gamma^r_{\mathbf{q}s}\right), \tag{4.7}$$

respectively, where we write generalized Grüneisen parameters as:

$$\gamma^a_{\mathbf{q}s} = -\frac{\partial(\log\omega_{\mathbf{q}s})}{\partial(\log a)}, \tag{4.8}$$

$$\gamma^\phi_{\mathbf{q}s} = -\frac{\partial(\log\omega_{\mathbf{q}s})}{\partial(\log \phi)}, \tag{4.9}$$

Table 4.1: Thermal expansion coefficients $\alpha$ of GeTe at 300 K for lattice constant $A$, the angle between the lattice vectors $\Phi$, and the Te atom position along the [111] direction $R$ in the non-primitive pseudo-cubic lattice. The thermal expansion coefficients from Refs. [179, 180, 181, 182, 183] were extracted by linearly fitting the measured lattice parameters between $\sim$ 300 K and $\sim 400-550$ K.

| | $\alpha_A$ ($10^{-6}$ K$^{-1}$) | $\alpha_\Phi$ ($10^{-6}$ K$^{-1}$) | $\alpha_R$ ($10^{-6}$ K$^{-1}$) |
|---|---|---|---|
| Our results (single crystal) | 12.3 | 7.7 | 15.5 |
| Ref. [179] (single crystal) | 13.4 | 23.3 | 16.9 |
| Refs. [180, 181] (powder) | 12.9 | 27.6 | 49.5 |
| Ref. [182] (powder) | 18.7 | 23.0 | – |
| Ref. [183] (powder) | 17.4 | 32.3 | – |

$$\gamma^r_{\mathbf{q},} = -\frac{\partial(\log \omega_{\mathbf{q}s})}{\partial(\log r)}. \tag{4.10}$$

Finally, for comparison with experiment, we transformed the obtained expressions into the coordinate system of the non-primitive pseudo-cubic lattice vectors where the lattice constant is given as $A = a(3 - 2\cos\phi)^{1/2}$, the angle between lattice vectors is $\cos\Phi = (2\cos\phi - 1)/(3 - 2\cos\phi)$, and the Te position along the [111] direction is $R = 0.25 - r/2$. The comparison of our computed thermal expansion coefficients for $A$, $\Phi$ and $R$ of GeTe at 300 K with the experimental values [179, 180, 181, 182, 183] is given in Table 4.1. We extracted the experimental coefficients by linearly fitting the reported lattice parameters between $\sim$ 300 K and $\sim 400-550$ K. Our computed thermal expansion coefficients are in reasonable agreement with experiments. We ascribe the discrepancies to our zero temperature representation of structural parameters and IFCs and the quasiharmonic approximation, as well as the uncertainties in fitting the sparse experimental data.

For PbTe, our calculated $\kappa_{\text{latt}}$ is $\sim$20% larger than the $\kappa_{\text{latt}}$ of undoped single- and poly-crystalline PbTe for $100 - 300$ K [154], see Fig. 4.6. For higher temperatures of $300 - 700$ K, we see very good agreement between our calculated $\kappa_{\text{latt}}$ and experiment [155]. We note that our $\kappa_{\text{latt}}$ calculated with a 128 atom supercell also agrees to within $\sim$7% of the value calculated on a 216 atom supercell with a cutoff of 8 nearest neighbours for anharmonic IFCs.

GeTe has a large electronic contribution to the total thermal conductivity. Nath *et al.* [184] and Levin *et al.* [182] estimated the lattice contribution by subtracting the electrical contribution from the measured total thermal conductivity

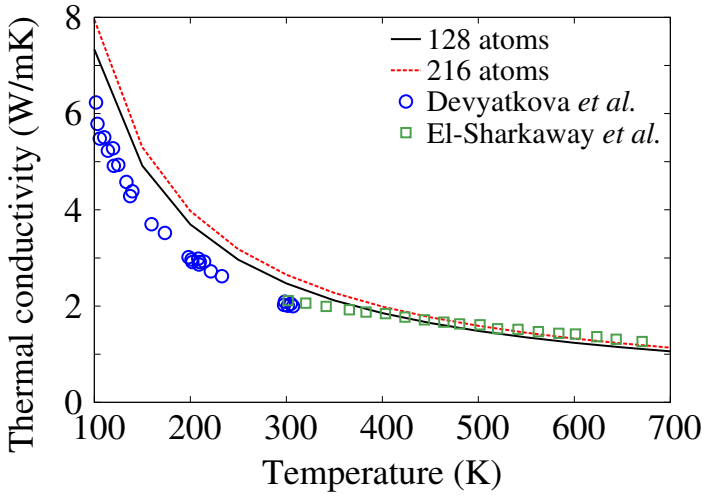



Figure 4.6: Lattice thermal conductivity of PbTe as a function of temperature: calculated using a supercell with 128 atoms (solid black line), calculated using a supercell with 216 atoms (dashed red line), measured by Devyatkova *et al.* [154] (blue circles), and measured by El-Sharkawy *et al.* [155] (green squares).

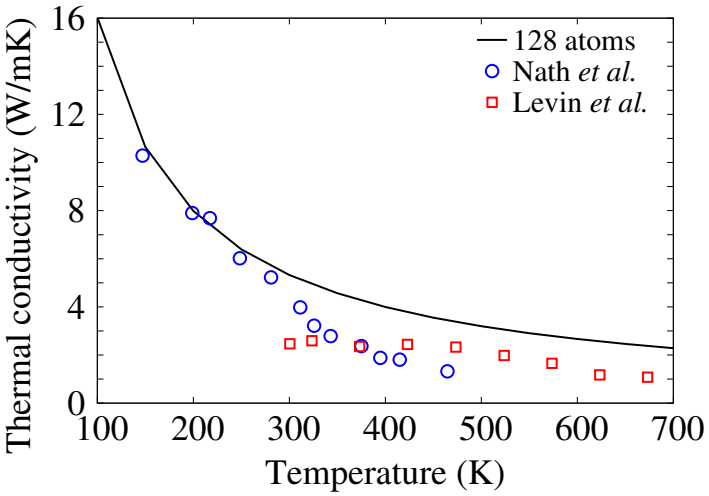



Figure 4.7: Lattice thermal conductivity of GeTe as a function of temperature: calculated using a 128 atom supercell (solid black line), measured by Nath *et al.* [184] (blue circles), and measured by Levin *et al.* [182] (red squares).

using the Wiedemann-Franz law. Within a temperature range of $100-300$ K, our computed $\kappa_{\text{latt}}$ is in very good agreement with that of a 9000 Å GeTe film with a hole concentration of $\sim 10^{20}$ cm$^{-3}$ measured using a transient technique [184], see Fig. 4.7. However, for $300-500K$ the $\kappa_{\text{latt}}$ of the same GeTe film measured using a steady-state technique [184] is a factor of $\sim 2$ lower than our calculated $\kappa_{\text{latt}}$. This factor of $\sim 2$ difference is also seen for the $\kappa_{\text{latt}}$ of GeTe with a hole concentration of $\sim 8\times10^{20}$ cm$^{-3}$ measured with the flash thermal diffusivity method [182] for

300 − 700 K. However, our model does not capture the phase transition in GeTe from the rhombohedral to rocksalt phases at ∼670 K [157, 182] due to the zero temperature representation of structural parameters and IFCs. Thus, we would expect some disagreement between our calculations and the experimental data at higher temperatures.

## 4.2 $Pb_{1-x}Ge_xTe$ and the ferroelectric phase transition

### 4.2.1 Virtual crystal model

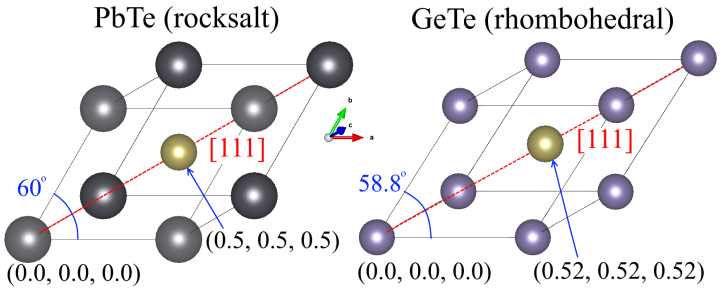



Figure 4.8: The rocksalt and rhombohedral structures of PbTe and GeTe, respectively. The differences between the two structures are the position of Te atom along the trigonal [111] axis and the angle between the primitive lattice vectors. The rocksalt phase is a special case of the rhombohedral phase with the relative Te position of $(0.5, 0.5, 0.5)$ within the primitive cell, and the angle of 60°.

PbTe crystallizes in the rocksalt structure, while GeTe forms a rhombohedral structure, shown in Fig. 4.8. The relative positions of Pb and Te atoms within the rocksalt primitive cell are $(0, 0, 0)$ and $(0.5, 0.5, 0.5)$, and the angle between the lattice vectors is $\phi = 60°$. In the rhombohedral lattice, the relative position of the second atom is $(0.5 + r, 0.5 + r, 0.5 + r)$, and the angle is $\phi = 60° - \theta$. Consequently, the rhombohedral lattice has a trigonal symmetry with respect to the [111] direction. In GeTe, the relative Te position is $(0.52, 0.52, 0.52)$, and the angle is $\phi = 58.8°$ [185, 186]. Thus, the rocksalt phase is a special case of the rhombohedral phase with $r = 0$ and $\theta = 0°$. By varying the alloy composition, $Pb_xGe_{1-x}Te$ alloys will undergo a second order phase transition between the rocksalt and rhombohedral phases. A typical feature of the second order phase transition is a continuous change of the values of various physical quantities at the phase transition.

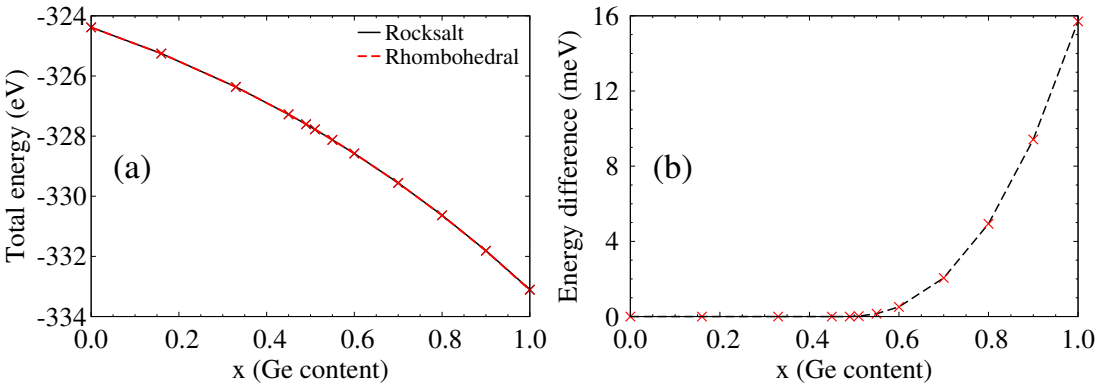



Figure 4.9: (a) Total energy of the rocksalt and rhombohedral phases of $Pb_xGe_{1-x}Te$ as a function of the alloy composition $x$. (b) Difference between the total energy of the rocksalt and rhombohedral phases as a function of $x$. The rocksalt structure is a special case of the rhombohedral structure, and they are identical for $x < 0.492$.

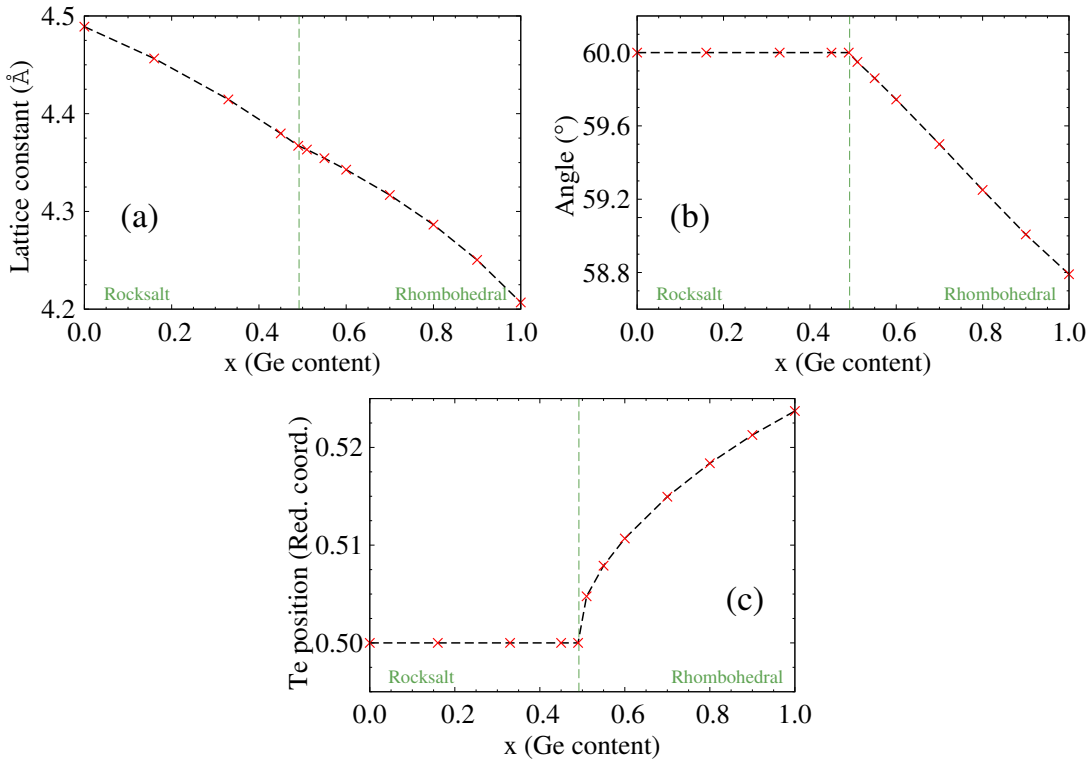



Figure 4.10: Calculated structural parameters as a function of $Pb_{1-x}Ge_xTe$ alloy composition: (a) lattice constant, (b) rhombohedral angle, and (c) sublattice position in the crystal lattice coordinates.

The total energy of both the rocksalt and rhombohedral phases of $Pb_xGe_{1-x}Te$ alloys versus Ge concentration, as well as their energy difference, are illustrated in Fig. 4.9. The two curves coincide for $x < 0.492$ since the rocksalt phase is a special

case of the rhombohedral phase with the relative Te position of $(0.5, 0.5, 0.5)$ within the primitive unit cell, and the angle between the primitive lattice vectors of 60°. Consequently, the relaxation of the rhombohedral structure for $x < 0.492$ results in the rocksalt structure, which is consistent with the second order phase transition. For $x > 0.492$, the rhombohedral phase has a lower total energy than the rocksalt phase, and is thus energetically preferable. The phase transition thus takes place at $x = 0.492$.

The calculated structural parameters of $Pb_{1-x}Ge_xTe$ alloys using the virtual crystal approximation are shown in Fig. 4.10 as a function of chemical composition. The lattice constant, the angle between the primitive lattice vectors, and the Te position along the [111] direction all vary continuously as a function of the alloy composition, as expected for the second-order phase transition. Te displacement changes most rapidly with the alloy composition, indicating that it is the primary order parameter for this phase transition. We note that the displacement of the Te atom along the [111] direction corresponds to the TO mode [146].

### 4.2.2 Impact on phonon frequencies

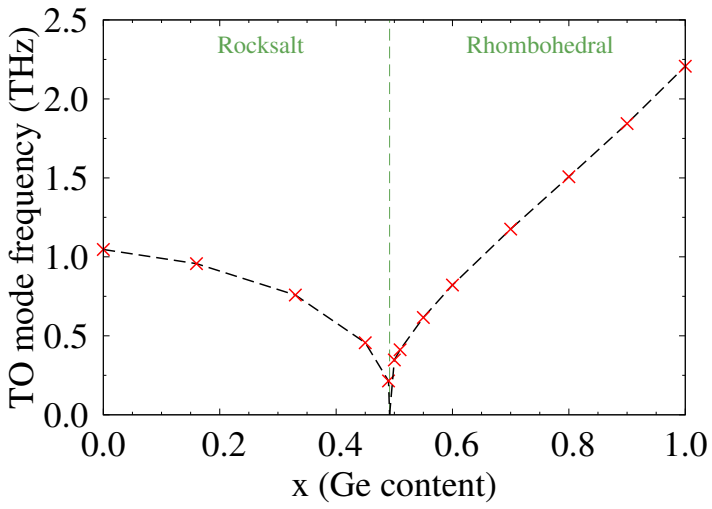



Figure 4.11: The frequency of the lowest transverse optical mode at the zone centre, TO(Γ), as a function of $Pb_{1-x}Ge_xTe$ alloy composition.

We illustrate the alloy composition at which the phase transition occurs for $Pb_{1-x}Ge_xTe$ alloys within our model by plotting the frequency of the lowest transverse optical mode at Γ, TO(Γ), as a function of $x$, see Fig. 4.11. The phase transition takes place for $x = 0.492$, when the frequency of TO(Γ) becomes

≈0 THz. For $0 \leq x < 0.492$ where the rocksalt structure is energetically preferable, the TO(Γ) frequency decreases smoothly with increasing $x$, from ∼1.0 THz in PbTe to ∼0.2 THz for $x = 0.49$. For $0.492 < x \leq 1$, where the rhombohedral structure is favourable, the TO(Γ) frequency decreases almost linearly with decreasing $x$, from ∼2.0 THz in GeTe to ∼0.4 THz at $x = 0.51$. We note that since the transition temperature of $Pb_{0.5}Ge_{0.5}Te$ is ∼450 K [157], our model best describes the soft TO modes and $\kappa_{\text{latt}}$ of $Pb_{1-x}Ge_xTe$ alloys near this temperature.

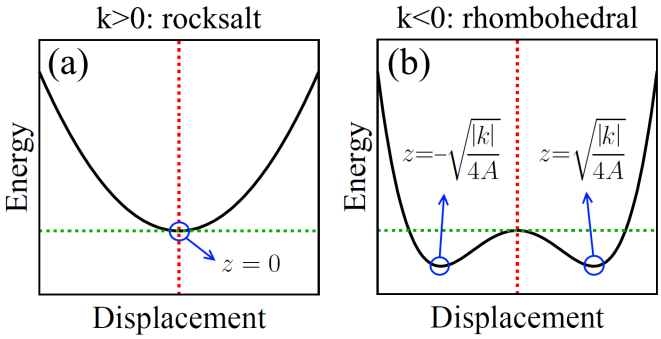



Figure 4.12: Cartoon of the total energy versus Te atomic displacement from its equilibrium position in the rocksalt structure along the [111] direction for: (a) the rocksalt phase, and (b) the rhombohedral phase.

In the immediate vicinity of the structural transition, the TO(Γ) frequency is higher in the rhombohedral phase compared to the rocksalt phase by a factor of $\sim \sqrt{2}$ (for $x = 0.491$ and $x = 0.493$, respectively, see Fig. 4.11). To explain this factor analytically, we examine the total energy of the atomic motion of the TO mode in $Pb_{1-x}Ge_xTe$ virtual alloys, which can be represented by the displacement of the Te atom from its equilibrium position in the rocksalt structure along the [111] direction.

We assume that the energy potential of such Te motion is of the form:

$$V(z) = \frac{1}{2}kz^2 + Az^4, \tag{4.11}$$

where $k$ and $A$ are the harmonic and quartic spring constants, respectively. Near the phase transition, we assume that the small harmonic spring constant $k$ changes its sign from positive to negative, keeping the same absolute value. This physically corresponds to changing the sign of a small restoring force which keeps atoms in one phase when positive, and causes the transition into a different phase when negative. We assume that the anharmonic spring constant $A$ is positive and does not change in this process.

We find the potential extrema from:

$$\frac{\partial V}{\partial z} = kz + 4Az^3 = 0, \tag{4.12}$$

which gives

$$z = 0 \quad \text{or} \quad z = \pm i\sqrt{\frac{k}{4A}}. \tag{4.13}$$

For $k > 0$, $z = 0$ is the only real minimum, which physically corresponds to the high-symmetry rocksalt phase (see Fig. 4.12 (a)). For $k < 0$, $z = 0$ is a local maximum, and the minima occur for $z = \pm(|k|/(4A))^{1/2}$, which correspond to the frozen-in displacement of the Te atom in the [111] direction and the distorted rhombohedral structure, shown in Fig. 4.12 (b).

Since the curvature of the potential varies as the square of the frequency ($\partial^2 V/\partial z^2 \sim \omega^2$), we find its values at the potential minima for the rocksalt phase at $z = 0$ and for the rhombohedral phase at $z = \pm(|k|/(4A))^{1/2}$:

$$\left.\frac{\partial^2 V}{\partial z^2}\right|_{z=0} = |k|, \quad k > 0; \tag{4.14}$$

$$\left.\frac{\partial^2 V}{\partial z^2}\right|_{z=\pm\sqrt{\frac{|k|}{4A}}} = 2|k|, \quad k < 0. \tag{4.15}$$

With $\partial^2 V/\partial z^2 \sim \omega_{\mathrm{TO}}^2$, we finally obtain:

$$\frac{\omega_{\mathrm{TO}}(x = 0.493)}{\omega_{\mathrm{TO}}(x = 0.491)} \sim \sqrt{2}. \tag{4.16}$$

Thus, the frequency of the TO mode at Γ differs by a factor $\sim \sqrt{2}$ between the rhombohedral $Pb_{1-x}Ge_xTe$ alloy very near the phase transition, $x = 0.493$, and its rocksalt counterpart, $x = 0.491$.

In addition to dramatic softening of TO(Γ) modes, we illustrate the full impact of increased proximity to the phase transition on the phonon dispersions of $Pb_{1-x}Ge_xTe$ alloys. Fig. 4.13 compares the phonon dispersions of two structures in the rhombohedral phase, GeTe and a composition on the verge of the phase transition, $Pb_{0.49}Ge_{0.51}Te$. Similarly, in the rocksalt phase we compare PbTe and $Pb_{0.51}Ge_{0.49}Te$, see Fig. 4.14. Away from the zone centre, phonon frequencies become significantly lower as the value of $x$ decreases in both the rocksalt and rhombohedral phases. This change in phonon frequency is largely due to the heavier mass as the alloy composition varies from GeTe to PbTe. At the phase transition, the phonon dispersions of the rocksalt and rhombohedral structures

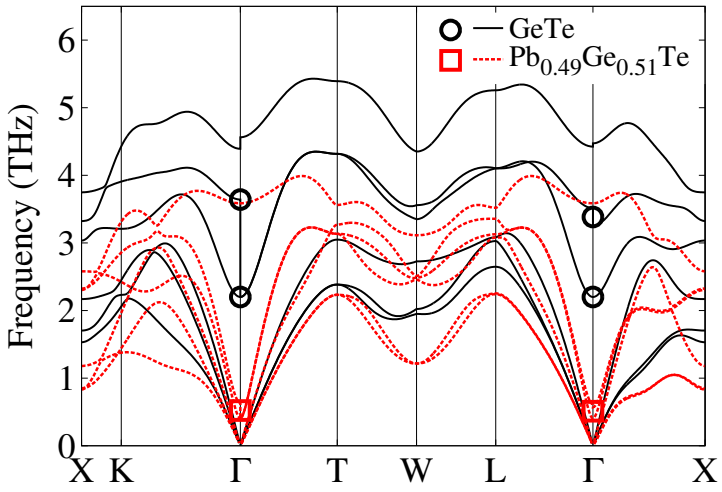



Figure 4.13: Phonon band structures at 0 K for GeTe (solid black line) and an alloy in the rhombohedral structure near the phase transition, $Pb_{0.49}Ge_{0.51}Te$ (dashed red line). The frequencies of the soft transverse optical phonon modes at the zone centre, TO(Γ), are highlighted in black circles for GeTe and red rectangles for $Pb_{0.49}Ge_{0.51}Te$.

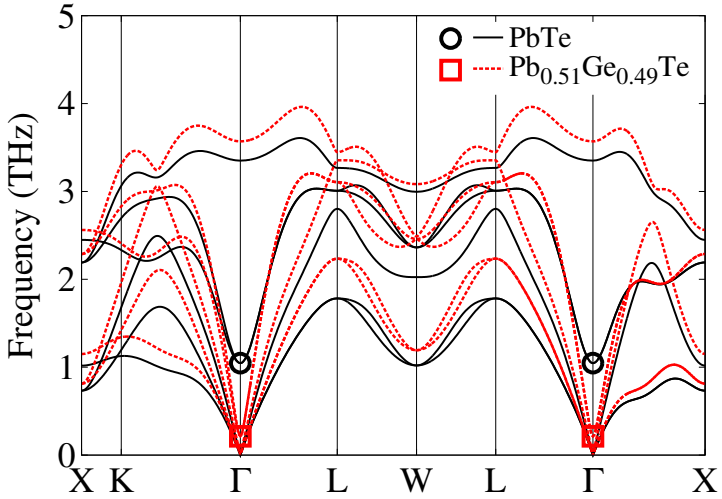



Figure 4.14: Phonon band structures at 0 K for PbTe (solid black line) and an alloy in the rocksalt structure near the phase transition, $Pb_{0.51}Ge_{0.49}Te$ (dashed red line). The frequencies of the soft transverse optical phonon modes at the zone centre, TO(Γ), are highlighted in black circles for PbTe and red rectangles for $Pb_{0.51}Ge_{0.49}Te$.

are remarkably similar, see Fig. 4.15. This is due to the fact that the soft optical mode phase transition in $Pb_{1-x}Ge_xTe$ alloys is second-order, which can also be seen from the continuous change in lattice parameters as a function of $x$ as shown previously.

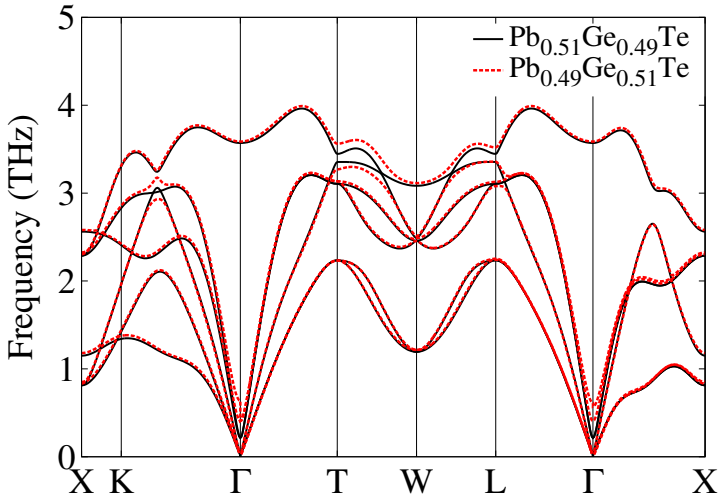



Figure 4.15: Phonon band structures at 0 K for alloy compositions in the rocksalt and rhombohedral phases near the phase transition: $Pb_{0.51}Ge_{0.49}Te$ (solid black line) and $Pb_{0.49}Ge_{0.51}Te$ (dashed red line), respectively.

## 4.3 Impact on phonon lifetimes

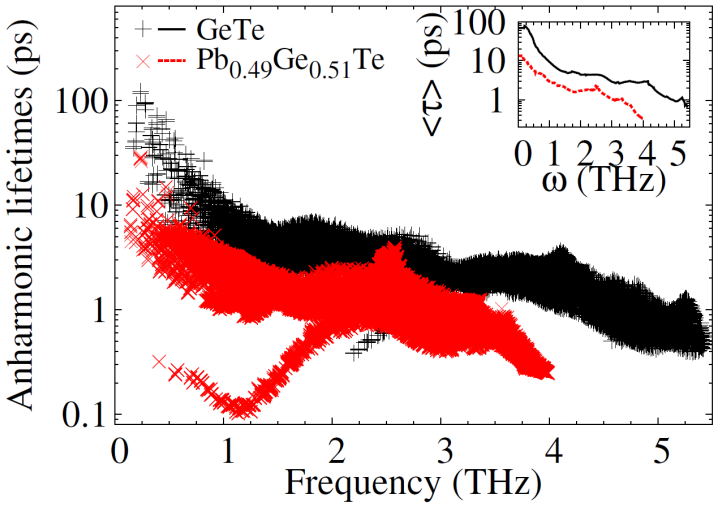



Figure 4.16: Anharmonic phonon lifetimes at 450 K and their averaged values (inset) as a function of frequency for GeTe (black pluses and solid line) and a rhombohedral alloy near the phase transition, $Pb_{0.49}Ge_{0.51}Te$ (red crosses and dashed line).

The extremely soft TO modes at the ferroelectric phase transition minimize the anharmonic phonon lifetimes of $Pb_{1-x}Ge_xTe$ alloys in both the rocksalt and rhombohedral phases. In the rhombohedral phase, three-phonon lifetimes are reduced by a factor of ~2 in $Pb_{0.49}Ge_{0.51}Te$ compared to GeTe at 450 K (Fig. 4.16). This reduction is maintained across the entire frequency spectrum, which is more

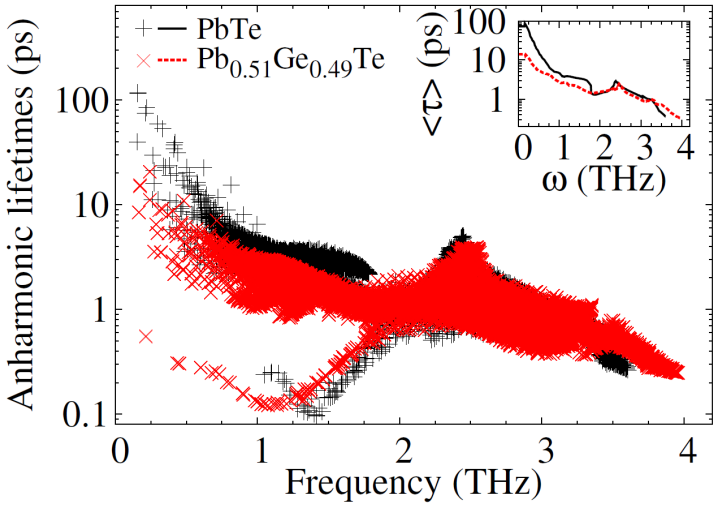



Figure 4.17: Anharmonic phonon lifetimes at 450 K and their averaged values (inset) as a function of frequency for PbTe (black pluses and solid line) and a rocksalt alloy near the phase transition, $Pb_{0.51}Ge_{0.49}Te$ (red crosses and dashed line).

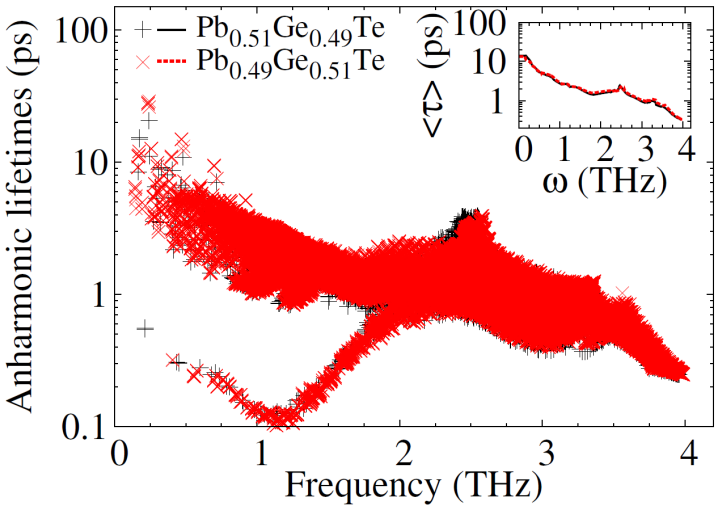



Figure 4.18: Anharmonic phonon lifetimes at 450 K and their averaged values (inset) as a function of frequency for rocksalt $Pb_{0.51}Ge_{0.49}Te$ (black pluses and solid line) and rhombohedral $Pb_{0.49}Ge_{0.51}Te$ (red crosses and dashed line).

clearly shown in the inset of Fig. 4.16 where averaged anharmonic lifetimes are plotted versus frequency. In the rocksalt phase, anharmonic $\tau$ are also minimized at the phase transition, as illustrated by their comparison for $Pb_{0.51}Ge_{0.49}Te$ and PbTe in Fig. 4.17. However, in this case the reduction is mainly concentrated to lower frequencies. The significant decrease of $\tau_{\text{anh}}$ at the phase transition offers new alternatives in the search for techniques to suppress lifetimes across the frequency spectrum. Furthermore, the $\tau_{\text{anh}}$ of the rocksalt and rhombohedral

structures in the vicinity of the phase transition are very similar (Fig. 4.18). This similarity is a direct result of the second-order phase transition, and results in the continuous change of $\tau_{\text{anh}}$ as the alloy composition is varied.

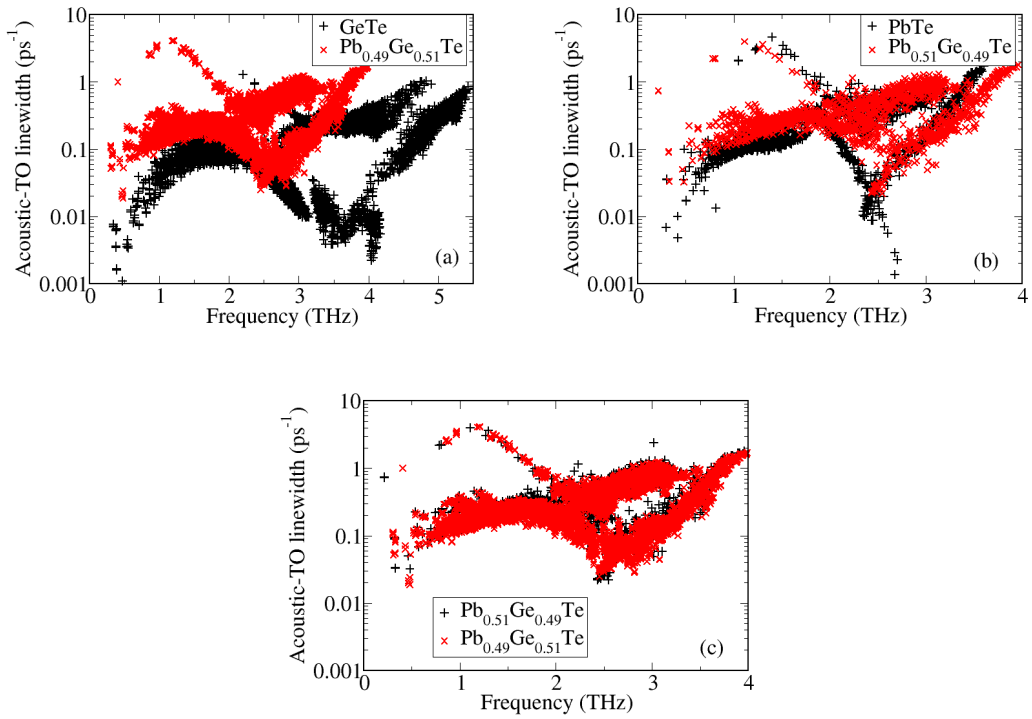



Figure 4.19: The acoustic-transverse optical (TO) contribution to the total anharmonic linewidth at 300 K versus frequency for (a) GeTe (black pluses) and a rhombohedral alloy near the phase transition, $Pb_{0.49}Ge_{0.51}Te$ (red crosses), (b) PbTe (black pluses) and a rocksalt alloy near the phase transition, $Pb_{0.51}Ge_{0.49}Te$ (red crosses), and (c) rocksalt $Pb_{0.51}Ge_{0.49}Te$ (black pluses) and rhombohedral $Pb_{0.49}Ge_{0.51}Te$ (red crosses).

To understand how the acoustic-TO anharmonic interaction changes with increased proximity to the phase transition, we calculated explicitly the acoustic-TO contribution to the total anharmonic linewidth in PbTe, $Pb_{0.51}Ge_{0.49}Te$, $Pb_{0.49}Ge_{0.51}Te$ and GeTe at 300 K, see Fig. 4.19, following the same procedure as described in the previous chapter. We found that the acoustic-TO contribution to the anharmonic linewidth dominates over the other contributions across the spectrum in all these materials. Further, the maximal softening of the TO mode at the zone centre is directly responsible for the maximal strength of the anharmonic coupling of TO modes with heat-carrying acoustic modes and the minimisation of anharmonic lifetimes at the phase transition. In the rhombohedral phase, this contribution becomes maximal at the phase transition as illustrated in

Fig. 4.19 (a) by comparing GeTe and an alloy composition very near the phase transition, $Pb_{0.49}Ge_{0.51}Te$. This is also the case for the rocksalt phase, as shown in Fig. 4.19 (b) by comparing PbTe and $Pb_{0.51}Ge_{0.49}Te$. The strength of the acoustic-TO contribution to the anharmonic linewidth is very similar for the two structures very close to the phase transition, see Fig. 4.19 (c), which is a typical feature of the second-order phase transition.

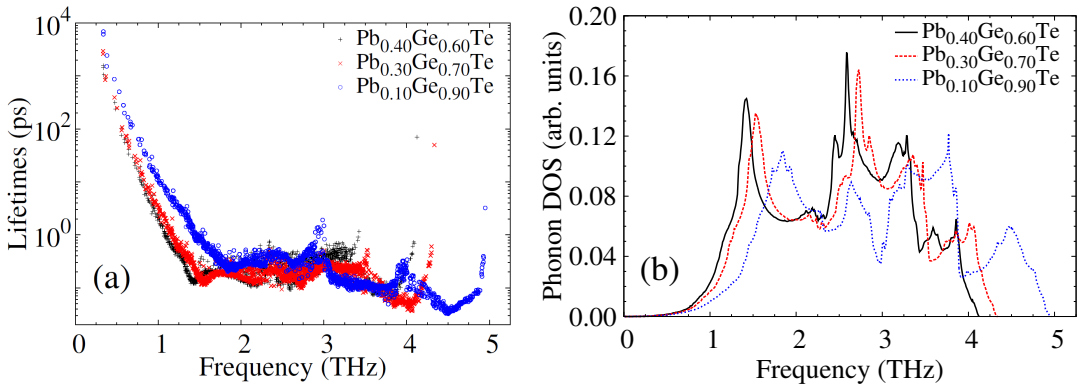



Figure 4.20: (a) Phonon lifetimes due to mass disorder versus frequency for three select compositions: $Pb_{0.40}Ge_{0.60}Te$ (black pluses), $Pb_{0.30}Ge_{0.70}Te$ (red crosses), and $Pb_{0.10}Ge_{0.90}Te$ (blue circles). (b) Calculated phonon density of states for $Pb_{0.40}Ge_{0.60}Te$ (solid black line), $Pb_{0.30}Ge_{0.70}Te$ (dashed red line), and $Pb_{0.10}Ge_{0.90}Te$ (dotted blue line). The integral of the density of states over frequency is normalized to unity.

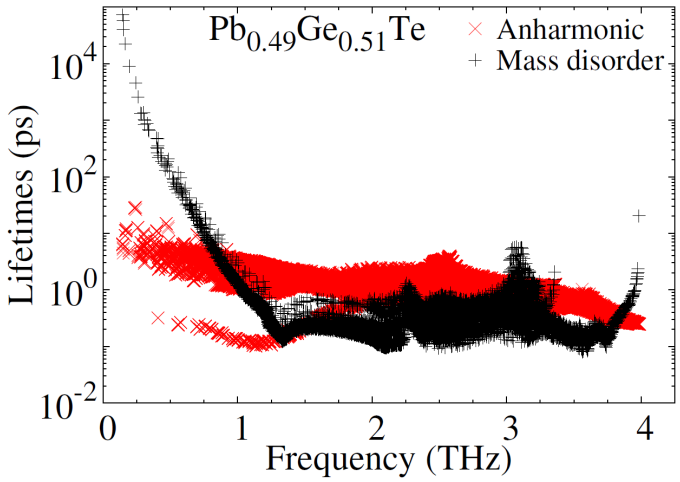



Figure 4.21: Phonon lifetimes due to anharmonic processes (black crosses) and mass disorder (red pluses) as a function of frequency for $Pb_{0.49}Ge_{0.51}Te$.

The effect of mass disorder on phonon lifetimes in $Pb_{1-x}Ge_xTe$ alloys is strongest for $x \approx 0.6$. The strength of mass disorder is given as $g = \sum_i f_i(1 -$

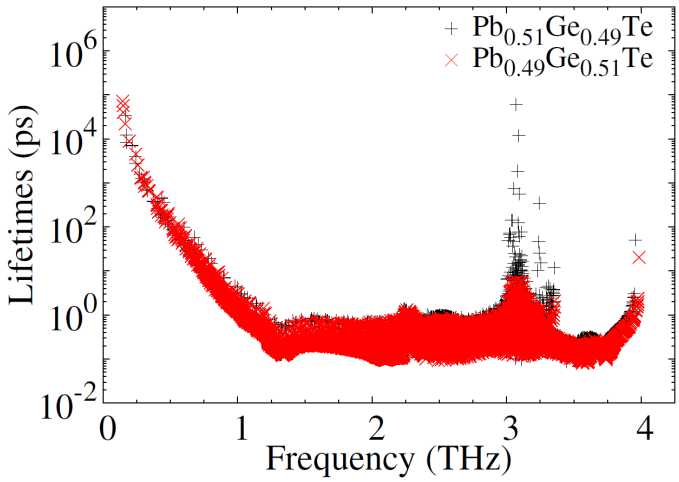



Figure 4.22: Phonon lifetimes due to mass disorder versus frequency for the rocksalt and rhombohedral structures very near the phase transition: $Pb_{0.51}Ge_{0.49}Te$ (black pluses) and $Pb_{0.49}Ge_{0.51}Te$ (red crosses), respectively.

$m_i/\bar{m})^2$ (Eq. (2.98)) where $f_i$ and $m_i$ are the concentration and atomic mass of species $i$, and $\bar{m}$ is its average mass [64, 126, 127, 149]. It can be derived analytically that $g$ reaches a maximum for $x = m_{\mathrm{Pb}}/(m_{\mathrm{Ge}} + m_{\mathrm{Pb}}) = 0.74$. Nevertheless, the larger density of states for compositions with smaller Ge content shifts the composition at which the overall scattering due to mass disorder is strongest to $x \approx 0.6$, see Fig. 4.20. Mass disorder is more effective at scattering mid- and high-frequency phonons in comparison to anharmonic processes. However, at low frequencies, anharmonic $\tau$ are smaller than those due to mass disorder by several orders of magnitude (see Fig. 4.21). This highlights the effectiveness of the strategy of combining soft modes and alloying to design materials with low thermal conductivity. Furthermore, the lifetimes due to mass disorder of the structures on the verge of the phase transition are very similar as a result of the second-order nature of the phase transition, see Fig. 4.22.

## 4.4 Impact on thermal conductivity

### 4.4.1 $Pb_{1-x}Ge_xTe$ alloys

The ferroelectric phase transition minimizes the anharmonic contribution to the lattice thermal conductivity of $Pb_{1-x}Ge_xTe$ alloys in both the rocksalt and rhombohedral phases. This is shown by the unfilled symbols in Fig. 4.23, which represents the anharmonic $\kappa_{\mathrm{latt}}$ as a function of $x$ at 450 K. In the rhombohedral

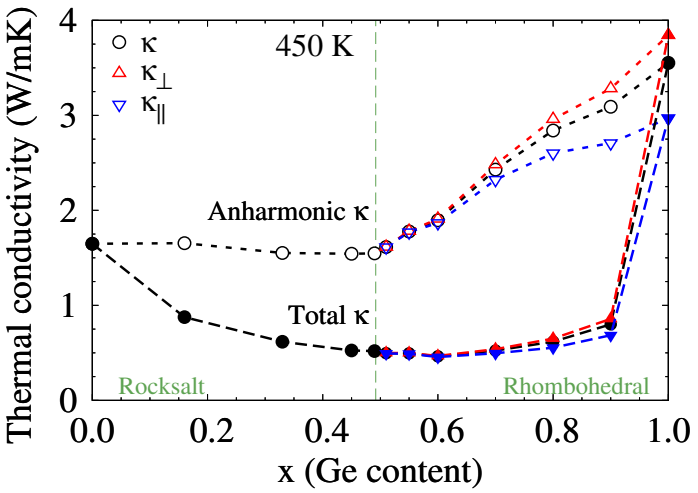



Figure 4.23: Lattice thermal conductivity of $Pb_{1-x}Ge_xTe$ as a function of alloy composition at 450 K. The unfilled symbols show the thermal conductivity due to anharmonic (three-phonon) processes only, and the filled symbols show the thermal conductivity due to anharmonic processes and mass disorder. Black circles show the thermal conductivity in the rocksalt phase and its isotropic average in the rhombohedral phase. Red up and blue down triangles show the thermal conductivity perpendicular and parallel to the trigonal [111] axis in the rhombohedral phase, respectively.

phase, the anharmonic $\kappa_{\text{latt}}$ of the composition very near the phase transition, $x = 0.51$, decreases by a factor of $\sim 2.4$ ($\sim 1.8$) in the direction perpendicular (parallel) to the trigonal [111] axis with respect to GeTe. These reductions are a direct result of the substantial decrease in the anharmonic $\tau$ of $Pb_{0.49}Ge_{0.51}Te$ (see Fig. 4.16), and are further enhanced by its lower group velocities due to the heavier average atomic mass. The anisotropy in the anharmonic $\kappa_{\text{latt}}$ of the rhombohedral structures decreases from $\sim 29\%$ in GeTe towards zero at the phase transition. In the rocksalt phase, the anharmonic $\kappa_{\text{latt}}$ initially slightly increases for low values of $x$, and then decreases as $x$ becomes larger. This effect is due to the larger group velocities competing with the reduced phonon lifetimes as the proximity to the phase transition is increased with $x$. Overall, there is a modest reduction by a factor of $\sim$1.05 in the anharmonic $\kappa_{\text{latt}}$ at $x = 0.49$ with respect to that of PbTe. This results in the asymmetric reductions of the anharmonic $\kappa_{\text{latt}}$ for the rocksalt and rhombohedral phases (see Fig. 4.23). Importantly, the anharmonic $\kappa_{\text{latt}}$ changes continuously as the alloy undergoes the second-order phase transition as a result of the continuous variation of phonon lifetimes and group velocities.

Neglecting the average mass difference among $Pb_{1-x}Ge_xTe$ compositions re-

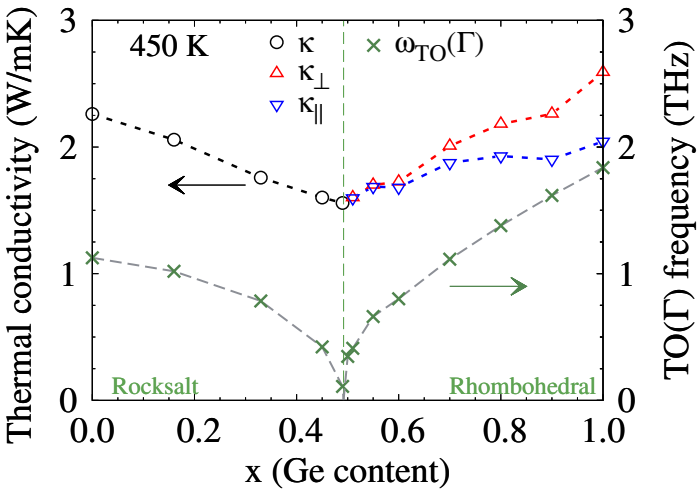



Figure 4.24: Anharmonic contribution to the lattice thermal conductivity of $Pb_{1-x}Ge_xTe$ as a function of the alloy composition at 450 K, where the group IV element mass of each alloy composition is artificially set to that of $Pb_{0.5}Ge_{0.5}Te$. Black circles show the thermal conductivity in the rocksalt phase, while red up and blue down triangles show the thermal conductivity perpendicular and parallel to the trigonal [111] axis in the rhombohedral phase, respectively. Also shown in green crosses is the frequency of the lowest transverse optical mode at the zone centre for the same mass of the group IV element as described above.

moves the asymmetric reductions in the anharmonic lattice thermal conductivity for the two phases, and further highlights its minimisation at the phase transition. This is illustrated in Fig. 4.24, where the mass difference is ignored by artificially setting the group IV element mass of each alloy composition to that of $Pb_{0.5}Ge_{0.5}Te$. The anharmonic $\kappa_{\text{latt}}$ decreases smoothly with increased proximity to the phase transition mostly due to reduced anharmonic $\tau$, which results in a factor of $\sim$1.5 reduction in both the rocksalt and rhombohedral phases with respect to $x = 0$ and $x = 1$. Therefore, the minimisation of anharmonic $\kappa_{\text{latt}}$ at the phase transition would be more pronounced for alloys with soft optical modes whose overall mass difference is smaller than that of $Pb_{1-x}Ge_xTe$ alloys, or for bulk materials driven to the phase transition via pressure or strain, as discussed in the previous chapter. However, the $\kappa_{\text{latt}}$ of such materials may not be as low as reported here since mass disorder would be irrelevant or weaker than in $Pb_{1-x}Ge_xTe$.

Mass disorder significantly reduces the lattice thermal conductivity of $Pb_{1-x}Ge_xTe$ alloys, thereby flattening the dip in its anharmonic contribution and shifting the minimum away from the phase transition (Fig. 4.23). The minimal $\kappa_{\text{latt}}$ occurs at $x \approx 0.6$ in our model where the scattering due to mass disorder is

maximized, and near the composition where the phase transition occurs ($x = 0.5$). Our results illustrate a general trend that the minimal $\kappa_{\text{latt}}$ in alloys with soft optical modes will be determined by the interplay among anharmonicity, average mass and mass disorder, and it will not necessarily occur at the phase transition. We find factors of ∼7.7 and ∼3.6 reduction in the isotropically averaged $\kappa_{\text{latt}}$ at its minimal value at 450 K with respect to GeTe and PbTe respectively. Interestingly, for the alloy composition of $x = 0.9$, scattering due to mass disorder is relatively strong at high frequencies due to the high density of states (see Fig. 4.20) resulting in the $\kappa_{\text{latt}}$ value which is comparable to the $\kappa_{\text{latt}}$ minimum at $x \approx 0.6$. We note that disorder in the force constants would further suppress the lattice thermal conductivity values reported here [152].

### 4.4.2 Frequency contribution to thermal conductivity

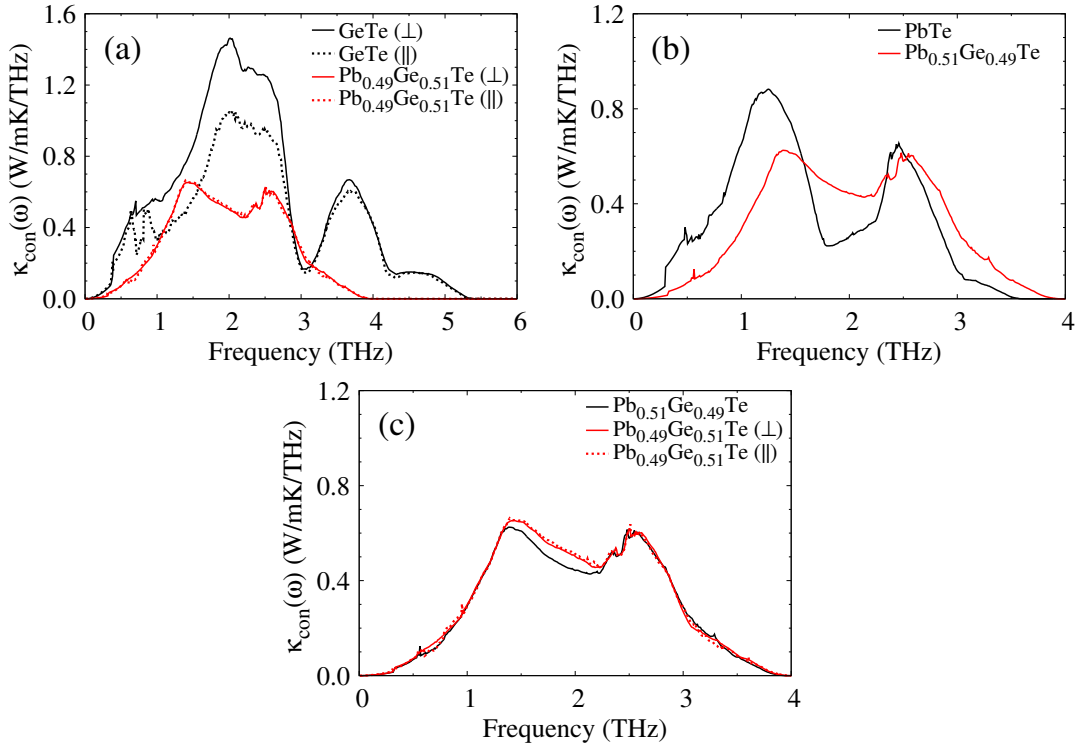



Figure 4.25: The contribution to the anharmonic lattice thermal conductivity $\kappa_{\text{con}}(\omega)$ at 450 K as a function of phonon frequency. $\kappa_{\text{con}}(\omega)$ is shown for (a) GeTe parallel and perpendicular to the trigonal axis (dotted and solid black lines) and $Pb_{0.49}Ge_{0.51}Te$ parallel and perpendicular to the trigonal axis (dotted and solid red lines), (b) PbTe (solid black line) and $Pb_{0.51}Ge_{0.49}Te$ (solid red line), (c) $Pb_{0.51}Ge_{0.49}Te$ (solid black line) and $Pb_{0.49}Ge_{0.51}Te$ parallel and perpendicular to the trigonal axis (dotted and solid red lines).

In this section we investigate the contribution to the anharmonic lattice thermal conductivity as a function of phonon frequency, $\kappa_{\rm con}(\omega)$, in $Pb_{1-x}Ge_xTe$ alloys. We define this contribution as:

$$\kappa_{\rm con}(\omega) = \frac{1}{N_{\mathbf{q}}\Omega}\sum_{\mathbf{q}s} c_{\mathbf{q}s} v^2_{\mathbf{q}s} \tau_{\mathbf{q}s} \delta(\omega - \omega_{\mathbf{q}s}), \tag{4.17}$$

where the anharmonic lattice thermal conductivity is then given as $\kappa_{\rm latt} = \int \kappa_{\rm con}(\omega) d\omega$.

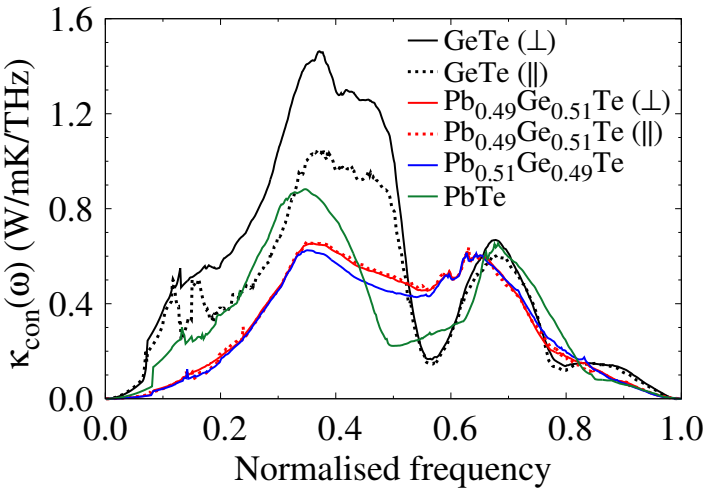



Figure 4.26: The contribution to the anharmonic lattice thermal conductivity $\kappa_{\rm con}(\omega)$ at 450 K as a function of normalised phonon frequency for GeTe parallel and perpendicular to the trigonal axis (dotted and solid black lines), $Pb_{0.49}Ge_{0.51}Te$ parallel and perpendicular to the trigonal axis (dotted and solid red lines), $Pb_{0.51}Ge_{0.49}Te$ (solid blue line), and PbTe (solid green line).

The contribution to the anharmonic lattice thermal conductivity from low-frequency ($\lesssim$ 1.5 THz) phonons is minimised at the phase transition in $Pb_{1-x}Ge_xTe$ alloys, see Fig. 4.25(a-c). Fig. 4.25(a) compares $\kappa_{\rm con}(\omega)$ of GeTe and the composition $x = 0.51$ very near the phase transition in the rhombohedral phase, while Fig. 4.25(b) compares $\kappa_{\rm con}(\omega)$ of PbTe and the composition $x = 0.49$ in the rocksalt phase. In the rhombohedral phase, $\kappa_{\rm con}(\omega)$ of the composition $x = 0.51$ decreases by a factor of $\sim$3 ($\sim$2) perpendicular (parallel) to the trigonal axis in the low frequency regime compared to GeTe, see Fig. 4.26, which shows $\kappa_{\rm con}(\omega)$ as a function of the phonon frequency normalised such that the highest longitudinal optical mode frequency for each composition is 1 respectively. In the rocksalt phase, $\kappa_{\rm con}(\omega)$ of $x = 0.49$ similarly decreases by a factor of $\sim$2 in comparison to PbTe. The minimisation of $\kappa_{\rm con}(\omega)$ in the low frequency regime follows as a direct result of the maximally softened TO($\Gamma$) frequency at the phase

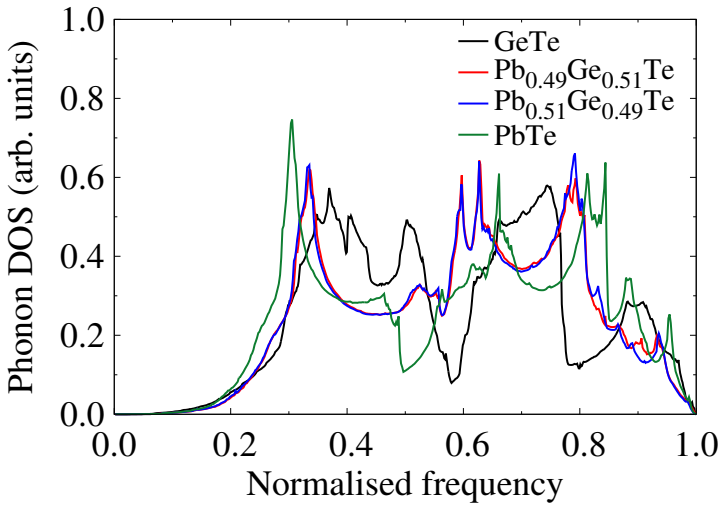



Figure 4.27: Calculated phonon density of states for GeTe (solid black line), $Pb_{0.49}Ge_{0.51}Te$ (solid red line), $Pb_{0.51}Ge_{0.49}Te$ (solid blue line), and PbTe (solid green line).

transition and its maximised anharmonic coupling with heat carrying acoustic mode phonons, as demonstrated previously. The frequency contribution to the anharmonic lattice thermal conductivity of $Pb_{0.49}Ge_{0.51}Te$ and $Pb_{0.51}Ge_{0.49}Te$ is almost identical, see Fig. 4.25(c), due to the continuous change of phonon frequencies at the second order phase transition.

The contribution to the anharmonic lattice thermal conductivity from high frequency phonons is approximately the same for all compositions of $Pb_{1-x}Ge_xTe$ alloys, see Fig. 4.26. This demonstrates that the maximally softened TO($\Gamma$) at the phase transition predominantly reduces the phonon lifetimes of low-frequency phonon modes, leaving higher frequencies relatively unaffected. Interestingly $\kappa_{\mathrm{con}}(\omega)$ due to phonons in the mid-frequency regime ($\sim$0.5 in normalised phonon frequency, see Fig. 4.26) increases with increased proximity to the phase transition. This is due to an increase in the density of states for mid-frequency phonons in those compositions at the phase transition versus those of PbTe and GeTe respectively, see Fig. 4.27.

### 4.4.3 Impact of structure and resonant bonding

If the overall mass difference in $Pb_{1-x}Ge_xTe$ alloys could be ignored, the anharmonic lattice thermal conductivity would be comparably suppressed in the rocksalt and rhombohedral structures with similar proximity to the phase transition. This is shown in Fig. 4.24, where the dependence of the anharmonic $\kappa_{\mathrm{latt}}$ on $x$ is compared with that of the TO($\Gamma$) frequency when the group IV

element mass of each alloy composition is set to that of $Pb_{0.5}Ge_{0.5}Te$. Here we consider the TO($\Gamma$) frequency as a rough measure of the proximity to the phase transition of both rocksalt and rhombohedral phases. The anharmonic $\kappa_{\text{latt}}$ of a rhombohedral structure is comparable to that of the rocksalt structure with a similar TO($\Gamma$) frequency, and it is notably even lower in the direction parallel to the trigonal axis. This is in contrast with the previous reports that high symmetry phases have lower $\kappa_{\text{latt}}$ compared to their lower symmetry counterparts [49, 71, 150]. However, these studies did not attempt to tune the proximity to the phase transition of these materials to fully investigate this effect. Our analysis suggests that the proximity to the phase transition, average atomic mass and mass disorder are more dominant mechanisms for the thermal conductivity reduction in $Pb_{1-x}Ge_xTe$ alloys than the symmetry of the phase.

Our findings are in partial disagreement with the recent claims that stronger resonant bonding leads to lower lattice thermal conductivity in rocksalt IV-VI and rhombohedral group-V materials [150]. Resonant bonding is characterized by half-saturated p-bonds typical for these materials, which results in delocalised electron densities and large electronic polarisabilities [150, 169, 170, 187]. This leads to large values of the harmonic IFCs for the $4^{\text{th}}$ and $8^{\text{th}}$ nearest neighbours (NNs) [150, 188], which correspond to the $2^{\text{nd}}$ and $3^{\text{rd}}$ NNs along the [001] direction in the rocksalt structure, respectively. Such non-monotonically decreasing harmonic IFCs can only be present due to the change in electronic distribution with atomic displacement as per the Hellmann-Feynman theorem [150]. It has been argued that, the larger the magnitude of these long-range IFCs (i.e. the stronger the degree of resonant bonding), the softer the TO mode and lower the $\kappa_{\text{latt}}$ of these materials [150].

The electronic polarisability relates a small external perturbation to the resulting change in electron density [189] and is defined as the dipole moment per unit volume of the crystal cell [16]. The Born effective charge (BEC) tensor relates, at linear order, the macroscopic polarisation $P_{mac}$ per unit cell created along the direction $\beta$ due to a displacement in the direction $\alpha$ of atoms belonging to the sublattice $l$ assuming zero electric field [134]:

$$Z^*_{l,\beta\alpha} = \frac{\Omega}{|e|}\frac{\partial P_{mac,\beta}}{\partial u^l_\alpha(\mathbf{q}=0)}. \tag{4.18}$$

The dielectric permittivity tensor relates $P_{mac}$ and the macroscopic electric field $\epsilon_{mac,\beta}$ in the linear regime. Neglecting the contribution from ionic displacements, we only consider the contribution to the dielectric permittivity tensor from the

electronic polarisation, dubbed the high-frequency dielectric constant [134]:

$$\epsilon_{\infty,\alpha\beta} = \delta_{\alpha\beta} - \frac{4\pi}{\Omega}\frac{\partial^2 E_{el}}{\partial\epsilon^*_\alpha \partial\epsilon_\beta} \tag{4.19}$$

where $E_{el}$ is the total electronic energy of the system, and $\epsilon_\alpha$ and $\epsilon_\beta$ are the electric fields along $\alpha$ and $\beta$ respectively. "High-frequency" in this context means high-frequency with respect to lattice vibrational frequencies, but low compared with atomic excitation frequencies [16]. Thus, the BEC tensor relates the change in polarisation due to lattice displacements, while the high frequency dielectric permittivity tensor relates changes in the polarisation due to changes in the electronic density. Further details of the computation of Born effective charges and dielectric constants from DFPT within the ABINIT code are given in Refs. [134, 135].

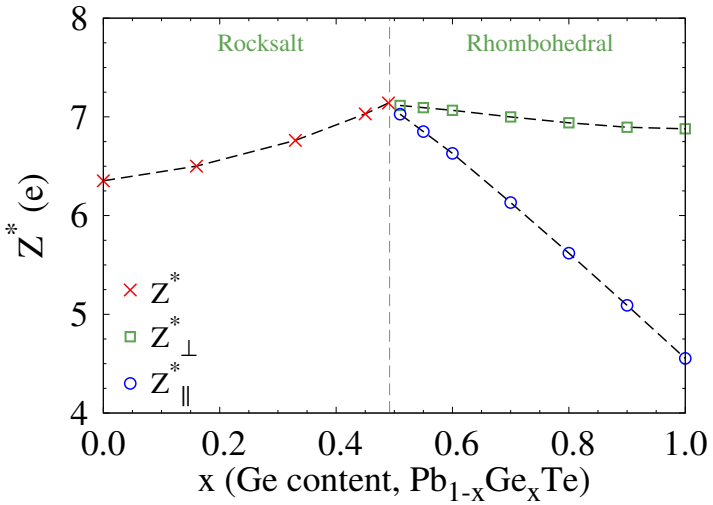



Figure 4.28: Born effective charge as a function of $Pb_{1-x}Ge_xTe$ alloy composition in the rocksalt phase (red crosses), perpendicular to the trigonal [111] axis in the rhombohedral phase (green squares), and parallel to the trigonal axis in the rhombohedral phase (blue circles).

We found that the electronic polarisability of $Pb_{1-x}Ge_xTe$ alloys is indeed maximized at the phase transition, which is indicative of very strong resonant bonding [150, 169, 187]. This is illustrated by plotting BECs as a function of the alloy composition, Fig. 4.28. BECs are typically viewed as an indicator of ferroelectric instability, and have been found to be considerably larger than nominal ionic values in ferroelectric or nearly ferroelectric materials [190, 191, 192]. In the case of $Pb_{1-x}Ge_xTe$ alloys, BECs are more than twice the nominal ionic value of +2 for Pb and Ge, and -2 for Te. As proximity to the phase transition is

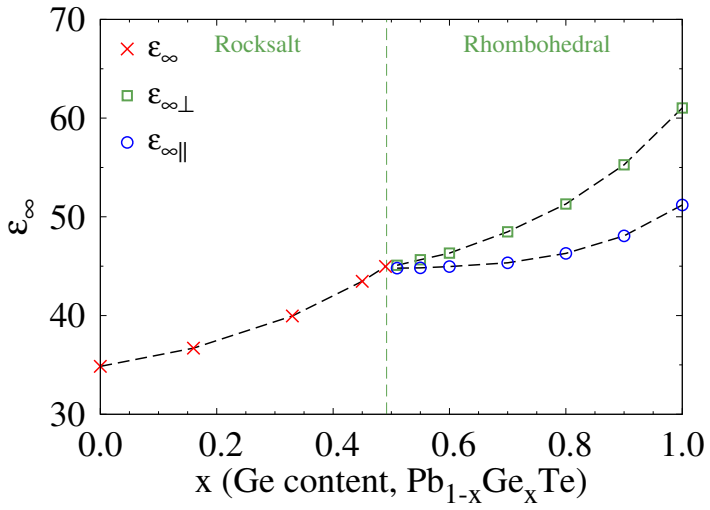



Figure 4.29: High-frequency dielectric constant as a function of $Pb_{1-x}Ge_xTe$ alloy composition in the rocksalt phase (red crosses), perpendicular to the trigonal axis in the rhombohedral phase (green squares), and parallel to the trigonal axis in the rhombohedral phase (blue circles).

increased, there is a considerable increase in BECs, indicative of the increase in electronic polarisability. The high-frequency dielectric constants are also large in $Pb_{1-x}Ge_xTe$ alloys (see Fig. 4.29), further illustrating the large electronic polarisability. The dielectric constants increase substantially, almost doubling in value from PbTe to GeTe, due to their inverse dependence on the average electronic gap [193].

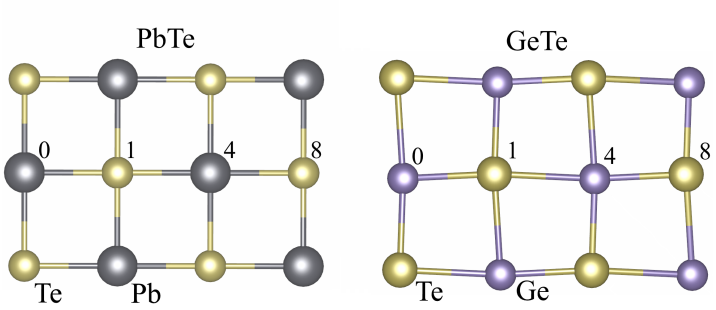



Figure 4.30: Nearest neighbours within the rocksalt structure of PbTe along the [001] direction, and their counterparts for the rhombohedral structure of GeTe.

We also find that long-range harmonic IFCs along the [001] direction are maximized at the phase transition in $Pb_{1-x}Ge_xTe$ alloys where the lattice thermal conductivity is minimized. The traces of the harmonic IFC tensors for several different alloy compositions are shown in Figs. 4.31 and 4.32 for the rhombohedral and rocksalt phases, respectively. In both phases, we see particularly strong IFCs

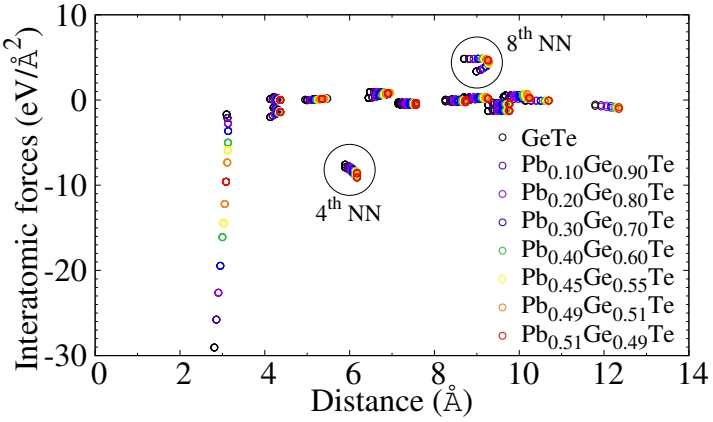



Figure 4.31: The trace of the harmonic interatomic force constant tensor versus atomic distance for several $Pb_{1-x}Ge_xTe$ alloy compositions in the rhombohedral phase. An alloy composition in the rocksalt phase near the phase transition, $Pb_{0.51}Ge_{0.49}Te$, is also included for comparison.

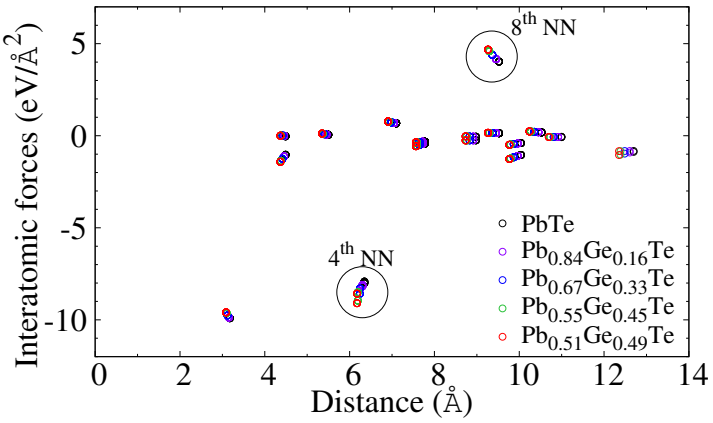



Figure 4.32: The trace of the harmonic interatomic force constant tensor versus atomic distance for several $Pb_{1-x}Ge_xTe$ alloy compositions in the rocksalt phase.

at ∼3 Å, ∼6 Å, and ∼9 Å, which correspond to the 1$^{st}$, 4$^{th}$, and 8$^{th}$ NNs in the rocksalt structure respectively, and their rhombohedral equivalents. IFCs change continuously between the rocksalt and rhombohedral phases as a consequence of the second-order phase transition. This can be seen by comparing the IFCs of $Pb_{0.49}Ge_{0.51}Te$ with those of $Pb_{0.51}Ge_{0.49}Te$, as shown in Fig. 4.31. As proximity to the phase transition increases, the magnitudes of the 4$^{th}$ and 8$^{th}$ equivalent neighbour IFCs increase substantially and reach maximum values at the phase transition. As discussed earlier, the TO(Γ) frequency reaches its minimal value at the phase transition, and the maximized anharmonic coupling between soft TO and acoustic modes results in the minimal $\kappa_{\text{latt}}$. Thus, we observe the correlation

between the large long-range IFCs along the [001] direction and the substantially reduced $\kappa_{\text{latt}}$ as proposed in Ref. [150].

However, in spite of weaker resonant bonds, the anharmonic lattice thermal conductivity values of the rhombohedral structures are as low as for the rocksalt structures with a similar proximity to the phase transition when their average mass difference is neglected. The short-range IFCs which correspond to the 1$^{\text{st}}$ NN increase rapidly in the rhombohedral phase with increasing $x$ with respect to the 4$^{\text{th}}$ and 8$^{\text{th}}$ IFCs, as shown in Fig. 4.31. The relative change between the short-range and the long-range IFCs is much smaller in the rocksalt than in the rhombohedral phase, which indicates much weaker resonant bonding in the rhombohedral structures due to the Te displacement. This stark difference in the strength of resonant bonding between the two phases does not result in larger values of the anharmonic $\kappa_{\text{latt}}$ of rhombohedral structures compared to rocksalt structures with the same average mass (Fig. 4.24). This conclusion is at variance with the previous argument that stronger resonant bonding causes lower lattice thermal conductivity in rocksalt IV-VI and rhombohedral group-V materials [150].

## 4.5 Discussion

### 4.5.1 Temperature dependence

Under the assumption of the displacive second-order phase transition, $Pb_{1-x}Ge_xTe$ alloys transform between the rocksalt and rhombohedral phases as a function of both the composition and temperature [157]. Consequently, the anharmonic contribution to the lattice thermal conductivity of $Pb_{1-x}Ge_xTe$ will be minimized at different compositions as a function of temperature. Similarly, the anharmonic lattice thermal conductivity for a given $x$ will have a dip in the vicinity of the corresponding transition temperature. The accurate treatment of these effects would require extending our model to include the temperature dependence of IFCs, for example, in Refs. [66, 74]. Including temperature dependent IFCs in our model would thus result in the shift of the composition at which the phase transition occurs to larger values of $x$ as the temperature increases. Additionally, the electronic thermal conductivity will be significant in Ge-rich alloys due to a large intrinsic vacancy concentration that effectively dopes the material [182, 184]. This combined with mass disorder will lead to a less pronounced dip in the total thermal conductivity. Nevertheless, the measured total thermal conductivities of some of the $Pb_{1-x}Ge_xTe$ materials reported in

Refs. [164, 167] exhibit dips near the transition temperature.

### 4.5.2 Structure of $Pb_{1-x}Ge_xTe$ alloys

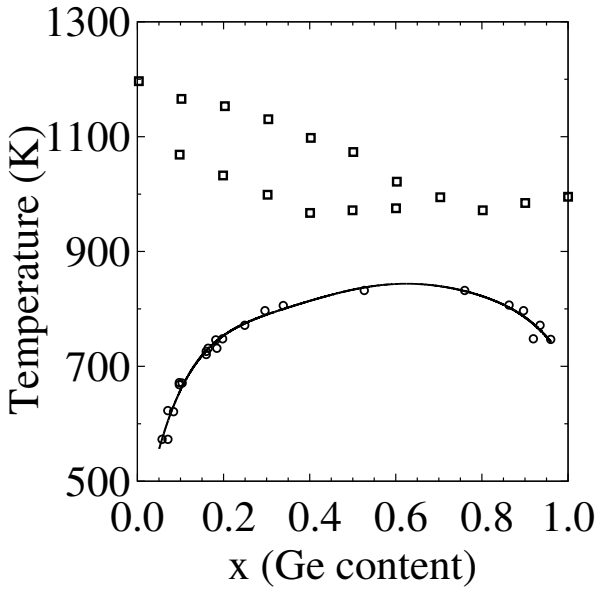



Figure 4.33: The quasi-binary phase diagram of $Pb_{1-x}Ge_xTe$ alloys, reproduced from experimental data from Ref. [157] and references therein. The miscibility gap is shown with black circles, the liquidus and solidus temperatures are shown in black squares for each alloy composition.

The experimental preparation of single phase $Pb_{1-x}Ge_xTe$ alloys must be handled with great care to avoid phase separation. In Fig. 4.33 we show the miscibility gap of $Pb_{1-x}Ge_xTe$, reproduced from experimental data as measured by Hohnke *et al.* [157]. This demonstrates the limits of the two-phase region, and yields complete solid solubility above 843 K. In order to retain a single phase alloy, it was necessary to anneal samples at 873 K for a period of 100-200 hours followed by rapid quenching on a time scale of $\sim$1 second [157]. This procedure was successfully applied to all compositions but $Pb_{0.40}Ge_{0.60}Te$, where the authors were unable to retain a single phase alloy, due to extremely rapid phase dissociation of the alloy. The authors stress that while extremely fast quench rates are necessary, annealling times of 18-24 hours may be sufficient to retain a single phase [157].

The question of whether there is a displacive or order-disorder soft mode phase transition in GeTe remains open. Older work on this topic suggested a displacive phase transition in GeTe [179, 194] with temperature. However, recent work has highlighted the pitfalls of techniques used in determining its nature [171]. This

lead to the conclusions of Matsunaga *et al.* [195] that an order-disorder model is more consistent with experiment when GeTe films are probed on shorter length scales than previous works. However, a thorough investigation by Wdowik *et al.* [173] has shown that perfectly ordered single crystalline GeTe undergoes a displacive phase transition with temperature. Experimental observations of an order-disorder phase transition [195] may be due to local defect structures in polycrystalline GeTe films. Thus, we have assumed a displacive second-order phase transition for $Pb_{1-x}Ge_xTe$ alloys within our model.

Furthermore, there exists considerable debate within the literature as to whether PbTe crystallizes in the ideal rocksalt structure at all temperatures, or forms local structural dipoles with increasing temperature [162]. This is supported by Kastberg *et al.* [196] who claim that the Pb atom off centres by as much as $\sim$0.3 Å at room temperature. However, this view is contradicted by Zhang *et al.* [197] who attribute the experimental observations to large amplitude thermal vibrations. Supporting data from extended x-ray absorption fine structure spectroscopy finds no evidence for an off-centring of the Pb atom [198]. Further work by Chen *et al.* [199] claims to have put the issue to rest after finding no appreciable breaking of the local or global symmetry in PbTe. Thus, we have assumed within our model that no such local structural dipoles (also termed ferroelectric nanodomains) form in the rocksalt phase of $Pb_{1-x}Ge_xTe$ alloys, giving an ideal rocksalt structure.

## 4.6 Summary

We predict from first principles virtual-crystal simulations that the anharmonic contribution to the lattice thermal conductivity of $Pb_{1-x}Ge_xTe$ alloys is minimized at the phase transition due to the maximized acoustic-optical anharmonic interaction. The total lattice thermal conductivity is further reduced due to mass disorder, which shifts the minimum value into the rhombohedral phase towards the composition at which scattering due to mass disorder is strongest. The total lattice thermal conductivity and its anharmonic contribution change continuously between the rocksalt and rhombohedral phases of the alloy as characteristic for the second-order phase transition. We show that lattice thermal conductivity is comparably suppressed in the rocksalt and rhombohedral structures with a similar proximity to the phase transition. Consequently, we argue that the structure and its degree of resonant bonding are less critical effects for suppressing lattice thermal conductivity in comparison to proximity to the phase transition,

average atomic mass, and mass disorder. Thus, tuning the soft optical modes of $Pb_{1-x}Ge_xTe$ alloys and other materials near soft optical mode phase transitions may be a promising strategy to increase their thermoelectric figure of merit.

# Chapter 5

# Electron-phonon coupling and mobility of $n$-type Ge and PbTe

## 5.1 Introduction

Up to this point, we have concerned ourselves with the computation of lattice thermal conductivity, largely ignoring other thermoelectric properties, namely the electrical conductivity, Seebeck coefficient, and electronic thermal conductivity. In this chapter, we take the first steps in calculating these quantities with the ultimate goal of predicting the thermoelectric figure of merit of PbTe-based materials driven near the ferroelectric phase transition. We start by calculating the electronic mobility, which contains all the information pertinent to electronic transport properties necessary to compute $ZT$ when coupled with lattice thermal conductivity calculations. We present results of these mobility calculations for $n$-type PbTe and Ge, which serves as a check to ensure correct implementation of the theory, and compare these results to experiment for the low carrier concentration and low temperature regime.

Remaining within the BTE-RTA framework, we calculate electronic lifetimes considering the effects of electron-phonon coupling on the low energy states near the conduction band minimum [83]. To achieve this, we use first principles techniques [83, 200] and deformation potential theory [79, 95, 201, 202, 203, 204]. This approach also easily allows us to compare the relative strength of different electron-phonon coupling mechanisms, such as intervalley, intravalley acoustic and polar optical scattering. In parallel, we present a discussion of the theoretical descriptions of the electronic band structures of PbTe and Ge. In contrast to Ge, the electronic bands of PbTe are notoriously difficult to reproduce within the DFT-LDA framework due to an inversion of the ordering of states at the band

gap when the effects of spin orbit interaction are taken into account [205, 206, 207]. Thus, we explore methods beyond DFT such as hybrid functionals to reproduce the band gap and effective masses of PbTe in agreement with experiment.

We find intravalley acoustic scattering to be the most dominant mechanism for electron-phonon coupling in Ge, and obtain excellent agreement for electronic mobility compared to experiment. From our calculations in PbTe polar optical scattering is the most dominant electron-phonon coupling mechanism in the low temperature and low carrier concentration regime, with several other scattering mechanisms forbidden by symmetry. Our calculated mobility of PbTe is in good agreement with experiment up to 200 K for low carrier concentrations. However, our calculated mobility differs from experiment by a factor of $\sim$2 at 300 K. Further work is necessary to resolve these discrepancies, and obtain an accurate *ab initio* description of the electronic mobility of PbTe.

## 5.2 Electronic band structure of Ge and PbTe

In this work, we limit ourselves to considering $n$-type Ge and PbTe in the low temperature and low carrier concentration regime. Within this limit, conduction band minima typically display an energy dispersion in $\mathbf{k}$-vector near the band edge of the form:

$$E(\mathbf{k}) = E_c + \frac{\hbar^2 \Delta k_{\parallel}^2}{2m_{\parallel}^*} + \frac{\hbar^2 \Delta k_{\perp}^2}{2m_{\perp}^*}. \tag{5.1}$$

where $E_c$ is the energy of the band edge, and $\Delta k_{\parallel}$ and $\Delta k_{\perp}$ are the components of $\mathbf{k}$ parallel and perpendicular to the $\mathbf{k}$-vector of the valley minimum, $\mathbf{k}_m$. Charge carriers behave as free electrons with effective masses $m_{\parallel}^*$ or $m_{\perp}^*$ depending on the direction of motion; along the longitudinal axis parallel to $\mathbf{k}_m$, or along the transverse axes perpendicular to $\mathbf{k}_m$. We verify this assumption and extract the values of $m_{\parallel}^*$ and $m_{\perp}^*$ from first principle calculations of the electronic band structure, along with values of the band gap. We then compare these quantities to experiment before proceeding with calculations of the electronic transport properties of Ge and PbTe. Unless otherwise stated, all calculations following this are performed using HGH pseudopotentials [110] with the Teter-Pade parametrisation [113] of the LDA exchange-correlation functional [97], using the ABINIT code [132].

Ge has an indirect band gap between the valence band maximum at $\Gamma$ and conduction band minimum at L, see Fig. 5.1, which shows the electronic band structure calculated without spin orbit interaction (SOI). The value of the band

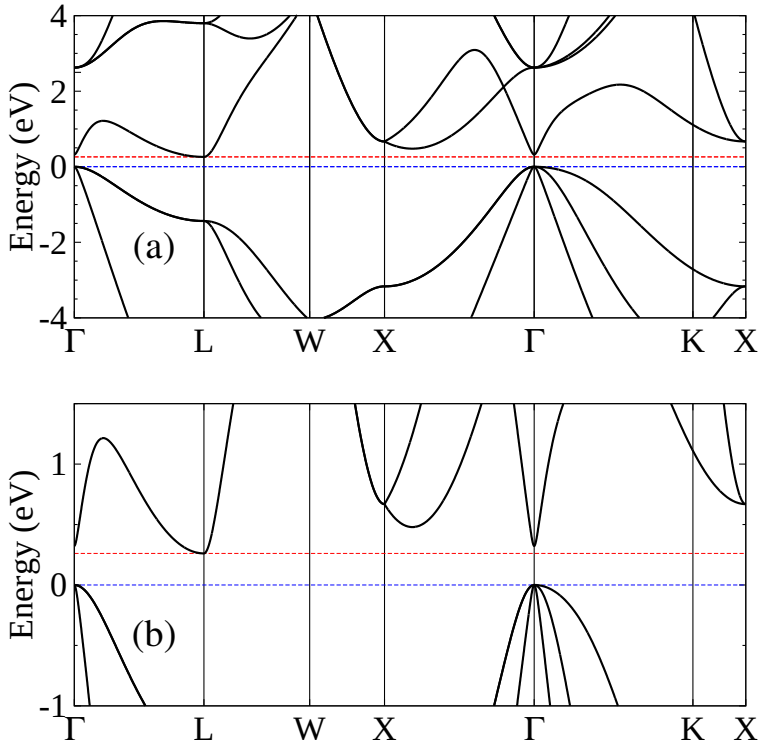



Figure 5.1: Electronic band structure of Ge, calculated using the LDA and HGH pseudopotentials excluding spin orbit interaction (a) showing several valence and conduction band states, and (b) zoomed in near the conduction band minimum to highlight the energy ordering of the L, Γ, and Δ valleys. The energies of the valence band maximum (blue dashed line) and conduction band minimum (red dashed line) are also highlighted.

Table 5.1: Electronic band gap and conduction band effective electron masses at L of Ge calculated using the LDA functional compared to experiment.

| Ge | LDA (exc. SOI) | Experiment |
|---|---|---|
| $E_g$ (eV) | 0.261 | 0.744[208] |
| $m_{\parallel}^{*,c,L}/m_e$ | 1.639 | 1.640[209] |
| $m_{\perp}^{*,c,L}/m_e$ | 0.083 | 0.082[209] |

gap is considerably underestimated compared to experiment, see Table 5.1, due to the well known tendency of the LDA functional to underestimate the electronic band gap in a range of semiconductors [210, 211]. Since the conduction band minimum in Ge is at the L point, we extract the effective electron masses along the directions parallel to L (L → Γ) and perpendicular to L (L → W), labelled $m_{\parallel}^{*,c,L}$ and $m_{\perp}^{*,c,L}$ respectively. We find that these effective electron masses are in extremely good agreement with experiment using the LDA functional.

This excellent agreement results from the fact that Ge is an indirect band-gap semiconductor where the conduction band minimum is not energetically close to other states of the same crystal momentum. Thus, the LDA functional should characterise electron transport properties involving the L valley very well in Ge.

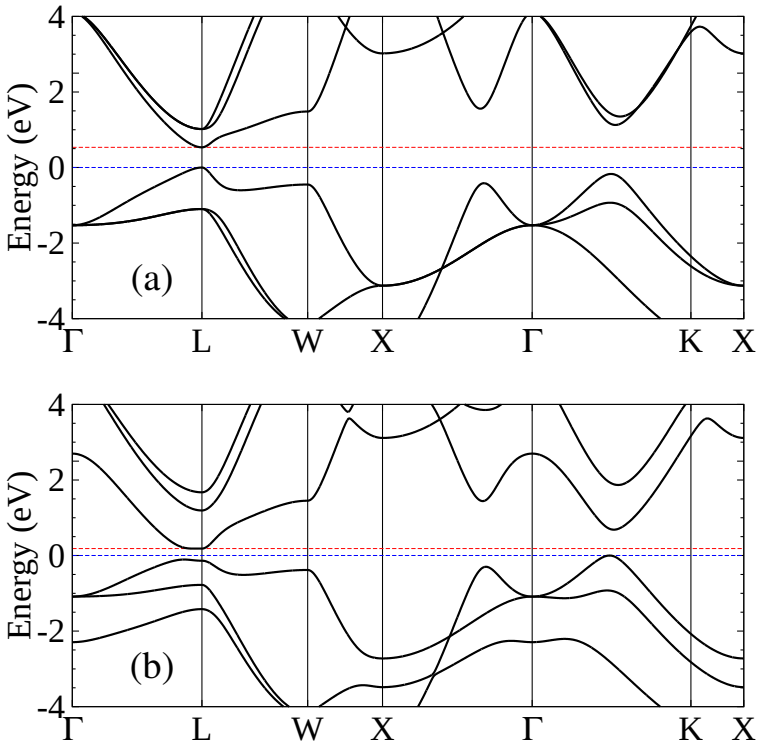



Figure 5.2: Electronic band structure of PbTe, calculated using the LDA and HGH pseudopotentials (a) excluding spin orbit interaction, and (b) including spin orbit interaction. The energies of the valence band maximum (blue dashed line) and conduction band minimum (red dashed line) are also highlighted.

In contrast to Ge, PbTe has a direct narrow band gap at the L point [212, 213, 214], see Fig. 5.2, which shows the electronic band structure of PbTe calculated excluding SOI in Fig. 5.2(a), and including SOI in Fig. 5.2(b). Within the LDA, the inclusion of SOI pushes the $\Sigma$ valley (along the $\Gamma$-K direction) upwards to become the valence band maximum forming an indirect band gap with the conduction band minimum at L, at odds with experimental observations [212, 213, 214].

The LDA excluding SOI overestimates the band gap in PbTe, yielding a value about twice that of experiment, see Table 5.2. This is due to the lack of relativistic effects which results in an opening of the band gap, counteracting the effect of the LDA underestimation of the band gap energy [205, 206]. Nevertheless, effective electron masses are in very good agreement with experiment. Thus,

Table 5.2: Direct electronic band gap and effective electron masses of PbTe calculated using the LDA functional including and excluding spin orbit interaction compared to experimental values measured at 4 K. The sign of the band gap is determined from the ordering of electronic states at L, as explained in the text.

| PbTe | LDA (exc. SOI) | LDA (inc. SOI) | Experiment 1 Ref. [212] | Experiment 2 Ref. [213] |
|---|---|---|---|---|
| $E_g$ (eV) | 0.54 | −0.32 | 0.19[a] | 0.19[a] |
| $m_{\parallel}^{*,v}/m_e$ | 0.294 | 0.834 | 0.255 | 0.310 |
| $m_{\perp}^{*,v}/m_e$ | 0.023 | 0.622 | 0.024 | 0.022 |
| $m_{\parallel}^{*,c}/m_e$ | 0.216 | 5.295 | 0.210 | 0.240 |
| $m_{\perp}^{*,c}/m_e$ | 0.037 | 0.031 | 0.021 | 0.024 |

[a] increasing to ∼0.3 eV at room temperature [214].

for calculating electronic transport properties of PbTe, we anticipate that the LDA excluding SOI may give reasonable results within the DFT level of theory. However, we note that the energy separation of the 1st and 2nd conduction band states without SOI is considerably smaller than in the case including SOI, which may lead to inaccuracies in the electron-phonon matrix element calculations.

We confirmed the presence of a positive electronic band gap in PbTe when SOI is excluded by calculating wavefunction overlaps as follows. Considering only the 1st electronic states on either side of the Fermi level at zero temperature (set to 0 eV, see Fig. 5.2) respectively, we labelled the periodic part of the wavefunction of the state with the lower energy $|u_{\mathbf{k},\mathrm{h}}\rangle$, and the periodic part of the wavefunction of the state with the higher energy $|u_{\mathbf{k},\mathrm{e}}\rangle$. We then computed the overlap between the periodic part of the wavefunction at L of the lower energy band, $|u_{L,\mathrm{h}}\rangle$, with $|u_{\mathbf{k},\mathrm{h}}\rangle$ and $|u_{\mathbf{k},\mathrm{e}}\rangle$ respectively, and the overlap of the periodic part of the wavefunction at L of the higher energy band, $|u_{L,\mathrm{e}}\rangle$, with $|u_{\mathbf{k},\mathrm{h}}\rangle$ and $|u_{\mathbf{k},\mathrm{e}}\rangle$ respectively, see Figs. 5.3(a) and 5.3(c). The wavevector $\mathbf{k}$ is along the Γ-L-W line, which corresponds to the directions along which we extract the values of $m_{\parallel}^*$ (L → Γ) and $m_{\perp}^*$ (L → W). We found that the state at L with the lower energy overlaps more strongly with the lower energy state along Γ-L-W than the higher energy state, and thus it mainly exhibits the character of the valence band. Similarly, the state at L with the higher energy overlaps more strongly with the higher energy state along Γ-L-W, and thus mainly exhibits the character of the conduction band. This confirms the correct ordering of states at L and a positive band gap in PbTe when SOI is excluded, and verifies that our effective electron

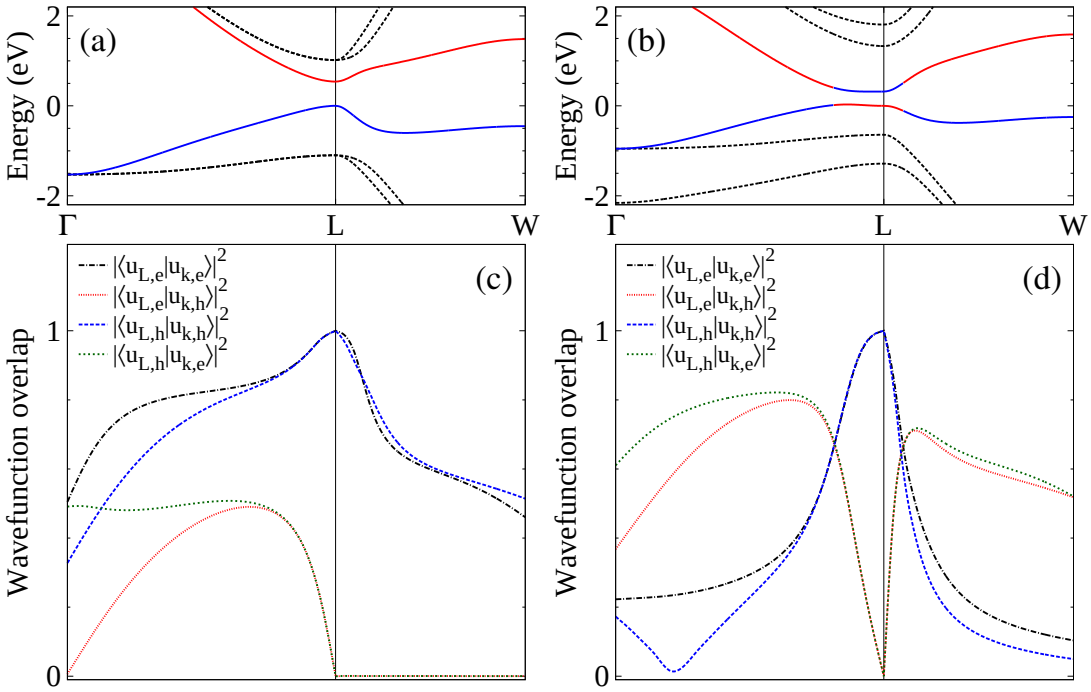



Figure 5.3: Electronic band structure of PbTe along the Γ-L-W line calculated using the LDA (a) excluding SOI and (b) including SOI. A solid red (blue) line shows a state whose character mostly corresponds to that of the conduction (valence) band as deduced from wavefunction overlaps. The overlaps of the cell periodic parts of the wavefunctions between the 1st electronic states counting upward (labelled as e) and downward (labelled as h) from the zero temperature Fermi level at L and those states at **k** are shown (c) excluding SOI and (d) including SOI. The following wavefunction overlaps are plotted: $|\langle u_{L,\mathrm{e}}|u_{\mathbf{k},\mathrm{e}}\rangle|^2$ (dot-dashed black line), $|\langle u_{L,\mathrm{e}}|u_{\mathbf{k},\mathrm{h}}\rangle|^2$ (dotted red line), $|\langle u_{L,\mathrm{h}}|u_{\mathbf{k},\mathrm{h}}\rangle|^2$ (large-dashed blue line), $|\langle u_{L,\mathrm{h}}|u_{\mathbf{k},\mathrm{e}}\rangle|^2$ (small-dashed green line).

masses are extracted from physically correct states.

The combination of LDA's tendency to underestimate the band gap and the effects of SOI result in an inverted band gap in PbTe. When relativistic effects are taken into account the previously degenerate 2nd and 3rd conduction and valence band states split, see Fig. 5.2. This spin orbit splitting causes the valence band maximum to be repelled upward, while the conduction band minimum is repelled downward [205, 206]. The resulting band gap is underestimated to such a degree that the topmost valence band and bottommost conduction band become interchanged and mix heavily at L [205, 206], which is an issue well known in the lead chalcogenides [207]. To confirm that this is indeed the case in our calculations when SOI is included, we again computed the previously defined overlap of the cell periodic parts of the wavefunctions, see Figs. 5.3(b) and 5.3(d). We found

that the state at L above the zero temperature Fermi level overlaps more strongly with the state below the Fermi level away from L, thus $|u_{L,\mathrm{e}}\rangle$ mainly exhibits the character of the valence band. Conversely, the state at L below the Fermi level overlaps more strongly with the state above the Fermi level away from L, thus $|u_{L,\mathrm{h}}\rangle$ mainly exhibits the character of the conduction band. This confirms the presence of an inverted band gap, and as a result, effective masses calculated with this approach are in very poor agreement with experiment, see Table 5.2.

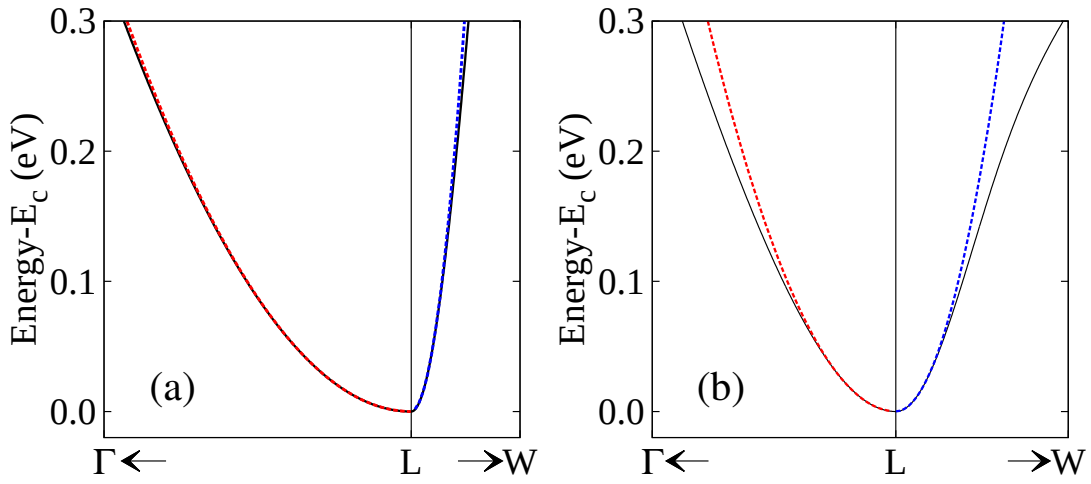



Figure 5.4: (a) Bottommost conduction band state of Ge calculated using LDA-HGH (solid black line) relative to the band minimum, compared to the parabolic bands fit shown with red and blue dashed lines, for 2/5 of the line L→Γ (parallel to L) and 1/5 of the line L→W (perpendicular to L). (b) Bottommost conduction band state of PbTe calculated using LDA-HGH (solid black line) relative to the band minimum compared to the parabolic bands fit shown with red and blue dashed lines, for 1/5 of the line L→Γ and 1/5 of the line L→W.

We find that the assumption of parabolic bands holds extremely well for both Ge and PbTe up to a value of ∼0.1 eV, see Figs. 5.4(a) and 5.4(b), which should be sufficient for transport calculations below 300 K and at low carrier concentrations circa $10^{18}$ cm$^{-3}$. We determined the parabolic bands by fitting Eq. (5.1) to our calculated DFT electronic bands in the vicinity of the conduction band minimum, which also yields the effective electron masses as given previously. In Ge, the conduction band has almost perfect parabolic behaviour up to energy values of ∼0.3 eV. On the other hand, there are clear deviations from parabolic behaviour at energies larger than ∼0.1 eV in PbTe, which is most striking along the L→W lines for energies higher than ∼0.2 eV. However, this non-parabolicity will only become significant in the high temperature or high carrier concentration regimes, outside the scope of this work.

Turning our attention to the LDA description of electronic polarisability in

Table 5.3: Born effective charges and high-frequency dielectric constant of PbTe calculated with the LDA excluding and including SOI compared to experimental measurements.

| | $Z^*$ (e) | $\epsilon_\infty$ |
|---|---|---|
| LDA (exc. SOI) | 6.35 | 34.85 |
| LDA (inc. SOI) | 7.47 | 70.35 |
| Experiment [153, 215] | 6.5 | 31.81 |

PbTe, the LDA excluding SOI gives values of the Born effective charges and high-frequency dielectric constant of PbTe in excellent agreement with experiment, see Table 5.3. On the other hand, the LDA including SOI overestimates the experimental BECs by $\sim 20\%$, and gives a value over twice that of experiment for the high-frequency dielectric constant. In the latter case, the overestimation is likely due to the closing of the average electronic gap [193], which results from the repulsion of valence (conduction) states upwards (downwards) when SOI is taken into consideration. Thus, we anticipate that parameters derived from the LDA excluding SOI characterise polar optical scattering more accurately than those obtained from the case including SOI.

## 5.3 Modelling electronic mobility

The charge carrier mobility within the BTE-RTA is given in Eq. (2.112). First, we convert the sum over $\mathbf{k}$ to an integral over energy:

$$\mu = \frac{e}{n} \int dE \sum_n \rho(E) \left( -\frac{\partial f^0(E)}{\partial E} \right) \mathbf{v}_{n\mathbf{k}}^2(E) \tau_{n\mathbf{k}}(E). \tag{5.2}$$

where $\rho(E)$ is the density of states per spin. Then, we make a number of assumptions to simplify this expression. Since we are dealing with the linear (ohmic) regime, we assume carriers are in thermal equilibrium and obey Maxwell-Boltzmann statistics, where $f^0 = e^{-(E_\mathbf{k} - E_\mathrm{F})/k_\mathrm{B}T}$ [200]. This is the approximate form of the Fermi-Dirac distribution valid when $E_\mathbf{k} - E_\mathrm{F} \gg k_\mathrm{B}T$. The carrier velocity $\mathbf{v}_\mathbf{k} = 1/\hbar \nabla_\mathbf{k} E(\mathbf{k})$ and density of states may be obtained taking the parabolic band approximation (see Eq. (5.1)), valid for the low temperature and low carrier concentration regime as discussed, where conduction only happens through the bottom degenerate conduction bands.

Thus, summing over the longitudinal and transverse directions, we obtain the

electron mobility as [83, 200]:

$$\mu = \frac{4}{9}\frac{eN_v}{k_{\mathrm{B}}Tn}\left(\frac{1}{m_{\parallel}^*}+\frac{2}{m_{\perp}^*}\right)\int_{E_c}^{\infty} dE e^{-\frac{E-E_{\mathrm{F}}}{k_{\mathrm{B}}T}}(E-E_c)\rho(E)\tau(E), \tag{5.3}$$

where $N_v$ is the valley degeneracy, and the density of states per spin at the carrier energy $E$ is given as [83]:

$$\rho(E) = \frac{(m_{\parallel}^*)^{1/2}m_{\perp}^*\sqrt{E-E_c}}{\sqrt{2}\pi^2\hbar^3}\Theta(E-E_c), \tag{5.4}$$

where $\Theta(E-E_c)$ is the unit step function, 0 if $E-E_c<0$, 1 otherwise. The carrier concentration is given as [83]:

$$n = 2N_v(m_{\parallel}^*)^{1/2}m_{\perp}^*\left(\frac{k_{\mathrm{B}}T}{2\pi\hbar^2}\right)^{\frac{3}{2}} e^{\frac{E_{\mathrm{F}}-E_c}{k_{\mathrm{B}}T}}, \tag{5.5}$$

In practise Eq. (5.3) does not need to be integrated up to infinity, instead we integrate up to 10 $k_{\mathrm{B}}T$ which is sufficient to capture finite electronic occupations due to the exponential decay of the Boltzmann distribution. $\tau(E)$ is calculated summing over the scattering rates of different electron-phonon coupling mechanisms using Matthiessen's rule, whose details are given next.

## 5.4 Electron-phonon coupling

When calculating electron scattering rates due to electron-phonon coupling, we are only considering $n$-type Ge and PbTe in the low temperature and low carrier concentration regime. Thus, we only consider electronic transport involving the L valleys, i.e.: scattering within an L valley via an acoustic or optical phonon, and between non-equivalent L valleys. We note that scattering involving the $\Gamma$ and $\Delta$ valleys in Ge will become significant at higher temperatures and carrier concentrations, see Fig. 5.1. However it is trivial to extend the theory to take these valleys into consideration. Similarly, in PbTe other conduction band valleys may become significant only at very high temperatures or carrier concentrations, see Fig. 5.2. Given that PbTe is a polar semiconductor, we must also consider the Fröhlich interaction (polar optical phonon scattering).

We divide these scattering mechanisms into three groups based on the computational approach used to obtain electron scattering rates. We first consider scattering between non-equivalent L valleys (intervalley), see Fig. 5.5, and scat-

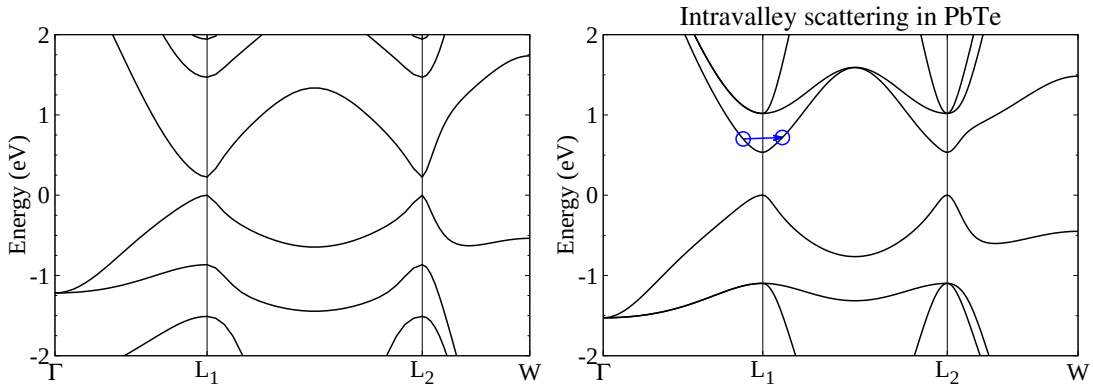



Figure 5.5: Cartoon illustrating (a) scattering between L valleys (intervalley) via an X-point phonon and (b) scattering within an L valley (intravalley) in the limit of $\mathbf{q} \to 0$ in PbTe.

tering within an L valley due to an optical phonon (intravalley optical), following the approach outlined by Murphy-Armando and Fahy [83]. For intravalley acoustic scattering, we turn to the deformation potential theory approach of Herring and Vogt [79, 83, 95, 200]. In both cases, we calculate electron-phonon coupling elements using the DFPT method implemented in the ABINIT code [132, 134, 135]. Finally, to describe polar-optical scattering we turn to the Fröhlich model as described in Ref. [77]. To reiterate, all DFT calculations from here on are performed with the LDA exchange-correlation excluding spin orbit interaction, unless otherwise stated.

### 5.4.1 Intervalley and intravalley optical scattering

We begin by returning to the electron scattering rate defined in Eq. 2.128 and setting the electronic populations $f^0_{m\mathbf{k}'}$ to zero in the limit of low doping, which we re-write as [83]:

$$\frac{1}{\tau^l_{n\mathbf{k}}} = \frac{2\pi}{\hbar}\frac{1}{N_l}\sum_{m\mathbf{k}'}\sum_{\mathbf{q}s} l^2_{\mathbf{q}s}\Big(F^{\mathbf{k}\mathbf{k}'}_{nm}(\epsilon_{m\mathbf{k}'}-\epsilon_{n\mathbf{k}})\bar{n}_{\mathbf{q}s}\Theta(\epsilon_{m\mathbf{k}'}-\epsilon_{n\mathbf{k}}) \\ \times F^{\mathbf{k}\mathbf{k}'}_{nm}(\epsilon_{n\mathbf{k}}-\epsilon_{m\mathbf{k}'})(\bar{n}_{\mathbf{q}s}+1)\Theta(\epsilon_{n\mathbf{k}}-\epsilon_{m\mathbf{k}'})\Big), \tag{5.6}$$

where $l_{\mathbf{q}s} = (\hbar/2m_c\omega_{\mathbf{q}s})^{1/2}$, and we have defined:

$$F^{\mathbf{k}\mathbf{k}'}_{nm}(E) = \sum_s \Big|\mathbf{H}_{mn}(\mathbf{k};\mathbf{q}s)\Big|^2\delta(E-\hbar\omega_{\mathbf{q}s}), \tag{5.7}$$

in terms of the electron-phonon matrix elements $\mathbf{H}_{mn}(\mathbf{k};\mathbf{q}s)$, defined previously in Eq. (2.119). The first term in Eq. (5.6) is due to phonon absorption and the

second due to phonon emission.

For intervalley and intravalley optical scattering near the conduction band valley minima, where carriers are concentrated, the electron phonon coupling elements have a weak dependence on $\mathbf{k}$ and $\mathbf{k}'$. Thus, we may approximate $F_{nm}^{\mathbf{k}\mathbf{k}'}$ as effectively being from a valley $\alpha$ (state $|\psi_{n\mathbf{k}}\rangle$) to valley $\beta$ (state $|\psi_{m\mathbf{k}'}\rangle$), $F_{nm}^{\mathbf{k}\mathbf{k}'} \approx F^{\alpha\beta}$ [83]. This allows us to calculate the scattering rate for an entire valley from that of the valley minima, and use Eq. (5.6) instead of the momentum relaxation time [142].

Converting Eq. (5.6) from a summation over $\mathbf{k}'$ to an integral over energy, and using the density of states in Eq. (5.4), the scattering rate for phonon absorption is [83]:

$$\frac{1}{\tau^{l,-}_{\alpha\to\beta}(E_{\mathbf{k}})} = \frac{n_v\Omega\sqrt{(m_{\perp}^{*,\beta})^2 m_{\parallel}^{*,\beta}}}{\hbar^2\sqrt{2}\pi m_c}\int_{E_{\mathbf{k}}}^{\infty} dE_{\mathbf{k}'}\frac{\sqrt{E_{\mathbf{k}'}-E_c^{\beta}}F^{\alpha\beta}(E_{\mathbf{k}'}-E_{\mathbf{k}})}{E_{\mathbf{k}'}-E_{\mathbf{k}}}n(E_{\mathbf{k}'}-E_{\mathbf{k}}), \tag{5.8}$$

and for phonon emission [83]:

$$\frac{1}{\tau^{l,+}_{\alpha\to\beta}(E_{\mathbf{k}})} = \frac{n_v\Omega\sqrt{(m_{\perp}^{*,\beta})^2 m_{\parallel}^{*,\beta}}}{\hbar^2\sqrt{2}\pi m_c}\int_{E_c^{\beta}}^{E_{\mathbf{k}}} dE_{\mathbf{k}'}\frac{\sqrt{E_{\mathbf{k}'}-E_c^{\beta}}F^{\alpha\beta}(E_{\mathbf{k}}-E_{\mathbf{k}'})}{E_{\mathbf{k}}-E_{\mathbf{k}'}}(n(E_{\mathbf{k}}-E_{\mathbf{k}'})+1), \tag{5.9}$$

where $\Omega$ is the volume of the primitive cell, and $E_c^{\beta}$ is the minimum energy of the valley $\beta$. $n_v$ is the number of valleys an electron can scatter to, and equals 1 for intravalley scattering, and 3 for intervalley scattering. $E_{\mathbf{k}}$ and $E_{\mathbf{k}'}$ are the energies of the initial and final states, and $E_{\mathbf{k}'}-E_{\mathbf{k}}$ and $E_{\mathbf{k}}-E_{\mathbf{k}'}$ are the phonon energies for the two processes respectively. Integration is performed up to a value of $E_{\mathbf{k}}+10k_{\mathrm{B}}T$. For Ge, intervalley scattering via an X-point phonon is limited to the LA and LO polarisations as per selection rules [216]. Electron scattering rates due to these types of electron-phonon coupling for Ge are plotted in Fig. 5.6.

The deformation potentials for intervalley and optical intravalley scattering are defined as a function of electron-phonon matrix elements as [83]:

$$D = \sqrt{\sum_{s}\left|\mathbf{H}_{mn}(\mathbf{k};\mathbf{q}s)\right|^2} \tag{5.10}$$

where $s$ is over optical modes for intravalley optical scattering, $D_{opL}$, and $s$ is over all modes for intervalley scattering, $D_{LL}$. We note that in Ge $s$ is only summed over longitudinal modes for intervalley scattering due to selection rules [216]. For Ge, we find excellent agreement with previous values from the literature and good agreement with experiment, see Table 5.4.

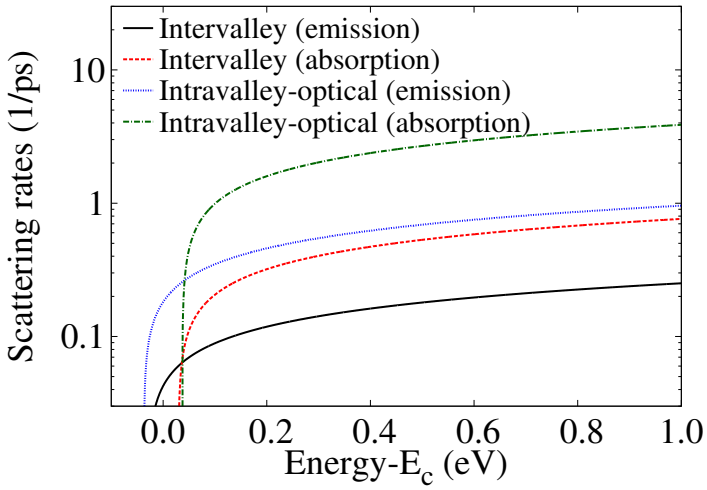



Figure 5.6: Electron scattering rates in an L valley as a function of electronic energy at 300 K in Ge. Scattering is due to electron-phonon coupling from intervalley emission (solid black line) and absorption (dashed red line), and intravalley optical emission (dotted blue line) and absorption (dot-dashed green line).

Table 5.4: Intervalley and intravalley optical deformation potentials for Ge compared to previous calculations from the literature and experiment.

| | Our results | Previous calculations [83] | Experiment [80, 217] |
|---|---|---|---|
| $D_{LL}$(eV/Å) | 1.12 | 1.11 | 3.00 |
| $D_{opL}$(eV/Å) | 5.09 | 5.11 | 5.50 |

Calculated intervalley and intravalley optical scattering rates are zero for PbTe, due to the fact that scattering between L valley minima via an X phonon, and scattering within an L valley via a Γ phonon is forbidden by symmetry [218, 219]. In PbTe, the centre of inversion is the Pb or Te site, and thus all X-point and Γ-point phonons have odd parity under inversion symmetry [220]. Odd parity phonons can only couple between electronic states of opposite parity, i.e. odd and even electronic states [220]. Thus, the electron-phonon matrix elements for intervalley and intravalley optical scattering in the conduction band vanish exactly at the L point. This is in contrast to Ge where optical phonons at X and Γ have even parity under inversion symmetry, since the centre of inversion is between two Ge atoms, and contribute to the electron-phonon scattering rate. We note that this argument also holds for scattering between L points in the valence band in PbTe, while interband scattering (between the conduction and

valence bands) is allowed. Crucially, intervalley scattering via an X phonon and intravalley scattering via a Γ phonon remain forbidden by symmetry when spin orbit interaction is taken into account, as confirmed by our DFPT calculations.

### 5.4.2 Intravalley acoustic scattering

#### 5.4.2.1 Deformation potential theory

To calculate electronic scattering rates due to long-wavelength acoustic mode phonons, we employ the deformation potential approach introduced by Bardeen and Shockley [95], which was generalised by Herring and Vogt [79] to include transverse as well as longitudinal phonons. We follow the procedure outlined by Fischetti and Laux [200] and Murphy-Armando and Fahy [83]. The fundamental idea of deformation potential theory is that the matrix element $\mathbf{k} \rightarrow \mathbf{k} \pm \mathbf{q}$ for absorption or emission of a long-wavelength acoustic phonon is practically equal to the shift of the band energy which would be produced from a homogeneous strain equal in magnitude to the local strain at a point $\mathbf{r}$ due to a phonon $\mathbf{q}s$. A deformation potential thus describes the change in electronic band energies at different parts of the Brillouin zone due to static distortions of the lattice.

To express this idea in another way, the expectation value of the partial derivative of the electronic Hamiltonian with respect to acoustic displacement may be approximated as [95]:

$$\frac{\partial H_e}{\partial \mathbf{u}(\mathbf{r})}\mathbf{u}(\mathbf{r}) \approx \frac{\partial \epsilon_{n\mathbf{k}}}{\partial \mathbf{u}(\mathbf{r})}\mathbf{u}(\mathbf{r}) \tag{5.11}$$

where $\partial\epsilon_{n\mathbf{k}}/\partial\mathbf{u}(\mathbf{r})$ is the shift of the electronic energy of a non-degenerate band due to a static displacement of the unit cell $\mathbf{u}(\mathbf{r})$, and is related to the deformation potentials of the crystal. We may describe the interaction between electrons and acoustic phonons with a slowly varying potential dependent on the deformation potential tensor $\Xi_{\alpha\beta}$ [77, 79]:

$$\hat{H}_{ep} = \sum_{\alpha\beta} \epsilon_{\alpha\beta}(\mathbf{r})\Xi_{\alpha\beta}, \tag{5.12}$$

where $\epsilon(\mathbf{r})$ is the local strain tensor at $\mathbf{r}$, given as $\epsilon_{\alpha\beta} = \frac{1}{2}(\frac{\partial u_\alpha}{\partial r_\beta} + \frac{\partial u_\beta}{\partial r_\alpha})$ [221].

The displacement $\mathbf{u}(\mathbf{r})$ of acoustic modes is written as [77]:

$$\mathbf{u}(\mathbf{r}) = N_l^{-\frac{1}{2}} \sum_{\mathbf{q}s} l_{\mathbf{q}s}\mathbf{e}^s(\mathbf{q}) \left(\hat{a}_{\mathbf{q}s} + \hat{a}^\dagger_{-\mathbf{q}s}\right) e^{i\mathbf{q}\cdot\mathbf{r}}, \tag{5.13}$$

where $\mathbf{e}^s(\mathbf{q})$ is the unit polarisation vector. The strain tensor components then read [77]:

$$\epsilon_{\alpha\beta}(\mathbf{r}) = N_l^{-\frac{1}{2}} \sum_{\mathbf{q}s} \frac{i}{2} l_{\mathbf{q}s} \left( \hat{a}_{\mathbf{q}s} + \hat{a}^\dagger_{-\mathbf{q}s} \right) \left( e^s_\alpha(\mathbf{q}) q_\beta + e^s_\beta(\mathbf{q}) q_\alpha \right) e^{i\mathbf{q}\cdot\mathbf{r}}. \tag{5.14}$$

Substituting into Eq. (5.12) we arrive at the Hamiltonian describing interaction between electrons and long-wavelength acoustic mode phonons [77]:

$$\hat{H}_{ep} = N_l^{-\frac{1}{2}} \sum_{\mathbf{q}s} \frac{i}{2} l_{\mathbf{q}s} \left( \hat{a}_{\mathbf{q}s} + \hat{a}^\dagger_{-\mathbf{q}s} \right) e^{i\mathbf{q}\cdot\mathbf{r}} \sum_{\alpha\beta} \Xi_{\alpha\beta} \left( e^s_\alpha(\mathbf{q}) q_\beta + e^s_\beta(\mathbf{q}) q_\alpha \right). \tag{5.15}$$

We then insert the above Hamiltonian into Fermi's Golden Rule to obtain the electron scattering rate:

$$\begin{aligned} \frac{1}{\tau^l_{n\mathbf{k}}} =& \frac{2\pi}{\hbar} \frac{1}{N_l} \sum_{m\mathbf{k}'} \sum_{\mathbf{q}s} l^2_{\mathbf{q}s} \Big| \langle u_{m\mathbf{k}'} | \frac{1}{2} \sum_{\alpha\beta} \Xi_{\alpha\beta} \left( e^s_\alpha(\mathbf{q}) q_\beta + e^s_\beta(\mathbf{q}) q_\alpha \right) | u_{n\mathbf{k}} \rangle_{\text{uc}} \Big|^2 \\ & \times \left( \left( \bar{n}_{\mathbf{q}s} + \frac{1}{2} \mp \frac{1}{2} \right) \delta \left( \epsilon_{n\mathbf{k}} - \epsilon_{m\mathbf{k}'} \pm \hbar\omega_{\mathbf{q}s} \right) \delta_{\mathbf{k}\pm\mathbf{q}-\mathbf{k}',\mathbf{G}} \right), \end{aligned} \tag{5.16}$$

where the upper sign is for phonon absorption, and the lower for phonon emission. The cell periodic part of the Bloch function, $u_{n\mathbf{k}}$, does not vary rapidly with $\mathbf{k}$ over states near the band edge, where charge carriers are concentrated. Thus we may assume $u_{n\mathbf{k}} \approx u_{n\mathbf{k}\pm\mathbf{q}}$ to obtain $\langle u_{m\mathbf{k}\pm\mathbf{q}} | u_{n\mathbf{k}} \rangle_{\text{uc}} = 1$ for parabolic bands [77]. For simplicity, we define $C = 1/2 \sum_{\alpha\beta} \Xi_{\alpha\beta} \left( e^s_{\alpha b}(\mathbf{q}) q_\beta + e^s_{\beta b}(\mathbf{q}) q_\alpha \right)$ to obtain:

$$\frac{1}{\tau^l_{n\mathbf{k}}} = \frac{2\pi}{\hbar} \frac{1}{N_l} \sum_{m\mathbf{k}'} \sum_{\mathbf{q}s} l^2_{\mathbf{q}s} |C|^2 \left( \left( \bar{n}_{\mathbf{q}s} + \frac{1}{2} \mp \frac{1}{2} \right) \delta \left( \epsilon_{n\mathbf{k}} - \epsilon_{m\mathbf{k}'} \pm \hbar\omega_{\mathbf{q}s} \right) \delta_{\mathbf{k}\pm\mathbf{q}-\mathbf{k}',\mathbf{G}} \right). \tag{5.17}$$

We now consider the momentum relaxation time for a simple case, a longitudinal phonon in a cubic crystal with a spherical band following the approach in chapter 3 of Ref. [77]. For the Γ valley shear strains do not produce a change in energy, and thus it can be shown that $C = \Xi^\Gamma_d q$, where $\Xi_d$ is the dilatation deformation potential and corresponds to the shift in band energy due to a dilatation in the two directions normal to the axis of the valley in consideration. We may approximate $\bar{n}_{\mathbf{q}s} \approx (k_B T)/(\hbar\omega_{\mathbf{q}s})$, assuming that the energy of a phonon is much less than the energy of an electron. It follows in the limit of $\bar{n}_{\mathbf{q}s} \gg 1$ that the rates of phonon emission and absorption processes become identical. Finally, neglecting the phonon energy $\hbar\omega_{\mathbf{q}s}$ in the argument of the delta function since only very low energy phonons are involved (the quasi-elastic approximation) [142], and accounting for the factor $(1 - \cos(\theta_{\mathbf{k}\mathbf{k}'}))$, the momentum relaxation time for

absorption or emission processes in this case is given as [77]:

$$\frac{1}{\tau} = \frac{(2m^{*,\Gamma})^{\frac{3}{2}} k_{\mathrm{B}} T}{4\pi\hbar^4 c_L} (\Xi_d^{\Gamma})^2 \sqrt{E_{\mathbf{k}} - E_c}, \tag{5.18}$$

where $m^{*,\Gamma}$ is the effective mass of the $\Gamma$ valley, and $c_L$ is the average elastic constant for longitudinal modes.

Herring and Vogt generalised deformation potential theory to include longitudinal and transverse acoustic phonons in a semiconductor with anisotropic scattering [79, 95]. Considering the $\Gamma$, L and X valleys of a cubic material, the deformation potential tensor consists of two linearly independent terms, $\Xi_d$, and $\Xi_u$. $\Xi_u$ is the uniaxial deformation potential, and corresponds to a uniaxial stretch along the direction of the valley in consideration, and a corresponding compression perpendicular to this so that volume is preserved. For the [111] L valley, the diagonal terms of the deformation potential tensor are given as [79]:

$$\Xi_{\alpha\alpha} = \Xi_d^{\mathrm{L}} + \frac{\Xi_u^{\mathrm{L}}}{3}, \tag{5.19}$$

with the non-diagonal terms ($\alpha \neq \beta$) given as [79]:

$$\Xi_{\alpha\beta} = \frac{\Xi_u^{\mathrm{L}}}{3}. \tag{5.20}$$

In this case, the electron-phonon coupling Hamiltonian can be written as [83, 201, 202]:

$$H_{ep} = \Xi_d^{\mathrm{L}} Tr[\boldsymbol{\epsilon}(\mathbf{r})] + \Xi_u^{\mathrm{L}} (\hat{\mathbf{k}}_{\mathrm{L}} \cdot \boldsymbol{\epsilon}(\mathbf{r}) \cdot \hat{\mathbf{k}}_{\mathrm{L}}). \tag{5.21}$$

where $\hat{\mathbf{k}}_{\mathrm{L}}$ is a unit vector parallel to the $\mathbf{k}$-vector of the L valley.

Herring and Vogt obtained the angular dependences of the momentum relaxation times for anisotropic valleys by interpolating the calculated squared matrix elements along symmetry directions of the phonon wavevector with spherical harmonics. For the directions parallel and perpendicular to the $\mathbf{k}$-vector of a given valley these momentum relaxation rates are written as [79]:

$$\frac{1}{\tau_{\parallel}} = \frac{3(m_{\parallel}^* m_{\perp}^{*2})^{\frac{1}{2}} k_{\mathrm{B}} T}{2^{\frac{3}{2}} \pi\hbar^4 c_l} \sqrt{E_{\mathbf{k}} - E_c} \left[ \xi_{\parallel} \Xi_d^2 + \eta_{\parallel} \Xi_d \Xi_u + \zeta_{\parallel} \Xi_u^2 \right], \tag{5.22}$$

$$\frac{1}{\tau_{\perp}} = \frac{3(m_{\parallel}^* m_{\perp}^{*2})^{\frac{1}{2}} k_{\mathrm{B}} T}{2^{\frac{3}{2}} \pi\hbar^4 c_l} \sqrt{E_{\mathbf{k}} - E_c} \left[ \xi_{\perp} \Xi_d^2 + \eta_{\perp} \Xi_d \Xi_u + \zeta_{\perp} \Xi_u^2 \right], \tag{5.23}$$

where $c_l = c_{12} + 2c_{44} + \frac{3}{5}(c_{11} - c_{12} - 2c_{44})$. $\xi_{\parallel}$, $\eta_{\parallel}$, $\zeta_{\parallel}$, $\xi_{\perp}$, $\eta_{\perp}$ and $\zeta_{\perp}$ are the deformation potential coefficients, defined in terms of elastic constants, effective

masses, and integrals over the scattering probability, as per Table VI of Ref. [79]. We have taken elastic constants from experimental measurements of Ge [222] and PbTe [223, 224] at room temperature respectively. Our calculated values of these coefficients are given in Table 5.5, which for Ge agree very well with those reported in Ref. [79].

Table 5.5: Calculated deformation potential coefficients for the L valleys of Ge and PbTe.

| | $\xi_\parallel$ | $\eta_\parallel$ | $\zeta_\parallel$ | $\xi_\perp$ | $\eta_\perp$ | $\zeta_\perp$ |
|---|---|---|---|---|---|---|
| Ge | 1.23 | 2.32 | 1.17 | 1.31 | 1.63 | 0.91 |
| PbTe | 1.57 | 2.83 | 2.34 | 1.36 | 1.46 | 2.31 |

Given the above expressions for the momentum relaxation times in terms of deformation potentials, we now detail how $\Xi_u$ and $\Xi_d$ may be calculated. Contrasting the electron scattering rate of Eq. (5.17) with that of Eq. (2.128), we find:

$$C = \frac{1}{2}\sum_{\alpha\beta}\Xi_{\alpha\beta}\left(e^s_\alpha(\mathbf{q})q_\beta + e^s_\beta(\mathbf{q})q_\alpha\right) = \mathbf{H}_{nn}(\mathbf{k};\mathbf{q}s), \tag{5.24}$$

where $C$ is determined by the phonon strain tensor and the acoustic deformation potentials. This may be calculated using the DFPT method implemented in the ABINIT code [132, 134, 135], as previously discussed.

We now deduce values of $C$ in terms of $\Xi_u$ and $\Xi_d$ accounting for the directions of the strain polarisations (given in Table III of Ref. [79]) and $\mathbf{q}$. For a transverse acoustic phonon along [010] we obtain:

$$C = \frac{1}{3}\Xi^{\mathrm{L}}_u q, \tag{5.25}$$

and for a longitudinal acoustic phonon along $[0\bar{1}1]$ we obtain:

$$C = \Xi^{\mathrm{L}}_d q. \tag{5.26}$$

These values of $C/q$ hold to be constant in the limit of $\mathbf{q} \to 0$, with $C$ deviating from linear behaviour at larger $\mathbf{q}$. Thus, we extract the deformation potentials from the linear term of a quadratic fit to $\mathbf{H}_{nn}(\mathbf{k};\mathbf{q}s)$ versus $|\mathbf{q}|$ for the specified phonon direction and polarisation. For the L valley we calculate the electron-phonon matrix elements coupling states L and L + $\mathbf{q}$ (labelled as L $\to$ L + $\mathbf{q}$), as well as the matrix elements coupling states L $-$ $\mathbf{q}/2$ and L + $\mathbf{q}/2$ (labelled as

$\mathrm{L} - \mathbf{q}/2 \rightarrow \mathrm{L} + \mathbf{q}/2$). We then extract the deformation potentials from quadratic fits to both sets of coupling elements respectively.

#### 5.4.2.2 Deformation potentials of Ge and PbTe

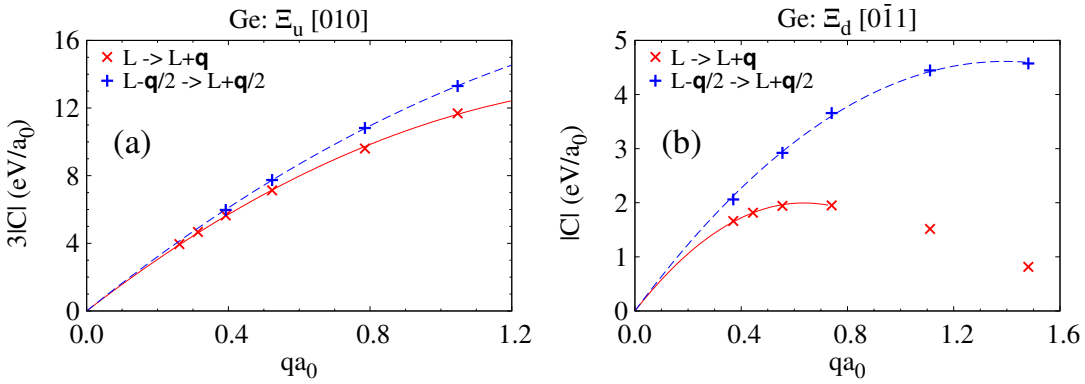



Figure 5.7: Calculated electron-phonon intravalley matrix elements in Ge as a function of phonon momentum $|\mathbf{q}|$, for transitions $\mathrm{L} \rightarrow \mathrm{L}+\mathbf{q}$ (red crosses) and $\mathrm{L}-\mathbf{q}/2 \rightarrow \mathrm{L}+\mathbf{q}/2$ (blue pluses). These yield (a) the uniaxial deformation potential, where $3C = \Xi_u^{\mathrm{L}}|\mathbf{q}|$ for an acoustic transverse phonon along [010], and (b) the dilatation deformation potential, where $C = \Xi_d^{\mathrm{L}}|\mathbf{q}|$ for an acoustic longitudinal phonon along $[0\bar{1}1]$. Quadratic fits to the matrix elements are shown with solid red and dashed blue lines. $a_0$ is the lattice constant of Ge.

Table 5.6: Deformation potentials for Ge compared to previous results from the literature and experiment. Deformation potentials are extracted from a quadratic fit to the $\mathrm{L} \rightarrow \mathrm{L} + \mathbf{q}$ matrix elements, and also from a quadratic fit to the $\mathrm{L} - \mathbf{q}/2 \rightarrow \mathrm{L} + \mathbf{q}/2$ matrix elements (in brackets).

| | Our results | Previous calculations | Experiment |
|---|---|---|---|
| $\Xi_u^{\mathrm{L}}$ (eV) | 16.67 (16.83) | 16.98[83], 16.80[200] | 16.20[225] |
| $\Xi_d^{\mathrm{L}}$ (eV) | −6.46 (−6.54) | −6.27[83], −4.43[200] | −12.30[226] |

The deformation potentials of Ge agree very well with previous results from the literature, and reasonably well with experiment, see Table 5.6. Fig. 5.7(a) shows the electron-phonon matrix elements for transitions $\mathrm{L} \rightarrow \mathrm{L} + \mathbf{q}$ and $\mathrm{L} - \mathbf{q}/2 \rightarrow \mathrm{L}+\mathbf{q}/2$ for a transverse acoustic phonon along [010], and Fig. 5.7(b) shows the matrix elements for these same transitions for a longitudinal acoustic phonon along $[0\bar{1}1]$. As the $\mathbf{q}$-vector becomes larger, the deviations from linearity, and thus from the deformation potential approximation, become larger. Along [010]

the deviation from linearity is relatively small, and the agreement between the matrix elements coupling states $\mathrm{L} \rightarrow \mathrm{L} + \mathbf{q}$ and $\mathrm{L} - \mathbf{q}/2 \rightarrow \mathrm{L} + \mathbf{q}/2$ is excellent, see Fig. 5.7(a). However, along $\mathbf{q} = [0\bar{1}1]$ there is a substantial deviation from linearity, and a significant disparity between the $\mathrm{L} \rightarrow \mathrm{L}+\mathbf{q}$ and $\mathrm{L}-\mathbf{q}/2 \rightarrow \mathrm{L}+\mathbf{q}/2$ matrix elements, see Fig. 5.7(b). Nevertheless, as $\mathbf{q} \rightarrow 0$ we see that the linear terms of the quadratic fits to the $\mathrm{L} \rightarrow \mathrm{L} + \mathbf{q}$ and $\mathrm{L} - \mathbf{q}/2 \rightarrow \mathrm{L} + \mathbf{q}/2$ matrix elements are nearly identical, resulting in values of $\Xi_u^{\mathrm{L}}$ and $\Xi_d^{\mathrm{L}}$ which differ by no more than $\sim 2\%$ from each other respectively, see Table 5.6. We note that this approach yields the absolute values of the deformation potentials only. Their signs are determined from an alternative method that calculates the energy shift of the conduction band due to strain, and will be discussed later in section 5.7.

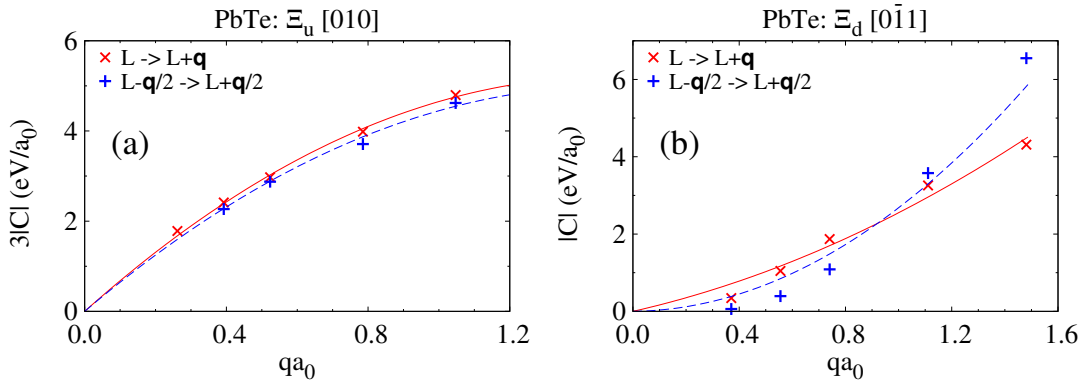



Figure 5.8: Calculated electron-phonon intravalley matrix elements in PbTe as a function of phonon momentum $|\mathbf{q}|$, for transitions $\mathrm{L} \rightarrow \mathrm{L} + \mathbf{q}$ (red crosses) and $\mathrm{L} - \mathbf{q}/2 \rightarrow \mathrm{L} + \mathbf{q}/2$ (blue pluses). These yield (a) the uniaxial deformation potential, where $3C = |\Xi_u^{\mathrm{L}}||\mathbf{q}|$ for an acoustic transverse phonon along [010], and (b) the dilatation deformation potential, where $C = |\Xi_d^{\mathrm{L}}||\mathbf{q}|$ for an acoustic longitudinal phonon along $[0\bar{1}1]$. Quadratic fits to the matrix elements are shown with solid red and dashed blue lines. $a_0$ is the lattice constant of PbTe.

Fig. 5.8(a) shows the electron-phonon matrix elements of PbTe for transitions $\mathrm{L} \rightarrow \mathrm{L} + \mathbf{q}$ and $\mathrm{L} - \mathbf{q}/2 \rightarrow \mathrm{L} + \mathbf{q}/2$ for a transverse acoustic phonon along [010], and Fig. 5.8(b) shows the matrix elements for these same transitions for a longitudinal acoustic phonon along $[0\bar{1}1]$. The uniaxial deformation potential of PbTe agrees reasonably well with experimental values and very well with respect to a previously calculated value of $\Xi_u^{\mathrm{L}} = 8.29$ eV [227], see Table 5.7. A value of $\Xi_u^{\mathrm{L}} = 3$ eV was obtained from piezoresistance measurements on $n$-type PbTe, whereas a value of $\Xi_u^{\mathrm{L}} = 4.5$ eV was obtained from the ultrasonic technique, see Refs. [228, 229] and references therein. There is a small deviation from linearity of the electron-phonon matrix elements along [010] in PbTe, and excellent agreement

Table 5.7: Deformation potentials for PbTe compared to previous results from the literature and experiment. Deformation potentials are extracted from a quadratic fit to the $L \rightarrow L + \mathbf{q}$ matrix elements, and also from a quadratic fit (where we enforce a positive linear term and neglect the matrix elements that are very close to zero) to the $L - \mathbf{q}/2 \rightarrow L + \mathbf{q}/2$ matrix elements (in brackets).

| | Our results | Previous calculation | Experiment |
|---|---|---|---|
| $\Xi_u^L$ (eV) | 7.23 (7.37) | 8.29 [227] | 3, 4.5 [228] |
| $\Xi_d^L$ (eV) | 1.92 (0.08) | −4.36 [227] | $21 - 22^a$ [228] |

[a] Obtained by fitting a model to electronic transport measurements.

between the $L \rightarrow L+\mathbf{q}$ and $L-\mathbf{q}/2 \rightarrow L+\mathbf{q}/2$ coupling elements, see Fig. 5.8(a), with a $\sim 2\%$ difference in our calculated values of $\Xi_u^L$. However, along $[0\bar{1}1]$ there is a break from linearity and a noticeable difference between the $L \rightarrow L + \mathbf{q}$ and $L - \mathbf{q}/2 \rightarrow L + \mathbf{q}/2$ coupling elements, see Fig. 5.8(b). In particular, the matrix elements $L - \mathbf{q}/2 \rightarrow L + \mathbf{q}/2$ increase rapidly with $\mathbf{q}$ and its first order term goes to zero as $\mathbf{q} \rightarrow 0$, see the blue crosses in Fig. 5.8(b). In this case, we calculate a value of $\Xi_d^L = 0.08$ eV from a quadratic fit to the $L - \mathbf{q}/2 \rightarrow L + \mathbf{q}/2$ transition where we enforce the linear term to be positive and neglect the matrix elements that are very close to zero. On the other hand, our extracted value of $\Xi_d^L$ from the $L \rightarrow L + \mathbf{q}$ transition is 1.92 eV. Again, we deduced the sign from an alternative calculation of band shifts due to strain as described in section 5.7. Our calculated values of $\Xi_d^L$ are in reasonable agreement with the previously calculated value of $\Xi_d^L = -4.36$ eV [227]. However, they are in poor agreement with the value of $\Xi_d^L = 21 - 22$ eV estimated by Ravich *et al.* [228] by fitting a model to electronic transport measurements. This discrepancy will be discussed in more detail in a later section. We note that the previously calculated values of $\Xi_u^L = 8.29$ eV and $\Xi_d^L = -4.36$ eV were obtained from first principles with an early, non-self-consistent augmented plane wave method [227].

### 5.4.3 Fröhlich interaction

In polar semiconductors there is another electron-phonon coupling mechanism to consider: Fröhlich interaction. This arises from the longitudinal optical motion of two oppositely charged ions generating a macroscopic electric field with which electrons interact. This interaction is so strong that polar optical scattering is the most dominant mechanism in group III-V and II-VI compounds [77].

For PbTe we need an estimate of the strength of Fröhlich interaction to

compare with intravalley acoustic scattering to see how both mechanisms limit the electronic mobility. Thus, we turn to the Fröhlich model as laid out in chapter 3 of Ref. [77]. The basic polar interaction energy is given by [77]:

$$\hat{H} = -\frac{1}{\epsilon_0}\int \mathbf{D}(\mathbf{R})\cdot\mathbf{P}(\mathbf{R})d\mathbf{R}. \tag{5.27}$$

where $\epsilon_0$ is the permittivity of free space. $\mathbf{D}(\mathbf{R})$ is the electric displacement at $\mathbf{R}$ associated with an electron at $\mathbf{r}$, which we take as simply [77]:

$$\mathbf{D}(\mathbf{R}) = -\nabla\left(\frac{\bar{e}}{4\pi|\mathbf{r}-\mathbf{R}|}e^{-q_0|\mathbf{r}-\mathbf{R}|}\right), \tag{5.28}$$

where $q_0$ is the reciprocal Debye screening length, and $\bar{e}$ is the electronic charge containing its sign. $\mathbf{P}(\mathbf{R}) = e^*\mathbf{u}^{lb}_{\text{opt}}/\Omega$ is the polarisation for an optical displacement and $e^*$ is the magnitude of the Born effective charge on the atoms [77]:

$$e^* = \left(m_r\Omega\omega_0^2\epsilon_0^2\left(\frac{1}{\epsilon_\infty}-\frac{1}{\epsilon_s}\right)\right)^{\frac{1}{2}}, \tag{5.29}$$

where $\epsilon_s$ is the static dielectric constant, $m_r$ is the reduced mass of the two atoms in the unit cell, $\Omega$ is the primitive cell volume, and $\omega_0$ is the longitudinal optical mode frequency at $\Gamma$.

Thus, for a long-wavelength optical displacement, we obtain the Hamiltonian [77]:

$$\hat{H} = -N_l^{-\frac{1}{2}}\sum_{\mathbf{q}s}\frac{\bar{e}e^*}{\Omega\epsilon_0}\frac{q}{q^2+q_0^2}\sum_b\left(\frac{\hbar}{2m_b\omega_{\mathbf{q}s}}\right)^{\frac{1}{2}}\mathbf{e}_b^s(\mathbf{q})\left(\hat{a}_{\mathbf{q}s}+\hat{a}^\dagger_{-\mathbf{q}s}\right)e^{i\mathbf{q}\cdot\mathbf{r}}. \tag{5.30}$$

This may be inserted into Fermi's Golden Rule to obtain the momentum relaxation time:

$$\begin{aligned}\frac{1}{\tau} =& \frac{\Omega}{8\pi^2 m_r\omega_0}\left(\frac{\bar{e}e^*}{\Omega\epsilon_0}\right)^2 \\ &\times\int\frac{q^2}{(q^2+q_0^2)^2}\left(\left(\bar{n}_{\mathbf{q}s}+\frac{1}{2}\mp\frac{1}{2}\right)\delta\left(\epsilon_{n\mathbf{k}}-\epsilon_{m\mathbf{k}'}\pm\hbar\omega_{\mathbf{q}s}\right)\delta_{\mathbf{k}\pm\mathbf{q}-\mathbf{k}',\mathbf{G}}\right)d\mathbf{k}',\end{aligned} \tag{5.31}$$

where we assume parabolic bands, and again the upper sign in the above equation is for phonon absorption processes, with the lower for phonon emission. However, we note that the momentum relaxation time may not be valid for polar-optical phonon scattering due to the large energy exchange that takes place between electrons and phonons. In principle, the BTE should be solved self-consistently

to account for these processes. Nevertheless, since PbTe has a very small LO frequency (∼14 meV) compared to most other materials, the use of the momentum relaxation time may be appropriate for all but the lowest temperatures.

Within the low carrier concentration regime, we may neglect the effects of screening, and set $q_0 = 0$. Thus, we obtain the momentum relaxation rate [77]:

$$\begin{aligned}\frac{1}{\tau} =& \frac{e^2\omega_0}{4\pi\hbar v_k}\left(\frac{1}{\epsilon_\infty}-\frac{1}{\epsilon_s}\right)\left(n(\omega_0)\left(1+\frac{\hbar\omega_0}{E_k}\right)^{\frac{1}{2}}+[n(\omega_0)+1]\left(1-\frac{\hbar\omega_0}{E_k}\right)^{\frac{1}{2}}\right.\\ &\left.+\frac{\hbar\omega_0}{E_k}\left[-n(\omega_0)\sinh^{-1}\left(\frac{E_k}{\hbar\omega_0}\right)^{\frac{1}{2}}+[n(\omega_0)+1]\sinh^{-1}\left(\frac{E_k}{\hbar\omega_0}-1\right)^{\frac{1}{2}}\right]\right).\end{aligned} \tag{5.32}$$

where the phonon absorption and emission terms have been weighted by the respective changes in momentum. We implement this model of Fröhlich interaction for PbTe in the following section, and obtain the electronic mobility limited by polar optical interaction.

## 5.5 Electron mobility

We calculate electronic lifetimes $\tau$ summing over electron-phonon coupling mechanisms using Matthiessen's rule [16]:

$$\frac{1}{\tau} = \frac{1}{\tau_{\text{intervalley}}}+\frac{1}{\tau_{\text{intravalley optical}}}+\frac{1}{\tau_{\text{intravalley acoustic}}}+\frac{1}{\tau_{\text{polar optical}}}. \tag{5.33}$$

We then calculate the electronic mobilities of Ge and PbTe inserting $\tau$ into Eq. (5.3).

Intravalley acoustic scattering is by far the most dominant contribution limiting the electronic mobility of Ge, see Fig. 5.9. We note that intravalley optical scattering becomes more significant with higher temperatures, while even at room temperature intervalley scattering does not play a significant role. We also find very good agreement for the electronic mobility of Ge compared with experimental measurements of a single crystalline sample with a carrier concentration of $2.4\times10^{14}$ cm$^{-3}$ at room temperature [230], see Fig. 5.10. The contribution due to ionized impurity scattering has been subtracted from experimental measurements assuming it follows the Brooks-Herring relation [80].

The electronic mobility of PbTe limited by polar optical scattering is one order of magnitude lower than that of intravalley acoustic scattering, see Fig. 5.11. In our model, the contributions of intervalley and intravalley optical scattering are zero, forbidden by symmetry as discussed. While there remain questions as to the

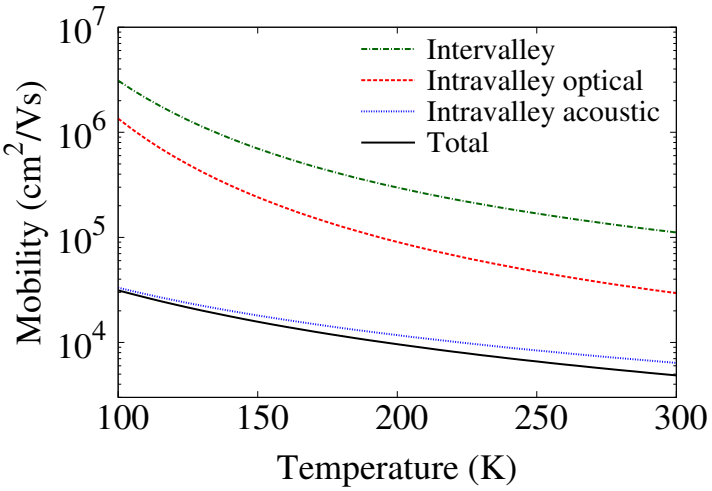



Figure 5.9: The calculated electronic mobilities of Ge limited by intervalley (green dot-dashed line), intravalley optical (dashed red line) and intravalley acoustic (dotted blue line) scattering. The total electronic mobility of Ge limited by electron-phonon coupling is shown by the solid black line.

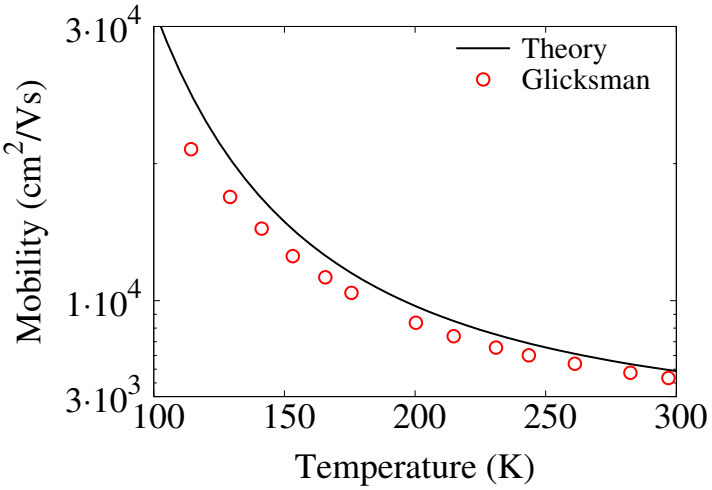



Figure 5.10: Calculated electronic mobility of Ge compared to measurements of a single crystalline sample by Glicksman [230].

reliability of the calculated deformation potentials of PbTe, notably $\Xi_d$, it is clear that Fröhlich interaction is by far the most dominant electron-phonon scattering mechanism in PbTe for low temperatures and low doping concentrations. Further, we find good agreement between the electronic mobility of PbTe compared to experimental measurements at $100 - 200$ K of a single crystalline sample with a carrier concentration of $1 \times 10^{18}$ cm$^{-3}$ by Allgaier and Scanlon [231], see Fig. 5.12. However, at 300 K our calculated mobility differs from experiment by a factor of $\sim$2.

There are several outstanding issues with our calculation that must be resolved

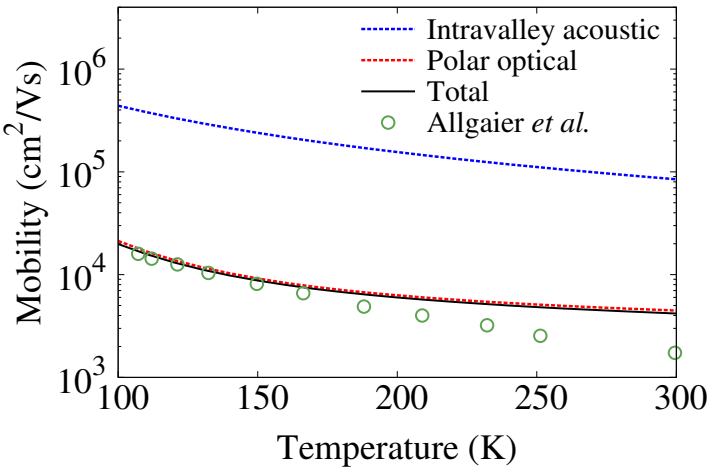



Figure 5.11: The calculated electronic mobilities of PbTe limited by intravalley acoustic (dotted blue line) and polar optical (dashed red line) scattering. The total electronic mobility of PbTe due to electron-phonon coupling is shown by the solid black line.

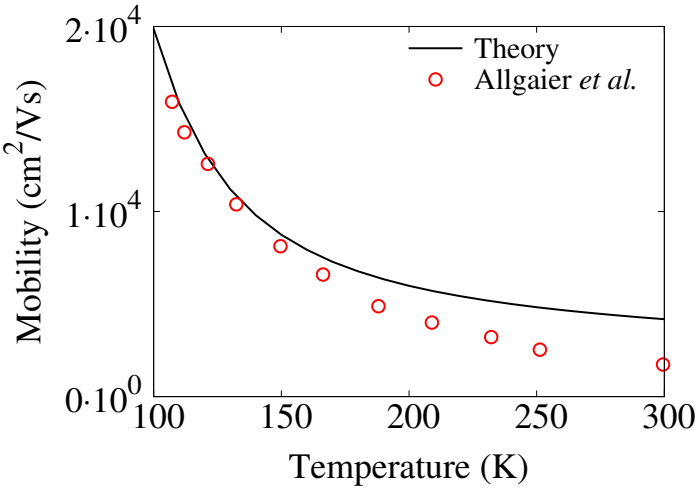



Figure 5.12: Calculated electronic mobility of PbTe compared to experimental measurements by Allgaier and Scanlon [231].

to obtain good agreement with experiment at room temperature. The most notable of these issues is the discrepancy between our calculated deformation potentials for PbTe and their values within the literature [227, 228]. This may stem from the inaccurate energy separation of the 1st and 2nd conduction band states in LDA without SOI, potentially leading to errors with the calculation of electron-phonon matrix elements. Thus, a higher level of theory is required to properly describe the electronic band structure of PbTe before progress may be made on this issue.

## 5.6 Electronic band structure from hybrid functionals

There exist multiple issues with the LDA description of the electronic band structure of PbTe for the purposes of calculating electronic transport due to electron-phonon coupling. These include the mixing of states at the band gap when SOI is included, which results in poor description of effective electron masses, or the inaccurate energy separation of the $1^{st}$ and $2^{nd}$ conduction bands when SOI is neglected. Thus we move to a higher level of theory beyond DFT to reproduce the electronic band structure of PbTe, in order to accurately describe the energy separation and curvature of the states near the band gap. We use the Vienna *ab initio* simulation package (VASP) [232, 233] to perform our electronic band structure calculations, which has recently been expanded to include a number of hybrid functionals [234]. The basis set for the one-electron wave functions is constructed with the Projector Augmented Wave (PAW) method [235, 236], a generalised form of the pseudopotential. In its standard mode VASP performs a fully relativistic calculation for core electron states, and treats valence states using a scalar relativistic approximation [237]. The effects of spin orbit coupling are included with a second variation procedure [237]. We note that we read in VASP's wavefunction files with the use of the WaveTrans code [238, 239]. All calculations presented from here on are performed with the VASP code, except where noted.

Hybrid functionals are constructed replacing some proportion of exchange and correlation energies from DFT with those from the exact Hartree-Fock solution [240], significantly improving the accuracy of electronic structure properties compared to experiment. One possible method to determine this mixing proportion of DFT and Hartree-Fock terms is by fitting to a dataset of measured atomisation energies, such as is done for B3LYP [237, 241]. Alternatively, in the case of PBE0, the correlation energy is taken as per DFT, with the exchange energy consisting of a portion $a$ from Hartree-Fock theory, with the remaining portion $(1-a)$ from DFT [241]:

$$E_{xc}^{\mathrm{PBE0}} = aE_x^{\mathrm{HF}} + (1-a)E_x^{\mathrm{PBE}} + E_c^{\mathrm{PBE}}, \tag{5.34}$$

where the value of the mixing parameter was found to be $a = 1/4$ from perturbation theory [241]. The inclusion of exchange energy only from Hartree-Fock theory helps to cancel out some of the notorious single electron "self interaction error" [242]. However, the computation of long-range integrals can be expensive in large solids and systems with metallic properties. Heyd, Scuseria, and Ernzerhof

[243] introduced the concept of a screened hybrid functional, modifying PBE0 to achieve significantly lower computational cost. A screened Coulomb potential is used to screen the long range part of the Hartree-Fock exchange, which is then replaced with the corresponding long range exchange as per DFT:

$$E_{xc}^{\mathrm{HSE}} = \frac{1}{4}E_x^{\mathrm{HF,SR}}(\mu) + \frac{3}{4}E_x^{\mathrm{PBE,SR}}(\mu) + E_x^{\mathrm{PBE,LR}}(\mu) + E_c^{\mathrm{PBE}} \tag{5.35}$$

where SR and LR signify short range and long range terms respectively. $\mu$ is the range separation parameter which determines the screening, and thus defines the range of Hartree-Fock correction. It has been empirically determined that a value of $\mu \approx 0.2 - 0.3$ Å$^{-1}$ is optimum for predicting electronic band structure properties [243, 244]. In VASP, setting $\mu = 0.3$ Å$^{-1}$ gives the HSE03 functional, and setting $\mu = 0.2$ Å$^{-1}$ yields the HSE06 functional [243, 245, 246, 247].

The effectiveness of screened hybrid functionals [243] in capturing structural, elastic, and electronic properties has previously been shown for a wide range of semiconductors [244, 248, 249]. In particular, the documented ability of the HSE03 functional to correctly reproduce the band gap and correct ordering of states with the inclusion of SOI in lead chalcogenides [205] is the main motivation for its use in this work. We show the electronic band structure of PbTe calculated with the HSE03 functional including SOI in Fig. 5.13.

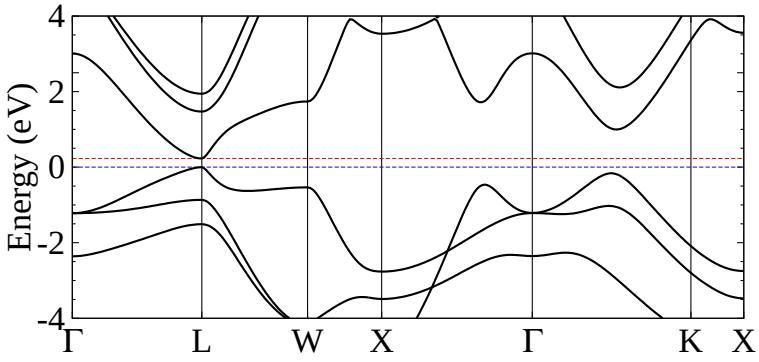



Figure 5.13: Electronic band structure of PbTe, calculated using the HSE03 hybrid functional and PAW potentials including spin orbit interaction. The energies of the valence band maximum (blue dashed line) and conduction band minimum (red dashed line) are also highlighted.

The HSE03 functional including SOI reproduces the band gap and effective electron masses of PbTe to excellent agreement with experiment and previous hybrid functional and quasi-particle self-consistent *GW* (QS*GW*) calculations, see Table 5.8. The agreement of the band gap with experiment is improved by the inclusion of the semicore $5d^{10}$ electrons of Pb in the valence region alongside

Table 5.8: The electronic band gap and effective electron masses of PbTe calculated with the PBE, HSE03, and HSE06 functionals respectively including SOI compared to HSE03 and quasi-particle self-consistent *GW* calculations from the literature and experiment, "+sc" signifies the inclusion of semicore electrons ($5d^{10}$ of Pb) in the valence region.

| | PBE[a] (+sc) | HSE03[a] (+sc) | HSE06[a] (+sc) | HSE03[b] [205] | QS*GW* [207] | Exp. 1 [212] | Exp. 2 [213] |
|---|---|---|---|---|---|---|---|
| $E_g$ (eV) | 0.081 | 0.237 | 0.325 | 0.20 | 0.29 | 0.19[c] | 0.19[c] |
| $m_{\parallel}^{*,v}/m_e$ | 0.618 | 0.341 | 0.411 | 0.296 | 0.338 | 0.255 | 0.310 |
| $m_{\perp}^{*,v}/m_e$ | 0.184 | 0.030 | 0.036 | 0.029 | 0.029 | 0.024 | 0.022 |
| $m_{\parallel}^{*,c}/m_e$ | 0.362 | 0.246 | 0.277 | 0.223 | 0.247 | 0.210 | 0.240 |
| $m_{\perp}^{*,c}/m_e$ | 0.120 | 0.027 | 0.033 | 0.027 | 0.027 | 0.021 | 0.024 |

[a] Calculated using the theoretically predicted lattice constant.

[b] Calculated using the low temperature experimental lattice constant.

[c] increasing to ∼0.3 eV at room temperature [214].

the $6s^26p^2$ states of Pb and $5s^25p^4$ states of Te typically included in *ab initio* pseudopotential calculations. The excellent agreement of the effective masses with experiment is in part due to the fact that HSE03 functional obtains the correct ordering of states at the band gap, which we confirmed by computing the previously defined overlap of the cell periodic parts of the wavefunctions. We found that the wavefunction of the state at L below the band gap has the character of the valence band, while the state above the band gap has the character of the conduction band, see Figs. 5.14(a) and 5.14(c). Thus, there is no mixing of the conduction and valence bands as seen using the LDA with SOI, see Fig. 5.15(b) [205]. Furthermore, the valence band maximum is found at L, not Σ as was the case for the LDA including SOI. The HSE03 functional also captures a much larger energy separation of the 1st and 2nd conduction band states compared to the LDA without SOI, see Fig. 5.15(a). This potentially resolves any issues whereby the 2nd conduction band is interfering with the calculation of electron-phonon matrix elements near the conduction band minimum. The HSE03 functional obtains a band gap and effective masses that are in better agreement with experiment than those calculated using the HSE06 functional. Thus, we use the HSE03 hybrid functional for calculations of PbTe here on.

The PBE functional including SOI obtains a very narrow band gap and poor effective masses compared to experiment, see Table 5.8, further demonstrating the necessity of moving to a higher level of theory beyond DFT-LDA/PBE.

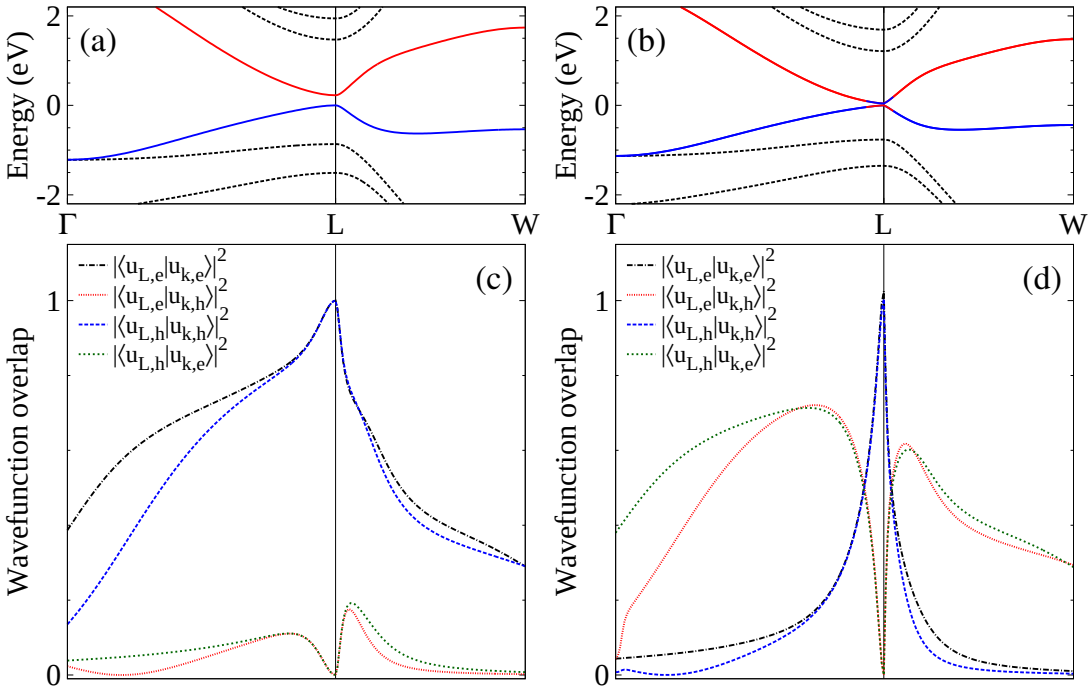



Figure 5.14: Electronic band structure of PbTe along the Γ-L-W line including SOI calculated using (a): the HSE03 hybrid functional, and (b): the PBE functional. A solid red (blue) line shows a state whose character mostly corresponds to that of the conduction (valence) band as deduced from wavefunction overlaps. The overlaps of the cell periodic parts of the wavefunctions between the 1$^{st}$ electronic states counting upward (labelled as e) and downward (labelled as h) from the zero temperature Fermi level at L and those states at **k** are shown for (c): the HSE03 hybrid functional and (d): the PBE functional. The following wavefunction overlaps are plotted: $|\langle u_{L,\mathrm{e}}|u_{\mathbf{k},\mathrm{e}}\rangle|^2$ (dot-dashed black line), $|\langle u_{L,\mathrm{e}}|u_{\mathbf{k},\mathrm{h}}\rangle|^2$ (dotted red line), $|\langle u_{L,\mathrm{h}}|u_{\mathbf{k},\mathrm{h}}\rangle|^2$ (large-dashed blue line), $|\langle u_{L,\mathrm{h}}|u_{\mathbf{k},\mathrm{e}}\rangle|^2$ (small-dashed green line).

Interestingly, using the theoretically predicted 0 K lattice constant of 6.568 Å, we obtain a positive band gap of 0.08 eV with this functional, unlike for LDA-HGH calculations which include SOI, see Table 5.2. However, using a room temperature experimental value of 6.443 Å [205], we predict a negative band gap of −0.04 eV with the PBE functional. We confirmed mixing of the conduction and valence band states by computing the previously defined overlaps of the cell periodic parts of the wavefunctions of the states above and below the zero temperature Fermi level at this experimental lattice constant, see Figs. 5.14(b) and 5.14(d), in agreement with the literature [205]. This suggests that the DFT-PBE framework is extremely sensitive to the value of the lattice parameter used, with small changes to its value resulting in a positive or negative band gap. Thus,

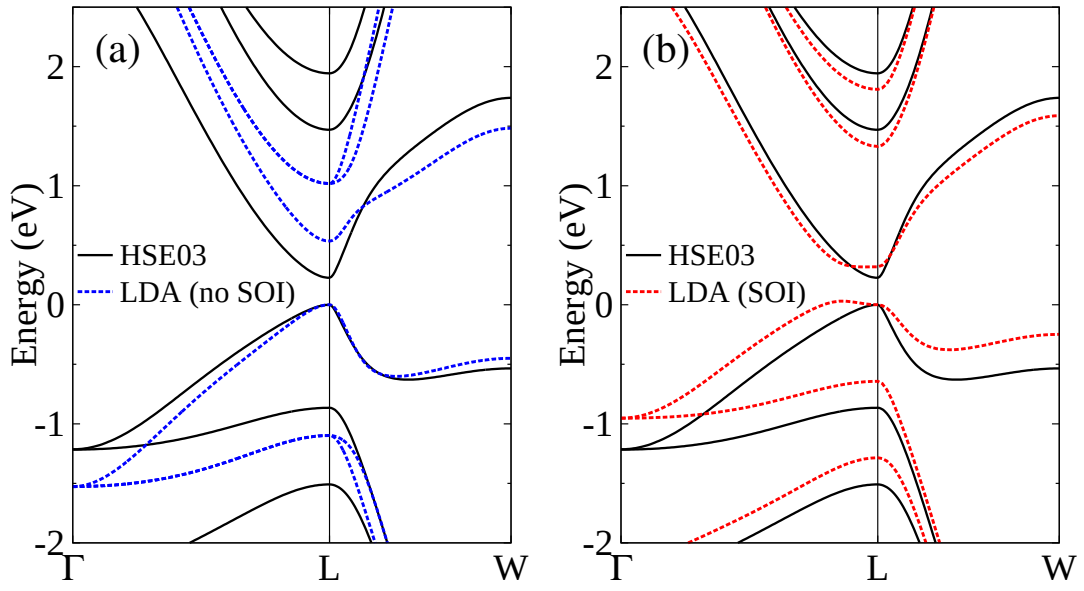



Figure 5.15: Electronic bands for PbTe calculated using the HSE03 functional including SOI (solid black lines) compared with those calculated using the LDA functional (a) excluding SOI (dashed blue lines) and (b) including SOI (dashed red lines).

the PBE is insufficient to describe the electron band structure of PbTe, requiring the use of hybrid functionals.

Table 5.9: Hydrostatic pressure gap coefficients for PbTe calculated with the LDA, PBE, and HSE03 functionals with and without SOI, compared to experimental measurements at 4 K, 7 K, and 300 K. Pressure was simulated by setting the lattice constant to $0.999 \times a_0$, where $a_0$ is its theoretically predicted equilibrium value.

| | $dE_g/dP$ (inc. SOI) ($\times 10^{-6}$ eV/Bar) | $dE_g/dP$ (exc. SOI) ($\times 10^{-6}$ eV/Bar) |
|---|---|---|
| LDA[a] | +2.1 | −4.6 |
| PBE | −4.9 | −4.7 |
| HSE03 | −7.0 | – |
| Exp. [215, 218, 224] | −7.4, −7.5 | −7.4, −7.5 |

[a] calculated with ABINIT

We further confirm the accurate description of the electronic band structure of PbTe using the HSE03 functional by comparing the calculated hydrostatic pressure gap coefficient with experiment, which is defined as the change in the electronic band gap with respect to pressure, $dE_g/dP$. The value of this

coefficient calculated with the HSE03 functional for PbTe compares very well with experimental data and describes a decreasing band gap with pressure, see Table 5.9. Thus, we expect that the hybrid functional will adequately capture changes in the electronic band structure due to strain or pressure, of particular importance when computing deformation potentials in the following section. The PBE functional also captures the correct sign of $dE_g/dP$ at the theoretical lattice constant, however its magnitude is in poor agreement with experiment. The calculated value with the LDA including SOI yields an increasing band gap with pressure due to the inverted ordering of the conduction and valence bands and heavy mixing of states at the band gap [205].

## 5.7 Deformation potentials from band shifts due to strain using hybrid functionals

In this section we calculate the deformation potentials of Ge and PbTe following the pioneering work of van de Walle and Martin [201, 202, 203, 204] on band shifts due to strain in semiconductors. We use this as an alternative method to compute the deformation potentials of PbTe in order to resolve the discrepancy between our calculated values using DFPT and those within the literature. Furthermore, coupling this method with hybrid functionals which give a much better representation of electronic states near the band gap compared to LDA allows us to include the effects of spin orbit coupling. The approach of van de Walle and Martin has been applied to a wide range of semiconductors to capture band offsets at semiconductor interfaces and deformation potentials to good agreement with experiment.

The calculation of $\Xi_u$ is relatively straightforward, given that we need only find the energy splitting between previously degenerate valleys in a strained material. On the other hand, $\Xi_d$ is significantly more involved as it requires knowledge of the conduction band energy shift under strain on an absolute scale [250].

### 5.7.1 Uniaxial deformation potential

Under uniaxial strain along [111] the L valleys of a cubic material cease to be degenerate and shift in energy proportional to the uniaxial deformation potential and the applied strain. These shifts in energy at the L point may be derived from Eq. (5.21), which yields the change in energy of the conduction bands [201, 202]:

$$\Delta E_c^{[111]} = 2\Xi_u^{\mathrm{L}}\epsilon_{xy}, \tag{5.36}$$

$$\Delta E_c^{[\bar{1}11],[1\bar{1}1],[11\bar{1}]} = -\frac{2}{3}\Xi_u^{\mathrm{L}}\epsilon_{xy}, \tag{5.37}$$

allowing us to write the uniaxial deformation potential:

$$\Xi_u^{\mathrm{L}} = \frac{3\Delta E_{\mathrm{L}}}{8\epsilon_{xy}} \tag{5.38}$$

where $\Delta E_{\mathrm{L}}$ is the energy difference between previously degenerate L valleys.

To calculate this energy splitting from DFT, we strain the lattice constant parallel to the trigonal axis, $a_{0,\parallel}$, and hold constant at a value $a_\parallel$. We then contract the lattice constant perpendicular to the trigonal axis, $a_{0,\perp}$, to a value $a_\perp$ such that the volume of the primitive cell remains constant. Strain is then defined as [201, 202]:

$$\epsilon_{xy} = \frac{1}{3}\left(\frac{a_\perp - a_{0,\perp}}{a_{0,\perp}} - \frac{a_\parallel - a_{0,\parallel}}{a_{0,\parallel}}\right). \tag{5.39}$$

Table 5.10: Uniaxial deformation potential of Ge calculated from the splitting of previously degenerate L-valleys under strain using the LDA and HGH pseudopotentials in ABINIT. $\Xi_u^{\mathrm{L}}$ is compared to our values calculated using DFPT, previous calculations from the literature, and experiment.

| | Ge | | | |
|---|---|---|---|---|
| | Band splitting | DFPT | Previous calculations | Experiment |
| $\Xi_u^{\mathrm{L}}$ (eV) | 15.80 | 16.67 | 16.98[83],16.80[200] | 16.2 [225] |

The calculated $\Xi_u^{\mathrm{L}}$ for Ge using this method is 15.8 eV, which agrees very well with our calculated value from DFPT and with respect to experiment, see Table 5.10. We note the excellent agreement between our two calculated values which are both performed within the LDA-HGH framework. For PbTe, the values calculated using different exchange-correlation functionals are broadly in agreement with each other, and in reasonable agreement with experiment and a previous calculation, see Table 5.11. In particular, $\Xi_u^{\mathrm{L}}$ calculated with the HSE03 functional agrees fairly well with the LDA results both from band splitting due to strain and DFPT. When SOI is taken into consideration at the LDA level of theory, we calculate a value of $\Xi_u^{\mathrm{L}} = 7.73$ eV from strain induced band splitting, in excellent agreement with the value calculated excluding SOI. This indicates

Table 5.11: Uniaxial deformation potential of PbTe calculated from the splitting of previously degenerate L-valleys under strain for the LDA, PBE (inc. SOI), and HSE03 (inc. SOI) functionals. They are compared to our values calculated using DFPT, a previous calculation from the literature, and experiment.

| | PbTe | | | | |
|---|---|---|---|---|---|
| | Band splitting | | DFPT | Previous calculation | Experiment |
| $\Xi_u^{\mathrm{L}}$ (eV) | LDA[a]: | 7.99 | 7.23 | 8.29 [227] | 3, 4.5 [228] |
| | LDA+SOI[a]: | 7.73 | | | |
| | PBE: | 7.25 | | | |
| | HSE03: | 5.48 | | | |

[a] calculated with ABINIT

that the character of the states at the band gap is not so important for the calculated value of $\Xi_u^{\mathrm{L}}$ since the conduction and valence bands at L move either downward or upward according to Eqs. (5.36) and (5.37) due to mirror symmetry. Furthermore, the value of $\Xi_u^{\mathrm{L}}$ for PbTe calculated with the LDA from strain induced splitting agrees extremely well with our value from DFPT, which both use the same pseudopotentials and functional.

### 5.7.2 Dilatation deformation potential

Within deformation potential theory and using Eq. (5.21) we may write the shift of the conduction band minimum at L for an isotropic deformation as [201, 202]:

$$\Delta E_c^{\mathrm{L}} = \left(\Xi_d + \frac{1}{3}\Xi_u\right) \bar{\bar{1}} : \bar{\bar{\epsilon}} = a_c \bar{\bar{1}} : \bar{\bar{\epsilon}} \tag{5.40}$$

where $\bar{\bar{1}}$ is the unit tensor, and $\bar{\bar{\epsilon}}$ is the strain tensor. $a_c$ is the hydrostatic deformation potential for the conduction band, and refers to changes of the electronic bands under strain or pressure on an absolute scale [250]. However, due to the long range nature of the Coulomb interaction the zero of energy is undefined for a bulk crystal, resulting in no intrinsic energy scale with which to reference energy levels [251]. To get around this issue, we calculate $a_c$ following the procedure of van de Walle and Martin [201, 202].

We start by performing separate calculations of the bulk unstrained and strained material to obtain the conduction band energies at L for either case, $E_c^{\mathrm{L}}(0)$ and $E_c^{\mathrm{L}}(\epsilon)$ respectively. These calculations also yield the total potential

acting on the electrons, defined as the sum of ionic, Hartree, and exchange-correlation potentials [201], the averages of which we denote as $V(0)$ and $V(\epsilon)$ respectively. Next, we construct a heterostructure which consists of unstrained and strained materials meeting at an interface, which allows us to obtain the average total potential energies of either region, $V'(0)$ and $V'(\epsilon)$ respectively, on an absolute scale. We then align the total potentials of the bulk calculations to those of the heterostructure, yielding the absolute splitting of the conduction band energies. Thus, we may write the hydrostatic deformation potential for the conduction band as:

$$a_c = \frac{\Delta E_c^{\mathrm{L}}}{\epsilon} = \frac{1}{\epsilon}\Big(\big(E_c^{\mathrm{L}}(\epsilon) - V(\epsilon)\big) - \big(E_c^{\mathrm{L}}(0) - V(0)\big) + \big(V'(\epsilon) - V'(0)\big)\Big). \quad (5.41)$$

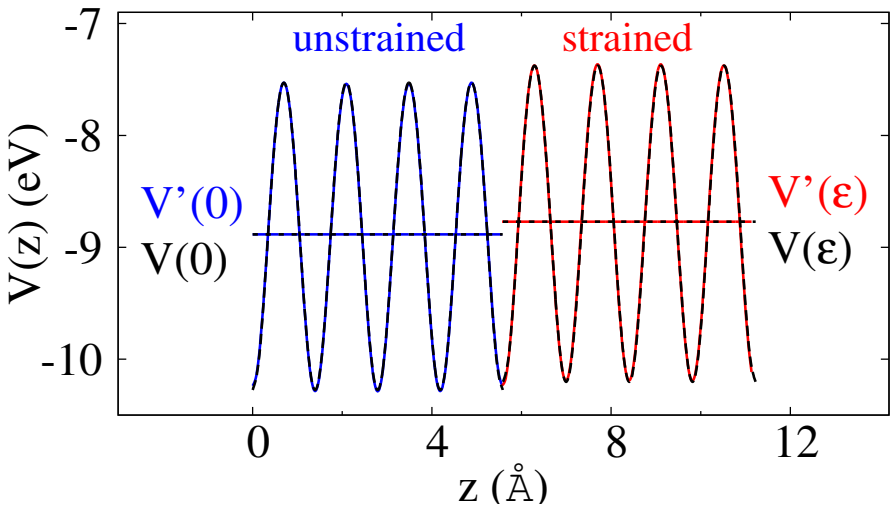



Figure 5.16: Total average potential $V(z)$ for an 8-atom Ge heterostructure consisting of unstrained and strained regions meeting at a (001) interface. The solid blue (red) lines show the total average potential of the unstrained (strained) region, with average potential energies $V'(0)$ and $V'(\epsilon)$ respectively. The total average potential for each value of $z$ in the bulk unstrained and strained material are shown with dashed black lines, aligned to the heterostructure such that $V(0) = V'(0)$ and $V(\epsilon) = V'(\epsilon)$ respectively.

For calculations presented here, we construct a (001) interface between the unstrained and strained regions, with 1% of strain applied perpendicular to the interface. Our calculations of the bulk unstrained and strained materials are performed on 4 atom supercells. The heterostructure is then grown by repeating 4 atom supercells of the unstrained and strained material along the $z$-direction to the desired length. The average potential at each value of $z$ along the [001]-

direction is defined as:

$$V(z) = \frac{1}{Na^2} \int \int V(\mathbf{r}) dx dy. \tag{5.42}$$

We show this average potential $V(z)$ for an 8-atom Ge heterostructure in Fig. 5.16, highlighting the unstrained and strained regions. The average potentials of bulk unstrained and strained Ge are overlaid on top (dashed black lines), shifted upwards/downwards in energy such that $V(0) = V'(0)$ and $V(\epsilon) = V'(\epsilon)$ respectively. We note the deviation of the average potential of the heterostructure from bulk behaviour in the vicinity of the interface. We assume that the atoms occupy the ideal positions of the strained structures. However, this is not the case for all interfaces, with certain directions producing a change in internal displacement parameter dependent on orientation. This is of particular importance for polar interfaces, where the change in atomic position produces a dipole shift [203, 252].

The use of a supercell introduces periodicity into the heterostructure calculation, the size of which must be converged in order to restore bulk behaviour for the average potential away from the interface. However, we found that our calculated values of $a_c$ did not converge with respect to increasing supercell size as anticipated. This numerical instability was due to the sparse set of computed points defining the average potential $V(z)$ in the heterostructure calculation, and the fact that these output points did not necessarily align to the peaks and troughs of $V(z)$. This introduced inconsistencies in the extraction of the values of $V'(0)$ and $V'(\epsilon)$. Thus, we performed a cubic spline interpolation of the average potential using GNUPLOT, to generate a sufficiently dense set of points. We extracted the average potential energies from the centre of the unstrained and strained regions of the heterostructure, where the average potential is most bulk-like. In doing so, we defined the region over which the average potential energy is calculated to be a 4-atom subsection of the supercell of the unstrained and strained parts of the heterostructure respectively. This procedure yielded convergence with respect to increasing supercell size.

Our calculated value of $\Xi_d^{\mathrm{L}} = -7.15$ eV for Ge agrees very well with previous calculations and with experiment, see Table 5.12. We also find very good agreement between our calculated values from band shifts due to strain and those calculated previously with DFPT which both use the same pseudopotential and functional. This serves as an additional check of both methods and demonstrates that there are no significant errors within the implementation. We note that convergence with respect to supercell size is of particular importance, however, a supercell size larger than 12 atoms is sufficient to get a reasonably converged

value, as previously claimed [201].

Table 5.12: Dilatation deformation potential of Ge calculated from the energy shift of the L-valley under strain using the LDA and HGH pseudopotentials in ABINIT. $\Xi_d^{\mathrm{L}}$ is compared to our values calculated using DFPT, previous calculations from the literature, and experiment.

| | Ge | | | |
|---|---|---|---|---|
| | Band shift | DFPT | Previous calculations | Experiment |
| $\Xi_d^{\mathrm{L}}$ (eV) | −7.15 | −6.46 | −6.27[83],−4.43[200] | −12.30[226] |

The calculated value of $\Xi_d^{\mathrm{L}} = 0.47$ eV for PbTe using the band shift method for the LDA functional without SOI is in fair agreement with the corresponding calculated values using DFPT of 0.08 eV and 1.92 eV, see Table 5.13, further highlighting the difficulties with extracting this parameter from first principles. However, since our calculated values of $\Xi_d^{\mathrm{L}}$ are small compared to typical values of this deformation potential in other semiconductors, and our values calculated using DFPT and from band offsets fall within ∼1 eV of each other, we deem their agreement good. The HSE03 functional yields a value of $\Xi_d^{\mathrm{L}} = 0.78$ eV, comparable to the values of $\Xi_d^{\mathrm{L}}$ calculated with the LDA and PBE functionals, see Table 5.14. This is despite the fact that it obtains a more accurate description of the electronic band structure compared to DFT methods. However, our calculated values of $\Xi_d^{\mathrm{L}}$ remain in poor agreement with the value of 21-22 eV obtained by Ravich *et al.* [228]. Nevertheless, the consistency of our calculated values suggests this discrepancy with the literature is unlikely to be due to an error in our implementation of either approach.

Indeed, we note that there may be issues with the values of the deformation potentials obtained by Ravich *et al* [228]. In extracting the deformation potentials of PbTe, Ravich *et al.* assumed that the electronic mobility as a function of carrier density at 77 K is entirely limited by three scattering mechanisms: impurity scattering, polar optical scattering, and acoustic phonon scattering. Using experimental parameters for the former two mechanisms, the electron mobility limited by these is subtracted from the experimental values. An effective deformation potential is then obtained by fitting a model to the remaining mobility which is assumed to be entirely due to acoustic phonon scattering. Thus, the discrepancy between our calculated deformation potentials and those estimated by Ravich *et al.* may be due to the more severe approximations used in that model versus ours, for example, neglecting the anisotropy in the momentum relaxation times.

Table 5.13: Deformation potentials of PbTe calculated from the energy shift of the L-valley under strain using the LDA and HGH pseudopotentials excluding SOI in ABINIT. They are compared to our values calculated using DFPT, and previous results from the literature, and experiment.

| | PbTe | | | |
|---|---|---|---|---|
| | Band shift | DFPT | Previous calculation | Experiment |
| $\Xi_u^{\mathrm{L}}$ (eV) | 7.99 | 7.23 | 8.29 [227] | $3, 4.5$ [228] |
| $\Xi_d^{\mathrm{L}}$ (eV) | 0.47 | 1.92 | $-4.36$ [227] | $21 - 22^{\mathrm{a}}$ [228] |

[a] Obtained by fitting a model to electronic transport measurements.

Table 5.14: Dilatation deformation potentials for PbTe calculated using the LDA functional excluding/including SOI in ABINIT and with the PBE and HSE03 functionals including SOI in VASP, shown for multiple supercell sizes.

| PbTe | $\Xi_d^{\mathrm{L}}$ (eV) | | | |
|---|---|---|---|---|
| Supercell size (atoms) | LDA exc. SOI | LDA inc. SOI | PBE | HSE03 |
| 8 | 3.67 | 2.41 | $-1.73$ | $-1.20$ |
| 16 | $-0.66$ | $-2.32$ | $-0.13$ | $-0.22$ |
| 24 | 0.21 | $-1.91$ | 0.01 | 0.91 |
| 32 | 0.35 | $-1.69$ | $-0.12$ | 0.69 |
| 40 | 0.39 | $-1.66$ | $-0.20$ | 0.78 |
| 48 | 0.47 | $-1.55$ | $-0.22$ | – |

Since our calculated values of the deformation potentials of PbTe using hybrid functionals are in good agreement with those calculated using the LDA excluding SOI, the calculated mobility of PbTe using the HSE03 functional is very similar to that of the LDA without SOI, see Fig. 5.12. While intravalley scattering via a $\Gamma$ phonon and intervalley scattering via an X phonon is forbidden by symmetry, the higher order contribution to these mechanisms may be significant. However, within the work of Ravich *et al.* [228, 229] and in the work presented here, the effect of this higher order contribution is taken to be zero. Thus, we are currently investigating the strength of the second order terms to non-polar optical and intervalley scattering in PbTe. Other possible reasons for the discrepancy of our calculated mobilities with experiment are the use of the Maxwell-Boltzmann distribution, parabolic approximation, as well as the temperature dependence

of the effective masses that was not accounted for in this work. Furthermore, while the HSE03 functional obtains an electronic band structure of PbTe that compares very well to experiment, formally speaking *GW* yields a more accurate description. In future work, calculating the deformation potentials of PbTe using the *GW* method may yield different results to those presented here, or at the very least serve as an additional check of our approach.

## 5.8 Electronic properties of PbTe-based materials near the phase transition

While we are not yet certain about the dominant transport processes in PbTe, our calculations allow for speculation on the impact to electronic thermoelectric properties as a result of increased proximity to the ferroelectric phase transition. We anticipate that driving PbTe-based materials to the verge of the phase transition via strain or alloying could preserve their high electrical conductivity and Seebeck coefficient while suppressing the lattice thermal conductivity. Our DFT calculations using HGH pseudopotentials with the LDA exchange-correlation show that biaxial tensile (001) strain of $\sim 1\%$ practically does not change the electronic band structure of PbTe and $PbSe_{0.5}Te_{0.5}$ close to the conduction (valence) band minimum (maxima). Further, we find that the electronic band structure of $Pb_{0.51}Ge_{0.49}Te$ in the vicinity of the conduction (valence) band minimum (maxima) is very similar to that of PbTe. Symmetry analysis [218] and our DFPT [132, 134, 135] calculations show that the electron-phonon coupling elements for the conduction band minimum or the valence band maximum with TO modes at $\Gamma$ in PbTe are zero. These results indicate that the electronic transport properties of PbTe strained close to the phase transition may not be deteriorated by the TO softening.

Driving $Pb_{1-x}Ge_xTe$ and strained $PbSe_{1-x}Te_x$ close to the phase transition substantially reduces the lattice thermal conductivity partly due to mass disorder. However, electronic properties beneficial for a large $ZT$ may also be hampered as a result of increased alloy scattering of the carriers, which we have not considered in our discussion of carrier mobility. Nevertheless, it is possible that the reduction to lattice thermal conductivity will outweigh the potential degradation to electrical conductivity and Seebeck coefficient, resulting in a substantial increase to $ZT$, similar to $Si_{1-x}Ge_x$ alloys [253].

## 5.9 Summary

Using first principles approaches we calculate the mobility of $n$-type Ge and PbTe in the low temperature and low carrier concentration regime. We find excellent agreement for the calculated electronic mobility of Ge compared to experiment. Our deformation potentials are consistent when calculated using DFPT and from band shifts due to strain, demonstrating the robustness of the methods employed within this chapter. We find good agreement with the experimental values of the mobility of PbTe at low temperatures up to 200 K and low doping concentrations circa $10^{18}$ cm$^{-3}$ when our first principles calculations are coupled with the use of the Fröhlich model for polar optical scattering. Further, we see that intravalley acoustic scattering is substantially less important in PbTe compared to Fröhlich interaction within the low carrier density and low temperature regime, and that intervalley and intravalley optical scattering processes are forbidden by symmetry. Nevertheless, resolving the discrepancies between our calculations and experiments at higher temperatures requires further work. Finally, while these calculations shine light on the great difficulties inherent in calculating electronic transport properties in PbTe, they also form the basis for future *ab initio* calculations of the thermoelectric figure of merit in PbTe-based materials.

# Chapter 6

# Conclusion

## 6.1 Conclusion

The aim of this thesis was to propose and investigate a new strategy which could improve the thermoelectric performance of PbTe and PbTe-based materials by exploiting their proximity to the ferroelectric phase transition, which gives rise to their intrinsically low lattice thermal conductivity. We have done this using first principles calculations of the lattice thermal conductivity within the Boltzmann transport framework. While we primarily focused on the impact on thermal transport arising from increased proximity to the phase transition, we have also taken the first steps to obtain electronic thermoelectric properties using *ab initio* calculations. This will form the basis of future calculations of the full impact of driving PbTe-based materials near the phase transition on the thermoelectric figure of merit.

We have predicted that driving PbTe to the verge of the ferroelectric phase transition via biaxial tensile (001) strain or alloying will be an effective strategy to impede phonon flow in the entire frequency spectrum, and thus to considerably reduce the lattice thermal conductivity. This proposed concept is based on the induced softening of the transverse optical modes at the zone centre, whose increased anharmonic interaction with heat carrying acoustic modes enhances phonon scattering. We have demonstrated this strategy by applying biaxial tensile (001) strain to PbTe to induce a maximally softened TO mode at the zone centre, substantially increasing anharmonic acoustic-TO interaction. As a direct result of this anharmonic phonon lifetimes are reduced by a factor of $\sim$2 across the frequency spectrum, and we achieve a reduction in the lattice thermal conductivity by a factor of 1.5. Subsequently, we applied biaxial tensile (001) strain to $PbSe_{0.5}Te_{0.5}$ alloy and found a reduction in the lattice thermal

conductivity by a factor of ∼2.4 with respect to that of PbTe. This decrease arises from the combination of reduced anharmonic phonon lifetimes and mass disorder. Finally, we alloyed PbTe with a rhombohedral material, GeTe, demonstrating a strategy to drive PbTe towards the verge of the phase transition which does not rely on strain. Ultimately, in $PbGe_{0.51}Te_{0.49}$ alloy we achieve a reduction in the lattice thermal conductivity by a factor of ∼2.9 with respect to that of PbTe at 450 K, rivalling the reductions achieved through the use of all-scale hierarchical architecturing [34]. The presented strategy is general, and would be applicable to other materials close to soft zone centre optical mode transitions.

Furthermore, we have shown explicitly that the substantial decrease of the anharmonic phonon lifetimes in strained PbTe and PbTe alloys driven to the phase transition is a direct consequence of the maximally softened TO modes and their increased anharmonic coupling with acoustic modes. We found that the acoustic-TO contribution to the linewidth dominates over all other contributions for PbTe, and increases by a factor of $2-3$ throughout the spectrum in PbTe driven to the verge of the phase transition via biaxial tensile (001) strain or alloying with GeTe. Furthermore, we found that a relatively small number of soft TO modes near the zone centre that interact strongly with acoustic modes play a disproportionally large role in shortening phonon lifetimes.

We further investigated and quantified the impact of proximity to the ferroelectric phase transition on the lattice thermal conductivity of $Pb_{1-x}Ge_xTe$ alloys. We show that the role of anharmonic scattering in limiting lattice thermal conductivity of $Pb_{1-x}Ge_xTe$ alloys is maximized at the phase transition due to the maximized acoustic-optical anharmonic interaction. The total lattice thermal conductivity is further reduced due to mass disorder, which shifts the minimum value away from the phase transition into the rhombohedral composition, where phonon lifetimes due to mass disorder are shortest. Neglecting the mass difference of $Pb_{1-x}Ge_xTe$ alloys, the anharmonic lattice thermal conductivity is comparably suppressed in the rocksalt and rhombohedral phases of the alloy with similar proximities to the phase transition. We thus argue that the structure and its degree of resonant bonding are less critical for suppressing lattice thermal conductivity in these alloys compared with proximity to the phase transition, average atomic mass, and mass disorder.

Moreover, we find that the electronic polarisability of $Pb_{1-x}Ge_xTe$ alloys is maximized at the phase transition, indicative of very strong resonant bonding [150, 169, 187]. IFCs along the [001] direction are also maximised at the phase transition, which coincides with the minimization of the anharmonic lat-

tice thermal conductivity of $Pb_{1-x}Ge_xTe$ alloys. Further, our analysis of the behaviour of short and long range IFCs indicates weaker resonant bonding in the rhombohedral phase compared to the rocksalt one, all of which are consistent with previous reports [150]. However, our lattice thermal conductivity calculations are at variance with the argument that stronger resonant bonding leads to lower thermal conductivity [150]. While it is clear that resonant bonding plays a role in determining the lattice thermal conductivities of group IV-VI and group V materials, more remains to be done before this effect is fully understood.

We have taken the first steps towards a full *ab initio* calculation of the thermoelectric figure of merit for PbTe by calculating the mobility of $n$-type Ge and PbTe limited by electron-phonon interaction. Our calculated electronic mobility for Ge is in very good agreement with experiment. For PbTe, our calculated mobility is in good agreement with experiment at low temperatures up to 200 K and low doping concentrations circa $10^{18}$ $cm^{-3}$ when our first principles calculations are coupled with the use of the Fröhlich model for polar optical scattering. However at room temperature our calculated mobility differs from experiment by a factor of $\sim$2. Disagreements between our results and those within the literature motivated the use of hybrid functionals for PbTe, enabling the inclusion of spin-orbit interaction and capturing the band gap and effective electron masses in excellent agreement with experiment. We found that our calculated deformation potentials, either from DFPT or from band shifts due to strain, agree well with each other. However, further work is necessary to resolve the discrepancies between our calculations and experiments at higher temperatures. Nevertheless, our presented calculations form the basis for future first principles calculations of the thermoelectric efficiency of PbTe-based materials driven near the phase transition.

By exploiting the proximity of PbTe to the ferroelectric phase transition we have demonstrated a new strategy to substantially reduce the lattice thermal conductivity. This may be combined with mass disorder to bring about even larger reductions. Due to the symmetry forbidden electron-phonon coupling between the TO mode at $\Gamma$ and the valence band maximum and conduction band minimum in PbTe [218], electronic properties beneficial for a high figure of merit may not be hindered by increased proximity to the phase transition. Thus, this approach offers new opportunities for suppressing lattice thermal conductivity and potentially greatly enhancing thermoelectric efficiency.

## 6.2 Outlook

Below are some thoughts on the potential directions of future research stemming from this work.

- The most important effect that was neglected in our lattice thermal conductivity calculations is higher than third order anharmonicity. This is of considerable importance for describing the zone centre transverse optical modes in PbTe-based materials near the phase transition, particularly at higher temperatures. One of the current state of the art methods to take such effects into account is the temperature-dependent effective potential approach of Hellman *et al.* [72, 73, 74] which uses *ab initio* molecular dynamics. Temperature dependent IFCs calculated using this approach combined with a solution to the Boltzmann transport equation beyond the relaxation time approximation [59, 60] may be used for future calculations.

- For electronic thermoelectric transport, considerable work remains before a reliable *ab initio* calculation of the figure of merit of PbTe-based materials near the phase transition is obtained. In addition to the approach presented in this thesis, one of the most promising developments for future calculations is the EPW code [254] to compute electron-phonon scattering rates. This makes use of Wannier interpolation schemes [85, 86, 91] to sample the Brillouin zone sufficiently densely and, as of its most recent version, contains a first principles treatment of Fröhlich interaction [88, 255], essential for polar semiconductors. However, this approach must be combined with an accurate description of the electronic band structure and electron-phonon matrix elements of PbTe, while the current EPW implementation includes only the insufficiently accurate LDA/PBE framework.

- SnSe is the current record-breaking thermoelectric material, reaching $ZT \sim$2.6 at 900 K [47]. It undergoes a soft mode phase transition with temperature, which coincides with a minimized lattice thermal conductivity and maximised power factor. While SnSe has been the subject of much research, there exists no thorough quantification of the interplay of proximity to the phase transition, temperature, and phase in minimizing the lattice thermal conductivity. An analysis similar to that of $Pb_{1-x}Ge_xTe$ alloys in this work combined with a study of its electronic transport properties would thus be of significant importance in the drive to improve thermoelectric performance.

- There is a growing trend in the literature towards the use of machine-learning algorithms and high-throughout calculations to scan thousands of materials for desirable properties. Such an approach was used recently by van Roekeghem *et al.* [256] to scan hundreds of semiconducting compounds in the search for low thermal conductivity materials that are also mechanically stable at high temperatures. Phonon dispersions for hundreds of materials may be computed quickly and scanned for potential new materials with high thermoelectric efficiency. In the spirit of this, there are a few features of phonon band structures indicative of low lattice thermal conductivity arising from our work: soft modes at the zone centre and high TO-LO splitting.

- Recent studies have reported extremely low lattice thermal conductivity values in marginally stable rocksalt structures [71, 150, 257, 258], in which it has been claimed that the phenomenon of resonant bonding plays a key role for group IV-VI compounds [150, 169, 170, 187]. Chemically similar near-rocksalt compounds, such as rhombohedral GeTe and orthorhombic SnSe similarly possess low lattice thermal conductivity and have also been linked to this phenomenon. Despite these indications, there remains a lack of a quantitative description within the literature of the exact role of resonant bonding and good thermoelectric performance. Thus, future work may revolve around a more thorough description of this phenomenon.

# Bibliography


[1] J. R. Sootsman, D.-Y. Chung and M. G. Kanatzidis. New and Old Concepts in Thermoelectric Materials. *Angewandte Chemie International Edition*, oct 2009. vol. 48, pages 8616. URL http://dx.doi.org/10.1002/anie.200900598.

[2] http://www.thermoelectrics.caltech.edu/thermoelectrics/history.html.

[3] M. Vedernikov and E. Iordanishvili. A.F. Ioffe and origin of modern semiconductor thermoelectric energy conversion. In *Seventeenth International Conference on Thermoelectrics. Proceedings ICT98 (Cat. No.98TH8365)*. IEEE, 1998 pages 37–42. URL http://dx.doi.org/10.1109/ICT.1998.740313.

[4] Z. H. Dughaish. Lead telluride as a thermoelectric material for thermoelectric power generation. *Physica B: Condensed Matter*, sep 2002. vol. 322, pages 205. URL http://dx.doi.org/10.1016/S0921-4526(02)01187-0.

[5] G. J. Snyder and E. S. Toberer. Complex thermoelectric materials. *Nature Materials*, feb 2008. vol. 7, pages 105. URL http://dx.doi.org/10.1038/nmat2090.

[6] L. E. Bell. Cooling, Heating, Generating Power, and Recovering Waste Heat with Thermoelectric Systems. *Science*, sep 2008. vol. 321, pages 1457. URL http://dx.doi.org/10.1126/science.1158899.

[7] https://flowcharts.llnl.gov.

[8] A. J. Minnich, M. S. Dresselhaus, Z. F. Ren and G. Chen. Bulk nanostructured thermoelectric materials: current research and future prospects. *Energy & Environmental Science*, 2009. vol. 2, pages 466. URL http://dx.doi.org/10.1039/b822664b.

[9] L. D. Hicks and M. S. Dresselhaus. Effect of quantum-well structures on the thermoelectric figure of merit. *Physical Review B*, may 1993. vol. 47, pages 12727. URL https://doi.org/10.1103/PhysRevB.47.12727.

[10] D. Nemir and J. Beck. On the Significance of the Thermoelectric Figure of Merit $Z$. *Journal of Electronic Materials*, sep 2010. vol. 39, pages 1897. URL http://dx.doi.org/10.1007/s11664-009-1060-4.

[11] A. Shakouri. Recent Developments in Semiconductor Thermoelectric Physics and Materials. *Annual Review of Materials Research*, aug 2011. vol. 41, pages 399. URL http://dx.doi.org/10.1146/annurev-matsci-062910-100445.

[12] C. B. Vining. An inconvenient truth about thermoelectrics. *Nature Materials*, feb 2009. vol. 8, pages 83. URL http://dx.doi.org/10.1038/nmat2361.

[13] M. Zebarjadi, K. Esfarjani, M. S. Dresselhaus, Z. F. Ren and G. Chen. Perspectives on thermoelectrics: from fundamentals to device applications. *Energy & Environmental Science*, 2012. vol. 5, pages 5147. URL http://dx.doi.org/10.1039/C1EE02497C.

[14] G. Tan, L.-D. Zhao and M. G. Kanatzidis. Rationally Designing High-Performance Bulk Thermoelectric Materials. *Chemical Reviews*, aug 2016. vol. 116, pages 12123. URL http://dx.doi.org/10.1021/acs.chemrev.6b00255.

[15] R. Franz and G. Wiedemann. Ueber die Wärme-Leitungsfähigkeit der Metalle. *Annalen der Physik*, 1853. vol. 165, pages 497. URL http://dx.doi.org/10.1002/andp.18531650802.

[16] N. Ashcroft and N. Mermin. *Solid State Physics*. Holt, Rinehart and Winston, 1976. URL https://books.google.ie/books?id=1C9HAQAAIAAJ.

[17] A. D. LaLonde, Y. Pei and G. J. Snyder. Reevaluation of $PbTe_{1-x}I_x$ as high performance n-type thermoelectric material. *Energy & Environmental Science*, 2011. vol. 4, page 2090. URL http://dx.doi.org/10.1039/c1ee01314a.

[18] Y. Pei, A. LaLonde, S. Iwanaga and G. J. Snyder. High thermoelectric figure of merit in heavy hole dominated PbTe. *Energy & Environmental Science*, 2011. vol. 4, pages 2085. URL http://dx.doi.org/10.1039/c0ee00456a.

[19] M. Carle, P. Pierrat, C. Lahalle-Gravier, S. Scherrer and H. Scherrer. Transport properties of n-type $Bi_2(Te_{1-x}Se_x)_3$ single crystal solid solutions ($x \leq 0.05$). *Journal of Physics and Chemistry of Solids*, 1995. vol. 56, pages 201. URL http://dx.doi.org/10.1016/0022-3697(94)00166-9.

[20] B. Poudel, Q. Hao, Y. Ma, Y. Lan, A. Minnich, B. Yu, X. Yan, D. Wang, A. Muto, D. Vashaee, X. Chen, J. Liu, M. S. Dresselhaus, G. Chen and Z. Ren. High-Thermoelectric Performance of Nanostructured Bismuth Antimony Telluride Bulk Alloys. *Science*, 2008. vol. 320. URL http://dx.doi.org/10.1126/science.1156446.

[21] C. B. Vining. Silicon Germanium. In D. Rowe (editor), *CRC Handbook of Thermoelectrics*, pages 329–338. CRC Press, 1995. URL `https://books.google.ie/books?id=Crtjc-luHlEC`.

[22] J. P. Heremans, M. S. Dresselhaus, L. E. Bell and D. T. Morelli. When thermoelectrics reached the nanoscale. *Nature Nanotechnology*, jul 2013. vol. 8, pages 471. URL `http://dx.doi.org/10.1038/nnano.2013.129`.

[23] G. S. Nolas, J. Poon and M. Kanatzidis. Recent developments in bulk thermoelectric materials. *MRS Bulletin*, mar 2006. vol. 31, pages 199. URL `http://www.scopus.com/inward/record.url?scp=33645384900&partnerID=8YFLogxK`.

[24] C. Uher, J. Yang, S. Hu, D. T. Morelli and G. P. Meisner. Transport properties of pure and doped *M*NiSn (*M*=Zr, Hf). *Physical Review B*, apr 1999. vol. 59, pages 8615. URL `http://dx.doi.org/10.1103/PhysRevB.59.8615`.

[25] A. D. LaLonde, Y. Pei, H. Wang and G. J. Snyder. Lead telluride alloy thermoelectrics. *Materials Today*, nov 2011. vol. 14, pages 526. URL `http://dx.doi.org/10.1016/S1369-7021(11)70278-4`.

[26] J. An, A. Subedi and D. J. Singh. *Ab initio* phonon dispersions for PbTe. *Solid State Communications*, dec 2008. vol. 148, pages 417. URL `http://dx.doi.org/10.1016/j.ssc.2008.09.027`.

[27] O. Delaire, J. Ma, K. Marty, A. F. May, M. A. McGuire, M.-H. Du, D. J. Singh, A. Podlesnyak, G. Ehlers, M. D. Lumsden and B. C. Sales. Giant anharmonic phonon scattering in PbTe. *Nature Materials*, jun 2011. vol. 10, pages 614. URL `http://dx.doi.org/10.1038/nmat3035`.

[28] T. Shiga, J. Shiomi, J. Ma, O. Delaire, T. Radzynski, A. Lusakowski, K. Esfarjani and G. Chen. Microscopic mechanism of low thermal conductivity in lead telluride. *Physical Review B*, apr 2012. vol. 85, page 155203. URL `http://dx.doi.org/10.1103/PhysRevB.85.155203`.

[29] D. Selli, S. E. Boulfelfel, P. Schapotschnikow, D. Donadio and S. Leoni. Hierarchical thermoelectrics: crystal grain boundaries as scalable phonon scatterers. *Nanoscale*, jan 2016. vol. 8, pages 3729. URL `http://dx.doi.org/10.1039/C5NR05279C`.

[30] G. D. Mahan and J. O. Sofo. The best thermoelectric. *Proceedings of the National Academy of Sciences*, 1996. vol. 93, pages 7436. URL `http://www.pnas.org/content/93/15/7436.abstract`.

[31] J. P. Heremans, V. Jovovic, E. S. Toberer, A. Saramat, K. Kurosaki, A. Charoenphakdee, S. Yamanaka and G. J. Snyder. Enhancement of Thermoelectric Efficiency in PbTe by Distortion of the Electronic Density of States. *Science*, jul 2008. vol. 321, pages 554. URL `http://dx.doi.org/10.1126/science.1159725`.

[32] Y. Gelbstein, Z. Dashevsky and M. Dariel. High performance n-type PbTe-based materials for thermoelectric applications. *Physica B: Condensed Matter*, 2005. vol. 363, pages 196. URL `http://dx.doi.org/10.1016/j.physb.2005.03.022`.

[33] Y. Pei, J. Lensch-Falk, E. S. Toberer, D. L. Medlin and G. J. Snyder. High Thermoelectric Performance in PbTe Due to Large Nanoscale $Ag_2Te$ Precipitates and La Doping. *Advanced Functional Materials*, jan 2011. vol. 21, pages 241. URL `http://dx.doi.org/10.1002/adfm.201000878`.

[34] K. Biswas, J. He, I. D. Blum, C.-I. Wu, T. P. Hogan, D. N. Seidman, V. P. Dravid and M. G. Kanatzidis. High-performance bulk thermoelectrics with all-scale hierarchical architectures. *Nature*, sep 2012. vol. 489, pages 414. URL `http://dx.doi.org/10.1038/nature11439`.

[35] Y. Pei, X. Shi, A. LaLonde, H. Wang, L. Chen and G. J. Snyder. Convergence of electronic bands for high performance bulk thermoelectrics. *Nature*, may 2011. vol. 473, pages 66. URL `http://dx.doi.org/10.1038/nature09996`.

[36] D. Wu, L.-D. Zhao, S. Hao, Q. Jiang, F. Zheng, J. W. Doak, H. Wu, H. Chi, Y. Gelbstein, C. Uher, C. Wolverton, M. Kanatzidis and J. He. Origin of the High Performance in GeTe-Based Thermoelectric Materials upon $Bi_2Te_3$ Doping. *Journal of the American Chemical Society*, aug 2014. vol. 136, pages 11412. URL `http://dx.doi.org/10.1021/ja504896a`.

[37] M. Hong, Z.-G. Chen, Y. Pei, L. Yang and J. Zou. Limit of $zT$ enhancement in rocksalt structured chalcogenides by band convergence. *Physical Review B*, oct 2016. vol. 94, page 161201. URL `http://dx.doi.org/10.1103/PhysRevB.94.161201`.

[38] Y. Lee, S.-H. Lo, J. Androulakis, C.-I. Wu, L.-D. Zhao, D.-Y. Chung, T. P. Hogan, V. P. Dravid and M. G. Kanatzidis. High-Performance Tellurium-Free Thermoelectrics: All-Scale Hierarchical Structuring of p-Type PbSe–MSe Systems (M = Ca, Sr, Ba). *Journal of the American Chemical Society*, apr 2013. vol. 135, pages 5152. URL `http://dx.doi.org/10.1021/ja400069s`.

[39] L. D. Zhao, H. J. Wu, S. Q. Hao, C. I. Wu, X. Y. Zhou, K. Biswas, J. Q. He, T. P. Hogan, C. Uher, C. Wolverton, V. P. Dravid and M. G. Kanatzidis. All-scale hierarchical thermoelectrics: MgTe in PbTe facilitates valence band convergence and suppresses bipolar thermal transport for high performance.

*Energy & Environmental Science*, 2013. vol. 6, page 3346. URL http://dx.doi.org/10.1039/c3ee42187b.

[40] G. Tan, L.-D. Zhao, F. Shi, J. W. Doak, S.-H. Lo, H. Sun, C. Wolverton, V. P. Dravid, C. Uher and M. G. Kanatzidis. High Thermoelectric Performance of p-Type SnTe via a Synergistic Band Engineering and Nanostructuring Approach. *Journal of the American Chemical Society*, may 2014. vol. 136, pages 7006. URL http://dx.doi.org/10.1021/ja500860m.

[41] L.-D. Zhao, V. P. Dravid and M. G. Kanatzidis. The panoscopic approach to high performance thermoelectrics. *Energy & Environmental Science*, 2014. vol. 7, pages 251. URL http://dx.doi.org/10.1039/C3EE43099E.

[42] M. S. Dresselhaus, G. Chen, M. Y. Tang, R. G. Yang, H. Lee, D. Z. Wang, Z. F. Ren, J.-P. Fleurial and P. Gogna. New Directions for Low-Dimensional Thermoelectric Materials. *Advanced Materials*, apr 2007. vol. 19, pages 1043. URL http://dx.doi.org/10.1002/adma.200600527.

[43] L. D. Hicks and M. S. Dresselhaus. Thermoelectric figure of merit of a one-dimensional conductor. *Physical Review B*, jun 1993. vol. 47, pages 16631. URL http://dx.doi.org/10.1103/PhysRevB.47.16631.

[44] M. G. Kanatzidis. Nanostructured Thermoelectrics: The New Paradigm? *Chemistry of Materials*, feb 2010. vol. 22, pages 648. URL http://dx.doi.org/10.1021/cm902195j.

[45] P. F. P. Poudeu, J. D'Angelo, H. Kong, A. Downey, J. L. Short, R. Pcionek, T. P. Hogan, C. Uher and M. G. Kanatzidis. Nanostructures versus Solid Solutions: Low Lattice Thermal Conductivity and Enhanced Thermoelectric Figure of Merit in $Pb_{9.6}Sb_{0.2}Te_{10-x}Se_x$ Bulk Materials. *Journal of the American Chemical Society*, nov 2006. vol. 128, pages 14347. URL http://dx.doi.org/10.1021/ja0647811.

[46] J. Androulakis, C.-H. Lin, H.-J. Kong, C. Uher, C.-I. Wu, T. Hogan, B. A. Cook, T. Caillat, K. M. Paraskevopoulos and M. G. Kanatzidis. Spinodal Decomposition and Nucleation and Growth as a Means to Bulk Nanostructured Thermoelectrics: Enhanced Performance in $Pb_{1-x}Sn_xTe$-PbS. *Journal of the American Chemical Society*, 2007. vol. 129, pages 9780. URL http://dx.doi.org/10.1021/ja071875h.

[47] L.-D. Zhao, S.-H. Lo, Y. Zhang, H. Sun, G. Tan, C. Uher, C. Wolverton, V. P. Dravid and M. G. Kanatzidis. Ultralow thermal conductivity and high thermoelectric figure of merit in SnSe crystals. *Nature*, apr 2014. vol. 508, pages 373. URL http://dx.doi.org/10.1038/nature13184.

[48] C. W. Li, J. Hong, A. F. May, D. Bansal, S. Chi, T. Hong, G. Ehlers and O. Delaire. Orbitally driven giant phonon anharmonicity in SnSe. *Nature Physics*, dec 2015. vol. 11, pages 1063. URL http://dx.doi.org/10.1038/nphys3492.

[49] J. M. Skelton, L. A. Burton, S. C. Parker, A. Walsh, C.-E. Kim, A. Soon, J. Buckeridge, A. A. Sokol, C. R. A. Catlow, A. Togo and I. Tanaka. Anharmonicity in the High-Temperature *Cmcm* Phase of SnSe: Soft Modes and Three-Phonon Interactions. *Physical Review Letters*, aug 2016. vol. 117, page 075502. URL http://dx.doi.org/10.1103/PhysRevLett.117.075502.

[50] L.-D. Zhao, G. Tan, S. Hao, J. He, Y. Pei, H. Chi, H. Wang, S. Gong, H. Xu, V. P. Dravid, C. Uher, G. J. Snyder, C. Wolverton and M. G. Kanatzidis. Ultrahigh power factor and thermoelectric performance in hole-doped single-crystal SnSe. *Science*, jan 2016. vol. 351, pages 141. URL http://dx.doi.org/10.1126/science.aad3749.

[51] G. P. Srivastava. *The Physics of Phonons*. Taylor & Francis Group, New York, U.S.A., 1990. URL https://books.google.ie/books?id=0E-bHd2gzVgC.

[52] P. K. Schelling, S. R. Phillpot and P. Keblinski. Comparison of atomic-level simulation methods for computing thermal conductivity. *Physical Review B*, apr 2002. vol. 65, page 144306. URL http://dx.doi.org/10.1103/PhysRevB.65.144306.

[53] F. Müller-Plathe. A simple nonequilibrium molecular dynamics method for calculating the thermal conductivity. *The Journal of Chemical Physics*, 1997. vol. 106, page 6082. URL http://dx.doi.org/10.1063/1.473271.

[54] M. Omini and A. Sparavigna. An iterative approach to the phonon Boltzmann equation in the theory of thermal conductivity. *Physica B: Condensed Matter*, jul 1995. vol. 212, pages 101. URL http://dx.doi.org/10.1016/0921-4526(95)00016-3.

[55] M. Omini and A. Sparavigna. Beyond the isotropic-model approximation in the theory of thermal conductivity. *Physical Review B*, apr 1996. vol. 53, pages 9064. URL http://dx.doi.org/10.1103/PhysRevB.53.9064.

[56] M. Omini and A. Sparavigna. Heat transport in dielectric solids with diamond structure. *Il Nuovo Cimento D*, 1997. vol. 19, pages 1537. URL https://www.sif.it/riviste/ncd/econtents/1997/019/10/article/5.

[57] A. Sparavigna. Influence of isotope scattering on the thermal conductivity of diamond. *Physical Review B*, jan 2002. vol. 65, page 064305. URL http://dx.doi.org/10.1103/PhysRevB.65.064305.

[58] A. Sparavigna. Lattice thermal conductivity in cubic silicon carbide. *Physical Review B*, nov 2002. vol. 66, page 174301. URL http://dx.doi.org/10.1103/PhysRevB.66.174301.

[59] D. A. Broido, A. Ward and N. Mingo. Lattice thermal conductivity of silicon from empirical interatomic potentials. *Physical Review B*, jul 2005. vol. 72, page 014308. URL http://dx.doi.org/10.1103/PhysRevB.72.014308.

[60] D. A. Broido, M. Malorny, G. Birner, N. Mingo and D. A. Stewart. Intrinsic lattice thermal conductivity of semiconductors from first principles. *Applied Physics Letters*, dec 2007. vol. 91, page 231922. URL http://dx.doi.org/10.1063/1.2822891.

[61] A. Ward, D. A. Broido, D. A. Stewart and G. Deinzer. *Ab initio* theory of the lattice thermal conductivity in diamond. *Physical Review B*, sep 2009. vol. 80, page 125203. URL http://dx.doi.org/10.1103/PhysRevB.80.125203.

[62] Y. He, I. Savić, D. Donadio and G. Galli. Lattice thermal conductivity of semiconducting bulk materials: atomistic simulations. *Physical Chemistry Chemical Physics*, 2012. vol. 14, page 16209. URL http://dx.doi.org/10.1039/c2cp42394d.

[63] K. Esfarjani, G. Chen and H. T. Stokes. Heat transport in silicon from first-principles calculations. *Physical Review B*, aug 2011. vol. 84, page 085204. URL http://dx.doi.org/10.1103/PhysRevB.84.085204.

[64] J. Garg, N. Bonini, B. Kozinsky and N. Marzari. Role of Disorder and Anharmonicity in the Thermal Conductivity of Silicon-Germanium Alloys: A First-Principles Study. *Physical Review Letters*, jan 2011. vol. 106, page 045901. URL http://dx.doi.org/10.1103/PhysRevLett.106.045901.

[65] L. Lindsay, D. A. Broido and T. L. Reinecke. *Ab initio* thermal transport in compound semiconductors. *Physical Review B*, apr 2013. vol. 87, page 165201. URL http://dx.doi.org/10.1103/PhysRevB.87.165201.

[66] A. H. Romero, E. K. U. Gross, M. J. Verstraete and O. Hellman. Thermal conductivity in PbTe from first principles. *Physical Review B*, jun 2015. vol. 91, page 214310. URL http://dx.doi.org/10.1103/PhysRevB.91.214310.

[67] W. Li, L. Lindsay, D. A. Broido, D. A. Stewart and N. Mingo. Thermal conductivity of bulk and nanowire $Mg_2Si_xSn_{1-x}$ alloys from first principles. *Physical Review B*, nov 2012. vol. 86, page 174307. URL http://dx.doi.org/10.1103/PhysRevB.86.174307.

[68] L. Lindsay. First Principles Peierls-Boltzmann Phonon Thermal Transport: A Topical Review. *Nanoscale and Microscale Thermophysical Engineering*, aug 2016. vol. 20, pages 67. URL http://dx.doi.org/10.1080/15567265.2016.1218576.

[69] G. Fugallo, A. Cepellotti, L. Paulatto, M. Lazzeri, N. Marzari and F. Mauri. Thermal Conductivity of Graphene and Graphite: Collective Excitations and Mean Free Paths. *Nano Letters*, nov 2014. vol. 14, pages 6109. URL http://dx.doi.org/10.1021/nl502059f.

[70] L. Lindsay, W. Li, J. Carrete, N. Mingo, D. A. Broido and T. L. Reinecke. Phonon thermal transport in strained and unstrained graphene from first principles. *Physical Review B*, apr 2014. vol. 89, page 155426. URL http://dx.doi.org/10.1103/PhysRevB.89.155426.

[71] M. D. Nielsen, V. Ozolins and J. P. Heremans. Lone pair electrons minimize lattice thermal conductivity. *Energy & Environmental Science*, 2013. vol. 6, pages 570. URL http://dx.doi.org/10.1039/C2EE23391F.

[72] O. Hellman, I. A. Abrikosov and S. I. Simak. Lattice dynamics of anharmonic solids from first principles. *Physical Review B*, nov 2011. vol. 84, page 180301. URL http://dx.doi.org/10.1103/PhysRevB.84.180301.

[73] O. Hellman, P. Steneteg, I. A. Abrikosov and S. I. Simak. Temperature dependent effective potential method for accurate free energy calculations of solids. *Physical Review B*, mar 2013. vol. 87, page 104111. URL http://dx.doi.org/10.1103/PhysRevB.87.104111.

[74] O. Hellman and I. A. Abrikosov. Temperature-dependent effective third-order interatomic force constants from first principles. *Physical Review B*, oct 2013. vol. 88, page 144301. URL http://dx.doi.org/10.1103/PhysRevB.88.144301.

[75] A. van Roekeghem, J. Carrete and N. Mingo. Anomalous thermal conductivity and suppression of negative thermal expansion in $ScF_3$. *Physical Review B*, jul 2016. vol. 94, page 020303. URL http://dx.doi.org/10.1103/PhysRevB.94.020303.

[76] P. Souvatzis, O. Eriksson, M. I. Katsnelson and S. P. Rudin. Entropy Driven Stabilization of Energetically Unstable Crystal Structures Explained from First Principles Theory. *Physical Review Letters*, mar 2008. vol. 100, page 095901. URL http://dx.doi.org/10.1103/PhysRevLett.100.095901.

[77] B. K. Ridley. *Quantum Processes in Semiconductors*. Oxford University Press, fourth edn., 1999. URL https://books.google.ie/books?id=am1R-6dsI%5C_4C.

[78] T. J. Scheidemantel, C. Ambrosch-Draxl, T. Thonhauser, J. V. Badding and J. O. Sofo. Transport coefficients from first-principles calculations. *Physical Review B*, sep 2003. vol. 68, page 125210. URL http://dx.doi.org/10.1103/PhysRevB.68.125210.

[79] C. Herring and E. Vogt. Transport and Deformation-Potential Theory for Many-Valley Semiconductors with Anisotropic Scattering. *Physical Review*, feb 1956. vol. 101, pages 944. URL http://dx.doi.org/10.1103/PhysRev.101.944.

[80] C. Jacoboni and L. Reggiani. The Monte Carlo method for the solution of charge transport in semiconductors with applications to covalent materials. *Reviews of Modern Physics*, jul 1983. vol. 55, pages 645. URL http://dx.doi.org/10.1103/RevModPhys.55.645.

[81] A. Abramo, L. Baudry, R. Brunetti, R. Castagne, M. Charef, F. Dessenne, P. Dollfus, R. Dutton, W. Engl, R. Fauquembergue, C. Fiegna, M. Fischetti, S. Galdin, N. Goldsman, M. Hackel, C. Hamaguchi, K. Hess, K. Hennacy, P. Hesto, J. Higman, T. Iizuka, C. Jungemann, Y. Kamakura, H. Kosina, T. Kunikiyo, S. Laux, Hongchin Lin, C. Maziar, H. Mizuno, H. Peifer, S. Ramaswamy, N. Sano, P. Scrobohaci, S. Selberherr, M. Takenaka, Ting-Wei Tang, K. Taniguchi, J. Thobel, R. Thoma, K. Tomizawa, M. Tomizawa, T. Vogelsang, Shiuh-Luen Wang, Xiaolin Wang, Chiang-Sheng Yao, P. Yoder and A. Yoshii. A comparison of numerical solutions of the Boltzmann transport equation for high-energy electron transport silicon. *IEEE Transactions on Electron Devices*, sep 1994. vol. 41, pages 1646. URL http://dx.doi.org/10.1109/16.310119.

[82] B. Xu and M. J. Verstraete. First Principles Explanation of the Positive Seebeck Coefficient of Lithium. *Physical Review Letters*, may 2014. vol. 112, page 196603. URL http://dx.doi.org/10.1103/PhysRevLett.112.196603.

[83] F. Murphy-Armando and S. Fahy. First-principles calculation of carrier-phonon scattering in $n$-type $Si_{1-x}Ge_x$ alloys. *Physical Review B*, jul 2008. vol. 78, page 035202. URL http://dx.doi.org/10.1103/PhysRevB.78.035202.

[84] J. Sjakste, N. Vast and V. Tyuterev. *Ab Initio* Method for Calculating Electron-Phonon Scattering Times in Semiconductors: Application to GaAs and GaP. *Physical Review Letters*, dec 2007. vol. 99, page 236405. URL http://dx.doi.org/10.1103/PhysRevLett.99.236405.

[85] F. Giustino, M. L. Cohen and S. G. Louie. Electron-phonon interaction using Wannier functions. *Physical Review B*, oct 2007. vol. 76, page 165108. URL http://dx.doi.org/10.1103/PhysRevB.76.165108.

[86] F. Giustino, J. R. Yates, I. Souza, M. L. Cohen and S. G. Louie. Electron-Phonon Interaction via Electronic and Lattice Wannier Functions: Superconductivity in Boron-Doped Diamond Reexamined. *Physical Review Letters*, jan 2007. vol. 98, page 047005. URL `http://dx.doi.org/10.1103/PhysRevLett.98.047005`.

[87] O. D. Restrepo, K. Varga and S. T. Pantelides. First-principles calculations of electron mobilities in silicon: Phonon and Coulomb scattering. *Applied Physics Letters*, may 2009. vol. 94, page 212103. URL `http://dx.doi.org/10.1063/1.3147189`.

[88] J. Sjakste, N. Vast, M. Calandra and F. Mauri. Wannier interpolation of the electron-phonon matrix elements in polar semiconductors: Polar-optical coupling in GaAs. *Physical Review B*, aug 2015. vol. 92, page 054307. URL `http://dx.doi.org/10.1103/PhysRevB.92.054307`.

[89] M. Fiorentini and N. Bonini. Thermoelectric coefficients of $n$-doped silicon from first principles via the solution of the Boltzmann transport equation. *Physical Review B*, aug 2016. vol. 94, page 085204. URL `http://dx.doi.org/10.1103/PhysRevB.94.085204`.

[90] M. Lüders, M. A. L. Marques, N. N. Lathiotakis, A. Floris, G. Profeta, L. Fast, A. Continenza, S. Massidda and E. K. U. Gross. *Ab initio* theory of superconductivity. I. Density functional formalism and approximate functionals. *Physical Review B*, jul 2005. vol. 72, page 024546. URL `http://dx.doi.org/10.1103/PhysRevB.72.024545`.

[91] M. Calandra, G. Profeta and F. Mauri. Adiabatic and nonadiabatic phonon dispersion in a Wannier function approach. *Physical Review B*, oct 2010. vol. 82, page 165111. URL `http://dx.doi.org/10.1103/PhysRevB.82.165111`.

[92] P. Vogl. Microscopic theory of electron-phonon interaction in insulators or semiconductors. *Physical Review B*, jan 1976. vol. 13, pages 694. URL `http://dx.doi.org/10.1103/PhysRevB.13.694`.

[93] T.-H. Liu, J. Zhou, B. Liao, D. J. Singh and G. Chen. First-principles mode-by-mode analysis for electron-phonon scattering channels and mean free path spectra in GaAs. *Physical Review B*, feb 2017. vol. 95, page 075206. URL `http://dx.doi.org/10.1103/PhysRevB.95.075206`.

[94] J.-J. Zhou and M. Bernardi. *Ab initio* electron mobility and polar phonon scattering in GaAs. *Physical Review B*, nov 2016. vol. 94, page 201201. URL `http://dx.doi.org/10.1103/PhysRevB.94.201201`.

[95] J. Bardeen and W. Shockley. Deformation Potentials and Mobilities in Non-Polar Crystals. *Physical Review*, oct 1950. vol. 80, pages 72. URL http://dx.doi.org/10.1103/PhysRev.80.72.

[96] M. Born and R. Oppenheimer. Zur Quantentheorie der Molekeln. *Annalen der Physik*, 1927. vol. 389, pages 457. URL http://dx.doi.org/10.1002/andp.19273892002.

[97] P. Hohenberg and W. Kohn. Inhomogeneous Electron Gas. *Physical Review*, nov 1964. vol. 136, pages B864. URL http://dx.doi.org/10.1103/PhysRev.136.B864.

[98] R. O. Jones. Density functional theory: Its origins, rise to prominence, and future. *Reviews of Modern Physics*, aug 2015. vol. 87, pages 897. URL http://dx.doi.org/10.1103/RevModPhys.87.897.

[99] S. Baroni, S. de Gironcoli, A. Dal Corso and P. Giannozzi. Phonons and related crystal properties from density-functional perturbation theory. *Reviews of Modern Physics*, jul 2001. vol. 73, pages 515. URL http://dx.doi.org/10.1103/RevModPhys.73.515.

[100] R. O. Jones and O. Gunnarsson. The density functional formalism, its applications and prospects. *Reviews of Modern Physics*, jul 1989. vol. 61, pages 689. URL http://dx.doi.org/10.1103/RevModPhys.61.689.

[101] W. Kohn and L. J. Sham. Self-Consistent Equations Including Exchange and Correlation Effects. *Physical Review*, nov 1965. vol. 140, pages A1133. URL http://dx.doi.org/10.1103/PhysRev.140.A1133.

[102] P.-O. Löwdin. Quantum Theory of Many-Particle Systems. III. Extension of the Hartree-Fock Scheme to Include Degenerate Systems and Correlation Effects. *Physical Review*, mar 1955. vol. 97, pages 1509. URL http://dx.doi.org/10.1103/PhysRev.97.1509.

[103] V. Sahni. Physical interpretation of density-functional theory and of its representation of the Hartree-Fock and Hartree theories. *Physical Review A*, mar 1997. vol. 55, pages 1846. URL http://dx.doi.org/10.1103/PhysRevA.55.1846.

[104] M. C. Payne, M. P. Teter, D. C. Allan, T. A. Arias and J. D. Joannopoulos. Iterative minimization techniques for *ab initio* total-energy calculations: molecular dynamics and conjugate gradients. *Reviews of Modern Physics*, oct 1992. vol. 64, pages 1045. URL http://dx.doi.org/10.1103/RevModPhys.64.1045.

[105] H. J. Monkhorst and J. D. Pack. Special points for Brillouin-zone integrations. *Physical Review B*, jun 1976. vol. 13, pages 5188. URL http://dx.doi.org/10.1103/PhysRevB.13.5188.

[106] J. C. Phillips. Energy-Band Interpolation Scheme Based on a Pseudopotential. *Physical Review*, nov 1958. vol. 112, pages 685. URL http://dx.doi.org/10.1103/PhysRev.112.685.

[107] J. C. Phillips and L. Kleinman. New Method for Calculating Wave Functions in Crystals and Molecules. *Physical Review*, oct 1959. vol. 116, pages 287. URL http://dx.doi.org/10.1103/PhysRev.116.287.

[108] W. E. Pickett. Pseudopotential methods in condensed matter applications. *Computer Physics Reports*, apr 1989. vol. 9, pages 115. URL http://dx.doi.org/10.1016/0167-7977(89)90002-6.

[109] D. R. Hamann, M. Schlüter and C. Chiang. Norm-Conserving Pseudopotentials. *Physical Review Letters*, nov 1979. vol. 43, pages 1494. URL http://dx.doi.org/10.1103/PhysRevLett.43.1494.

[110] C. Hartwigsen, S. Goedecker and J. Hutter. Relativistic separable dual-space Gaussian pseudopotentials from H to Rn. *Physical Review B*, aug 1998. vol. 58, pages 3641. URL http://dx.doi.org/10.1103/PhysRevB.58.3641.

[111] W. Kohn. Nobel Lecture: Electronic structure of matter—wave functions and density functionals. *Reviews of Modern Physics*, oct 1999. vol. 71, pages 1253. URL http://dx.doi.org/10.1103/RevModPhys.71.1253.

[112] M. Schlesinger. *Modern Aspects of Electrochemistry No. 44: Modelling and Numerical Simulations II*. Springer New York, 2009. URL http://dx.doi.org/10.1007/978-0-387-49586-6.

[113] S. Goedecker, M. Teter and J. Hutter. Separable dual-space Gaussian pseudopotentials. *Physical Review B*, jul 1996. vol. 54, pages 1703. URL http://dx.doi.org/10.1103/PhysRevB.54.1703.

[114] J. P. Perdew, J. A. Chevary, S. H. Vosko, K. A. Jackson, M. R. Pederson, D. J. Singh and C. Fiolhais. Atoms, molecules, solids, and surfaces: Applications of the generalized gradient approximation for exchange and correlation. *Physical Review B*, sep 1992. vol. 46, pages 6671. URL http://dx.doi.org/10.1103/PhysRevB.46.6671.

[115] J. P. Perdew, K. Burke and M. Ernzerhof. Generalized Gradient Approximation Made Simple. *Physical Review Letters*, oct 1996. vol. 77, pages 3865. URL http://dx.doi.org/10.1103/PhysRevLett.77.3865.

[116] F. Furche and J. P. Perdew. The performance of semilocal and hybrid density functionals in 3*d* transition-metal chemistry. *The Journal of Chemical Physics*, jan 2006. vol. 124, page 044103. URL http://dx.doi.org/10.1063/1.2162161.

[117] R. P. Feynman. Forces in Molecules. *Physical Review*, aug 1939. vol. 56, pages 340. URL http://dx.doi.org/10.1103/PhysRev.56.340.

[118] H. B. Schlegel. Optimization of equilibrium geometries and transition structures. *Journal of Computational Chemistry*, jun 1982. vol. 3, pages 214. URL http://dx.doi.org/10.1002/jcc.540030212.

[119] A. Togo, L. Chaput and I. Tanaka. Distributions of phonon lifetimes in Brillouin zones. *Physical Review B*, mar 2015. vol. 91, page 094306. URL http://dx.doi.org/10.1103/PhysRevB.91.094306.

[120] D. J. Ecsedy and P. G. Klemens. Thermal resistivity of dielectric crystals due to four-phonon processes and optical modes. *Physical Review B*, jun 1977. vol. 15, pages 5957. URL http://dx.doi.org/10.1103/PhysRevB.15.5957.

[121] R. E. Peierls. *Quantum Theory of Solids*. Clarendon Press, Oxford, 1955. URL https://books.google.ie/books?id=WvPcBUsSJBAC.

[122] P. A. M. Dirac. The Quantum Theory of the Emission and Absorption of Radiation. *Proceedings of the Royal Society A: Mathematical, Physical and Engineering Sciences*, mar 1927. vol. 114, pages 243. URL http://dx.doi.org/10.1098/rspa.1927.0039.

[123] E. Fermi. *Nuclear Physics*. University of Chicago Press, 1950. URL https://books.google.ie/books?id=WQtkYCWTcicC.

[124] B. Abeles. Lattice Thermal Conductivity of Disordered Semiconductor Alloys at High Temperatures. *Physical Review*, sep 1963. vol. 131, pages 1906. URL http://dx.doi.org/10.1103/PhysRev.131.1906.

[125] P. Ghosez, D. Desquesnes, X. Gonze and K. M. Rabe. First-principles study of lattice instabilities in $Ba_xSr_{1-x}TiO_3$. In *AIP Conference Proceedings*, vol. 535. AIP, 2000 pages 102–110. URL http://dx.doi.org/10.1063/1.1324445.

[126] S.-i. Tamura. Isotope scattering of dispersive phonons in Ge. *Physical Review B*, jan 1983. vol. 27, pages 858. URL http://dx.doi.org/10.1103/PhysRevB.27.858.

[127] S.-i. Tamura. Isotope scattering of large-wave-vector phonons in GaAs and InSb: Deformation-dipole and overlap-shell models. *Physical Review B*, jul 1984. vol. 30, pages 849. URL http://dx.doi.org/10.1103/PhysRevB.30.849.

[128] T. Murakami, T. Shiga, T. Hori, K. Esfarjani and J. Shiomi. Importance of local force fields on lattice thermal conductivity reduction in $PbTe_{1-x}Se_x$alloys. *EPL (Europhysics Letters)*, may 2013. vol. 102, page 46002. URL http://dx.doi.org/10.1209/0295-5075/102/46002.

[129] A. Togo, F. Oba and I. Tanaka. First-principles calculations of the ferroelastic transition between rutile-type and $CaCl_2$-type $SiO_2$ at high pressures. *Physical Review B*, oct 2008. vol. 78, page 134106. URL http://dx.doi.org/10.1103/PhysRevB.78.134106.

[130] L. Chaput, A. Togo, I. Tanaka and G. Hug. Phonon-phonon interactions in transition metals. *Physical Review B*, sep 2011. vol. 84, page 094302. URL http://dx.doi.org/10.1103/PhysRevB.84.094302.

[131] A. Togo, L. Chaput, I. Tanaka and G. Hug. First-principles phonon calculations of thermal expansion in $Ti_3SiC_2$, $Ti_3AlC_2$, and $Ti_3GeC_2$. *Physical Review B*, may 2010. vol. 81, page 174301. URL http://dx.doi.org/10.1103/PhysRevB.81.174301.

[132] X. Gonze, B. Amadon, P. M. Anglade, J. M. Beuken, F. Bottin, P. Boulanger, F. Bruneval, D. Caliste, R. Caracas, M. Côté, T. Deutsch, L. Genovese, P. Ghosez, M. Giantomassi, S. Goedecker, D. R. Hamann, P. Hermet, F. Jollet, G. Jomard, S. Leroux, M. Mancini, S. Mazevet, M. J. T. Oliveira, G. Onida, Y. Pouillon, T. Rangel, G. M. Rignanese, D. Sangalli, R. Shaltaf, M. Torrent, M. J. Verstraete, G. Zerah and J. W. Zwanziger. ABINIT: First-principles approach to material and nanosystem properties. *Computer Physics Communications*, dec 2009. vol. 180, pages 2582. URL http://dx.doi.org/10.1016/j.cpc.2009.07.007.

[133] A. Togo and I. Tanaka. First principles phonon calculations in materials science. *Scripta Materialia*, 2015. vol. 108, pages 1. URL http://dx.doi.org/10.1016/j.scriptamat.2015.07.021.

[134] X. Gonze and C. Lee. Dynamical matrices, Born effective charges, dielectric permittivity tensors, and interatomic force constants from density-functional perturbation theory. *Physical Review B*, apr 1997. vol. 55, pages 10355. URL http://dx.doi.org/10.1103/PhysRevB.55.10355.

[135] X. Gonze. First-principles responses of solids to atomic displacements and homogeneous electric fields: Implementation of a conjugate-gradient algorithm. *Physical Review B*, apr 1997. vol. 55, pages 10337. URL http://dx.doi.org/10.1103/PhysRevB.55.10337.

[136] Y. Wang, J. J. Wang, W. Y. Wang, Z. G. Mei, S. L. Shang, L. Q. Chen and Z. K. Liu. A mixed-space approach to first-principles calculations of phonon frequencies for polar materials. *Journal of Physics: Condensed Matter*, 2010. vol. 22, page 202201. URL http://dx.doi.org/10.1088/0953-8984/22/20/202201.

[137] G. Benenti, G. Casati, K. Saito and R. S. Whitney. Fundamental aspects of steady-state conversion of heat to work at the nanoscale. *Physics Reports*, 2017. vol. 694, pages 1. URL http://dx.doi.org/10.1016/J.PHYSREP.2017.05.008.

[138] F. Giustino. Electron-phonon interactions from first principles. *Reviews of Modern Physics*, feb 2017. vol. 89, page 015003. URL http://dx.doi.org/10.1103/RevModPhys.89.015003.

[139] T. Gunst, T. Markussen, K. Stokbro and M. Brandbyge. First-principles method for electron-phonon coupling and electron mobility: Applications to two-dimensional materials. *Physical Review B*, jan 2016. vol. 93, page 035414. URL http://dx.doi.org/10.1103/PhysRevB.93.035414.

[140] W. G. Vandenberghe and M. V. Fischetti. Deformation potentials for band-to-band tunneling in silicon and germanium from first principles. *Applied Physics Letters*, jan 2015. vol. 106, page 013505. URL http://dx.doi.org/10.1063/1.4905591.

[141] T. Kawamura and S. Das Sarma. Phonon-scattering-limited electron mobilities in $Al_xGa_{1-x}As$/GaAs heterojunctions. *Physical Review B*, feb 1992. vol. 45, pages 3612. URL http://dx.doi.org/10.1103/PhysRevB.45.3612.

[142] C. Herring. Transport Properties of a Many-Valley Semiconductor. *Bell System Technical Journal*, mar 1955. vol. 34, pages 237. URL http://dx.doi.org/10.1002/j.1538-7305.1955.tb01472.x.

[143] K. Kaasbjerg, K. S. Thygesen and K. W. Jacobsen. Unraveling the acoustic electron-phonon interaction in graphene. *Physical Review B*, apr 2012. vol. 85, page 165440. URL http://dx.doi.org/10.1103/PhysRevB.85.165440.

[144] S. Baroni, P. Giannozzi and A. Testa. Green's-function approach to linear response in solids. *Physical Review Letters*, may 1987. vol. 58, pages 1861. URL http://dx.doi.org/10.1103/PhysRevLett.58.1861.

[145] X. Gonze. Adiabatic density-functional perturbation theory. *Physical Review A*, aug 1995. vol. 52, pages 1096. URL http://dx.doi.org/10.1103/PhysRevA.52.1096.

[146] K. M. Rabe and J. D. Joannopoulos. *Ab initio* relativistic pseudopotential study of the zero-temperature structural properties of SnTe and PbTe. *Physical Review B*, aug 1985. vol. 32, pages 2302. URL http://dx.doi.org/10.1103/PhysRevB.32.2302.

[147] Y. Zhang, X. Ke, C. Chen, J. Yang and P. R. C. Kent. Thermodynamic properties of PbTe, PbSe, and PbS: First-principles study. *Physical Review B*, jul 2009. vol. 80, page 024304. URL http://dx.doi.org/10.1103/PhysRevB.80.024304.

[148] J. M. Skelton, S. C. Parker, A. Togo, I. Tanaka and A. Walsh. Thermal physics of the lead chalcogenides PbS, PbSe, and PbTe from first principles. *Physical Review B*, may 2014. vol. 89, page 205203. URL `http://dx.doi.org/10.1103/PhysRevB.89.205203`.

[149] Z. Tian, J. Garg, K. Esfarjani, T. Shiga, J. Shiomi and G. Chen. Phonon conduction in PbSe, PbTe, and $PbTe_{1-x}Se_x$ from first-principles calculations. *Physical Review B*, may 2012. vol. 85, page 184303. URL `http://dx.doi.org/10.1103/PhysRevB.85.184303`.

[150] S. Lee, K. Esfarjani, T. Luo, J. Zhou, Z. Tian and G. Chen. Resonant bonding leads to low lattice thermal conductivity. *Nature Communications*, apr 2014. vol. 5, page 3525. URL `http://dx.doi.org/10.1038/ncomms4525`.

[151] K. Esfarjani and H. T. Stokes. Method to extract anharmonic force constants from first principles calculations. *Physical Review B*, apr 2008. vol. 77, page 144112. URL `http://dx.doi.org/10.1103/PhysRevB.77.144112`.

[152] P. G. Klemens. The Scattering of Low-Frequency Lattice Waves by Static Imperfections. *Proceedings of the Physical Society. Section A*, dec 1955. vol. 68, pages 1113. URL `http://dx.doi.org/10.1088/0370-1298/68/12/303`.

[153] W. Cochran, R. A. Crowley, G. Dolling and M. M. Elcombe. The Crystal Dynamics of Lead Telluride. *Proceedings of the Royal Society of London A: Mathematical, Physical and Engineering Sciences*, 1966. vol. 293, page 433. URL `http://dx.doi.org/10.1098/rspa.1966.0182`.

[154] E. D. Devyatkova and I. A. Smirnov. The Effect of Halogen Additions on the Thermal Conductivity of Lead Telluride. *Soviet Physics Solid State, USSR*, 1962. vol. 3, pages 1666.

[155] A. A. El-Sharkawy, A. M. Abou El-Azm, M. I. Kenawy, A. S. Hillal and H. M. Abu-Basha. Thermophysical properties of polycrystalline PbS, PbSe, and PbTe in the temperature range 300-700 K. *International Journal of Thermophysics*, 1983. vol. 4, pages 261. URL `http://dx.doi.org/10.1007/BF00502357`.

[156] X. Gonze, J.-C. Charlier, D. C. Allan and M. P. Teter. Interatomic force constants from first principles: The case of $\alpha$-quartz. *Physical Review B*, nov 1994. vol. 50, pages 13035. URL `http://dx.doi.org/10.1103/PhysRevB.50.13035`.

[157] D. Hohnke, H. Holloway and S. Kaiser. Phase relations and transformations in the system PbTe-GeTe. *Journal of Physics and Chemistry of Solids*, 1972. vol. 33, pages 2053. URL `http://dx.doi.org/10.1016/S0022-3697(72)80235-X`.

[158] L. Lindsay and D. A. Broido. Three-phonon phase space and lattice thermal conductivity in semiconductors. *Journal of Physics: Condensed Matter*, apr 2008. vol. 20, page 165209. URL http://dx.doi.org/10.1088/0953-8984/20/16/165209.

[159] E. D. Devyatkova and V. V. Tikhonov. Scattering of Phonons and Electrons in Solid Solutions. *Soviet Physics Solid State, USSR*, 1965. vol. 7, pages 1427.

[160] J. Akhtar, M. Afzaal, M. A. Vincent, N. A. Burton, I. H. Hillier and P. O'Brien. Low temperature CVD growth of PbS films on plastic substrates. *Chemical Communications*, 2011. vol. 47, page 1991. URL http://dx.doi.org/10.1039/c0cc05036a.

[161] I. Grozdanov. Deposition of Electrically Conductive, Microwave Shielding, and IR-Detecting Inorganic Coatings on Polymer Films. *Chemistry Letters*, mar 1994. vol. 23, pages 551. URL http://dx.doi.org/10.1246/cl.1994.551.

[162] E. S. Božin, C. D. Malliakas, P. Souvatzis, T. Proffen, N. A. Spaldin, M. G. Kanatzidis and S. J. L. Billinge. Entropically stabilized local dipole formation in lead chalcogenides. *Science*, dec 2010. vol. 330, pages 1660. URL http://dx.doi.org/10.1126/science.1192759.

[163] C. W. Li, O. Hellman, J. Ma, A. F. May, H. B. Cao, X. Chen, A. D. Christianson, G. Ehlers, D. J. Singh, B. C. Sales and O. Delaire. Phonon Self-Energy and Origin of Anomalous Neutron Scattering Spectra in SnTe and PbTe Thermoelectrics. *Physical Review Letters*, apr 2014. vol. 112, page 175501. URL http://dx.doi.org/10.1103/PhysRevLett.112.175501.

[164] Z. Lu, J. Li, C. Wang, Y. Li, F. Liu and W. Ao. Effects of Mn substitution on the phases and thermoelectric properties of $Ge_{0.8}Pb_{0.2}Te$ alloy. *Journal of Alloys and Compounds*, feb 2015. vol. 621, pages 345. URL http://dx.doi.org/10.1016/j.jallcom.2014.09.198.

[165] Y. Gelbstein, J. Davidow, S. N. Girard, D.-Y. Chung and M. Kanatzidis. Controlling Metallurgical Phase Separation Reactions of the $Ge_{0.87}Pb_{0.13}Te$ Alloy for High Thermoelectric Performance. *Advanced Energy Materials*, jun 2013. vol. 3, pages 815. URL http://dx.doi.org/10.1002/aenm.201200970.

[166] S. Li, J. Li, Q. Wang, L. Wang, F. Liu and W. Ao. Synthesis and thermoelectric properties of the $(GeTe)_{1-x}(PbTe)_x$ alloys. *Solid State Sciences*, feb 2011. vol. 13, pages 399. URL http://dx.doi.org/10.1016/j.solidstatesciences.2010.11.045.

[167] Y. Gelbstein and J. Davidow. Highly efficient functional $Ge_xPb_{1-x}Te$ based thermoelectric alloys. *Physical Chemistry Chemical Physics*, aug 2014. vol. 16, pages 20120. URL http://dx.doi.org/10.1039/C4CP02399D.

[168] S. Perumal, S. Roychowdhury and K. Biswas. High performance thermoelectric materials and devices based on GeTe. *Journal of Materials Chemistry C*, 2016. vol. 4, pages 7520. URL http://dx.doi.org/10.1039/C6TC02501C.

[169] G. Lucovsky and R. M. White. Effects of Resonance Bonding on the Properties of Crystalline and Amorphous Semiconductors. *Physical Review B*, jul 1973. vol. 8, pages 660. URL http://dx.doi.org/10.1103/PhysRevB.8.660.

[170] K. Shportko, S. Kremers, M. Woda, D. Lencer, J. Robertson and M. Wuttig. Resonant bonding in crystalline phase-change materials. *Nature Materials*, aug 2008. vol. 7, pages 653. URL http://dx.doi.org/10.1038/nmat2226.

[171] P. Fons, A. V. Kolobov, M. Krbal, J. Tominaga, K. S. Andrikopoulos, S. N. Yannopoulos, G. A. Voyiatzis and T. Uruga. Phase transition in crystalline GeTe: Pitfalls of averaging effects. *Physical Review B*, oct 2010. vol. 82, page 155209. URL http://dx.doi.org/10.1103/PhysRevB.82.155209.

[172] E. Steigmeier and G. Harbeke. Soft phonon mode and ferroelectricity in GeTe. *Solid State Communications*, aug 1970. vol. 8, pages 1275. URL http://dx.doi.org/10.1016/0038-1098(70)90619-8.

[173] U. D. Wdowik, K. Parlinski, S. Rols and T. Chatterji. Soft-phonon mediated structural phase transition in GeTe. *Physical Review B*, jun 2014. vol. 89, page 224306. URL http://dx.doi.org/10.1103/PhysRevB.89.224306.

[174] P. Bauer Pereira, I. Sergueev, S. Gorsse, J. Dadda, E. Müller and R. P. Hermann. Lattice dynamics and structure of GeTe, SnTe and PbTe. *Physica Status Solidi (b)*, jul 2013. vol. 250, pages 1300. URL http://dx.doi.org/10.1002/pssb.201248412.

[175] R. Shaltaf, E. Durgun, J.-Y. Raty, P. Ghosez and X. Gonze. Dynamical, dielectric, and elastic properties of GeTe investigated with first-principles density functional theory. *Physical Review B*, nov 2008. vol. 78, page 205203. URL http://dx.doi.org/10.1103/PhysRevB.78.205203.

[176] J. Fabian and P. B. Allen. Thermal Expansion and Grüneisen Parameters of Amorphous Silicon: A Realistic Model Calculation. *Physical Review Letters*, sep 1997. vol. 79, pages 1885. URL http://dx.doi.org/10.1103/PhysRevLett.79.1885.

[177] R. Dalven. A review of the semiconductor properties of PbTe, PbSe, PbS and PbO. *Infrared Physics*, dec 1969. vol. 9, pages 141. URL http://dx.doi.org/10.1016/0020-0891(69)90022-0.

[178] P. K. Schelling and P. Keblinski. Thermal expansion of carbon structures. *Physical Review B*, jul 2003. vol. 68, page 035425. URL http://dx.doi.org/10.1103/PhysRevB.68.035425.

[179] T. Chattopadhyay, J. X. Boucherle and H. G. von Schnering. Neutron diffraction study on the structural phase transition in GeTe. *Journal of Physics C: Solid State Physics*, 1987. vol. 20, pages 1431. URL http://dx.doi.org/10.1088/0022-3719/20/10/012.

[180] T. Chatterji, C. M. N. Kumar and U. D. Wdowik. Anomalous temperature-induced volume contraction in GeTe. *Physical Review B*, feb 2015. vol. 91, page 054110. URL http://dx.doi.org/10.1103/PhysRevB.91.054110.

[181] D. Yang, T. Chatterji, J. A. Schiemer and M. A. Carpenter. Strain coupling, microstructure dynamics, and acoustic mode softening in germanium telluride. *Physical Review B*, apr 2016. vol. 93, page 144109. URL http://dx.doi.org/10.1103/PhysRevB.93.144109.

[182] E. M. Levin, M. F. Besser and R. Hanus. Electronic and thermal transport in GeTe: A versatile base for thermoelectric materials. *Journal of Applied Physics*, aug 2013. vol. 114, page 083713. URL http://dx.doi.org/10.1063/1.4819222.

[183] H. Wiedemeier and P. A. Siemers. The Thermal Expansion of GeS and GeTe. *Zeitschrift für anorganische und allgemeine Chemie*, jun 1977. vol. 431, pages 299. URL http://dx.doi.org/10.1002/zaac.19774310134.

[184] P. Nath and K. L. Chopra. Thermal conductivity of amorphous and crystalline Ge and GeTe films. *Physical Review B*, oct 1974. vol. 10, pages 3412. URL http://dx.doi.org/10.1103/PhysRevB.10.3412.

[185] A. Onodera, I. Sakamoto, Y. Fujii, N. Moˆri and S. Sugai. Structural and electrical properties of GeSe and GeTe at high pressure. *Physical Review B*, oct 1997. vol. 56, pages 7935. URL http://dx.doi.org/10.1103/PhysRevB.56.7935.

[186] J. Goldak, C. S. Barrett, D. Innes and W. Youdelis. Structure of Alpha GeTe. *The Journal of Chemical Physics*, may 1966. vol. 44, pages 3323. URL http://dx.doi.org/10.1063/1.1727231.

[187] P. B. Littlewood and V. Heine. The infrared effective charge in IV-VI compounds. I. A simple one-dimensional model. *Journal of Physics C: Solid State Physics*,

nov 1979. vol. 12, pages 4431. URL http://dx.doi.org/10.1088/0022-3719/12/21/011.

[188] M. P. Jiang, M. Trigo, I. Savić, S. Fahy, É. D. Murray, C. Bray, J. Clark, T. Henighan, M. Kozina, M. Chollet, J. M. Glownia, M. C. Hoffmann, D. Zhu, O. Delaire, A. F. May, B. C. Sales, A. M. Lindenberg, P. Zalden, T. Sato, R. Merlin and D. A. Reis. The origin of incipient ferroelectricity in lead telluride. *Nature Communications*, jul 2016. vol. 7, page 12291. URL http://dx.doi.org/10.1038/ncomms12291.

[189] M. Cohen and S. Louie. *Fundamentals of Condensed Matter Physics*. Cambridge University Press, 2016. URL https://books.google.ie/books?id=KC3xCwAAQBAJ.

[190] W. Zhong, R. D. King-Smith and D. Vanderbilt. Giant LO-TO splittings in perovskite ferroelectrics. *Physical Review Letters*, may 1994. vol. 72, pages 3618. URL http://dx.doi.org/10.1103/PhysRevLett.72.3618.

[191] P. Ghosez, J.-P. Michenaud and X. Gonze. Dynamical atomic charges: The case of $ABO_3$ compounds. *Physical Review B*, sep 1998. vol. 58, pages 6224. URL http://dx.doi.org/10.1103/PhysRevB.58.6224.

[192] U. V. Waghmare, N. A. Spaldin, H. C. Kandpal and R. Seshadri. First-principles indicators of metallicity and cation off-centricity in the IV-VI rocksalt chalcogenides of divalent Ge, Sn, and Pb. *Physical Review B*, mar 2003. vol. 67, page 125111. URL http://dx.doi.org/10.1103/PhysRevB.67.125111.

[193] M. S. Hybertsen and S. G. Louie. *Ab initio* static dielectric matrices from the density-functional approach. I. Formulation and application to semiconductors and insulators. *Physical Review B*, apr 1987. vol. 35, pages 5585. URL http://dx.doi.org/10.1103/PhysRevB.35.5585.

[194] K. M. Rabe and J. D. Joannopoulos. Theory of the structural phase transition of GeTe. *Physical Review B*, oct 1987. vol. 36, pages 6631. URL http://dx.doi.org/10.1103/PhysRevB.36.6631.

[195] T. Matsunaga, P. Fons, A. V. Kolobov, J. Tominaga and N. Yamada. The order-disorder transition in GeTe: Views from different length-scales. *Applied Physics Letters*, dec 2011. vol. 99, page 231907. URL http://dx.doi.org/10.1063/1.3665067.

[196] S. Kastbjerg, N. Bindzus, M. Søndergaard, S. Johnsen, N. Lock, M. Christensen, M. Takata, M. A. Spackman and B. Brummerstedt Iversen. Direct Evidence of Cation Disorder in Thermoelectric Lead Chalcogenides PbTe and PbS. *Advanced*

*Functional Materials*, nov 2013. vol. 23, pages 5477. URL http://dx.doi.org/10.1002/adfm.201300722.

[197] Y. Zhang, X. Ke, P. R. C. Kent, J. Yang and C. Chen. Anomalous Lattice Dynamics near the Ferroelectric Instability in PbTe. *Physical Review Letters*, oct 2011. vol. 107, page 175503. URL http://dx.doi.org/10.1103/PhysRevLett.107.175503.

[198] T. Keiber, F. Bridges and B. C. Sales. Lead Is Not Off Center in PbTe: The Importance of $r$-Space Phase Information in Extended X-Ray Absorption Fine Structure Spectroscopy. *Physical Review Letters*, aug 2013. vol. 111, page 095504. URL http://dx.doi.org/10.1103/PhysRevLett.111.095504.

[199] Y. Chen, X. Ai and C. A. Marianetti. First-Principles Approach to Nonlinear Lattice Dynamics: Anomalous Spectra in PbTe. *Physical Review Letters*, sep 2014. vol. 113, page 105501. URL http://dx.doi.org/10.1103/PhysRevLett.113.105501.

[200] M. V. Fischetti and S. E. Laux. Band structure, deformation potentials, and carrier mobility in strained Si, Ge, and SiGe alloys. *Journal of Applied Physics*, 1996. vol. 80, pages 2234. URL http://dx.doi.org/10.1063/1.363052.

[201] C. G. Van de Walle and R. M. Martin. Theoretical calculations of heterojunction discontinuities in the Si/Ge system. *Physical Review B*, oct 1986. vol. 34, pages 5621. URL http://dx.doi.org/10.1103/PhysRevB.34.5621.

[202] C. G. Van de Walle. Band lineups and deformation potentials in the model-solid theory. *Physical Review B*, jan 1989. vol. 39, pages 1871. URL http://dx.doi.org/10.1103/PhysRevB.39.1871.

[203] C. G. Van de Walle and R. M. Martin. Theoretical study of band offsets at semiconductor interfaces. *Physical Review B*, may 1987. vol. 35, pages 8154. URL http://dx.doi.org/10.1103/PhysRevB.35.8154.

[204] C. G. Van de Walle and R. M. Martin. "Absolute" deformation potentials: Formulation and *ab initio* calculations for semiconductors. *Physical Review Letters*, apr 1989. vol. 62, pages 2028. URL http://dx.doi.org/10.1103/PhysRevLett.62.2028.

[205] K. Hummer, A. Grüneis and G. Kresse. Structural and electronic properties of lead chalcogenides from first principles. *Physical Review B*, may 2007. vol. 75, page 195211. URL http://dx.doi.org/10.1103/PhysRevB.75.195211.

[206] S.-H. Wei and A. Zunger. Electronic and structural anomalies in lead chalcogenides. *Physical Review B*, may 1997. vol. 55, pages 13605. URL http://dx.doi.org/10.1103/PhysRevB.55.13605.

[207] A. Svane, N. E. Christensen, M. Cardona, A. N. Chantis, M. van Schilfgaarde and T. Kotani. Quasiparticle self-consistent *GW* calculations for PbS, PbSe, and PbTe: Band structure and pressure coefficients. *Physical Review B*, jun 2010. vol. 81, page 245120. URL http://dx.doi.org/10.1103/PhysRevB.81.245120.

[208] M. S. Hybertsen and S. G. Louie. Electron correlation in semiconductors and insulators: Band gaps and quasiparticle energies. *Physical Review B*, oct 1986. vol. 34, pages 5390. URL http://dx.doi.org/10.1103/PhysRevB.34.5390.

[209] R. N. Dexter, H. J. Zeiger and B. Lax. Cyclotron Resonance Experiments in Silicon and Germanium. *Physical Review*, nov 1956. vol. 104, pages 637. URL http://dx.doi.org/10.1103/PhysRev.104.637.

[210] J. P. Perdew. Density functional theory and the band gap problem. *International Journal of Quantum Chemistry*, jun 1985. vol. 28, pages 497. URL http://dx.doi.org/10.1002/qua.560280846.

[211] J. Ma and L.-W. Wang. Using Wannier functions to improve solid band gap predictions in density functional theory. *Scientific Reports*, apr 2016. vol. 6, page 24924. URL http://dx.doi.org/10.1038/srep24924.

[212] H. Pascher and G. Bauer. Optical Properties and Low-Dimensional Systems of IV-VI Semiconductors. In D. Khokhlov (editor), *Lead Chalcogenides: Physics and Applications*, pages 211–298. Taylor & Francis, New York, 2003. URL https://books.google.ie/books?id=y4P4Kf399l8C.

[213] R. Dalven. Electronic Structure of PbS, PbSe, and PbTe. In H. Ehrenreich, F. Seitz and D. Turnbull (editors), *Solid State Physics*, vol. 28, pages 179–224. Academic Press, 1974. URL http://dx.doi.org/10.1016/S0081-1947(08)60203-9.

[214] Y. W. Tsang and M. L. Cohen. Calculation of the Temperature Dependence of the Energy Gaps in PbTe and SnTe. *Physical Review B*, feb 1971. vol. 3, pages 1254. URL http://dx.doi.org/10.1103/PhysRevB.3.1254.

[215] N. M. Ravindra and V. K. Srivastava. Properties of PbS, PbSe, and PbTe. *Physica Status Solidi (a)*, mar 1980. vol. 58, pages 311. URL http://dx.doi.org/10.1002/pssa.2210580139.

[216] J. L. Birman, M. Lax and R. Loudon. Intervalley-Scattering Selection Rules in III-V Semiconductors. *Physical Review*, may 1966. vol. 145, pages 620. URL http://dx.doi.org/10.1103/PhysRev.145.620.

[217] C. Jacoboni, F. Nava, C. Canali and G. Ottaviani. Electron drift velocity and diffusivity in germanium. *Physical Review B*, jul 1981. vol. 24, pages 1014. URL http://dx.doi.org/10.1103/PhysRevB.24.1014.

[218] M. Schlüter, G. Martinez and M. L. Cohen. Pressure and temperature dependence of electronic energy levels in PbSe and PbTe. *Physical Review B*, jul 1975. vol. 12, pages 650. URL http://dx.doi.org/10.1103/PhysRevB.12.650.

[219] M. L. Cohen and V. Heine. The Fitting of Pseudopotentials to Experimental Data and Their Subsequent Application. In H. Ehrenreich, F. Seitz and D. Turnbull (editors), *Solid State Physics: Advances in Research and Applications.*, pages 37–248. Elsevier Science, 1970. URL https://books.google.ie/books?id=eyb2hkpLjYwC&dq.

[220] M. S. Dresselhaus, G. Dresselhaus and A. Jorio. *Group Theory: Application to the Physics of Condensed Matter*. Springer Berlin Heidelberg, 2008. URL https://books.google.ie/books?id=sKaH8vrfmnQC.

[221] P. Y. Yu and M. Cardona. *Fundamentals of Semiconductor: Physics and Materials Properties*. Springer Berlin Heidelberg, third edn., 2005. URL https://books.google.ie/books?id=4VQMswEACAAJ.

[222] O. H. Nielsen and R. M. Martin. Stresses in semiconductors: *Ab initio* calculations on Si, Ge, and GaAs. *Physical Review B*, sep 1985. vol. 32, pages 3792. URL http://dx.doi.org/10.1103/PhysRevB.32.3792.

[223] B. Houston, R. E. Strakna and H. S. Belson. Elastic Constants, Thermal Expansion, and Debye Temperature of Lead Telluride. *Journal of Applied Physics*, jul 1968. vol. 39, pages 3913. URL http://dx.doi.org/10.1063/1.1656874.

[224] I. I. Zasavitskii, E. A. de Andrada e Silva, E. Abramof and P. J. McCann. Optical deformation potentials for PbSe and PbTe. *Physical Review B*, sep 2004. vol. 70, page 115302. URL http://dx.doi.org/10.1103/PhysRevB.70.115302.

[225] I. Balslev. Influence of Uniaxial Stress on the Indirect Absorption Edge in Silicon and Germanium. *Physical Review*, mar 1966. vol. 143, pages 636. URL http://dx.doi.org/10.1103/PhysRev.143.636.

[226] D. Mirlin, V. Sapega, I. Karlik and R. Katilius. Hot photoluminescence spectroscopy investigations of L-valley splitting and intervalley scattering in uniaxially stressed gallium arsenide. *Solid State Communications*, mar 1987. vol. 61, pages 799. URL http://dx.doi.org/10.1016/0038-1098(87)90481-9.

[227] L. G. Ferreira. Deformation Potentials of Lead Telluride. *Physical Review*, mar 1965. vol. 137, pages A1601. URL http://dx.doi.org/10.1103/PhysRev.137.A1601.

[228] Y. I. Ravich, B. A. Efimova and V. I. Tamarchenko. Scattering of Current Carriers and Transport Phenomena in Lead Chalcogenides II. Experiment. *Physica Status*

*Solidi (b)*, feb 1971. vol. 43, pages 453. URL http://dx.doi.org/10.1002/pssb.2220430202.

[229] Y. I. Ravich, B. A. Efimova and V. I. Tamarchenko. Scattering of Current Carriers and Transport Phenomena in Lead Chalcogenides I. Theory. *Physica Status Solidi (b)*, jan 1971. vol. 43, pages 11. URL http://dx.doi.org/10.1002/pssb.2220430102.

[230] M. Glicksman. Mobility of Electrons in Germanium-Silicon Alloys. *Physical Review*, jul 1958. vol. 111, pages 125. URL http://dx.doi.org/10.1103/PhysRev.111.125.

[231] R. S. Allgaier and W. W. Scanlon. Mobility of Electrons and Holes in PbS, PbSe, and PbTe between Room Temperature and 4.2°K. *Physical Review*, aug 1958. vol. 111, pages 1029. URL http://dx.doi.org/10.1103/PhysRev.111.1029.

[232] G. Kresse and J. Furthmüller. Efficiency of *ab initio* total energy calculations for metals and semiconductors using a plane-wave basis set. *Computational Materials Science*, jul 1996. vol. 6, pages 15. URL http://dx.doi.org/10.1016/0927-0256(96)00008-0.

[233] G. Kresse and J. Furthmüller. Efficient iterative schemes for *ab initio* total-energy calculations using a plane-wave basis set. *Physical Review B*, oct 1996. vol. 54, pages 11169. URL http://dx.doi.org/10.1103/PhysRevB.54.11169.

[234] J. Paier, R. Hirschl, M. Marsman and G. Kresse. The Perdew–Burke–Ernzerhof exchange-correlation functional applied to the G2-1 test set using a plane-wave basis set. *The Journal of Chemical Physics*, jun 2005. vol. 122, page 234102. URL http://dx.doi.org/10.1063/1.1926272.

[235] P. E. Blöchl. Projector augmented-wave method. *Physical Review B*, dec 1994. vol. 50, pages 17953. URL http://dx.doi.org/10.1103/PhysRevB.50.17953.

[236] G. Kresse and D. Joubert. From ultrasoft pseudopotentials to the projector augmented-wave method. *Physical Review B*, jan 1999. vol. 59, pages 1758. URL http://dx.doi.org/10.1103/PhysRevB.59.1758.

[237] J. Hafner. *Ab initio* simulations of materials using VASP: Density-functional theory and beyond. *Journal of Computational Chemistry*, oct 2008. vol. 29, pages 2044. URL http://dx.doi.org/10.1002/jcc.21057.

[238] http://www.andrew.cmu.edu/user/feenstra/wavetrans/.

[239] R. M. Feenstra, N. Srivastava, Q. Gao, M. Widom, B. Diaconescu, T. Ohta, G. L. Kellogg, J. T. Robinson and I. V. Vlassiouk. Low-energy electron reflectivity

from graphene. *Physical Review B*, jan 2013. vol. 87, page 041406. URL http://dx.doi.org/10.1103/PhysRevB.87.041406.

[240] R. M. Martin. *Electronic Structure: Basic Theory and Practical Methods*. Cambridge University Press, 2004. URL https://books.google.ie/books?id=dmRTFLpSGNsC.

[241] J. P. Perdew, M. Ernzerhof and K. Burke. Rationale for mixing exact exchange with density functional approximations. *The Journal of Chemical Physics*, 1996. vol. 105, pages 9982. URL http://dx.doi.org/10.1063/1.472933.

[242] J. P. Perdew and A. Zunger. Self-interaction correction to density-functional approximations for many-electron systems. *Physical Review B*, 1981. vol. 23, page 5048. URL https://doi.org/10.1103/PhysRevB.23.5048.

[243] J. Heyd, G. E. Scuseria and M. Ernzerhof. Hybrid functionals based on a screened Coulomb potential. *The Journal of Chemical Physics*, may 2003. vol. 118, pages 8207. URL http://dx.doi.org/10.1063/1.1564060.

[244] J. Paier, M. Marsman, K. Hummer, G. Kresse, I. C. Gerber and J. G. Ángyán. Screened hybrid density functionals applied to solids. *The Journal of Chemical Physics*, apr 2006. vol. 124, page 154709. URL http://dx.doi.org/10.1063/1.2187006.

[245] J. Heyd and G. E. Scuseria. Efficient hybrid density functional calculations in solids: Assessment of the Heyd–Scuseria–Ernzerhof screened Coulomb hybrid functional. *The Journal of Chemical Physics*, jul 2004. vol. 121, pages 1187. URL http://dx.doi.org/10.1063/1.1760074.

[246] J. Heyd, G. E. Scuseria and M. Ernzerhof. Erratum: "Hybrid functionals based on a screened Coulomb potential" [J. Chem. Phys. 118, 8207 (2003)]. *The Journal of Chemical Physics*, jun 2006. vol. 124, page 219906. URL http://dx.doi.org/10.1063/1.2204597.

[247] A. V. Krukau, O. A. Vydrov, A. F. Izmaylov and G. E. Scuseria. Influence of the exchange screening parameter on the performance of screened hybrid functionals. *The Journal of Chemical Physics*, dec 2006. vol. 125, page 224106. URL http://dx.doi.org/10.1063/1.2404663.

[248] J. Heyd, J. E. Peralta, G. E. Scuseria and R. L. Martin. Energy band gaps and lattice parameters evaluated with the Heyd-Scuseria-Ernzerhof screened hybrid functional. *The Journal of Chemical Physics*, nov 2005. vol. 123, page 174101. URL http://dx.doi.org/10.1063/1.2085170.

[249] J. Paier, M. Marsman, K. Hummer, G. Kresse, I. C. Gerber and J. G. Ángyán. Erratum: "Screened hybrid density functionals applied to solids" [J. Chem. Phys. 124, 154709 (2006)]. *The Journal of Chemical Physics*, dec 2006. vol. 125, page 249901. URL http://dx.doi.org/10.1063/1.2403866.

[250] J. A. Vergés, D. Glötzel, M. Cardona and O. K. Andersen. Absolute Hydrostatic Deformation Potentials of Tetrahedral Semiconductors. *Physica Status Solidi (b)*, oct 1982. vol. 113, pages 519. URL http://dx.doi.org/10.1002/pssb.2221130217.

[251] L. Kleinman. Comment on the average potential of a Wigner solid. *Physical Review B*, dec 1981. vol. 24, pages 7412. URL http://dx.doi.org/10.1103/PhysRevB.24.7412.

[252] K. Kunc and R. M. Martin. Atomic structure and properties of polar Ge-GaAs(100) interfaces. *Physical Review B*, sep 1981. vol. 24, pages 3445. URL http://dx.doi.org/10.1103/PhysRevB.24.3445.

[253] B. Abeles, D. S. Beers, G. D. Cody and J. P. Dismukes. Thermal Conductivity of Ge-Si Alloys at High Temperatures. *Physical Review*, jan 1962. vol. 125, pages 44. URL http://dx.doi.org/10.1103/PhysRev.125.44.

[254] S. Poncé, E. Margine, C. Verdi and F. Giustino. EPW: Electron–phonon coupling, transport and superconducting properties using maximally localized Wannier functions. *Computer Physics Communications*, dec 2016. vol. 209, pages 116. URL http://dx.doi.org/10.1016/j.cpc.2016.07.028.

[255] C. Verdi and F. Giustino. Fröhlich Electron-Phonon Vertex from First Principles. *Physical Review Letters*, oct 2015. vol. 115, page 176401. URL http://dx.doi.org/10.1103/PhysRevLett.115.176401.

[256] A. van Roekeghem, J. Carrete, C. Oses, S. Curtarolo and N. Mingo. High-Throughput Computation of Thermal Conductivity of High-Temperature Solid Phases: The Case of Oxide and Fluoride Perovskites. *Physical Review X*, dec 2016. vol. 6, page 041061. URL http://dx.doi.org/10.1103/PhysRevX.6.041061.

[257] D. T. Morelli, V. Jovovic and J. P. Heremans. Intrinsically Minimal Thermal Conductivity in Cubic I−V−$VI_2$ Semiconductors. *Physical Review Letters*, jul 2008. vol. 101, page 035901. URL http://dx.doi.org/10.1103/PhysRevLett.101.035901.

[258] E. J. Skoug and D. T. Morelli. Role of Lone-Pair Electrons in Producing Minimum Thermal Conductivity in Nitrogen-Group Chalcogenide Compounds. *Physical*

*Review Letters*, nov 2011. vol. 107, page 235901. URL `http://dx.doi.org/10.1103/PhysRevLett.107.235901`.